A comparison of PCA- and energy-based fault detection and isolation in a physical heated two-tank process

W Wolmarans



orcid.org/0000-0000-0000-0000

Dissertation accepted in fulfilment of the requirements for the degree *Master of Engineering in Computer and Electronic Engineering* at the North-West University

Supervisor: Prof G van Schoor

Co-supervisor: Prof KR Uren

Graduation: November 2022

Student number: 24087459

ABSTRACT

The demands for petrochemical (PC) plant productivity and safety are increasing and with it the need for effective fault detection and isolation (FDI) methods. One of the more well-known and widely tested methods is principal component analysis (PCA), which uses process history as its basis for FDI. Another viable and more recently developed technique, namely energy graph-based visualisation (EGBV), has shown promising FDI results in complex processes.

Comparison studies of FDI methods are a frequent occurrence in literature and with good reason - they provide valuable insight into the strengths and weaknesses of each. For this reason, a valid research question may be asked concerning EGBV and PCA: How does EGBV compare to the more established PCA FDI method? This work aims to answer this question, using a modelled and practical heated two-tank system as the benchmark process.

To address this research question and conduct a fair comparison, the following objectives were followed. First, a literature survey was conducted to clarify the relevant FDI terminology and theory. Subsequently, an existing Simulink® model of the process was modified to match the practical plant's performance, so that it may act as a reference system for the comparison. This system was then used to verify the application of EGBV and PCA, followed by their validation using the practical process data. Finally, an objective comparison was made between EGBV and PCA using the results from the model and the practical system.

The literature survey revealed three key FDI performance metrics that allowed for an

objective comparison between the methods, namely robustness, sensitivity and promptness. The Simulink® model of the heated two-tank process was successfully adapted to match the practical plant specifications and to include twenty process faults varying in type, location and magnitude. The model modifications were verified and subsequently validated using the practical process's results. The model closely resembled the practical plant's performance.

The theory of EGBV and PCA was explained and applied to the model to verify its implementation. Both methods were subsequently validated using practical results. EGBV successfully detected fifteen out of the twenty faults in the practical process, while PCA detected only nine. PCA was found to be the more robust method, exhibiting fewer false alarms than EGBV. The EGBV method, however, responds quicker to faults and is a more sensitive method, depending on the chosen EGBV detection philosophy. EGBV is also found to have superior fault isolation ability compared to PCA. Additionally, EGBV exhibits more ideal FDI method attributes than PCA. Ultimately, the preferred FDI method will depend on the priorities of the plant practitioner.

Keywords: *Fault detection and isolation, Energy graph-based visualisation, Principal component analysis, Heated two-tank process*

CONTENTS

1 Introduction **1**

1.1 Background & motivation 1

1.2 Research question 4

1.3 Research objectives & methodology 5

1.3.1 Literature survey of relevant process monitoring concepts 5

1.3.2 Verification & validation of the heated two-tank process model . . . 5

1.3.3 Application, verification & validation of EGBV 5

1.3.4 Application, verification & validation of PCA 6

1.3.5 Comparison of EGBV & PCA 6

1.4 Dissertation outline 6

2 Literature Survey **8**

2.1 Introduction 8

2.2 Fault monitoring terminology 9

2.2.1 State definitions 9
2.2.2 Function definitions 10
2.3 FDI performance requirements 11
2.4 PCA & data-driven methods 12
2.4.1 Multivariate vs. univariate 13
2.4.2 Applying the data-driven approach 13
2.4.3 PCA-focused studies 15
2.4.4 Comparative PCA studies 18
2.5 Energy-based methods 21
2.5.1 Quantitative vs. qualitative modelling 22
2.5.2 The EGBV approach 23
2.5.3 EGBV case studies 24
2.6 Critical review 27

3 Process Model **29**

3.1 Introduction 29
3.2 Process description 30
3.2.1 Process unit 1 31
3.2.2 Process unit 2 31
3.3 Model derivation 32
3.3.1 Mass balance derivation 32
3.3.2 Energy balance derivation 33
3.4 Model Configuration 35
3.4.1 Process parameters 35
3.4.2 Controller parameters 37

3.4.3 Noise & disturbance parameters . . . 38
3.4.4 Valve modelling . . . 40
3.4.5 Model assumptions . . . 43
3.4.6 Normal operation validation . . . 44
3.5 Fault modelling, verification & validation . . . 47
3.5.1 Fault 1: Clogging . . . 48
3.5.2 Fault 2: Leakage . . . 51
3.5.3 Fault 3: Stuck Valve . . . 55
3.5.4 Fault 4: Sensor Drift . . . 57
3.5.5 Fault 5: Fouling . . . 62
3.6 Conclusion . . . 63

4 Energy graph-based visualisation 65

4.1 Introduction . . . 65
4.2 Feature space . . . 66
4.2.1 The concept of exergy . . . 66
4.2.2 Graph representation . . . 68
4.3 Decision space . . . 70
4.3.1 Node signature matrix development . . . 70
4.3.2 Cost matrix calculation . . . 73
4.4 Class space . . . 75
4.4.1 Singular value decomposition . . . 75
4.4.2 Exponentially weighted moving average . . . 77
4.4.3 Threshold determination . . . 78
4.4.4 Fault detection & isolation . . . 79

4.5 FDI results & validation . . . 82
4.5.1 Fault 1: Clogging . . . 82
4.5.2 Fault 2: Leakage . . . 85
4.5.3 Fault 3: Stuck valve . . . 87
4.5.4 Fault 4: Sensor drift . . . 88
4.5.5 Fault 5: Fouling . . . 91
4.6 Conclusion . . . 92

5 Principal component analysis **95**

5.1 Introduction . . . 95
5.2 Model development & verification . . . 97
5.2.1 Data processing . . . 97
5.2.2 Variation analysis . . . 98
5.2.3 Dimension reduction . . . 100
5.2.4 Detection function . . . 104
5.2.5 Threshold determination & fault detection . . . 107
5.2.6 Fault identification & isolation . . . 109
5.3 FDI results & validation . . . 112
5.3.1 Fault 1: Clogging . . . 112
5.3.2 Fault 2: Leakage . . . 115
5.3.3 Fault 3: Stuck valve . . . 118
5.3.4 Fault 4: Sensor drift . . . 120
5.3.5 Fault 5: Fouling . . . 123
5.4 Conclusion . . . 125

6 EGBV & PCA comparison **127**

6.1 Introduction . . . 127
6.2 Fault detection comparison . . . 129
6.2.1 Robustness . . . 129
6.2.2 Sensitivity . . . 133
6.2.3 Promptness . . . 136
6.3 Fault isolation comparison . . . 140
6.3.1 Detection & isolation comparison summary . . . 143
6.4 Comparison of ideal attributes . . . 144
6.4.1 Quick detection & diagnosis . . . 144
6.4.2 Isolability . . . 145
6.4.3 Robustness . . . 145
6.4.4 Novelty identifiability . . . 145
6.4.5 Classification error estimate . . . 145
6.4.6 Adaptability . . . 146
6.4.7 Explanation facility . . . 146
6.4.8 Modelling requirements . . . 146
6.4.9 Storage & computation . . . 147
6.4.10 Multiple fault identifiability . . . 147
6.4.11 Ideal attribute comparison summary . . . 147
6.5 Conclusion . . . 148

7 Conclusion **150**

7.1 Summary & conclusions . . . 150
7.2 Future work & recommendations . . . 151
7.2.1 Practical pilot plant improvements . . . 151

7.2.2 Model improvements 152
7.2.3 EGBV enhancements 152
7.2.4 Additional comparisons 153
7.3 Closure 153

Bibliography **153**

A Model & practical process results **164**

B EGBV results **186**

C Principal component analysis isolation results **218**

D Instrumentation design & implementation **224**

LIST OF FIGURES

2.1 Process sample plots illustrating univariate vs. multivariate analysis 14

2.2 T^2 and SPE plots showing a comparison between PCA and FDA for multi-fault detection 19

2.3 Fault identification performance of PCA and FDA 20

2.4 Qualitative fault signature results for tank 1 and 2 24

3.1 Process diagram of a two-tank heated system 30

3.2 Disturbance of level PVs in the practical system 39

3.3 Deviating trend of practical temperature T_1 due to varying external temperature T_3 of F_3. 39

3.4 Deviating trend of practical temperature T_2 due to varying external temperature T_4 of F_4. 40

3.5 The characteristics of linear, quick opening and equal percentage valve operation 41

3.6 Practical control valve characteristics and their linear approximation 42

3.7 Valve characteristic changes due to non-constant pressure drops across valves 43

3.8 Normal, steady state operation of PU1 model and practical system 45

3.9 Normal, steady state operation of PU2 model and practical system 46

3.10 PU1 clog valve characteristic 49

3.11 Modelled and practical process response of a 30% clog in PU1 at sample 900 51

3.12 Modelled and practical process response of a 30% clog in PU2 at sample 729 52

3.13 Modelled and practical process response of a 30% leak in PU1 at sample 900 54

3.14 Modelled and practical process response of a 30% leak in PU2 at sample 900 54

3.15 Simulink® model of 20% open stuck valve in PU1 55

3.16 Modelled and practical process response of a 20% open stuck valve in PU1 at sample 500 57

3.17 Modelled and practical process response of a 10% open stuck valve in PU2 at sample 500 58

3.18 Simulink® model extract of sensor drift implementation 59

3.19 Modelled and practical process response of a 2% sensor drift in PU1 at sample 900 60

3.20 Modelled and practical process response of a 2% sensor drift in PU2 at sample 900 61

4.1 Stages of fault signature development 66

4.2 Derivation of graph G from the heated two-tank process diagram 69

4.3 Timeseries data of $\tilde{\sigma}_1$ during NOC for EWMA-filtered and original SVD results 78

4.4 Detection of a stuck valve in PU1 at sample 500 80

4.5 SVD detection plots of a model and practical 30% clog in PU1 at sample 900 82

4.6 SVD detection plots of a model and practical 30% clog in PU2 at sample 729 83

4.7 SVD detection plots of a model and practical 30% leak in PU1 at sample 900 85

4.8 SVD detection plots of a model and practical 30% leak in PU2 at sample 900 86

4.9 SVD detection plots of a model and practical stuck valve in PU1 at sample 500 87

4.10 SVD detection plots of a model and practical stuck valve in PU2 at sample 500 88

4.11 SVD detection plots of a model and practical 5% Sensor drift in PU1 at sample 900 90

4.12 SVD detection plots of a model and practical 5% Sensor drift in PU2 at sample 900 91

4.13 SVD detection plots of a model and practical fouling in PU1 91

4.14 SVD detection plots of a model and practical fouling in PU2 92

5.1 A flowchart of PCA FDI 96

5.2 Three-dimensional illustration of principal component determination 99

5.3 Scree plot showing eigenvalues in decreasing order 102

5.4 Visual illustration of model NOC score space 103

5.5 Comparison plots of T^2 and V^2 on a 20% modelled clog in PU1 106

5.6 Illustration of the threshold for PCA fault detection 108

5.7 PCA V^2-function result for a modelled 10% leak in PU2 at sample 900 . . . 109

5.8 Illustration of fault detection and identification of a 2% sensor drift in PU1 at sample 900 111

5.9 Plots of FDI results of all clogs in PU1 at sample 900 for the model and practical process 113

5.10 Plots of FDI results of all clogs in PU2 at sample 729 for the model and practical process 115

5.11 Plots of FDI results of all leaks in PU1 at sample 900 for the model and practical process 116

5.12 Plots of FDI results of all leaks in PU2 at sample 900 for the model and practical process 117

5.13 Plots of FDI results of a stuck valve in PU1 at sample 500 for the model and practical process . . . 118

5.14 Plots of FDI results of a stuck valve in PU2 at sample 500 for the model and practical process . . . 119

5.15 Model and practical contribution plots of F_2 for the PU2 stuck valve fault . 120

5.16 Plots of FDI results of sensor drifts in PU1 at sample 900 for the model and practical process . . . 121

5.17 Plots of FDI results of sensor drifts in PU2 at sample 900 for the model and practical process . . . 122

5.18 Plots of FDI results of fouling in PU1 for the model and practical process . 124

5.19 Plots of FDI results of fouling in PU2 for the model and practical process . 125

6.1 False alarm rate comparison plots of PCA and EGBV . . . 132

6.2 True alarm rate comparison plots of PCA and EGBV . . . 136

6.3 Detection delay comparison plot of PCA and EGBV . . . 139

6.4 Heat maps of the isolability of EGBV . . . 141

6.5 Heat maps of the isolability of PCA . . . 143

LIST OF TABLES

1.1 EEMUA alarm guidelines compared to industry results 3

2.1 Summary of capabilities of each fault monitoring function 11

2.2 Summary of surveyed PCA-based case studies 17

2.3 Summary of surveyed comparative case studies 22

2.4 Summary of surveyed energy-based case studies 26

3.1 Summary of PVs measured in PU1 31

3.2 Summary of PVs measured in PU2 32

3.3 List of model-applicable parameters specified for practical process 35

3.4 List of observed external PVs from the practical system 36

3.5 List of steady-state PVs observed from the practical system 36

3.6 List of calculated variables and parameters required for process model . . . 36

3.7 Controller gain values 38

3.8 Maximum saturated flows of the practical heated two-tank process 43

3.9 Steady-state comparison between model and practical results 47
3.10 Model verification for PU1 clogs 49
3.11 Model verification for PU2 clogs 50
3.12 Model verification for PU1 leaks 53
3.13 Model verification for PU2 leaks 53
3.14 Model verification for PU1 stuck valve 56
3.15 Model verification for PU2 stuck valve 56
3.16 Model verification for PU1 sensor drift 59
3.17 Model verification for PU2 sensor drift 60
3.18 Process change for fouling in PU1 63
3.19 Process change for fouling in PU2 63

4.1 Node descriptions 69
4.2 Description of the heated two-tank graph elements 70
4.3 Fault signature for PU1 stuck valve 81
4.4 Modelled PU1 30% Clog 84
4.5 Practical PU1 30% Clog 84
4.6 Modelled PU2 30% Clog 84
4.7 Practical PU2 30% Clog 84
4.8 Modelled PU1 30% Leak 86
4.9 Practical PU1 30% Leak 86
4.10 Modelled PU2 30% Leak 86
4.11 Practical PU2 30% Leak 86
4.12 Modelled PU1 stuck valve 89
4.13 Practical PU1 stuck valve 89

4.14 Modelled PU2 stuck valve 89
4.15 Practical PU2 stuck valve 89
4.16 Modelled PU1 5% sensor drift 90
4.17 Practical PU1 5% sensor drift 90
4.18 Modelled PU2 5% sensor drift 90
4.19 Practical PU2 5% sensor drift 90
4.20 Modelled PU1 20% fouling 93
4.21 Practical PU1 20% fouling 93
4.22 Modelled PU2 20% fouling 93
4.23 Practical PU2 20% fouling 93

5.1 Contribution values for a modelled PU1 20% clog 111

6.1 Numeric designations for process faults 128
6.2 False alarm rates for EGBV [%] 130
6.3 False alarm rates for PCA [%] 131
6.4 True alarm rates for EGBV [%] 134
6.5 True alarm rates [%] for PCA 135
6.6 Detection delay for EGBV [samples] 137
6.7 Detection delay for PCA [samples] 138
6.8 Ranking of FDI methods according to benchmarks 144
6.9 Summary of ideal attributes comparison 148

LIST OF ABBREVIATIONS

AO	Analogue Output
ARX	Autoregressive with Exogenous input
ATR	Autothermal Reformer
C & I	Control and Instrumentation
CLTS	Coupled Liquid Tank System
CPV	Cumulative Percent Variance
CSTR	Continuously stirred tank reactor
CV	Control Volume
DCS	Distributed Control System
DD	Detection Delay
DPCA	Dynamic Principal Component Analysis
D/P	Differential Pressure
EES®	Engineering Equation Solver
EEMUA	Engineering Equipment and Materials Users Association
EGBV	Energy graph-based visualisation
ESD	Emergency Shutdown System
FAR	False Alarm Rate
FC	Flow Controller
FDI	Fault Detection & Identification
FDD	Fault Detection & Diagnosis
FDR	False Detection Rate
GLRT	Generalized Likelihood Ratio Test
GOPA	Generalized Orthogonal Procrustes Analysis

HEOM	Heterogeneous Euclidean Overlap Metric
HMI	Human Machine Interface
HTGR	High temperature gas-cooled reactor
Hz	Hertz
ICA	Independent Component Analysis
IEC	International Electrotechnical Commission
IO	Input/Output
LC	Level Controller
MDR	Missed Detection Rate
MEWMA	Multivariate Exponentially Weighted Moving Average
MS	Multivariate Statistic
MV	Manipulated Variables
NOC	Normal Operating Conditions
NWU	North-West University
PAS	Process Automation System
PCA	Principal Component Analysis
PLC	Programmable Logic Controller
PV	Process Variable
PID	Proportional Integral Differential
PRESS	Predicted Error Sum of Squares
P& ID	Piping and Instrumentation Diagram
QFSM	Qualitative Fault Signature Matrix
RAT	Range, Alarm & Trip List
RLC	Resistor, Inductor, Capacitor
SIS	Safety Instrumented System
SDG	Signed Digraph
SP	Set Point
SPE	Squared Prediction Error
SVD	Singular Value Decomposition
TAR	True Alarm Rate
TC	Temperature controller
TEP	Tennessee Eastman Process
TIA	Totally Integrated Portal
VAC	Voltage Alternating Current
VDC	Voltage Direct Current
VDM	Value Difference Metric
VRE	Variance of Reconstruction Error
WWTP	Wastewater Treatment Plant

LIST OF SYMBOLS, SUBSCRIPTS & OPERATORS

Symbol	Description	Unit
A	Area	[m^2]
α	Significance level	[-]
$aHeat$	Heat transfer coefficient	[kJ/m^3· K]
b	Heat transfer coefficient	[-]
$\dot{B}$	Exergy transfer rate	[kW]
C_p	Specific heat at constant pressure	[kJ/kg · K]
C_v	Valve flow coefficient	[gpm]
F	Flow	[m^3/s]
H	Enthalpy	[kJ]
h	Specific enthalpy	[kJ/kg]
$\dot{H}$	Total enthalpy transfer rate	[kW]
k_L	Level constant	[m^3/s/$m^{0.5}$]
L	Level	[m]
	Control limit width	[-]
m	Mass	[kg]
$\dot{m}$	Mass flow	[kg/s]
σ	Standard deviation	[-]
P	Pressure	[kPa]
ρ	Density	[kg/m^3]
$\dot{Q}$	Rate of heat transfer	[kW]

r	EWMA/MEWMA smoothing constant	[-]
s	Specific entropy	[kJ/kg·K]
$\dot{S}$	Entropy transfer rate	[kJ/s·K]
T	Temperature	[°C]
t	Time	[s]
U	Internal energy	[kJ]
μ	Mean	[-]
V	Volume	[m^3]
$\dot{W}_s$	Shaft work rate	[kW]

Subscript	**Description**	**Example**
0	Reference environmental conditions	h_0
1, 2, 3,...	Numeric parameter designator	F_1
i	Generic parameter designator	T_i
	Vector entry number	$\tilde{\sigma}_i$
	Matrix row number	$\tilde{z}_{ij}$
in	Flow into control volume	$F_{1,in}$
j	Matrix column number	$\tilde{z}_{ij}$
k	Process sample number	$\tilde{\sigma}_{i,k}$
out	Flow out of control volume	$F_{2,out}$
ref	Reference process conditions	$\mathbf{C}_{ref}$

Operator	**Description**	**Example**
$\dot{}$	Rate of change per second	$\dot{E}_{51}$
$\tilde{}$	Normalised value	$\tilde{z}_{25}$
Δ	Difference	$\Delta\dot{B}_1$

CHAPTER

1

INTRODUCTION

This chapter motivates the relevance of FDI in the field of industrial and petrochemical processes. The purpose, objectives and dissertation outline are described.

1.1 Background & motivation

Large-scale industrial petrochemical plants and factories utilize complex chemical processes to reliably produce a given product or products. They consist of several interlinked processing units to allow for multiple production outputs. A refinery, for example, has the capability of producing several chemical products from crude oil. In [1], it is illustrated how the modern refinery utilizes different process units to produce chemical products, including aviation and automotive gasoline, jet fuel and lubricants. Its complexity becomes apparent in the interdependence of the process units. If a single unit were to fail, all of its downstream dependants are compromised. Moreover, each process unit consists of a combination of process equipment which may also be considered complex in nature.

Several procedures and systems are typically put in place to minimize unit failures in these complex systems. After safe process design, a distributed control system (DCS) is responsible for plant-wide process control as well as alarming individual out-of-boundary process conditions [2]. These out-of-boundary process conditions due to abnormal events or malfunctions are called *faults* [3]. Critical alarms are visually and audibly distinctive from DCS alarms to signal urgency to the plant operator. If the operator fails to respond

to the alarm, or in the case of a sudden process fault causing dangerous process conditions, the emergency shutdown (ESD) system will trip the process to a fail-safe state [2, 4].

Venkatasubramanian et al. [5] and Russel et al. [6] refer to different categories of faults and are described as follows:

Alterations in process parameters. Not all process parameters are measured in a petrochemical plant, due to budget constraints or practicality. In these cases, the parameter is assumed or found in the technical documentation of the applicable equipment. However, some parameters are subject to change over time, i.e. gross parameter change. An example of gross parameter change is the change in the heat transfer coefficient of a heat exchanger due to chemical product build-up, known as fouling [7].

Structural faults. A structural fault refers to a physical change in process equipment that leads to process equipment malfunctions. Examples include a stuck valve due to a lack of maintenance and process line leakage due to worn-out gaskets between flanges.

Sensor faults. A process instrument, if not properly maintained, can provide incorrect process measurement values to the DCS. This might result in controller malfunction if the latter instrument is part of a process control loop.

Industrial plants are becoming more complex and thus more prone to the previously described faults. This increase in complexity can be attributed to multiple drivers and demands, the most prominent of which are environmental regulations [8–10], increased safety requirements [10, 11] and increased cost-effectiveness [12, 13]. Additionally, improved product quality [11], overall performance increase [12] and production reliability [14] are all factors leading to plant owners expanding their facilities, thereby increasing their complexity. It is fair to expect that the competence of a plant's alarm philosophy should increase with its complexity such that beneficial operation is maintained amid these increasing demands.

However, it is argued by Izadi et al. [13] that the current alarm philosophies enforced are not sufficient in their attempt to alert the operator in the event of a fault. This is mainly due to the ease with which alarms can be added to the DCS system, leading to alarm flooding. Alarm flooding and nuisance alarms make it harder for the operator to distinguish between valid alarmed faults and non-essential alerts. Table 1.1 shows a comparison between the Engineering Equipment and Materials Users Association (EEMUA) recommendations and alarm statistics from the oil and gas, petrochemical and power industries. The average number of alarms per hour in industry is at least six times higher than the recommendation. The average standing alarms per hour from the industry are at least five times higher than the recommendation, indicating that the plant personnel are not able to attend to the faults quick enough to clear the alarm. The amount of peak alarms per hour is at least eighteen times higher in industry than is recommended and

the priority distribution shows that the occurrence of medium- and high-priority alarms are significantly higher than the specification. It is therefore clear from Table 1.1 that the industry's current alarm framework allows for an excessive amount of nuisance alarms [13].

Table 1.1: EEMUA alarm guidelines compared to industry results [13]

Specification	EEMUA	Oil and Gas	Petrochemical	Power
Average alarms per hour	$\leq$6	36	54	48
Average standing alarms	9	50	100	65
Peak alarms per hour	60	1320	1080	2100
Distribution% (low/med/high)	80/15/5	25/40/35	25/40/35	25/40/35

Furthermore, industries have sustained significant personnel and monetary losses due to abnormal situations. The Piper Alpha Oil Rig incident is a notable catastrophic incident, which resulted in 167 deaths. Another example is the Phillips 66 Complex incident, amassing 23 deaths in 1989. The United States of America's petrochemical industry suffers losses of 10 to 20 billion dollars annually, with industry damage claims over 2.2 billion dollars [13, 15]. It is found that more than 70% of the incidents may be attributed to human error [15], which is unsurprising given the mental load induced on plant operators by the overwhelming amount of alarms in Table 1.1.

The problem of insufficient alarming and process monitoring techniques has not gone unnoticed - the topic of *advanced process monitoring* is an active area of research within the academic community aiming to address this. Generally, these advanced systems are referred to as *fault detection and isolation* (FDI) systems. Their purpose is to improve upon fault detection when compared to traditional systems, with the added functionality of determining the fault type and location [3] to reduce the mental load of plant operators and by extension, operator error.

Venkatasubramanian et al. [16] define two main categories for FDI systems, namely *model-based* approaches and *process history-based* approaches. Model-based approaches can be subdivided into qualitative and quantitative, each with its advantages and disadvantages. Quantitative models are analytical in nature and are costly to accurately develop and maintain due to the complex nature of plants [8, 17]. Qualitative models do not require mathematical relationships within a process as quantitative models do but instead rely on *a priori* knowledge of the relationships between process units to develop digraphs or fault trees [5]. Process history methods (also referred to as data-driven methods) utilize historic process data to apply FDI and have gained traction in industry as historic process data are readily available [8]. *Principal component analysis* (PCA) stands out as the benchmark method within the data-driven category as it has been widely applied in industry as an FDI method, including DuPont chemical company [18]. Within the former and the latter

categories, various FDI techniques have been developed over the past twenty years and tested to varying extents [19].

More recently, hybrid approaches have gained popularity and aim to address the shortcomings of model- and history-based FDI methods by combining methods from each category [20]. The *energy graph-based visualisation* (EGBV) approach is an example since it combines a process-history approach with a qualitative energy model of a process for FDI [10]. The method has been applied successfully on a CO2 trans-critical heat pump [21], as well as on a Brayton cycle process [22].

The Tennessee Eastman Process (TEP) is a popular process to use for FDI testing. Approximately 37% of all data-driven process monitoring studies from 2017 and 2021 have used the TEP. Another popular process is the continuously stirred tank reactor (CSTR) system, which is used by 10% of the studies in the same period [23]. Different configurations of the CSTR exist (for example, the number of tanks may vary)[24, 25]. The two-tank heated process is a CSTR variant that comprises two subsequently connected tanks that are temperature controlled. Cold fluid is passed through the tanks, while hot fluid is circulated via coils in the tanks to achieve a target temperature for the fluid in each tank. The process is simple in principle, yet sufficiently complex in terms of operation dynamics to use for FDI testing.

Amidst numerous FDI techniques, comparison studies are useful for learning the advantages and shortcomings of the FDI techniques being compared and for clarifying the circumstances for which each method is optimal. A notable study was done by Russel et al. [6] on data-driven techniques specifically. Similar smaller comparison studies have followed [11, 26, 27]. Since the EGBV technique is relatively novel, its comparison to a well-established FDI approach, such as PCA would provide valuable insight into its performance.

1.2 Research question

The purpose of this study is to answer the following question: *How does the EGBV FDI method compare to the more established PCA method?* To answer this question, a comparison study between EGBV and PCA will be conducted using a physical heated two-tank system as the benchmark process. Comparisons will be made using a modelled version of the process as well to further support the conclusions. Using objective FDI performance metrics, the strengths and limitations of EGBV will be revealed, since the abilities of PCA are well known within the academic community. The scope is limited to using Hotelling's T^2 PCA method for the comparison.

1.3 Research objectives & methodology

1.3.1 Literature survey of relevant process monitoring concepts

A thorough literature survey will be conducted to clarify relevant concepts and terminology of process monitoring. Previous application examples of PCA and EGBV will be presented to gain insight into their FDI abilities.

1.3.2 Verification & validation of the heated two-tank process model

A MATLAB® Simulink® model of the heated two-tank system developed by Lindner and Auret [28] will be studied to comprehend the theoretical foundation of the process and will then be modified to:

1. Match the practical plant specifications and
2. Include process fault simulation ability.

The process faults to be tested will include the following fault types, in line with the different fault categories defined in Section 1.1:

1. **Clogging** - A blockage occurring in the gravity feed between the tanks.
2. **Leakage** - A leak occurring in the main water feed to the tank.
3. **Stuck valve** - Feed valve failing in its current position.
4. **Sensor drift** - Biased sensor reading from a failed temperature sensor.
5. **Fouling** - A decrease in the heat transfer coefficient of the heating coils within each tank.

These faults will be applied to both tanks, thus varying the fault location. Fault types 1, 2 and 4 will be varied in size as well. The model will be verified and finally validated using the practical process data.

1.3.3 Application, verification & validation of EGBV

The EGBV FDI approach, as implemented in [21] and [22] will be studied and applied using MATLAB®. The method will be verified as it is applied to the modelled process faults and its application to the practical results will serve as method validation.

1.3.4 Application, verification & validation of PCA

Following EGBV, the PCA FDI approach will be described and explained. The correctness of the method will be verified as it is applied to the model results. For validation, the method will be applied to the practical process data.

1.3.5 Comparison of EGBV & PCA

First, the fault *detection* performance of EGBV and PCA will be compared. This will be done according to key performance metrics for FDI methods, as found in literature, hereby ensuring an objective comparison. Then, the fault *isolation* performance of each method will be compared. The comparison will be done for the model results and practical results to support the comparison conclusions.

1.4 Dissertation outline

Chapter 2 will provide a literature survey of process monitoring concepts that is relevant to the topic of this work. The chapter will also provide an overview of popular model-based and data-driven FDI methods. Application examples within each domain will be provided and critically reviewed.

The theoretical inner workings of the Simulink® model are explained in **Chapter 3**, as well as the modifications made to the model to introduce the faulty process conditions. The method is then verified and validated using the normal and faulty process outputs.

Chapter 4 focuses on the application of EGBV as an FDI method. The chapter explains how the FDI method is applied by guiding the reader through the theoretical core of EGBV as it is implemented in the MATLAB®simulation environment and applied to the heated two-tank system. The FDI results are discussed, verified and validated.

Chapter 5 is dedicated to PCA and its application as an FDI method. This chapter follows the same philosophy and structure as Chapter 4, as it explains the theoretical approach to applying PCA in a simulated environment and then on practical data. Finally, the FDI results are verified and validated.

The main research question of the study is answered in **Chapter 6**. The FDI performance of EGBV and PCA are compared using the results of Chapters 4 & 5 using key performance metrics of FDI. Additionally, the methods' compliance with other ideal attributes of FDI methods is discussed. The author will comment on the suitability of both methods.

Chapter 7 concludes the study by summarizing the results and highlights of each FDI. Recommendations are provided for future studies.

CHAPTER

2

LITERATURE SURVEY

This chapter aims to discuss relevant literature by addressing terminology, performance requirements and different methods of fault monitoring. The application of each method is discussed with reference to previous studies. The chapter closes with a critical review of the surveyed literature.

2.1 Introduction

In Chapter 1, the motivation for FDI research and its applicability within the processing industry was made clear. This chapter aims to discuss literature within the field of fault monitoring that is relevant to the scope of this work. Firstly, the general terminology of fault monitoring will be clarified. Next, the key performance metrics for fault monitoring as observed in literature will be discussed. This will allow for insightful evaluation and comparison of FDI methods within the scope of the study.

The relevant data-driven FDI approach literature will be discussed, with a focus on PCA. The author will elaborate on past PCA-related case studies and their results to provide context for PCA's performance in different processes. Related data-driven methods are also surveyed in comparison to PCA to provide insight into PCA's performance within the data-driven approach domain.

A brief introduction to the model-based approach will be provided, with a focus on energy-based fault monitoring. Once more, example case studies will be discussed and

summarised. Finally, a critical review will be provided by the author to highlight the applicability of the surveyed literature to this work.

2.2 Fault monitoring terminology

Before discussing the FDI methods in literature, the terminology within the field needs to be clarified. As noted in [3] and [6], the terminology used throughout literature is not consistent, which impedes the reader from understanding fundamental terms. Terminology will be discussed in terms of the process *state* during an anomaly, as well as the *functions* to address this.

2.2.1 State definitions

When something goes wrong such that a process state changes from normal to abnormal, the cause of the upset can be attributed to one or multiple events, namely a disturbance, a malfunction, a failure or a fault [3].

A *disturbance* is an unknown and uncontrolled input acting externally on the process system [3]. Svrcek et al. [29] refer to this more specifically as load disturbances, causing the process variable (PV) to deviate from the set point (SP) value in a controlled process. Due to the unpredictable nature of disturbances, automatic process controllers are employed to compensate for and minimize the effect of disturbances [29].

A *malfunction* appears when a component in the process system temporarily deviates from its intended function [3]. Malfunctions may occur in process instrumentation, such as transmitters [30] or process equipment [31].

In contrast to a malfunction, the permanent loss of the component's ability to perform its intended task is called a *failure* [3]. Unlike disturbances, modern controllers are not designed to compensate for failures [9].

A *fault*, as briefly defined in Chapter 1, is the unpermitted deviation of a property or process characteristic from its normal range [3, 5]. Jiang et al. [8] refer to a fault as an abnormal event in a process. Furthermore, it can be said that the term *fault* acts as an umbrella term for the aforementioned process malfunctions and failures, as the former and the latter fits the definition of a fault [24]. This is supported by Venkatasubramanian et al. [5] who refer to failures and malfunctions as *basic events* or the cause of a fault.

2.2.2 Function definitions

Different functions exist within the fault monitoring domain, namely detection, isolation, identification, diagnosis and prognosis, each more advanced than its listed predecessor [3, 32].

Fault *detection* deals with determining the presence and time of a fault's occurrence [3, 24]. Detection forms the first step in fault monitoring and is usually followed by either fault isolation or diagnosis as found in several previous studies [8, 14, 21, 24, 33, 34].

Fault *isolation* requires the determination of the fault kind and location, including the requirements of fault detection [3]. In a study by Asokan and Sivakumar et al. [24], the location parameter is understood to be the process component (PC).

Fault *identification* is similar to isolation, but contains time-variant behaviour and magnitude as well [3]. Jiang et al. [8] define fault identification to be variable-specific, as opposed to the more general component location requirement of fault isolation. Gertler [35] notes that fault identification is typically not added to practical systems as the extra effort to find the fault magnitude is not justified.

Fault *diagnosis* involves performing all of the above, so that the time, location, size and kind of fault are known [3, 35]. Although some studies, including [24],[14] and [21], regard fault isolation and fault identification to be synonymous with fault diagnosis, literature from Isermann and Ballé [3], as well as Gertler [35] clearly define a difference between isolating and identifying a fault in a system.

Finally, fault *prognosis* is defined in the field of condition monitoring as the prediction of faults based on the condition of current systems [32]. Fault prognosis, therefore, provides a lead time to component failure and uses the diagnosis process as a basis for prediction. Once a fault is diagnosed (assuming the fault is not a component failure) the prognosis system then calculates the remaining operational lifetime of the diagnosed faulty component until failure will occur [32]. It provides an advantage to plant operators in terms of the scheduling of procurement and repair of plant components. However, current prognostic algorithms are not producing consistent results and are not yet ready for reliable industry application [36].

To demonstrate the capability of the discussed fault monitoring functions, a summary is provided by Table 2.1 indicating the fault parameters provided by each function.

Table 2.1: Summary of capabilities of each fault monitoring function

Fault Parameter	Detection	Isolation	Identification	Diagnosis	Prognosis
Occurrence	•	•	•	•	•
Time-stamp	•	•	•	•	•
Kind		•		•	•
Location		•		•	•
PV			•	•	•
Magnitude			•	•	•
Component health					•
Time to Fail					•

2.3 FDI performance requirements

In literature and previous case studies of FDI systems, it is noticed that the authors state the desirable characteristics of the FDI/FDD scheme at hand, either implicitly or explicitly. This is important because one needs to determine how well said FDI/FDD system is performing within pre-defined circumstances, especially in a domain where multiple approaches exist. The aforementioned desirable characteristics, therefore, become key performance metrics or benchmarks applicable to all FDI/FDD approaches [5]. The three main benchmarks observed are robustness [5, 6, 24, 32, 35], sensitivity [6, 8, 11, 13, 35], and promptness [5, 6, 8, 35, 37].

Robustness, as defined by Russel et al. [6], is the measurement of an FDI/FDD system's false alarm rate (FAR). As derived from the term, the goal is to minimize the FAR. Venkatasubramanian et al. [5] refer to robustness as the system's noise rejection capability, which correlates with the FAR measurement since poor noise rejection will lead to a high FAR.

Sensitivity is a measurement of an FDI/FDD system's missed detections [6]. A trade-off exists between the robustness of the FDI/FDD system and its sensitivity performance. If a system is too sensitive, it will have a low missed detection rate (MDR), but also a high FAR. Likewise, if a system is not sensitive, it will have a low FAR, but a high number of missed detections [5, 18].

Promptness or *system speed* measures the lag between the time of the fault and the time of detection and should ideally be minimized [6, 35]. In [5], it is noted that a high system speed will make it prone to noise, leading to a high FAR. Therefore, a trade-off exists between promptness and robustness.

Some surveyed studies use a combination of the above-mentioned benchmarks rather than

all three. A study by Harrou et al. [38] uses fault detection count in conjunction with the missed detection count when observing faults only. Chen et al. [11] use fault detection rate (FDR) and FAR as performance benchmarks. Fazia et al. [39] measure the performance using FAR and system speed.

Additional ideal characteristics of FDI/FDD systems are listed by Venkatasubramanian et al. [5] as follows:

1. **Isolability** - In terms of isolation performance, the FDI/FDD system should reliably distinguish between true fault isolation and modelling uncertainties.
2. **Novelty identifiability** - The system should be able to distinguish between new and previously encountered faults.
3. **Classification error estimate** - The system should ideally provide feedback to the operator on the confidence level of its results.
4. **Adaptability** - Plants may have different operating conditions and the FDI/FDD system should function correctly in each 'normal' operating profile.
5. **Explanation facility** - The system should elaborate on the fault occurrence and propagation as an aid to operators.
6. **Modelling requirements** - If the system is model-based, the model itself should ideally be set up with minimum effort, as model-based systems take a considerable amount of time to develop, depending on the plant's complexity.
7. **Storage and computational requirements** - The computer system tasked with fault monitoring should have sufficient storage for process data and computational ability for model calculations.
8. **Multiple fault identifiability** - The system should be able to identify and distinguish between multiple faults occurring at once. This is regarded as a challenging task.

2.4 PCA & data-driven methods

Even though a rise of interest in model-based approaches to FDI/FDD occurred in 1996 [3], Russel et al.[18] insist that data-driven methods have dominated the literature in the decade before the year 2000, as industrial processes are producing a considerable amount of data [13]. Moreover, this led to the data-driven approach being more successful in practice [18]. Several subcategories of the data-driven approach are reviewed in [16]. However, this study focuses specifically on multivariate statistic (MS) data-driven approaches.

2.4.1 Multivariate vs. univariate

The term *multivariate*, as opposed to *univariate*, describes an FDI/FDD system that takes into account multiple related process variables. The correlation of the different PVs is exploited to provide insightful feedback [6, 13]. *Univariate* is understood to take into account only one variable at a time, which forms the basis of current plant alarming systems. Limit checking is then employed to determine if a variable is faulty [6, 35].

Figure 2.1 shows how multivariate detection outperforms univariate detection. On the left and at the bottom of the figure, variables A and B are plotted separately, thus forming univariate plots. In each of these plots, the thresholds of abnormal conditions are indicated by red lines. Two specific data points, • and + are of interest. It is observed that in these two plots, the '•' data point falls outside of normal operating conditions for both variables, whereas the '+' data points are within normal range. This will lead to two alarm indications. Next, observe the top right plot that combines the data points of A and B to form a joint distribution, indicating multivariate monitoring. It is clear from this plot that A and B are process correlated variables. The ellipse shows the detection range of the process when both variables are taken into account. It is observed that the '•' data points, previously shown to be abnormal, are within the ellipse and therefore within normal range when considering process correlation. The '+' data point falls outside the ellipse, possibly indicating a fault that was not previously indicated by the univariate plots [13]. From the figure, it is concluded that multivariate monitoring not only provides more accurate alarm feedback but also reduces the number of alarms to be monitored.

2.4.2 Applying the data-driven approach

Applying MS data-driven fault detection generally consists of three stages: data-processing, dimension reduction and variation detection [6, 14, 34]. To apply FDI and FDD, additional steps are required, depending on the isolation/diagnosis methodology.

The process of *data processing* within the context of MS methods involves the preparation of the dataset to ensure accurate analysis. Data-processing in itself contains three major stages [6, 14]:

1. Variable removal - The dataset considered should only contain process correlated variables. Therefore, process variables that are not related to the process should be removed.

2. Auto-scaling - Because process variables widely differ in range, each set of process variables should be transformed to have unit variance and zero mean. This ensures that high process values do not dominate the set.

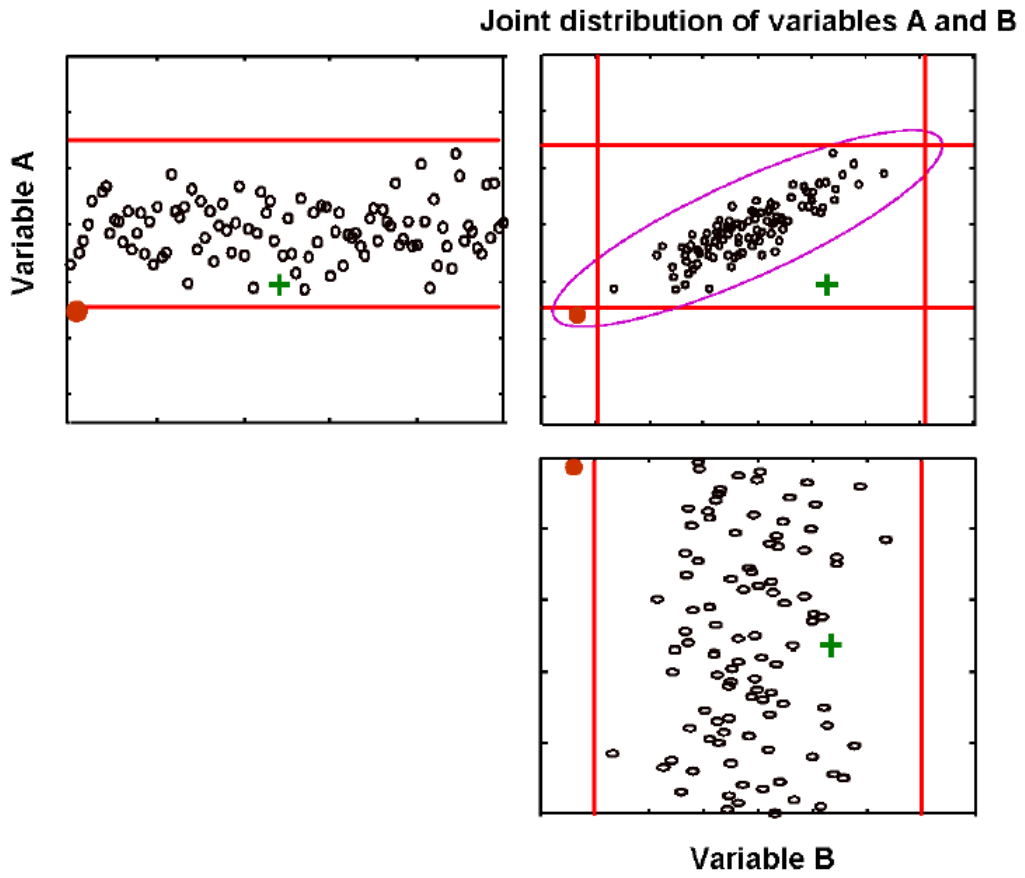


Figure 2.1: Process sample plots illustrating univariate vs. multivariate analysis [13]

3. Outlier removal - With regard to the dataset used to represent normal operation, removing erroneous data improves the fault detection capability of the system.

Dimension reduction techniques aim to reduce the dimension of the dataset, which has been found to improve the FDI/FDD systems' performance. Studies have been conducted where dimension reduction has not been applied [6, 11]. However, results from a study by Russel et al. [6] show that using a dimension reduction technique results in fewer fault misclassifications. The most prominent techniques are surveyed later in the chapter.

Finally, *variation detection* involves the application of MS techniques, such as Hotelling's T^2 or Q statistic to highlight anomalies in the data, i.e. process faults. These techniques typically use a threshold to distinguish normal from abnormal behaviour [6, 37].

2.4.3 PCA-focused studies

Principal component analysis (PCA) is a linear dimensionality reduction technique [40]. Simply put, it is a tool used to find the directions and value of maximum variance in a multivariate dataset. In process monitoring, the study of multivariate variance is relevant, because it is tied to process deviations. If the directions and values of maximum variance are found within a dataset with verified normal operating conditions (NOC), then a data model is essentially created. One may then elect to extract the directions and values corresponding to the highest variance (the values itself are the variance), thereby eliminating process noise. The data model is constructed entirely from historic process data [6].

The abundance of available process data led to PCA being widely applied in the process industry, including DuPont chemical company [6, 18, 38]. It should be noted that studies regularly refer to the construction of PCA models or data models, which should not be confused with model-based approaches.

In the sections that follow, case studies are provided of previous PCA applications for process monitoring. The studies considered are selected for their applicability and serve to inform on the results expected from the FDI method.

Case study 1: Two-tank study by Villegas et al.

Villegas et al. [34] conducted a study to investigate PCA's robustness as an FDD method on a two-tank system. It mentions that the two-tank system is a non-linear process and speculates that a non-linear PCA approach may be better suited. FDD is achieved by creating a PCA model for normal process behaviour as well as for each fault. Then, a fault is diagnosed by applying the faulty data to each model and observing each Q statistic, as the fault model that corresponds with the faulty data will have a Q statistic below its threshold.

A Simulink® model of the process was developed, as well as a pilot plant version of the process for validation. The faults considered were tank outlet blockages and level sensor faults. Even though the T^2 and Q statistics were calculated, only the Q statistic was used as it provided better results. The study successfully detected and diagnosed all faults in the pilot plant with varying operating points, hereby showing that PCA is sufficient for use in a non-linear process.

Case study 2: Ozone measurements study by Harrou et al.

Harrou et al. [38] use multivariate exponentially weighted moving average (MEWMA) as a PCA-based detection method on faulty ozone measurements in France and compared it against the traditional T^2 and Q statistics. While the data type of the study is not within the process industry scope of this study, its application and results are still applicable. Harrou et al. [38] highlight the shortcomings of the T^2 and Q statistics. They argue that the T^2 statistic is insensitive to moderate process upsets contained in its latent process variables, resulting in missed detections. The Q statistic is found to be more sensitive than the T^2 statistic, but also more prone to modelling errors. The MWEMA-enhanced detection method is proposed to address these shortcomings.

When applied to data from air measurements from Upper Normandy, the MEWMA-enhanced Q statistic outperformed the T^2 statistic and traditional Q statistic. The MEWMA achieved a detection rate of 70%, whereas the T^2 and Q statistics achieved approximately 10% and 40% respectively. The results are validated against fault detections made by Air Normandy experts.

Case study 3: Wastewater Treatment Plant study by Garcia-Alvarez

Garcia-Alvarez [41] applied PCA-based fault detection to a Wastewater Treatment Plant (WWTP) in a MATLAB® and Simulink® environment. The steady state of the plant is considered in a dynamic model of the plant. Three process-specific faults are introduced to the system to evaluate the performance of the T^2 statistic and Q statistic in a PCA model of the plant. Only the relevant PVs are used in the constructed PCA model, as prescribed by Russel et al. [6]. A Cumulative Percent Variance (CPV) test and a scree test are conducted to determine the optimal amount of principal components (PCs) to capture the variance in the plant data.

The study shows that both the T^2 and Q statistic successfully detected all three faults, with the Q statistic showing slightly better detection performance for the less impactful process fault. A fourth scenario in the form of a disturbance is then conducted, to highlight that the traditional PCA approach is not suited for processes where the normal operating point of the process may shift. In this case, the weather-related disturbance causes the process to have said shift. In response, Garcia-Alvarez [41] proposed that a PCA model should be created for each operation point, used in conjunction with a switching system to select the applicable PCA model for each range of operation.

To prove the concept of switch-PCA, the original PCA model in the study was tested with the new NOC data introduced by the disturbance, which resulted in false detection. Then, a new PCA model was constructed for the new NOC dataset. The new model did

not give the same false alarm, hereby indicating that the concept of switch-PCA is valid.

Case study 4: Continuously Stirred Tank Reactor study by Mansouri et al.

Mansouri et al. [37] conducted a study to compare the traditional PCA Q statistic with a Generalized Likelihood Ratio Test (GLRT) PCA approach for fault detection in a simulated CSTR process. The GLRT method involves the use of hypothesis testing, where the alternative hypothesis contains an unknown mean vector (or fault value). This fault value is approximated through maximum likelihood estimation. The author first determines the principal components of interest and then enhances the PCA model with a generalized likelihood ratio function and threshold. Three faults were considered, with all faults being sensor drifts. Singular and simultaneous fault occurrences were simulated.

For each fault scenario, both the GLRT and Q statistic successfully detected the fault. However, the GLRT method showed better performance with no false alarms for all scenarios considered. The Q statistic had multiple fault alarms in each scenario. The results show that the GLRT method has the same sensitivity as the Q statistic, but does not suffer from false detections as linked to the sensitivity requirement.

Table 2.2 summarises the surveyed PCA case study results.

Table 2.2: Summary of surveyed PCA-based case studies

Author	Process	Fault types	Monitoring aim	Methods	Result
Villegas et al. [34]	Two tank	Clogging, sensor error	Diagnosis Detection	T^2, Q.	Better results from Q, diagnosed via multi-model PCA
Harrou et al. [38]	Ozone	Sensor error	Detection	T^2, Q, MEWMA.	Superior detection via MEWMA enhancement
Garcia-Alvarez [41]	WWTP	Chemical	Detection	T^2, Q.	Better results from Q, multi-model PCA recommended
Mansouri et al. [37]	CSTR	Sensor error	Detection	Q, GLRT.	GLRT enhancement better than Q

2.4.4 Comparative PCA studies

PCA is not the only data-driven technique available for FDI use - other methods have been investigated in literature and compared to PCA. Many studies have been conducted on various processes to clarify the advantages that one data-driven method has over others. To this extent, the following section discusses studies where PCA has been compared against another data-driven method. For brevity, a single case study will be discussed for every other prominent method that is comparable to PCA.

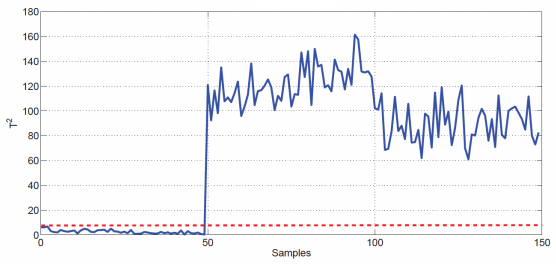
Case study 1: PCA and FDA study by Adil et al.

A Coupled Liquid Tank System (CLTS) is used as a benchmark process by Adil et al. [26] to investigate and compare the performance of PCA and Fisher Discriminant Analysis (FDA) techniques for FDI.

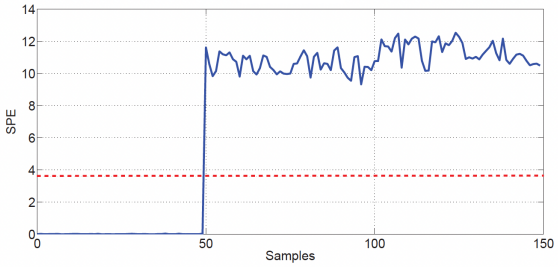
Like PCA, FDA is a linear dimensionality reduction technique that focuses on classes of data. These classes contain faulty data from the process, with each class assigned to a specific fault. The separation amongst said classes is maximised, hereby discriminating amongst faults. Separation within each class is also minimised. As this is FDA's primary goal, it has better fault identification performance compared to PCA [6]. The results are discussed using figures extracted from the study.

Figures 2.2a and 2.2b show the fault detection performance of the PCA-based T^2 statistic and Q statistic, respectively. The FDA-based T^2 statistic is shown in Fig. 2.2c. The blue line indicates the calculated statistic and the red line in each plot shows the calculated threshold for each statistic. When the actuator fault is applied to the system at sample 50, the statistic exceeds the threshold in each plot and indicates that both PCA and FDA have successfully detected the fault. When the sensor 1 fault is applied at sample 100, only the FDA detection plot shows the presence of multiple faults as seen by the second increase in its T^2. In comparison, the PCA T^2 statistic plot shows a slight mean change at sample 100 but is not as clear as the FDA graph. The Q statistic for PCA shows no change at sample 100. Therefore, it can be seen that all approaches are sufficient for single fault detection for the given faults, but FDA shows better detection performance in the presence of multiple faults.

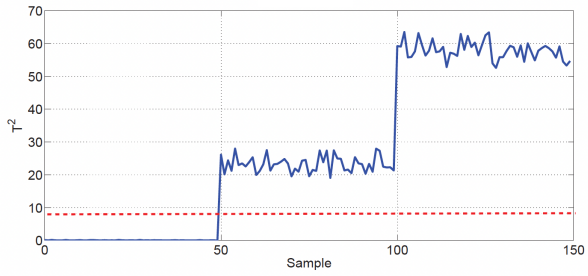
Figure 2.3 shows the PCA and FDA fault identification performance. Contribution plots are a popular fault identification method within the data-driven FDI domain and are shown in this figure. The contribution plot provides a unitless indication of how much each measured PV can be associated with a fault, thus providing the operator with meaningful fault information. A PV with a high contribution value means that it can be strongly associated with the fault. Conversely, low contributing PVs can therefore be ignored for



(a) Fault detection using PCA T^2 method



(b) Fault detection using PCA Q method



(c) Fault detection using FDA T^2 method

Figure 2.2: T^2 and SPE plots showing a comparison between PCA and FDA for multi-fault detection [26]

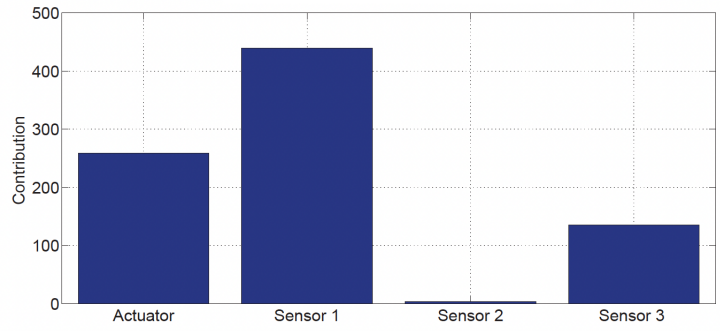
further fault analysis [42].

The contribution index of each variable/element is calculated and plotted for the faults shown in Fig. 2.2. In both plots, both faulty elements are correctly identified. However, the FDA contribution plot shows a lower contribution for sensor 3 in comparison with the PCA plot, therefore providing more accurate feedback on the faulty elements in the process.

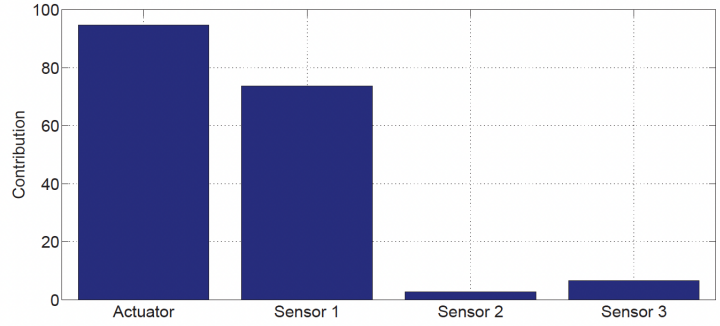
Case Study 2: PCA, DPCA and CVA study by Russel et al.

Russel et al. [18] conducted a study where PCA, Dynamic PCA (DPCA) and Canonical Variate Analysis (CVA) are used as fault detection techniques for the Tennessee Eastman process. Additionally, a novel residual-based CVA statistic is proposed. The goal of the study is to compare the previously mentioned data-driven approaches in terms of their robustness, sensitivity and promptness.

One of the main shortcomings of traditional PCA is that the method assumes that data points in a sample are statistically independent. For long sampling periods this is valid, but not for short sampling periods. When short sampling periods are considered, a serial correlation may be observed within the variable set. DPCA aims to take this into account by the addition of sample lags in its observation matrix, leading to faster detection. As



(a) Fault identification using PCA



(b) Fault identification using FDA

Figure 2.3: Fault identification performance of PCA and FDA [26]

part of the DPCA approach, a multivariate autoregressive with exogenous input (ARX) model is developed [6, 18].

CVA may also be regarded as a dimensionality reduction technique. In the field of fault detection, it is distinguished by its focus on maximising the correlation between two observation sets. It takes into account serial correlation in the data without the need for an ARX model, as required by DPCA. This is advantageous to CVA since the ARX model is regarded as inflexible when working with dynamic processes [6, 8, 18].

The study found that DPCA, when applying the T^2 statistic, is the most robust method as tested on 21 simulated faults with a FAR of 0.006. PCA also performed well, with FARs of 0.014 and 0.016 for the T^2 and Q statistics, respectively. CVA was found to be the least robust, with a minimum FAR of 0.083.

However, CVA was found to be the most sensitive, especially when using the proposed novel residual-based approach. PCA and DPCA Q-statistic approaches showed similar performance.

Concerning promptness, the CVA residual approach was also found to be the quickest

detection method. Even though Q statistics of both PCA and DPCA performed similarly, their Q-statistic is shown to be more prompt than their T^2 statistic counterparts.

Case study 3: PCA and PLS study by Russel et al.

In [6], Russel et al. included the Partial Least Squares (PLS) approach in the same study discussed in the previous section.

PLS aims to maximize the covariance between a predictor (input variables) matrix and a predicted (output variables) matrix [6, 43]. The PLS approach differs from PCA in that PCA only maximises the variance in one observation matrix [44]. When the predicted matrix is populated with fault data, PLS may produce better fault monitoring performance [6].

All 21 faults of the Tennessee Eastman process were simulated to test the fault diagnosis capability of multiple fault monitoring methods. The main benchmark used is the rate of misclassifications. It is observed that on average, all tested PLS methods achieved a lower misclassification rate than the different PCA approaches. There is, however, one exception to this result, namely the single-model PCA, which outperformed most PLS approaches in various stages of the process [6].

Table 2.3 summarises the PCA comparative studies surveyed.

2.5 Energy-based methods

Energy is defined by Çengel and Boles [45] as the ability to cause change. It is the underlying quantifier of all physical actions and is not restricted to a single domain. As described by Van Schoor et al. [10], this characteristic enables energy-based system monitoring as a promising approach to multi-domain FDI.

The term multi-domain in the context of energy systems may include electrical, mechanical, chemical and thermal-fluid. It is common for energy to be transferred between domains and therefore, it can be said that the use of graphs (consisting of nodes and links) is an ideal platform for energy-related fault monitoring [10]. In 2009, Du Rand et al. [46] introduced the concept of an enthalpy-entropy ($h-s$) graph method in a Brayton cycle HTGR for fault diagnosis, proving the viability of energy graph-based monitoring. This concept was explored and expanded in [47] and [48] on multiple components of the same process, further establishing its validity.

However, Du Rand et al. [46–48] and Van Schoor et al. [10, 49] were not the first to

Table 2.3: Summary of surveyed comparative case studies

Author	Process	Fault types	Monitoring aim	Methods	Result
Adil et al. [26]	CLTS	Actuator error, sensor error, leakage	Detection Identification	PCA T^2, PCA Q, FDA T^2.	FDA provides better multi-fault detection and slightly better identification.
Russel et al. [18]	Tenessee Eastman	PV deviation	Detection	PCA T^2, PCA Q, DPCA T^2, DPCA Q, CVA T^2, CVA Q.	CVA is quickest and most sensitive. DPCA most robust. Q statistic outperforms T^2.
Russel et al. [6]	Tenessee Eastman	PV deviation	Diagnosis	PCA T^2, PCA Q, PLS.	Except for single model PCA T^2, CVA has better diagnosis performance.

investigate energy-related graph modelling and monitoring of industrial processes. In 1983, Chinneck and Chandrashekar [50] presented a graph approach to modelling an industrial system, which is based on energy flows and exergy loss within the system. Nikulshin et al. [51] presented the signed digraph (SDG) modelling method for calculating the exergetic efficiency of a nuclear power plant in 2002. Chen et al. [52] presented energy-based fault detection for dissipative systems and used an RLC circuit as a case study. Furthermore, the work of Chen [12] presents an energy-balance approach to fault detection in non-linear systems. These works include examples of qualitative and quantitative modelling, which requires clarification.

2.5.1 Quantitative vs. qualitative modelling

In contrast to the data-driven approach, which has been shown to rely solely on process data, model-based approaches require *a priori* knowledge of the process being monitored. One of the key advantages of the model-based approach is that it is deterministic, which cannot be said for data-driven approaches. Furthermore, models allow the generation

of faults offline, while data-driven approaches require the availability of faulty process data [53]. A fundamental understanding of the process is required to develop either a quantitative model or a qualitative model for fault monitoring [5].

A *quantitative* model expresses a process in mathematical terms. As a result, the development of detailed plant models is costly and complex to develop, shifting the industry focus to data-driven approaches. These models are used to generate analytical redundant inputs and outputs, which are compared to the actual process to calculate process *residuals* [43, 54]. The residuals will highlight sensor failures when evaluating outputs and actuator faults (structural changes) when evaluating inputs. However, it is unable to monitor gross parameter changes, i.e. parameter shifts occurring below the detail of the model [5]. Examples of gross parameter changes as provided by Venkatasubramanian et al. [5] include a change in the concentration of a process reactant and fouling within a heat exchanger.

A *qualitative* model focuses on the functional interaction between units, rather than mathematical input-output modelling. An example is the abstraction hierarchy approach, where a process is decomposed into its subsystems or process units (PUs). This is useful as the overall process behaviour can be inferred from the behaviour of its subsystems. Another example is the causal digraph model approach, which aims to draw cause-effect relationships using process nodes and arcs. When the direction of interaction between nodes is defined, it is known as SDGs [54]. The SDG model forms the basis of the EGBV approach, as addressed in this work.

2.5.2 The EGBV approach

The energy graph-based visualisation FDI method was developed by Van Schoor et al. [10] and Uren et al. [9]. It exploits the SDG methodology to form a qualitative model of a given process and can be regarded as a *hybrid* FDI method.

Hybrid FDI methods aim to amalgamate different FDI philosophies, such that the strengths of the individual philosophies are combined [20]. The EGBV FDI method may be regarded as a hybrid for the following reasons. First, as mentioned in the previous paragraph, the EGBV method involves the use of an SDG approximation of the process, which may be regarded as a qualitative model. This provides the advantage of being deterministic, without being as costly and difficult to maintain as a quantitative model. Second, EGBV requires a process-history of NOC data before faults can be isolated, similar to the PCA approach, and is characteristic of a data-driven model [10]. This data-driven component provides the benefit of practical NOC training for accurate and realistic fault detection, as opposed to using idealistic process specifications. Furthermore, the fact that its energy-based provides the ability to detect gross parameter change faults (for example fouling)

better than quantitative models, as it is captured within the chemical energy domain of the process [53].

This approach will be discussed in detail in Chapter 4 as it's applied to the heated two-tank system. It should be noted that the term *energy-based* within the scope of this work will henceforth include the exergy component of the energy interactions.

2.5.3 EGBV case studies

This section discusses previous EGBV studies and their findings.

Case study 1: Heated two-tank study by Uren et al.

In [9], Uren et al. explores the EGBV approach in a heated two-tank system with aim of detection and isolation in a simulated environment. The process faults considered include sensor faults, fouling within the heat exchanger system, valve failure and tank leakage.

Uren et al. [9] first determine the mass balance equation of the process, then determine the energy and exergy transfer equations between the process components. The process components, namely the tanks and heat exchangers, are represented as nodes in an attributed SDG. The energy transfer between said components is represented by links. From the graph, an attributed signature matrix is developed for the normal operating case and each fault case. The Heterogeneous Euclidean Overlap Metric (HEOM) is used as a means of comparison between the normal and faulty matrices, called graph matching. The result of each comparison is qualitatively analysed to detect and isolate the faults.

$\mathcal{F}_1$	$\mathcal{F}_2$	$\mathcal{F}_3$	$\mathcal{F}_4$	$\mathcal{F}_5$
−	−	−	+	+
−	−	−	+	+
+	+	+	−	+
−	−	−	+	−
−	−	−	+	−

(a) Tank 1 fault signatures

$\mathcal{F}_1$	$\mathcal{F}_2$	$\mathcal{F}_3$	$\mathcal{F}_4$	$\mathcal{F}_5$
−	−	−	−	−
−	−	−	−	−
−	−	−	−	+
+	+	+	+	−
+	+	+	+	−

(b) Tank 2 fault signatures

Figure 2.4: Qualitative fault signature results for tank 1 and 2 from Uren et al. [9]

Figure 3.2 shows the case study results after graph matching analysis, with Fig. 2.4a and 2.4b showing the results of faults applied to tank 1 and tank 2 respectively. Fault 1 to 5

are represented by $\mathcal{F}_{1,2,..,5}$. Each fault column contains '+' and '-' signs as a qualitative representation of its quantitative result. If no fault is detected, a '0' sign would have been used throughout the column. The ideal result would be for each fault column to have a unique combination of symbols amongst all considered faults, known as a *fault signature*.

It is observed that all faults are detected since no '0' symbol columns appear within either matrix. Fault 1 (level sensor error), fault 2 (temperature sensor error) and fault 3 (fouling) are indistinguishable within the scope of each tank and therefore cannot be isolated. However, the first three faults are isolable in terms of the process unit, since $\mathcal{F}_{1,2,3}$ in tank 1 have a different symbol combination than that of $\mathcal{F}_{1,2,3}$ in tank 2. Fault 4 (valve failure) and fault 5 (leakage) in tank 1 are unique within the tank and within the overall process. Fault 4 in tank 2 is not isolable within the scope of the tank. Fault 5 is isolable within the scope of the tank, but not within the overall process.

The proposed FDI method was therefore able to successfully detect all faults, but not all faults were isolated.

Case Study 2: Brayton cycle study by Neser et al.

A Brayton cycle-based high-temperature gas-cooled reactor (HTGR) process is used as an application example for energy-based FDI in the work of Neser et al. [22]. The study compares three energy-based methods, namely residual-based technique, enthalpy-entropy technique and eigendecomposition-based technique. The latter is closely related to EGBV.

Similar to [9], an attributed SDG model is developed of the Brayton cycle power conversion unit and simulated using a validated Flownex® model. The energy, exergy, entropy and enthalpy are calculated for five different faults, which include changes in pressure ratio, efficiency decrease and heat losses. A key difference between the EGBV technique in [9] and the eigendecomposition technique in this study, is that this study investigates eigenvector and eigenvalue results, whereas Uren et al. [9] only investigated eigenvalues.

It is shown that the eigendecomposition-based technique has the best fault detection performance, while the best fault isolation performance was found using the residual-based method. The results of the study also show the trade-off between sensitivity and robustness, as discussed by Venkatasubramanian et al. [16]. The study recommends a residual-eigendecomposition hybrid approach for improved FDI. Regardless, it is shown that all methods are competent FDI techniques.

Case study 3: Transcritical CO_2 heat pump study by Uren et al.

In an article by Uren et al. [21], the application of EGBV is investigated as a means of FDI in a transcritical CO_2 heat pump system. As part of the study, a simulation model is developed in EES® and validated with practical data from a test facility.

An approach similar to [9] is followed, involving the use of an attributed graph representation of the process. Subsequently, a node signature matrix is developed for normal operation and three faulty operation instances. Graph matching is applied using HEOM and eigendecomposition is done to develop a qualitative representation or *signature* of the faulty process conditions.

The study investigated fluid leakage, compressor failure and gas cooler fouling, resulting in the detection and isolability of all three faults. As in [22], the combined use of eigenvalues and eigenvectors forms the fault signature. This study further extends the approach in [9] by calculating the degree of isolability as a quantified performance measurement.

The results of the surveyed studies are summarised in Table 2.4.

Table 2.4: Summary of surveyed energy-based case studies

Author	Process	Fault types	Monitoring aim	Methods	Result
Uren et al. [9]	Heated two-tank process	Sensor error, actuator error, leakage, fouling.	Detection, Isolation.	EGBV	All faults detected poor isolation results.
Neser et al. [22]	HTGR Brayton-cycle	Pressure drop, efficiency drop, heat loss.	Detection, Isolation.	EGBV, Enthalpy-entropy, residual-based.	EGBV has best detection, residual-based has best fault isolation.
Uren et al. [21]	Trans-critical CO_2 heat pump	Equipment failure, leakage, fouling.	Detection, Isolation.	EGBV	Successful detection and isolation, with eigenvector inclusion.

2.6 Critical review

A fundamental understanding of the terminology within the field of fault monitoring is of paramount importance when fault monitoring is to be executed. As the purpose of this work is to compare FDI methods after being applied to a practical process, the clarification of terminology concerning state definitions and function definitions in fault monitoring was provided. The fact that terminology within the field is used inconsistently serves to enforce the importance of its clarification. The most prominent and applicable terms were therefore defined and discussed.

In the presence of multiple available FDI/FDD methods, the establishment of performance benchmarks is in order. Either implicitly or explicitly, the authors of various studies use one or more of three main performance benchmarks, namely robustness, sensitivity and promptness. This work aims to compare energy-based and PCA data-driven FDI methods. That said, the author intends to utilize the aforementioned benchmarks as performance indicators when conducting the comparison. Additionally, the author believes that the desirable characteristics provided by Venkatasubramanian [5] are relevant requirements when considering industry FDI application and will also be discussed as part of the comparison results produced in this work.

Regarding the data-driven PCA approach to FDI, it is clear that PCA is by no means the best-performing approach in any given performance benchmark within the data-driven domain. It is shown in [6] that overall, PLS exhibits better diagnosis performance when compared to some PCA schemes and in [18], it is proven that CVA is quicker and more sensitive than PCA. Furthermore, it is indicated in [18] that DPCA is the most robust.

However, PCA is a proven FDI method in the petrochemical industry, given its industry adoption by DuPont chemical company [18]. A closer inspection of the surveyed studies reveals the competence of PCA. In [26], PCA successfully detected all applied faults and correctly identified the faulty variables. Villegas et al. [34] successfully isolated the applied faults using PCA on a practical non-linear process. In [41] and [37] all process faults were detected using PCA. An exception to the improved diagnosis performance of PLS over PCA is the single model PCA approach, which outperformed PLS in [6]. In light of these findings, PCA can still be regarded as a suitable fault monitoring approach and is therefore sufficient for use within this work. Regarding fault isolation via PCA, the survey reveals that the contribution plot method shown by Adil et al. [26] and explained in Russel et al. [6] is a simple and well-proven approach for identifying faulty behaviour. For this reason, the contribution plot methodology will be employed in this work.

Within the domain of PCA, different variation techniques were surveyed including the T^2 and Q statistic, which may be enhanced further by GLRT and MEWMA. It is observed that the T^2 and Q statistics are the most prominent techniques used. The Q statistic is

found to be the superior approach compared to the T^2 statistic, as seen in [34], [41] and [38]. Regardless, the T^2 statistic can still be regarded as sufficient for use and as such, will be used in this work. It is highly recommended that the Q statistic form part of a future comparison study.

The hybrid EGBV approach is shown to combine *a priori* process knowledge in constructing a qualitative model, with process data from the data-driven domain to analyse the energy and exergy information of a system. In [9], [22] and [21], different processes have been investigated with varying fault isolation success. In this work, the model used in [9] will be modified to introduce varying faulty behaviour and will be validated by a pilot plant version of the process. The addition of eigenvectors as introduced in [21] and [22] will be applied to improve isolation results.

CHAPTER

3

PROCESS MODEL

This chapter describes the heated two-tank process and the Simulink® model of this process. The theoretical foundation of the model and its modifications are explained. The model results for normal and faulty process states are verified and validated.

3.1 Introduction

In Chapter 2, the literature survey highlighted the performance results of PCA and EGBV as FDI methods in different processes. Since this study aims to compare the performance of these methods on a heated two-tank process, an accurate process model is required. The model will act as a *theoretical* reference system so that the evaluations and conclusions of the *practical* results can be made with confidence.

The MATLAB® Simulink® model used in this work was developed by B.S. Lindner and L. Auret [28]. However, the model has been modified in two key areas. The model was modified to include process faults, as outlined in Chapter 1 and also configured to match the specifications of the practical pilot plant.

The aim of this chapter is therefore to discuss the configuration, verification and validation of the modified heated two-tank process model, such that the PCA- and EGBV techniques may be reliably tested in subsequent chapters.

3.2 Process description

Figure 3.1 shows a high-level overview of the heated two-tank process. The process is simple enough to practically implement as a pilot plant, yet also provides enough complexity to study the effects of interdependent process variables (PVs) when faults occur. The process consists of two main process units (PUs), namely PU1 and PU2. The designation of *process unit* is used since tank 1 and tank 2 have multiple functions: temporarily storing the liquid and also maintaining the temperature of the liquid. The term *process unit* will henceforth be used when referring to a tank including its associated process components, whereas *tank* will be used when referring to the storage component of the specific PU.

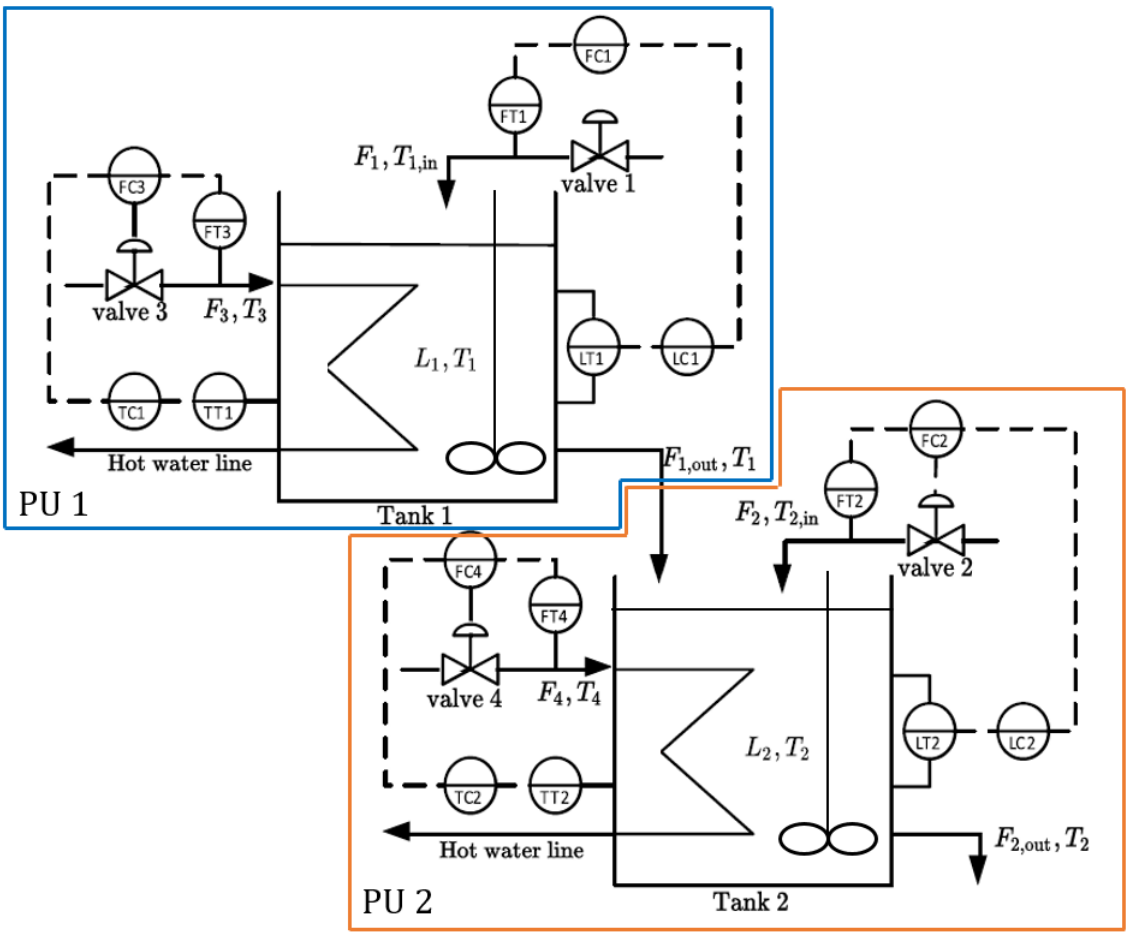


Figure 3.1: Process diagram of a two-tank heated system [9]

The goal of the process is to maintain pre-set liquid water levels in tank 1 (L_1) and tank 2 (L_2), while also maintaining the temperature of the liquid in tank 1 (T_1) and tank 2 (T_2) at pre-set values. Both tank 1 and tank 2 contain agitators to improve heat transfer within the tank.

3.2.1 Process unit 1

Cold water (F_1) feeds into tank 1 from a cold water reservoir at temperature $T_{1,in}$. The feed is controlled via valve 1 by a level controller (LC1) based on L_1. The liquid is gravity-fed from tank 1 to tank 2.

Hot water (F_3) flows through coiled tubing inside tank 1 at a pre-set temperature T_3 for heat transfer to the liquid content of tank 1 and exits to a geyser for re-heating. The temperature of tank 1 is therefore controlled by a temperature controller TC1, which adjusts the hot water flow with valve 3. The measured PVs in PU1 are summarised in Table 3.1.

Table 3.1: Summary of PVs measured in PU1

Parameter	Description	Unit
F_1	Cold water feed flow to PU1	[m^3/s]
$F_{1,out}$	Gravity feed flow from PU1 to PU2	[m^3/s]
F_3	Hot water feed flow to PU1	[m^3/s]
L_1	Tank 1 level	[m]
$T_{1,in}$	Cold water feed temperature to PU1	[°C]
T_1	Tank 1 temperature	[°C]
T_3	Hot water feed temperature to PU1	[°C]

3.2.2 Process unit 2

Similar to PU1, cold water (F_2) feeds to tank 2 from the same cold water reservoir used by PU1 at temperature $T_{2,in}$. Valve 2 is used to throttle F_2 based on the level L_2 observed by the level controller LC2. Additionally, a liquid feed is received from tank 1. The liquid is gravity-fed back to the cold water reservoir from tank 2.

Hot water is circulated at temperature T_4 through a coil into and out of tank 2 for heat transfer to the liquid in tank 2. Temperature T_2 of tank 2 is controlled by a temperature controller TC2 by throttling the hot water flow F_4 through the coil.

Since PU2 is receiving process input from PU1, it is expected that faults in PU1 will be visible in the PVs of PU2. The measured PVs in PU2 are summarised in Table 3.2.

In Appendix D the practical system is discussed and illustrated, and also includes the author's electrical and instrumentation design diagrams used for its construction.

Table 3.2: Summary of PVs measured in PU2

Parameter	Description	Unit
F_2	Cold water feed flow to PU2	[m^3/s]
$F_{2,out}$	Gravity feed flow from PU2 to reservoir	[m^3/s]
F_4	Hot water feed flow to PU2	[m^3/s]
L_2	Tank 2 level	[m]
$T_{2,in}$	Cold water feed temperature to PU 2	[°C]
T_2	Tank 2 temperature	[°C]
T_4	Hot water feed temperature to PU2	[°C]

3.3 Model derivation

This section deals with the mathematical structure of the model. While the theory in this section is thoroughly explained in [55], [28] and [9], it is provided here as contextual preamble for the sections that follow.

In a study on process modelling assumptions, it is formally recognized by Hangos and Cameron [56] that elementary dynamic units or *balance volumes* may be used as a means of dynamic process modelling, which includes mass balances and energy balances. The Simulink® model is structured in this manner, using mass balance equations to calculate tank level and energy balance equations to calculate the tank temperatures.

3.3.1 Mass balance derivation

When calculating the mass balance of a process, the principle of mass conservation applies and is defined by Çengel [45] as:

'The net mass transfer to or from a control volume during a time interval Δt is equal to the net change in the total mass within the control volume during Δt.'

The principle is then mathematically formulated as [45]:

$$\frac{dm_{CV}}{dt} = \dot{m}_{in} - \dot{m}_{out}, \tag{3.1}$$

where $\dot{m}_{in}$ and $\dot{m}_{out}$ are the mass flow rates entering and exiting the control volume respectively and m_{CV} is the mass of the control volume (CV). As tank 1 and tank 2 can be seen as control volumes, their mass balance equations may be developed from (3.1). The mass balance for tank 1 is given by

$$\frac{dm_{Tank1}}{dt} = \dot{m}_{F_1} - \dot{m}_{F_{1,out}}, \tag{3.2}$$

with $\dot{m}_{F_1}$ representing the mass flow of the water inlet stream into tank 1 and $\dot{m}_{F_{1,out}}$ representing the tank outlet feed mass flow. The same can be shown for tank 2 using streams F_2, $F_{1,out}$ and outlet stream $F_{2,out}$:

$$\frac{dm_{Tank2}}{dt} = \dot{m}_{F_2} + \dot{m}_{F_{1,out}} - \dot{m}_{F_{2,out}}. \tag{3.3}$$

Equations (3.2) and (3.3) can be rewritten in terms of the PVs measured in Fig. 3.1 and tank 1's area A_1, yielding [9, 28]:

$$A_1 \frac{dL_1}{dt} = F_1 - F_{1,out}, \tag{3.4}$$

for tank 1 with

$$F_{1,out} = k_L \times \sqrt{L_1}. \tag{3.5}$$

The latter equation serves as an approximation for the flow generated by the static pressure in a tank in relation to its level, with k_L as the level constant [55]. Similarly, tank 2's mass balance equation is revised as [9, 28]:

$$A_2 \frac{dL_2}{dt} = F_2 + F_{1,out} - F_{2,out}. \tag{3.6}$$

Equations (3.4) and (3.6) can therefore be used to simulate the level control within PU1 and PU2 respectively, which is the first main function of the process. The second main function, namely temperature control within PU1 and PU2, requires an energy balance approach.

3.3.2 Energy balance derivation

A natural transition can be made from a mass balance domain to an energy balance domain as the energy balance equation encapsulates the spectrum of system interactions, including heat transfer. The mass balance equation only considers the exchange of physical matter, i.e. liquid streams contributing to the tank volumes.

The first law of thermodynamics states that in a process, energy cannot be created nor destroyed, but only change form. This is also known as the energy conservation principle [45, 57, 58]. The principle is applied by Marlin [55] to the process as:

$$\frac{dU}{dt} = \dot{H}_{out} - \dot{H}_{in} + \dot{Q} + \dot{W}_s, \tag{3.7}$$

showing that the change in internal energy U is influenced by the enthalpy rate of the input liquid stream ($\dot{H}_{in}$) and outlet liquid stream ($\dot{H}_{out}$), as well as by the heat transfer rate ($\dot{Q}$) and shaft work rate ($\dot{W}_s$). Only mass flow and heat transfer are applicable to the heated two-tank process as the work done by the mixer shaft work in each tank may be regarded as negligible [55].

The rate of enthalpy transfer $\dot{H}$ by a liquid stream i is given by [9, 28, 55]:

$$\dot{H}_i = \rho C_p F_i (T_i - T_{ref}). \tag{3.8}$$

Uren et al. [9] show that for the heated two-tank process specifically, the heat transfer rate $\dot{Q}$ within a PU is calculated by:

$$\dot{Q} = -\frac{aHeat \cdot F_i^{b+1}}{F_i + \frac{aHeat \cdot F_i^b}{2\rho C_p}} \cdot (T_{tank} - T_{coil,in}), \tag{3.9}$$

with $aHeat$ and b as the heat transfer coefficients and F_i as the flow in coil i. The constants C_p and ρ represent the heat capacity and density of water respectively. T_{tank} is the temperature of the liquid content of the tank observed, whereas $T_{coil,in}$ is the temperature of the heating liquid flowing through the coil i before entering the tank.

To substitute (3.9) and (3.8) into (3.7), the first term of (3.7) needs to be defined within the framework of the heated two-tank process. For each PU, the rate of change in internal system energy is calculated as [9, 28, 55]:

$$\frac{dU}{dt} = \rho C_p \frac{dVT_{tank}}{dt}, \tag{3.10}$$

with V denoting the volume of the tank considered.

Finally, the energy balance for each PU can be written in terms of the parameters in Fig. 3.1 by substituting (3.8), (3.9) and (3.10) into (3.7), yielding:

$$\rho C_p \frac{dV_1 T_1}{dt} = \rho C_p (F_1 T_{1,in} - F_{1,out} T_1) - \frac{aHeat \cdot F_3^{b+1}}{F_3 + \frac{aHeat \cdot F_3^b}{2\rho C_p}} \cdot (T_1 - T_3) \tag{3.11}$$

for PU1 and

$$\rho C_p \frac{dV_2 T_2}{dt} = \rho C_p (F_{1,out} T_1 + F_2 T_{2,in} - F_{2,out} T_2) - \frac{aHeat \cdot F_4^{b+1}}{F_4 + \frac{aHeat \cdot F_4^b}{2\rho C_p}} \cdot (T_2 - T_4) \tag{3.12}$$

for PU2 [9, 28].

3.4 Model Configuration

3.4.1 Process parameters

To achieve model validity by means of a practical system, the original model required parameter configuration and verification within the design specifications of the practical process components. The process, mechanical and piping design of the practical system forms part of a separate study within the NWU Faculty of Engineering. As such, the system parameters of the Simulink® model were configured to match these specifications and are outlined in Table 3.3.

Table 3.3: List of model-applicable parameters specified for practical process

Parameter	Description	Value	
C_p	Heat capacity of water	4.187	[kJ/kg · K]
ρ	Density of water	997	[kg/m^3]
A_1	Cross-sectional area of tank 1	0.373	[m^2]
A_2	Cross-sectional area of tank 2	0.373	[m^2]
F_{pump}	Cold water pump flow	1.5×10^{-3}	[m^3/s]

The observed external PVs of the practical plant are listed in Table 3.4 and the normal steady-state averages for the practical PVs are listed in Table 3.5. The steady-state values for the tank temperatures and levels are also their set point (SP) values.

Table 3.4: List of observed external PVs from the practical system

Process Variable	Value	Unit
$T_{1,in}$	25.2	[°C]
$T_{2,in}$	25.6	[°C]
T_3	33	[°C]
T_4	33	[°C]

Table 3.5: List of steady-state PVs observed from the practical system

Process variable	Value	Unit
F_1	3.55×10^{-4}	[m^3/s]
F_2	1.68×10^{-4}	[m^3/s]
F_3	2.37×10^{-4}	[m^3/s]
F_4	2.37×10^{-4}	[m^3/s]
L_1	0.505	[m]
L_2	0.505	[m]
T_1	28	[°C]
T_2	29	[°C]

Table 3.6: List of calculated variables and parameters required for process model

Process variable	Value	Unit
$F_{1,out}$	3.55×10^{-4}	[m^3/s]
$F_{2,out}$	5.23×10^{-4}	[m^3/s]
$k_{L,1}$	5.1×10^{-4}	[$m^3/s/m^{0.5}$]
$k_{L,2}$	7.5×10^{-4}	[$m^3/s/m^{0.5}$]
$aHeat_1$	89.71	[$kJ/m^3 \cdot K$]
$aHeat_2$	125.18	[$kJ/m^3 \cdot K$]
b	0.5	[-]

With the specifications listed in Table 3.3 and the observed external PVs of the practical system as listed in Table 3.4, the remaining model parameters were calculated, allowing the model to be compared to the practical process results in Table 3.5.

First, k_L was determined for each tank. Knowing that the level in both tanks should remain constant, the differential terms in (3.2) and (3.3) are set to zero, leading to

$$\dot{m}_{F_{1,out}} = \dot{m}_{F_1} \tag{3.13}$$

and

$$\dot{m}_{F_{2,out}} = \dot{m}_{F_2} + \dot{m}_{F_{1,out}}, \tag{3.14}$$

which translates to

$$F_{1,out} = F_1 \tag{3.15}$$

and

$$F_{2,out} = F_2 + F_{1,out}, \tag{3.16}$$

since the density of all liquid streams are equal. The value for k_L for each tank may now be calculated using (3.5).

The value of $aHeat$ needed to be determined to complete the heat transfer portion of the model. This was achieved by solving (3.11) and (3.12) with the differential term set to zero, to obtain the coefficient for tank 1 ($aHeat_1$) and tank 2 ($aHeat_2$). The value of b in these equations is set to 0.5, as in [9] and [55]. The results of the calculated parameters are tabulated in Table 3.6.

3.4.2 Controller parameters

The PI-controller is the most widely used controller type in the chemical process industry [2] and is employed within this model for level and temperature control in both PUs. The PI controller differs from the PID controller in that the derivative term is set to zero. The purpose of the derivative term is to enable a faster controller response, but if the system is noisy, the derivative action will lead to noise amplification [2].

In the practical system, a Siemens S7-1200 programmable logic controller (PLC) was used for general process control and monitoring. The PLC features built-in PID control functions, one of which is called "PID_Compact" technology and was found to be suitable for use in the practical system among other advanced features. The PID_Compact" function allows for automatic, online PI tuning to determine the optimal PI gain values. The tuning procedure follows a pre-tuning and fine-tuning phase, employing step-response and oscillatory evaluation, respectively to determine said values. These values are tabulated in Table 3.7. The same PI-values were used in the Simulink® model.

Table 3.7: Controller gain values

Controller	P-gain	I-gain	D-gain
LC1	5.76	0.32	0.0
LC2	0.83	0.05	0.0
TC1	49.91	0.54	0.0
TC2	49.91	0.54	0.0

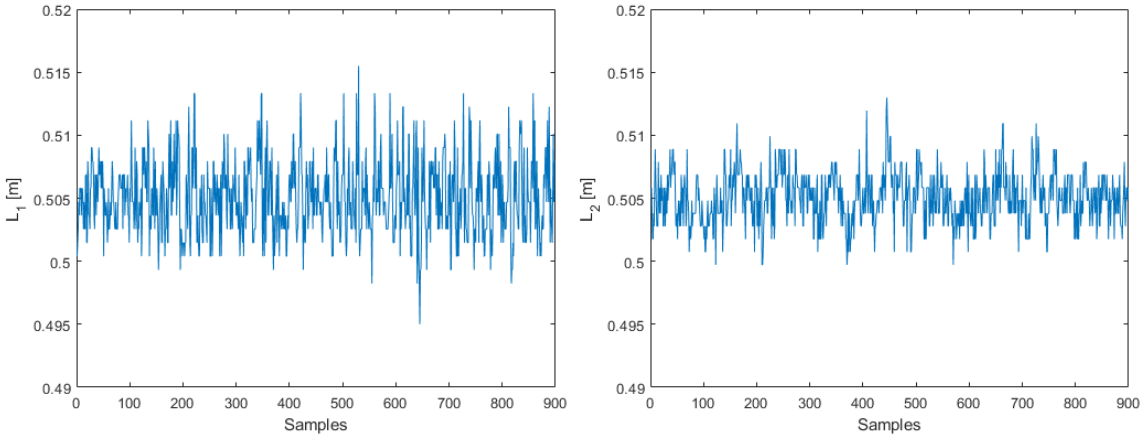
3.4.3 Noise & disturbance parameters

Noise and disturbance modelling is important because the model must be able to predict the effect of external interferences and hereby create a more realistic platform for FDI testing.

Noise, with reference to measurement instrumentation, is defined as random measurement error induced by environmental, sensor and transmission noise [59]. Sensor noise refers to errors occurring within the instrument transducer. Transmission noise may occur if higher voltage cables are nearby, leading to electromagnetic interference. As part of the instrumentation design phase of the pilot plant, high-quality sensors with industry-grade accuracy were specified. Care was taken to keep sensor cable routes separate from high voltage cable runs. More importantly, given their accuracy and routing scheme, the influence of sensor noise is negligibly small when compared to process disturbances and for this reason, sensor noise was excluded from the model.

As defined in Chapter 2, disturbances are uncontrolled inputs that cause a PV to deviate from its SP value. The main controlled variables that are subject to said deviation in the heated two-tank system are temperature T and level L.

The main sources of level disturbance in the PUs are incoming water feeds and tank agitators. Figures 3.2a and 3.2b show the recorded practical level of PU1 and PU2, indicating the presence of the disturbance and how the controllers maintained the levels at their set points of 0.505 m throughout the recorded 900 samples of operation. From Fig. 3.2a, the amplitude of the disturbance with reference to the SP is ± 10 mm or $\pm 2\%$. Therefore, a Gaussian distribution signal with a maximum deviation of 2% was added to the level signal in the model. The maximum level deviation in PU2 is ± 5 mm, with two outliers at 7.5mm, as shown in Fig. 3.2b. Likewise, a uniformly-generated Gaussian signal of 1% was added to the PU2 level in the model.

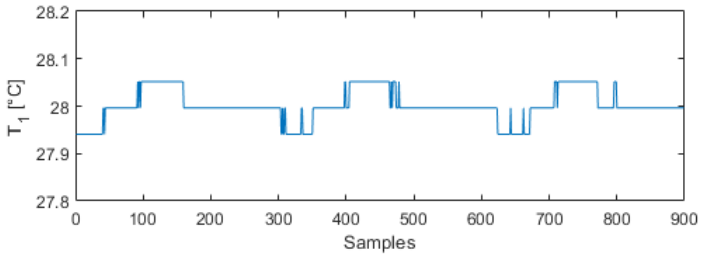


(a) Practical level L_1 disturbance on PU1

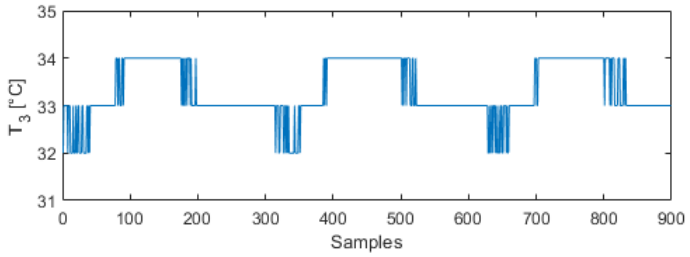
(b) Practical level L_2 disturbance on PU2

Figure 3.2: Disturbance of level PVs in the practical system

Temperature disturbances were also observed in the practical system for both PUs. The root cause of the disturbance was found to be the varying temperature of the hot flow streams (T_3 and T_4). Figures 3.3 and 3.4 illustrate how a change of 1 °C in T_3 and T_4 lead to a slight temperature deviation of 0.05 °C in T_1 and T_2, respectively.

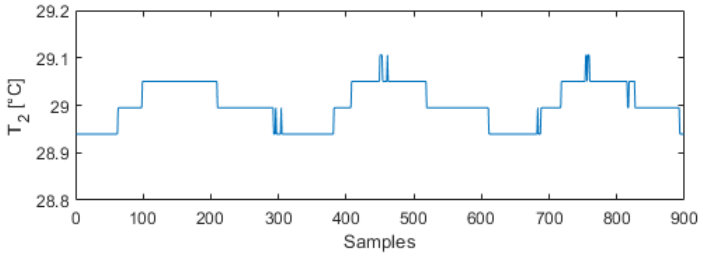


(a) Practical temperature T_1 disturbance of PU1

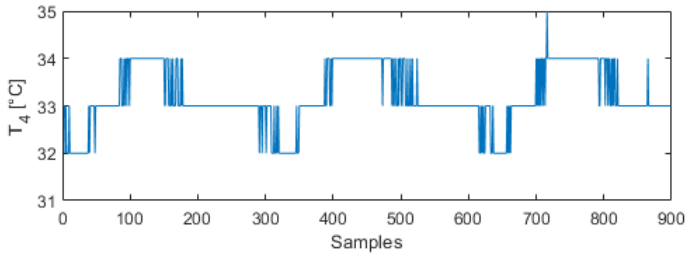


(b) Deviation of hot water temperature T_3

Figure 3.3: Deviating trend of practical temperature T_1 due to varying external temperature T_3 of F_3.



(a) Practical temperature T_2 disturbance of PU2



(b) Deviation of hot water temperature T_4

Figure 3.4: Deviating trend of practical temperature T_2 due to varying external temperature T_4 of F_4.

A clear correlation in Figures 3.3 and 3.4 is visible. For both PUs, it follows that when the temperature of the hot water stream increases, so does the temperature of the liquid in the PU and vice versa.

The oscillating behaviour of T_3 and T_4 is not predictable and is dependent on the control systems outside of the main process scope outlined in Fig. 3.1. However, it is still important to include this disturbance in the model, as it will enable accurate FDI testing. For this reason, the practical values for external hot water temperatures T_3 and T_4, as well as external cold water temperatures $T_{1,in}$ and $T_{2,in}$ are used as model inputs.

3.4.4 Valve modelling

Valve behaviour is another critical aspect to be considered when constructing a realistic process model. The methodology followed to achieve this is described next.

The relationship between the movement of the valve stem and the corresponding flow change through the valve is known as *valve characteristic*. Three valve characteristics are prevalent in the industry, namely linear, equal percentage and quick opening. These characteristics are visualised in Fig. 3.5 [60].

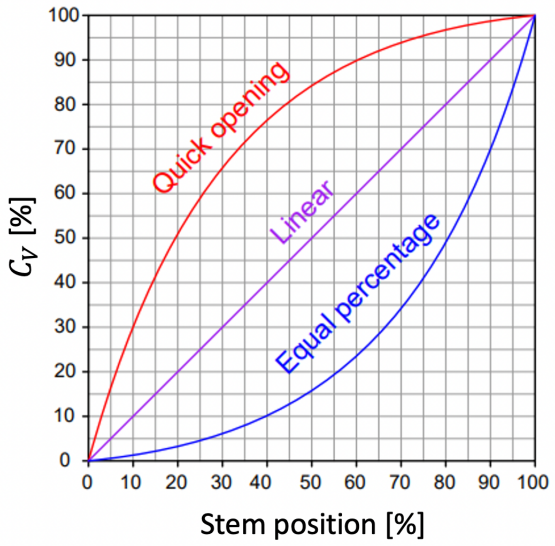
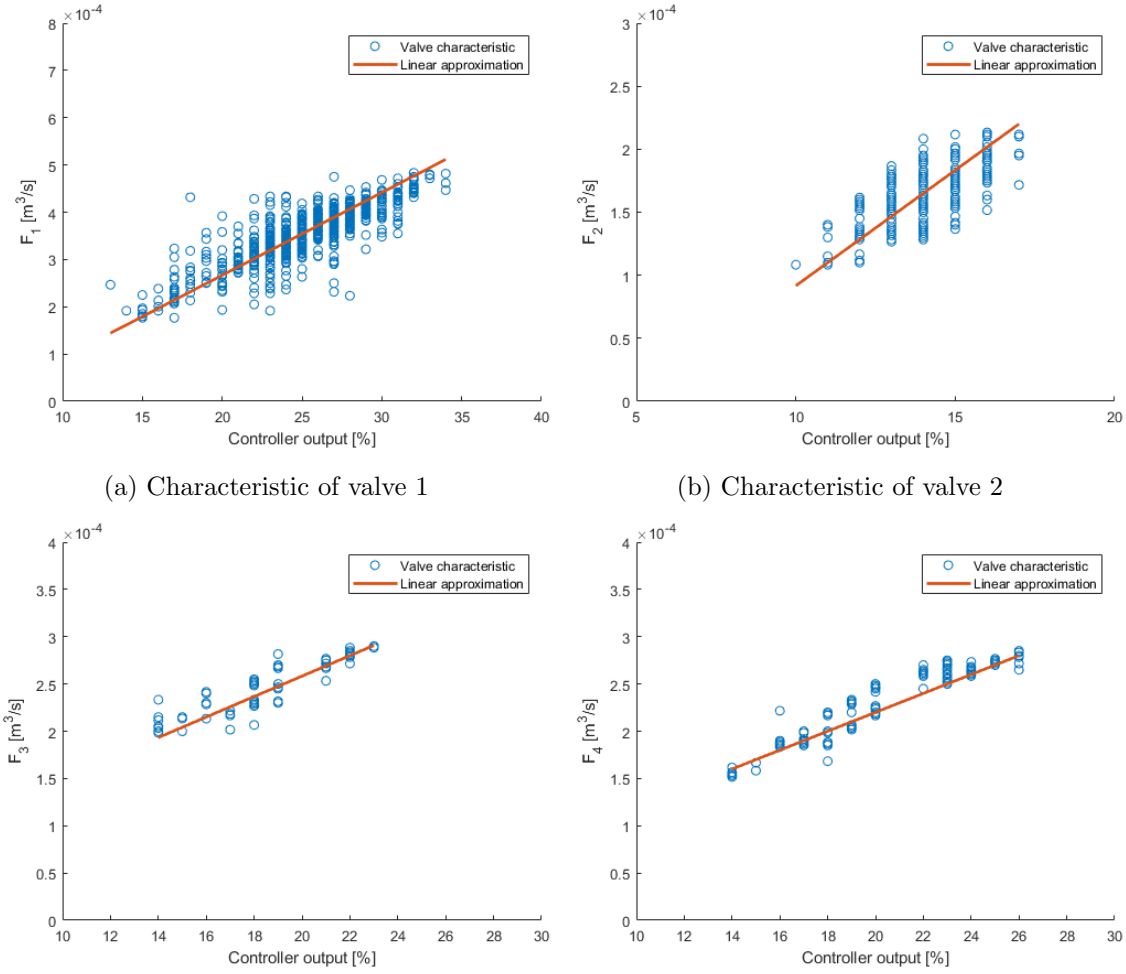


Figure 3.5: The characteristics of linear, quick opening and equal percentage valve operation [60]

Figure 3.5 shows that for the linear valve characteristic, a linear increase in the stem position leads to a linear increase in valve flow coefficient (C_v). The quick opening and equal percentage valve characteristics produce a non-linear C_v. The practical heated two-tank system is equipped with linear control valves. From a modelling perspective, it may therefore be assumed based on Fig. 3.5 that a single gain multiplier can be used to convert the PI-controller percentage into a flow value. The gain value would be proportional to the C_v per percentage, assuming the PID output and final stem position are equal.

Figure 3.6 shows the practical valve behaviour from the pilot plant and the corresponding best-fit linear approximation for normal, steady-state operation. Across all plots, it is shown that the practical valve characteristic does not form an exact line, but rather an oval shape. This may be attributed to several mechanical factors including hysteresis, stiction, valve deadband and dead zones [61, 62]. The modelling of these factors is complex and efforts have been made to address them [61–65]. For this study, the linear approximations given in Fig. 3.6 were used in the model.

A second noteworthy observation from Fig. 3.6 is that the linear approximation line gradient varies for each valve, even though valves 1 to 4 are the same size. The different gradients are caused by the *installed characteristics* of the valves, as opposed to the *inherent characteristics* of the valves as shown in Fig. 3.5. In Fig. 3.7, this behaviour is illustrated. The inherent or ideal characteristic assumes a constant pressure drop through the valve as flow increases. In practice, however, the pressure drop across the valve does not remain constant, as the upstream pressure P_1 and downstream pressure P_2 change with flow, illustrated in Fig. 3.7a. These pressure changes are caused by the upstream



(a) Characteristic of valve 1

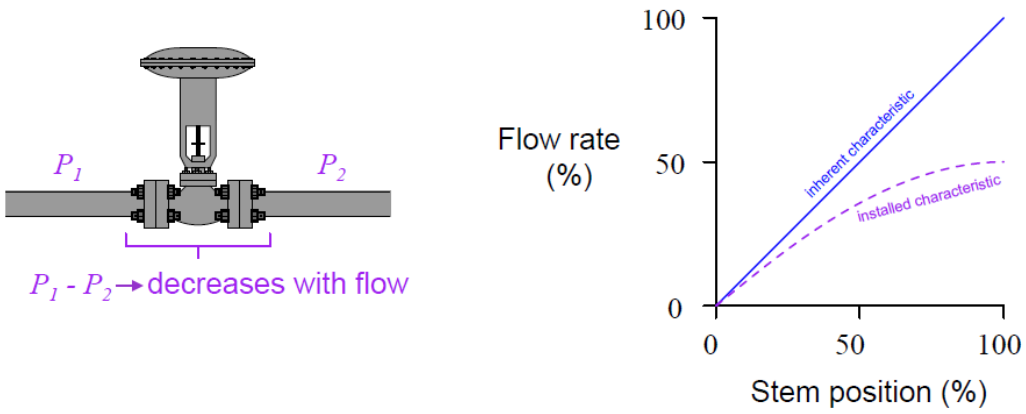
(b) Characteristic of valve 2

(c) Characteristic of valve 3

(d) Characteristic of valve 4

Figure 3.6: Practical control valve characteristics and their linear approximation

and downstream piping connected to the valve. Consequently, the valve will eventually enter a state of saturation, where an increase in stem position will not cause the flow to increase [60]. This behaviour is visible in Fig. 3.7b, where a flatter gradient is indicative of flow saturation. The pressure drop curves across the piping components are not included in this model, but the true maximum flows observed in the practical system are included as maximum flow limits for all flows in the model and listed in Table 3.8. Even though this process does not operate near its flow saturation limits, it is important to include them in the model for accurate fault simulation.



(a) Pressure differential across value

(b) Inherent vs. installed valve characteristic

Figure 3.7: Valve characteristic changes due to non-constant pressure drops across valves [60]

Table 3.8: Maximum saturated flows of the practical heated two-tank process

Flow variable	Observed maximum	Unit
F_1	1.0×10^{-3}	$[m^3/s]$
F_2	0.86×10^{-3}	$[m^3/s]$
F_3	0.4×10^{-3}	$[m^3/s]$
F_4	0.4×10^{-3}	$[m^3/s]$

3.4.5 Model assumptions

In addition to the modelling assumptions and approaches discussed in previous sections, the following general assumptions are made for the heated two-tank process model. Since the model was developed by Lindner and Auret [28] based on the work of Marlin [55], the same assumptions apply:

1. The energy stored in the tank walls and within the heating coils is negligible when compared to the energy stored in the liquid contained in the tank.
2. In the presence of agitators, the liquid temperatures T_1 and T_2 are homogeneous throughout each tank.
3. As a result of the assumption of perfect mixing conditions, it is assumed that the liquid temperature of $F_{1,out}$ is equal to T_1 and $F_{2,out}$ is equal to T_2.

4. Initial steady state operation is assumed.
5. All physical properties of the liquid are constant.
6. The pipe lengths from valves to process components are short enough such that liquid transport delay is negligibly small.
7. Measurement of process variables is cyclic and instantaneous.

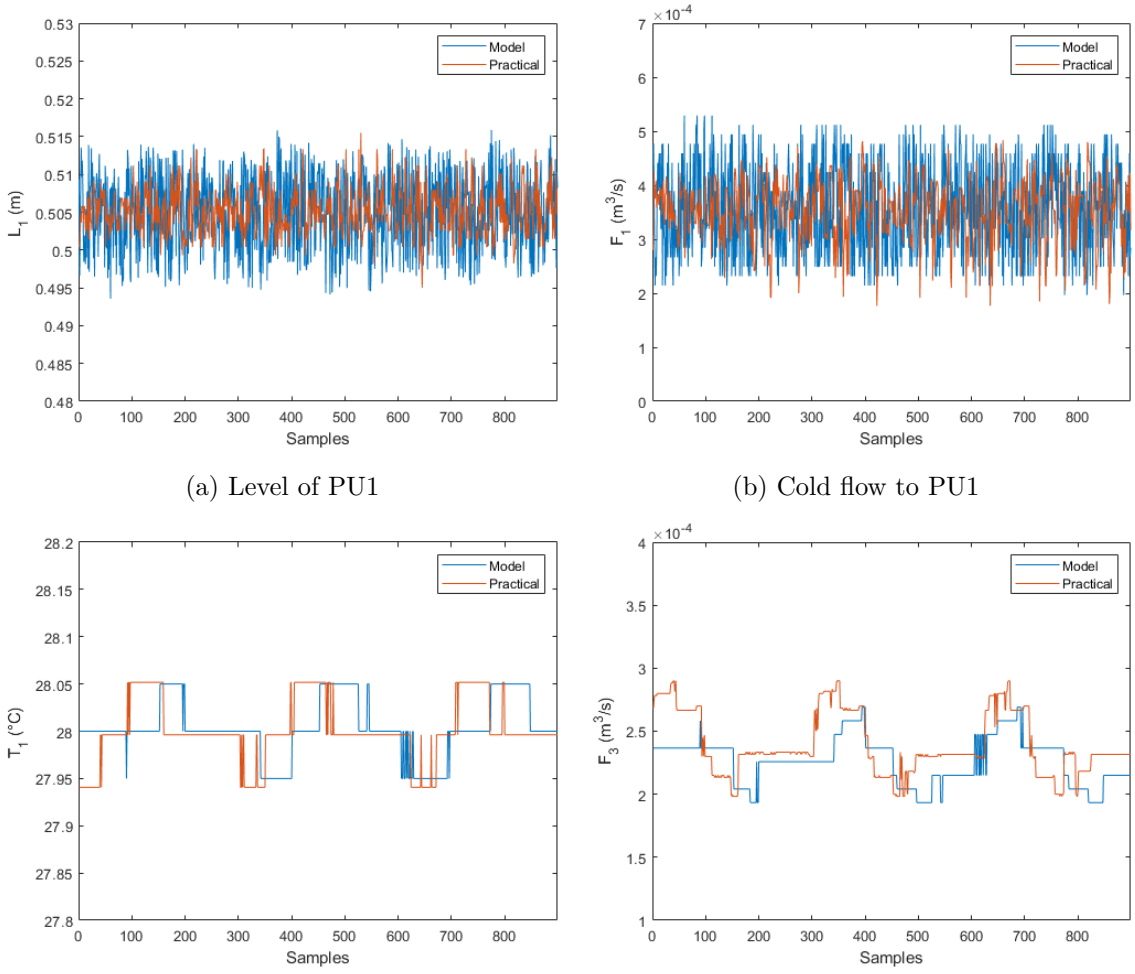
3.4.6 Normal operation validation

Before continuing to fault modelling and testing, the normal operation of the heated two-tank process with the model updates discussed throughout Section 3.4 must first be validated. Note that is section aims only to validate the model operation, as no major process modifications were made to the original model from [28] and therefore, the testing performed in [28] is accepted as sufficient verification. Additionally, since the purpose of the modifications discussed in this section is to match the operation of the practical system, validation is appropriate.

Figure 3.8 shows the results for normal steady-state operation in PU1 for both the model (blue lines), as well as the practical plant (orange lines) over 30 minutes with a sample rate of 1 Hz. In Fig 3.8a, the model shows a L_1 with a disturbance signature that is similar to the practical level. Since F_1 is controlled to maintain L_1, a matching signature is observed in Fig. 3.8b, at the same average flow rate as the practical system.

The model and practical T_1 of PU1 are shown Fig. 3.8c with the corresponding hot water flow F_3 in Fig. 3.8d. Both the model and practical T_1 were controlled at a set point of 28 °C with matching disturbance patterns. The modelled and practical F_3 likewise show similar behaviour but are not identical. Close inspection of Fig. 3.8c and 3.8d reveal that the practical variables are leading, while the model variables are lagging. This is caused by the mismatch in the control interval between the PLC system and the Simulink® model. The PLC is programmed to execute control actions every 900 ms while logging data every 1000 ms. The Simulink® model executes control actions and logs every 1000 ms. This leads to the practical system exhibiting a slightly quicker dynamic response to process variations. For future studies, it is recommended that the configuration of the PLC be updated so that the control interrupt sequence and logging have matching frequencies.

Figure 3.9 illustrates the PU2 model behaviour in comparison with the practical system. The level of the model and practical system show similar disturbance patterns and are both controlled at 0.505 m in Fig. 3.9a. However, the corresponding F_2 in Fig. 3.9b are not similar. The practical F_2 fluctuates more than the model F_2, which is indicative of an oversized valve. In [66], it is explained that oversized valves lead to over-sensitivity



(a) Level of PU1

(b) Cold flow to PU1

(c) Temperature of PU1

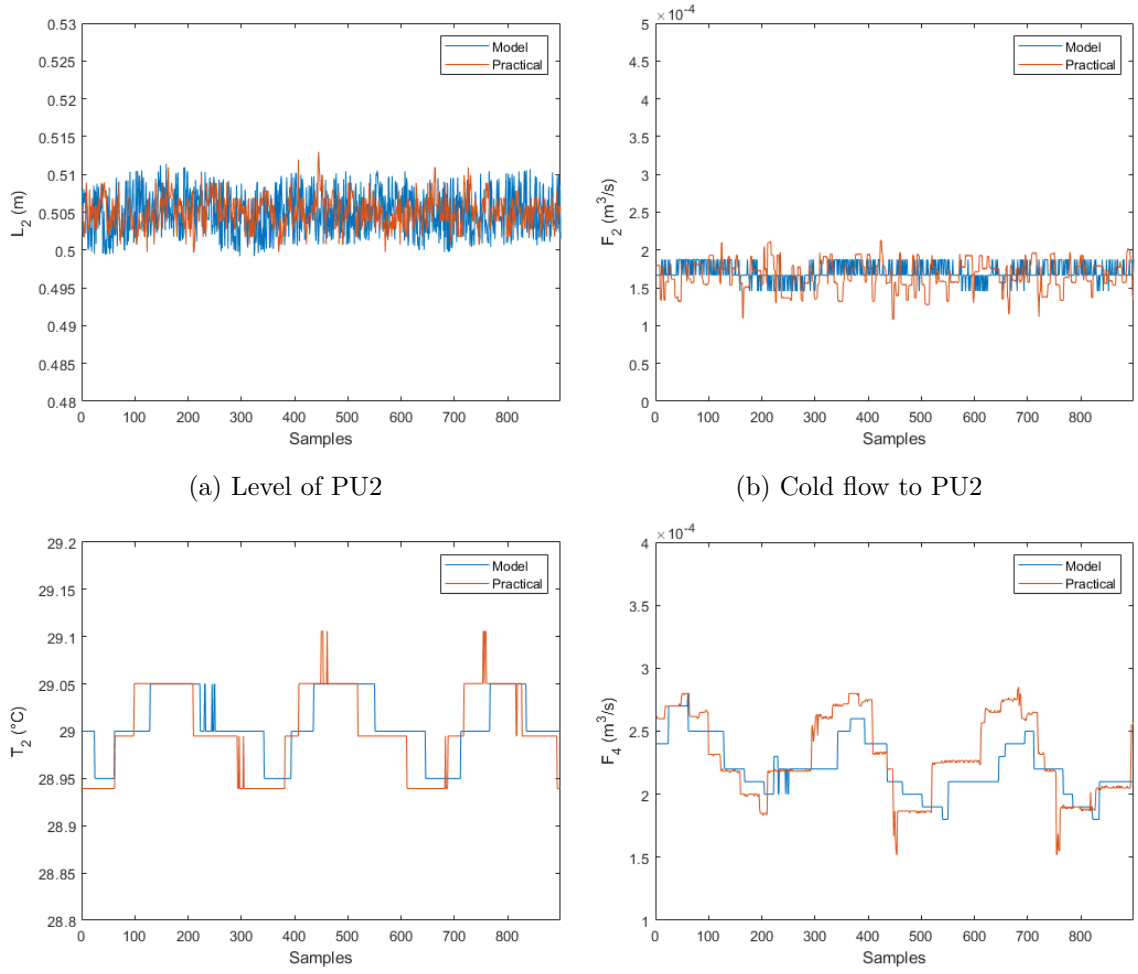
(d) Hot flow to PU1

Figure 3.8: Normal, steady state operation of PU1 model and practical system

in control actions, such that small control changes lead to a large flow change. From Table 3.5, F_2 is shown to be the smallest flow variable, which explains the fact that this fluctuating behaviour is not observed in the other flow PVs. Furthermore, the control range of 10% - 17% as shown in Fig. 3.6b supports this argument, as valve operation below 20% is regarded as suboptimal [66].

The behaviour of the PU2 heating system is similar to the modelled and practical systems. In Fig. 3.9c, an average of 29 °C was maintained for T_2 by both systems in the presence of external disturbance. Both F_4 variables are shown to have the same profile and also reflect the lagging effect shown in the PU1 results.

Table 3.9 shows a comparison between the average of each key PV from the process model and practical system, including their controller outputs. The main purpose of the table is to validate the steady-state results of the model using the practical system. The table



(a) Level of PU2

(b) Cold flow to PU2

(c) Temperature of PU2

(d) Hot flow to PU2

Figure 3.9: Normal, steady state operation of PU2 model and practical system

shows that the normal, steady-state model output is within a 6% error margin of the practical system.

Table 3.9: Steady-state comparison between model and practical results

Parameter	Model average	Practical average	Unit	Difference
F_1	3.56×10^{-4}	3.55×10^{-4}	[m^3/s]	0.3%
F_2	1.71×10^{-4}	1.67×10^{-4}	[m^3/s]	2.4%
F_3	2.27×10^{-4}	2.4×10^{-4}	[m^3/s]	5.4%
F_4	2.22×10^{-4}	2.3×10^{-4}	[m^3/s]	4.3%
L_1	0.505	0.505	[m]	0%
L_2	0.505	0.505	[m]	0%
T_1	28.0	28.0	[°C]	0%
T_2	29.0	29.0	[°C]	0%
LC1	25.1	25.3	[% open]	0.8%
LC2	14.2	14.1	[% open]	0.7%
TC1	17.1	18.0	[% open]	5%
TC2	20.2	20.4	[% open]	1%

From Fig. 3.8, Fig. 3.9 and Table 3.9 it is concluded that for normal steady state operation, the model produces the required process outputs as listed in Table 3.5, based on the physical parameters listed in Table 3.3 to 3.6. Within the definition of verification [67, 68], the author believes the model is sufficiently verified for normal steady-state operation.

Validation is achieved when the model results are acceptably accurate for a given set of applied experimental conditions [68]. Based on this definition, it can also be concluded that the model is validated for normal, steady state behaviour as the model results closely resemble the practical results.

3.5 Fault modelling, verification & validation

With the NOC of the model validated, it is now appropriate to discuss the modelling, verification and validation of the process faults. The subsections that follow each discuss a fault type and how they were modelled, followed by its verification and validation. Due to the amount of PVs, this section will only show the most appropriate figures related to fault validation. The comprehensive model and practical system results are provided in Appendix A.

3.5.1 Fault 1: Clogging

Description

The first fault implemented is a clog on the outlet of tank 1 and tank 2. The clog was executed with a magnitude of 10%, 20% and 30%. A fault magnitude of 10% means that the internal area of the pipe orifice was reduced to 90% of its original value. In the practical system, this was achieved by adjusting a drain value. To emulate a clog of 10%, the drain valve was set to 90% open, and so on.

Modelling

The primary PV affected by this fault, is $F_{1,out}$ for PU1 and $F_{2,out}$ PU2. When the outlet of, for example, tank 1 is clogged, it is expected that the gravity feed flow F_{1out} will decrease proportionally to the size of the clog.

Figure 3.10 shows the installed (blue) and ideal (orange) characteristic of the PU1 clog valve. The same trend as shown in Fig. 3.7b is found here but in reverse. It can be seen that as the clog valve is closed more (clog size increase), the rate at which F_{1out} changes also increases, creating a non-linear flow curve, as opposed to the linear, ideal characteristic. This is indicative of an oversized valve in practice. To accurately model this behaviour, a linear approximation function (yellow) was used to appropriately adapt F_{1out}. The function is given by:

$$F_{1,out} = -1.67 \times 10^{-6}x + 3.55 \times 10^{-4}, \tag{3.17}$$

with x as the clog size percentage. The same is done for the clog valve of PU2, which yields a linear function of:

$$F_{2,out} = -8.5 \times 10^{-6}x + 5.22 \times 10^{-4}, \tag{3.18}$$

Verification

To verify the clog implementation, the model response is evaluated. With a clog occurring in PU1, it is expected that LC1 will lower F_1 to match $F_{1,out}$. Additionally, F_2 will be increased by LC2 to compensate for the lower F_1. This process response is confirmed in Table 3.10.

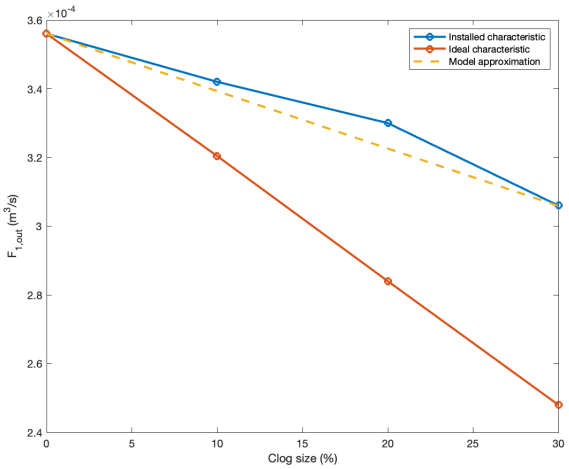


Figure 3.10: PU1 clog valve characteristic

Table 3.10: Model verification for PU1 clogs

	$F_{1,avg}$		$F_{2,avg}$	
Clog size	Value [m^3/s]	Change [%]	Value [m^3/s]	Change [%]
0%	3.56×10^{-4}	0	1.71×10^{-4}	0
10%	3.39×10^{-4}	−4.78	1.88×10^{-4}	+9.94
20%	3.23×10^{-4}	−9.26	2.04×10^{-4}	+19.29
30%	3.06×10^{-4}	−14.04	2.21×10^{-4}	+29.24

For a clog in PU2, it is also expected that F_2 will be decreased by LC2. Recall from (3.16) that the inflow of PU2 is comprised of F_2 and $F_{1,out}$, with F_2 being the lesser of the two. This means that even if LC2 reduces F_2 to zero, there is a chance of loss of control of L_2, if $F_{2,out} < F_{1,out}$. Additionally, it is expected that F_4 will also be adapted by TC2 since the cold F_2 is reduced.

Table 3.11 confirms these predictions. It can be seen that the 0.505 m setpoint of L_2 is no longer maintained at 20% clog size, even with F_2 at zero. Furthermore, since the cold F_2 stopped, hot water feed F_4 is shown to be reduced, since the temperature of $F_{1,out}$ is near the setpoint of T_2. From these results, it is concluded that the clog is modelled correctly.

Table 3.11: Model verification for PU2 clogs

	$F_{2,avg}$		$L_{2,avg}$		$F_{4,avg}$	
Clog size	Value [m^3/s]	Change [%]	Value [m]	Change [%]	Value [m^3/s]	Change [%]
0%	1.71×10^{-4}	0	0.505	0	2.22×10^{-4}	0
10%	0.86×10^{-4}	−49.7	0.505	0	1.27×10^{-4}	−42.79
20%	0	−100	0.518	+2.57	0.58×10^{-4}	−73.87
30%	0	−100	0.61	+20.79	0.52×10^{-4}	−76.58

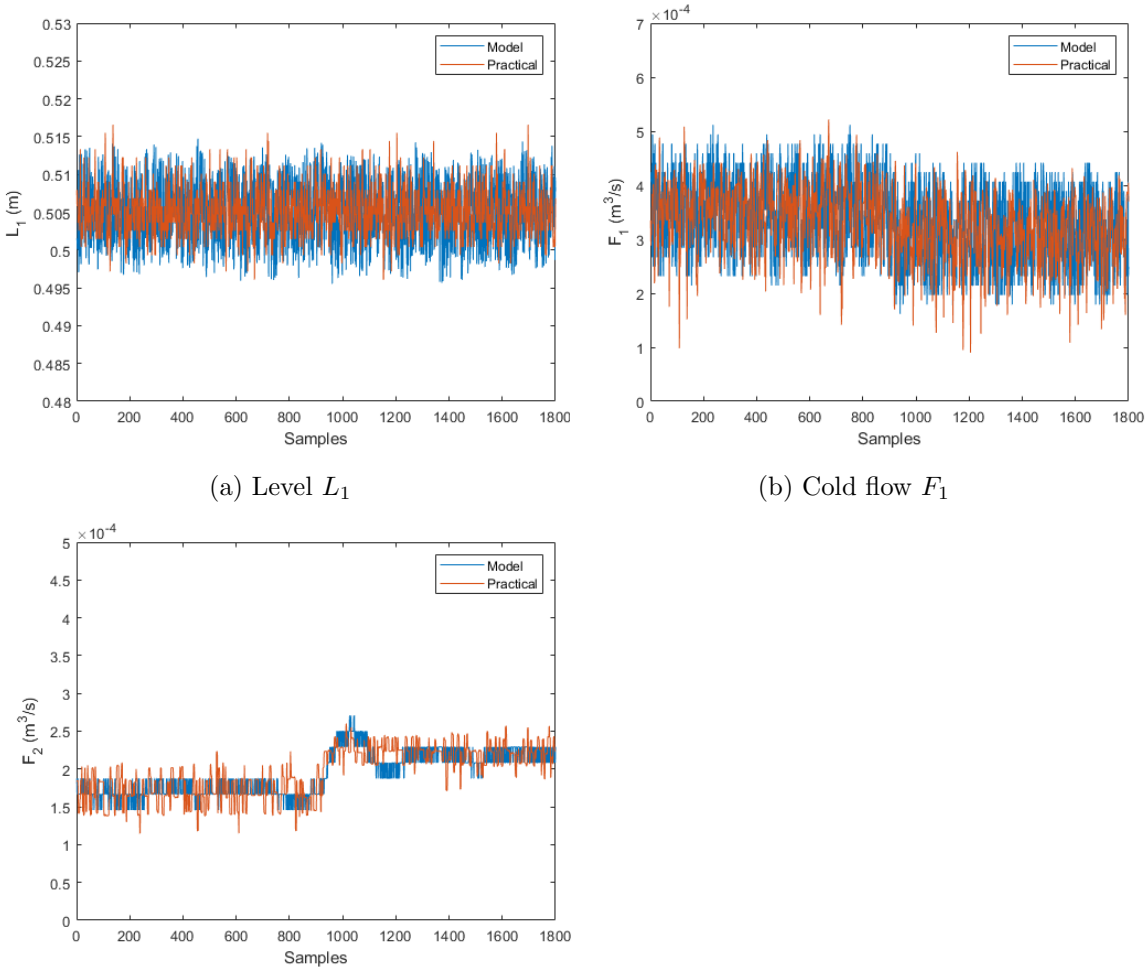
Validation

For validation, the modelled clog process response is compared to the practical response. Fig. 3.11 shows the 30% clogging fault occurring at sample 900 in PU1. It is shown how the L_1 is maintained, F_1 is lowered and F_2 increased as tabulated in Table 3.10. Furthermore, it is illustrated how the model response accurately describes the practical result.

Similarly, the 30% clog occurring at sample 729 in PU2 is illustrated in Fig. 3.12. The model predictions from Table 3.11 are shown to be correct in practice, as the practical system responds similarly to the model. However, it can be seen how the practical level shows a steeper gradient than the model. This anomaly may be attributed to the following factors:

1. **Manual drain valve** - The practical system is equipped with a manual drain valve on PU2, which introduces a greater margin of error when controlling flow (and clog size) than an automated valve.
2. **Agitator-induced pressure** - The agitators of the practical system generate a high-pressure zone below the impeller, which causes a slightly higher outflow and therefore a slower increase in level.

Despite the latter discrepancies, it is concluded that the modelled clog is validated by the practical results shown in Fig. 3.11, 3.12 and the results in Appendix A.



(a) Level L_1

(b) Cold flow F_1

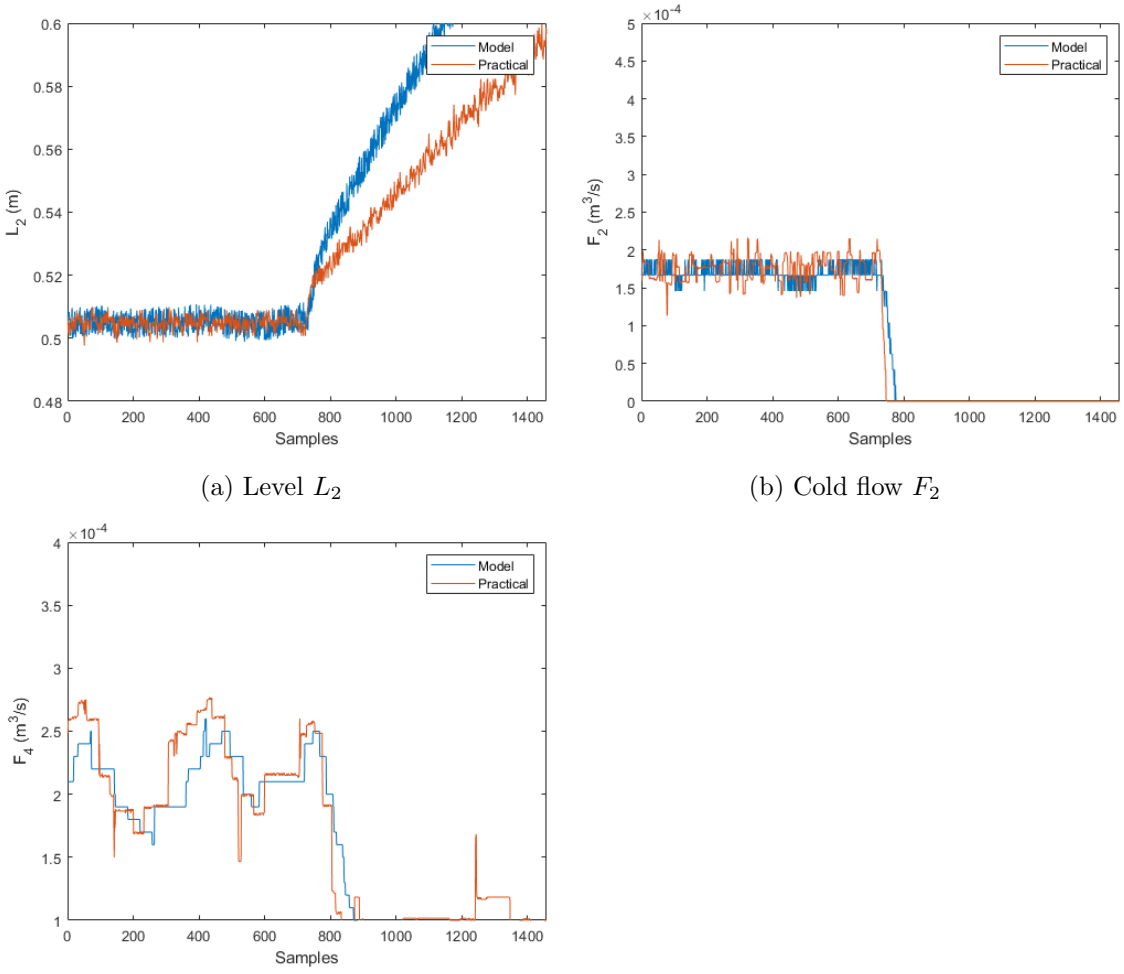
(c) Cold flow F_2

Figure 3.11: Modelled and practical process response of a 30% clog in PU1 at sample 900

3.5.2 Fault 2: Leakage

Description

The second fault tested in the heated two-tank system is a leak in the cold water inlet flow of PU1 and PU2. Like the clogging fault from the previous section, the leakage fault can be classified as a structural fault within the categorization of Venkatasubramanian et al. [5] and Russel et al. [6]. Fault magnitudes of 10%, 20% and 30% are tested on both PUs. A 10% leak, for example, is defined as an additional, unintended flow path with an orifice area that is 10% of the intended flow path. Practically, this was achieved with a bypass valve on the flow paths of F_1 and F_2.



(a) Level L_2

(b) Cold flow F_2

(c) Hot flow F_4

Figure 3.12: Modelled and practical process response of a 30% clog in PU2 at sample 729

Modelling

The leak modelling approach is similar to that of the valve modelling explained in Section 3.4.4 and clog modelling in Section 3.5.1. Since the concept of non-ideal valve characteristics was illustrated and explained in these sections, only the linear approximation functions are provided here.

When a leak occurs downstream of the flow meters, the measured flow (F_1) is no longer the actual flow entering the tank ($F_{1,in}$). Using the practical data, a linear function was derived to estimate $F_{1,in}$ using the measured flow F_1 for a given leak size x. For PU1, the leak function is given by:

$$F_{1,in} = \frac{3.55 \times 10^{-4}}{4.83 \times 10^{-6}x + 3.55 \times 10^{-4}} \times F_1. \tag{3.19}$$

For PU2, the function is given by:

$$F_{2,in} = \frac{5.22 \times 10^{-4}}{6.38 \times 10^{-7}x + 5.22 \times 10^{-4}} \times F_2. \tag{3.20}$$

Notice that as x increases, $F_{1,in}$ and $F_{2,in}$ decreases if the measured flows F_1 and F_2 remain unchanged. Therefore, the applicable controller is forced to increase the measured F to ensure that F_{in} is sufficient to maintain the level of the PU.

Verification

To verify the leak modelling approach for PU1, the F_1 and LC1 values are evaluated for the different leak sizes. Table 3.12 confirms the increased F_1 and LC1 values.

Table 3.12: Model verification for PU1 leaks

	$F_{1,avg}$		LC1	
Leak size	Value [m^3/s]	Change [%]	Value [% open]	Change [%]
0%	3.56×10^{-4}	0	25.1	0
10%	4.05×10^{-4}	+13.76	27.89	+11.12
20%	4.53×10^{-4}	+27.25	30.67	+22.19
30%	5.02×10^{-4}	+41.01	33.44	+33.22

The same applies to PU2, where an increased F_2 is expected, as well as an increased LC2 output value. This is confirmed in Table 3.13.

Table 3.13: Model verification for PU2 leaks

	$F_{2,avg}$		LC2	
Leak size	Value [m^3/s]	Change [%]	Value [% open]	Change [%]
0%	1.71×10^{-4}	0	14.2	0
10%	1.77×10^{-4}	+3.51	14.48	+1.97
20%	1.83×10^{-4}	+7.02	14.8	+4.23
30%	1.90×10^{-4}	+11.11	15.13	+6.55

Validation

Figure 3.13 shows how the cold feed flow F_1 increases when a 30% leak is created at sample 900. Both the model and practical results show a sudden rise in flow, which is maintained throughout the fault state. No disturbance was observed in the rest of the PVs, which may be viewed in Appendix A.

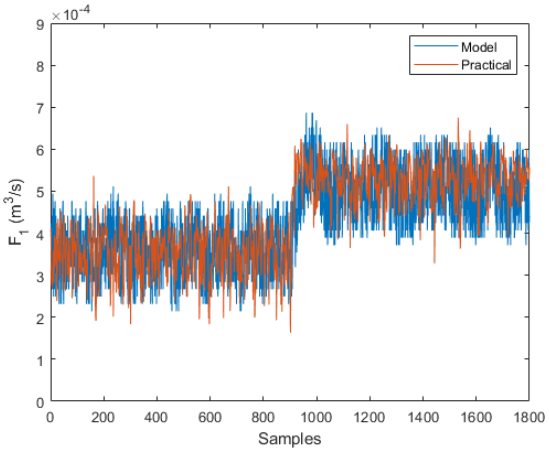


Figure 3.13: Modelled and practical process response of a 30% leak in PU1 at sample 900

Figure 3.14 shows the comparison between the modelled and practical F_2 for a 30% leak occurring at sample 900. The disturbance is significantly smaller when compared to the same fault in PU1. The slight upset is justified by the fact that F_2 only accounts for 33% of the inflow for PU2. Similar to PU1, no deviations were observed in the other main PVs.

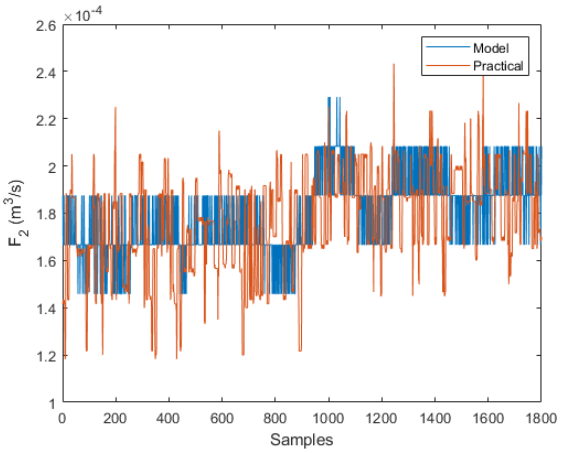


Figure 3.14: Modelled and practical process response of a 30% leak in PU2 at sample 900

Based on the results given in Table 3.12 and 3.13, as well as Fig. 3.13 and 3.14, it is concluded that the leak modelling approach is verified and validated.

3.5.3 Fault 3: Stuck Valve

Description

Next, a stuck valve fault was tested. Valves that are in constant motion are more vulnerable to internal wear and if the valves are not maintained, they may fail in position during operation. In this study, the level control valves are used to show the effect of this fault in a process. In the practical plant, this fault was emulated by overriding the applicable LC output with a fixed output to the valve. For PU1, a fixed valve output of 20% open was used and for PU2, a value of 10% was used.

Modelling

Figure 3.15 shows how this behaviour is implemented in the model for PU1 in the form of a Simulink® flow diagram. The LC1 controller value is imported at port 1 and connects to switch blocks 1 and 2. Switch block 1 will override the LC1 value with '20' at the time instant set in the sample trigger block. Switch block 2 is the master fault enable/disable switch. Therefore, if the Fault on/off block is off, the LC1 value will pass through to output port 1 unmodified. If the Fault on/off block is on, a controller value of 20% will exit output port 1 from the time instant of the sample trigger and LC1's value will be ignored. This mimics the logic implemented in the practical system. The same implementation is used for PU2, except that the fault size is set to 10% open.

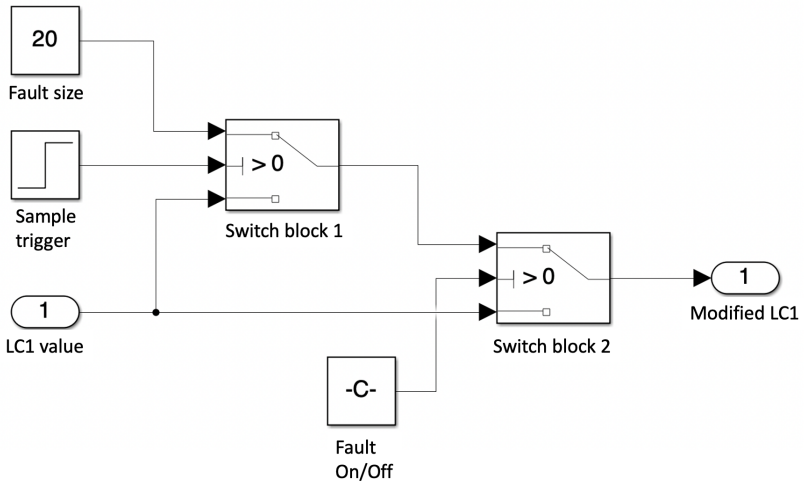


Figure 3.15: Simulink® model of 20% open stuck valve in PU1

Verification

When the stuck valve occurs, the flow (F_1 in the case of PU1) will remain constant. Since the 20 % open position is lower than the average LC1 value of 25.1 %, a decline in PU1 level is expected and with it, a decline in hot water flow F_3. Table 3.14 shows the normal and fault values, which confirms this behaviour. Likewise, this fault in PU2 will have a similar influence on F_2, L_2 and F_4 as shown in Table 3.15.

Table 3.14: Model verification for PU1 stuck valve

Behaviour	$F_{1,avg}$		$L_{1,avg}$		$F_{3,avg}$	
	Value [m^3/s]	Change [%]	Value [m]	Change [%]	Value [m^3/s]	Change [%]
NOC	3.56×10^{-4}	0	0.505	0	2.27×10^{-4}	0
Stuck valve	2.67×10^{-4}	−25	0.454	−10	1.63×10^{-4}	−28.19

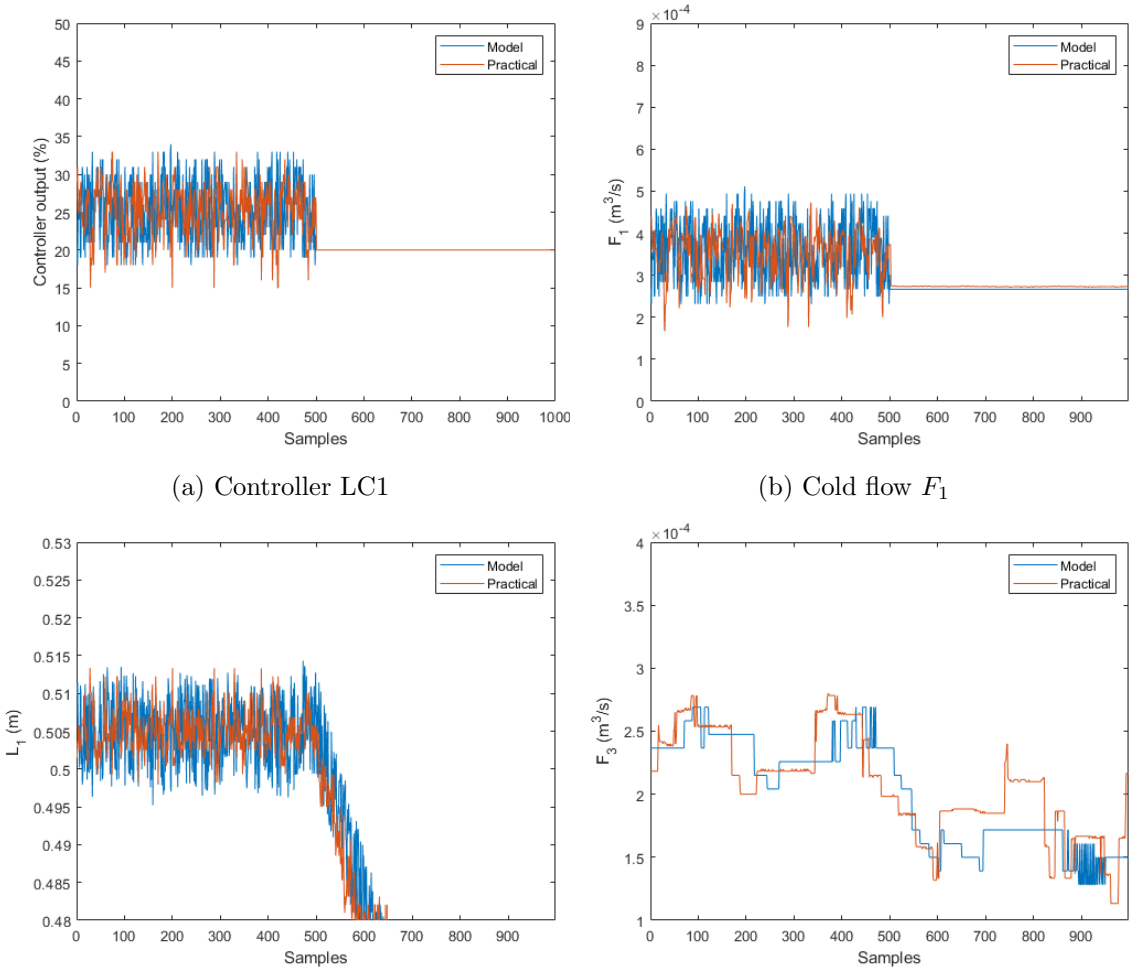
Table 3.15: Model verification for PU2 stuck valve

Behaviour	$F_{2,avg}$		$L_{2,avg}$		$F_{4,avg}$	
	Value [m^3/s]	Change [%]	Value [m]	Change [%]	Value [m^3/s]	Change [%]
NOC	1.71×10^{-4}	0	0.505	0	2.22×10^{-4}	0
Stuck valve	0.83×10^{-4}	−51.46	0.459	−9.10	1.37×10^{-4}	−38.28

Validation

To confirm the validity of this behaviour, it is compared to the practical process response shown in Fig 3.16. The level control valve of PU1 froze in the 20% open position, as indicated by Fig. 3.16a at sample 500. As a result, the cold water flow F_1 in Fig. 3.16b also froze at a fixed flow of approximately 3 $\times 10^{-4}$ m^3/s. Since the flow is lower, a decline in level is observed in L_1 (Fig. 3.16c) for the model and the practical system. Additionally, the hot flow F_3 was lowered to avoid overheating the smaller volume of water in PU1.

The 10 % open stuck valve fault for PU2 is shown in Fig. 3.17, which shows a response similar to that of PU1. Overall, the model has shown acceptable results for the stuck valve fault. The close resemblance to the practical results sufficiently validates its behaviour.



(a) Controller LC1

(b) Cold flow F_1

(c) Level L_1

(d) Hot flow F_3

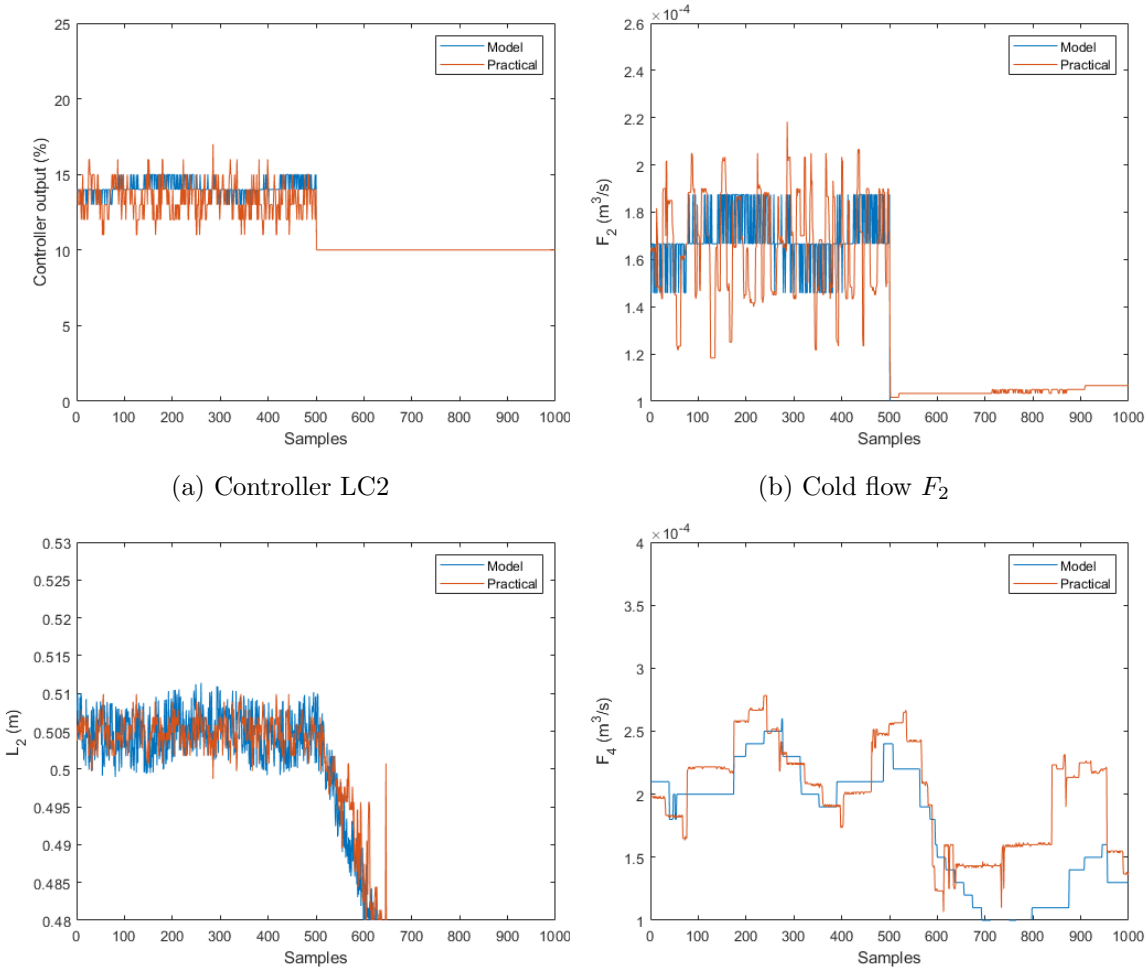
Figure 3.16: Modelled and practical process response of a 20% open stuck valve in PU1 at sample 500

3.5.4 Fault 4: Sensor Drift

Description

A sensor drift fault occurs when the sensor provides the PLC with an inaccurate reading of the measured variable. If the sensor is part of a control loop, the system will respond to the now-biased reading, affecting other PVs as a result. In the practical process, this fault was applied to the temperature sensor of each PU, which is indeed part of a control system.

The drift is instantaneous and is tested in two fault sizes, namely 2% and 5%. A drift size of, for example, 5% means that the PLC reads a sensor value that is 5% higher than



(a) Controller LC2

(b) Cold flow F_2

(c) Level L_2

(d) Hot flow F_3

Figure 3.17: Modelled and practical process response of a 10% open stuck valve in PU2 at sample 500

the true measurement. As with the other faults, a single drift fault of a given size was implemented at a time. Thus, four drift faults in total were tested across PU1 and PU2.

Modelling

A modelling approach similar to the stuck valve is followed, where the sensor input is adjusted using a dual switch block system shown in Fig. 3.15, except that the fault size block is now adjustable between 2% and 5%. As shown in Fig. 3.18, for PU1, this is implemented upstream of the TC1 controller, so that the controller reads a faulty sensor value. The implementation for PU2 is identical and is applicable for T_2 and TC2.

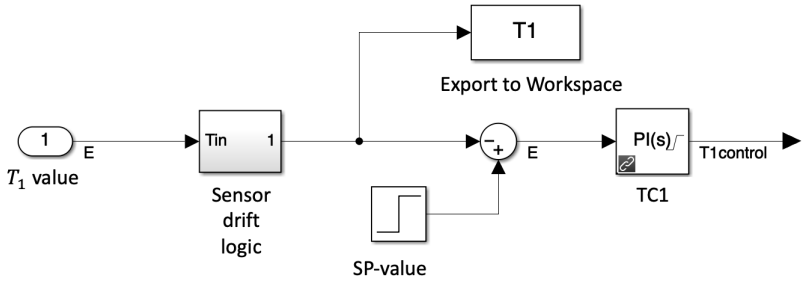


Figure 3.18: Simulink® model extract of sensor drift implementation

Verification

It is clear from Fig. 3.18 that the sensor drift will cause the TC to change the hot flow F_3 incorrectly. This will also lead to PU2 adjusting its hot flow F_4 to compensate for the temperature errors of PU1.

Table 3.16 shows how the F_3 decreases as TC1 responds to a faulty T_1 value. The effect is visible downstream in PU2 as well, with an increase in F_4. The change in PV becomes more significant with increased fault size, as expected.

Table 3.16: Model verification for PU1 sensor drift

	$F_{3,avg}$		$F_{4,avg}$	
Drift size	Value [m^3/s]	Change [%]	Value [% open]	Change [%]
0%	2.27×10^{-4}	0	2.22×10^{-4}	0
2%	1.24×10^{-4}	−45.37	2.80×10^{-4}	+26.12
5%	0.52×10^{-4}	−77.09	3.17×10^{-4}	+29.96

Table 3.17 shows how F_4 is lower in the presence of a sensor drift of T_2. From these results and those given in Table 3.16, it is accepted that the sensor drift fault implementation is correct.

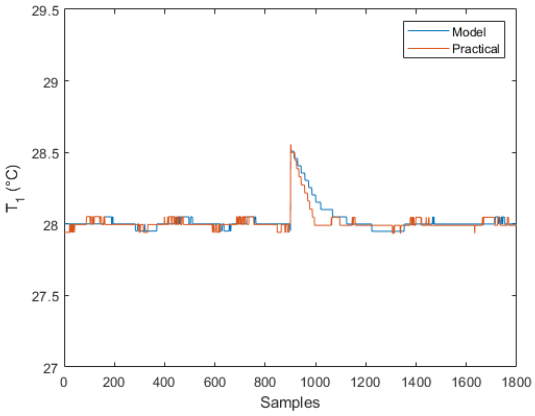
Validation

The model output is now compared to the practical results. Figure 3.19 shows the model and practical results for a 2% upwards drift at sample 900 in the temperature sensor measuring T_1. Figure 3.19a indicates the sudden temperature rise and a gradual recovery to the set point value, as predicted. The hot water flow F_3 initially decreases to zero,

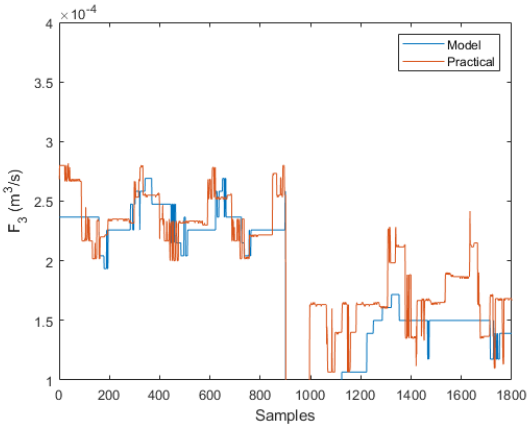
and slowly starts to recover after the fault (Fig. 3.19b). As described earlier, the effects of the fault occurring in PU1 are visible in PU2 as well, as PU2 temperature T_2 and hot water flow F_4 deviate from their normal condition in Fig 3.19c and 3.19d, respectively. The increase in F_4 is due to a colder gravity feed, which in turn is caused by the sudden decline in F_3.

Table 3.17: Model verification for PU2 sensor drift

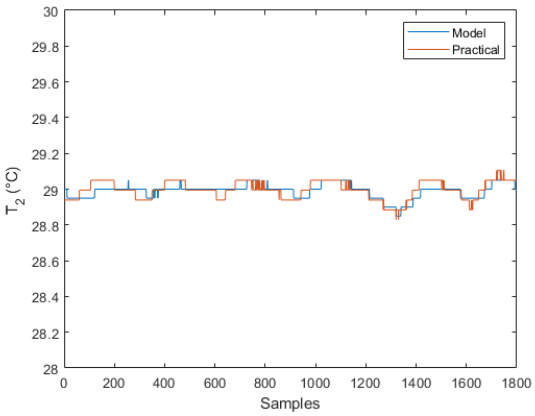
	$F_{4,avg}$	
Drift size	Value [m^3/s]	Change [%]
0%	2.22×10^{-4}	0
2%	1.15×10^{-4}	−48.20
5%	$0.28 \times 10^{-4} \times 10^{-4}$	−87.39



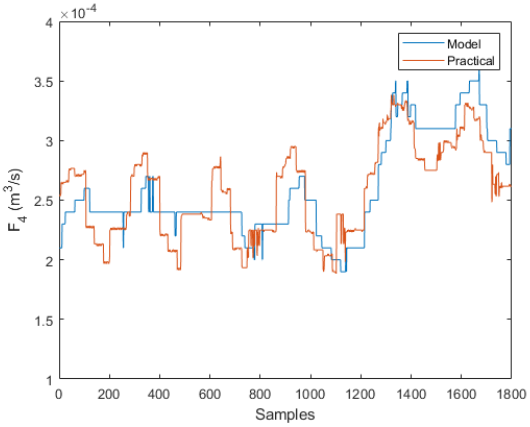
(a) Temperature T_1



(b) Hot flow F_3



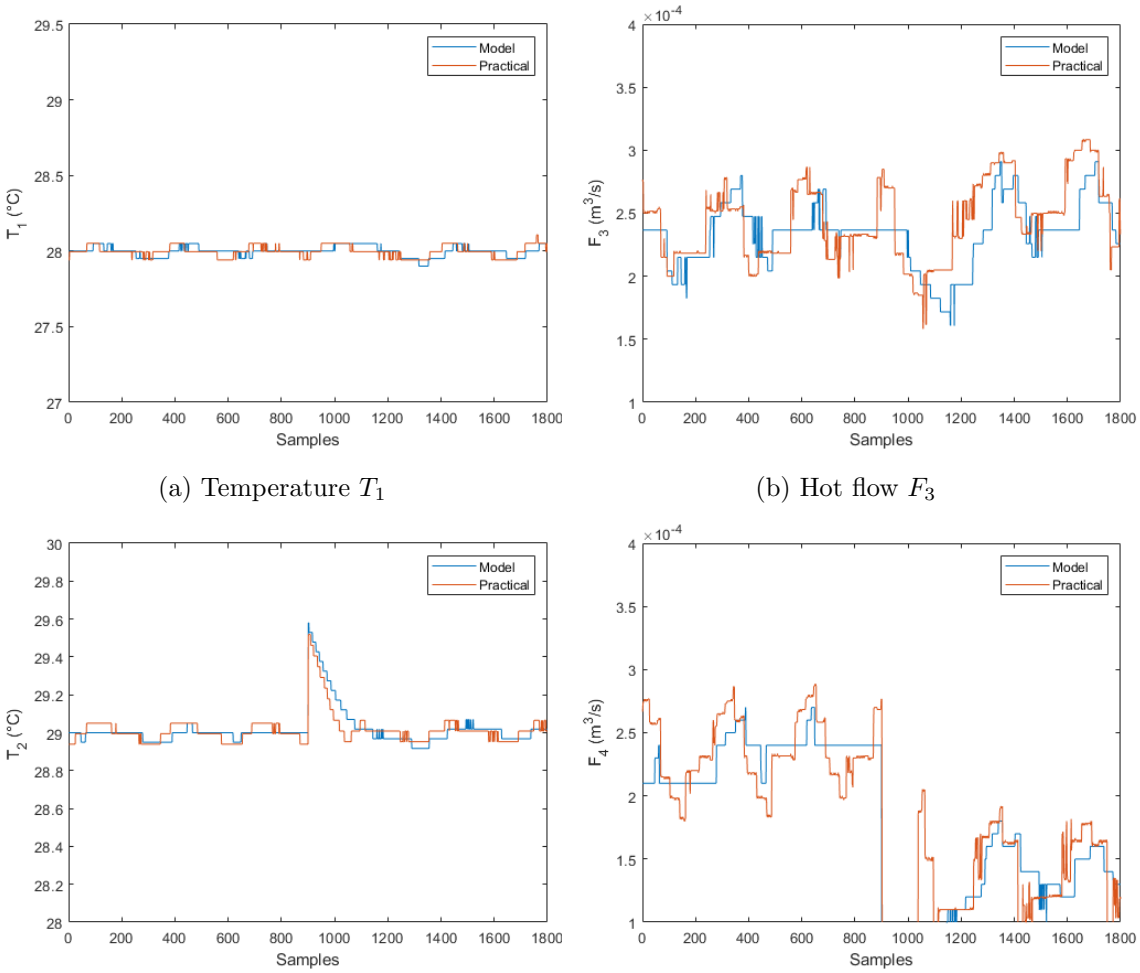
(c) Temperature T_2



(d) Hot flow F_4

Figure 3.19: Modelled and practical process response of a 2% sensor drift in PU1 at sample 900

When the 2% temperature drift is applied in PU2, the same behaviour is observed where the temperature T_2 starts to recover after the fault occurs at sample 900. The hot water flow F_4 initially decreased to zero but then recovered to a lower flow in the model and practical system. Temperature T_1 remains undisturbed (Fig. 3.20a), as the fault occurred downstream of PU1. Hot flow F_3, however, exhibited a higher flow oscillation than normal. This is reflected in the practical system and model in Fig. 3.20b and is caused by a change in external temperature T_3.



(a) Temperature T_1

(b) Hot flow F_3

(c) Temperature T_2

(d) Hot flow F_4

Figure 3.20: Modelled and practical process response of a 2% sensor drift in PU2 at sample 900

It is concluded that the drift fault applied to PU2 was significant enough to disrupt the hot water regulation equipment external to the process. The author strongly advises that said regulation equipment be upgraded as part of a future study, to provide uninterrupted external control when conducting experiments. Regardless, the model sufficiently matches the practical behaviour of a sensor drift fault in PU1 and PU2.

3.5.5 Fault 5: Fouling

Description

The last fault tested on the system is coil fouling and is categorised as a gross parameter change [6, 16]. To emulate fouling in the practical plant, 4 mm thick silicon hose segments were clamped onto the coils of the applicable PU (one PU at a time). The segments were equally spaced over the coil to cover 20% of the total coil area, hereby representing 20% fouling. Additionally, due to the method of fault emulation, fouling is not introduced as a step function, but rather as a persistent fault from start-up, leading to different steady-state conditions.

Modelling

To model this fault, the formula upon which the heat transfer component in (3.11) and (3.12) is based, must be considered [55]:

$$UA = aHeat \times F_{hot}^{b}, \tag{3.21}$$

where UA is the product of the overall heat transfer coefficient and the total coil area as defined by Marlin [55]. When A is reduced by 20%, (3.21) translates to:

$$UA_{foul} = 0.8 \times aHeat \times F_{hot}^{b} \tag{3.22}$$

Therefore, a 0.8 gain multiplier was applied to the applicable $aHeat$ when simulating fouling. It follows from (3.22) that an increased hot flow is required to compensate for the lost coil area.

Verification & Validation

For this fault, the verification and validation will be done simultaneously using Tables 3.18 and 3.19. The full set of process plots is available in Appendix A.

The effects of fouling in PU1 and PU2 are clear when considering the increased hot flow average in both cases. In Table 3.18, an increase of 23.2% and 18.5% is observed in F_3 in the model and practical system, respectively. In Table 3.19, the same behaviour is observed for PU2 fouling, in that F_4 increased by 5%.

In both tables, it is observed that the hot flow of the fouled PU increased substantially with reference to its normal hot flow. However, in Table 3.18 a higher F_4 is also present in the model and practical system during fouling in PU1. This behaviour is explained by the deviation in the cold water feed temperature $T_{2,in}$ from 25.6 °C to 25.1 °C, which led to an increased F_4 to make up the 0.5 °C difference. By comparing the flow change percentages of the model to that of the practical system, it is clear that the model approximation for fouling is valid.

Table 3.18: Process change for fouling in PU1

		Model			Practical		
PV	Unit	Normal	Fault	Change	Normal	Fault	Change
T_1	[°C]	28	28	0%	28	28	0%
T_2	[°C]	29	29	0%	29	29	0%
F_3	[m^3/s]	2.37×10^{-4}	2.92×10^{-4}	23.2%	2.27×10^{-4}	2.69×10^{-4}	18.5%
F_4	[m^3/s]	2.37×10^{-4}	2.68×10^{-4}	13%	2.27×10^{-4}	2.53×10^{-4}	11.5%

Table 3.19: Process change for fouling in PU2

		Model			Practical		
PV	Unit	Normal	Fault	Change	Normal	Fault	Change
T_1	[°C]	28	28	0%	28	28	0%
T_2	[°C]	29	29	0%	29	29	0%
F_3	[m^3/s]	2.37×10^{-4}	2.39×10^{-4}	0.8%	2.27×10^{-4}	2.24×10^{-4}	1.3%
F_4	[m^3/s]	2.37×10^{-4}	2.5×10^{-4}	5.5%	2.27×10^{-4}	2.4×10^{-4}	5.7%

3.6 Conclusion

This chapter explained the theoretical foundation of the heated two-tank model and elaborated on the model updates made to match the practical system behaviour in normal and faulty process conditions. From the results shown in Section 3.4.6 and Appendix A, it can be seen that the model closely resembles the practical behaviour for all the tested process conditions. It is therefore concluded that the model is a sufficiently valid reference for the practical process within the scope of this study and may be used in subsequent chapters to verify FDI results.

However, the performance of the practical system is suboptimal. Among various shortcomings, two key components need to be addressed in the practical system, namely valve

sizing and external control utility. As described in Section 3.4.6, the valves of the process are oversized, resulting in over-sensitive controlled variables. From Sections 3.5.4 and 3.5.5, it is clear that a small deviation in the external control utilities (hot water regulation and cold water reservoir system) leads to significant and unintended shifts in operating conditions. In turn, this will directly affect the configuration and the performance of the FDI methods in subsequent chapters.

Nonetheless, the author believes these results are still sufficient for use in FDI testing, especially since not all industrial processes are optimally configured. The unexpected process influence of the suboptimal external control devices is likely to re-appear in multiple test runs and for this reason, must be treated as part of the fault signature in which it appears. It is still recommended that these issues be addressed as part of a future study, not only to produce more consistent process results but also to increase the longevity of the practical system.

CHAPTER

4

ENERGY GRAPH-BASED VISUALISATION

This chapter describes the method of applying energy graph-based visualisation on the heated two-tank system for fault detection and isolation. The method is applied to the Simulink® model for verification and to the practical fault tests for validation.

4.1 Introduction

In Chapter 3, the mathematical model of the heated two-tank process was verified and validated for normal and faulty behaviour. In this chapter the first fault detection and isolation (FDI) technique, namely energy graph-based visualisation (EGBV), will be explained, verified and validated. Chapter 3 also introduced an energy balance equation as part of the modelling of the heated two-tank process, which is fundamental in the application of the EGBV approach.

To detect and uniquely identify a fault through EGBV, a sequence of phases or spaces is identified by Venkatasubramanian et al. [5] and is shown in Figure 4.1. The *measurement space* is the first phase in the fault signature development sequence and requires the development of the process mass balance equations, as developed in Chapter 3.

Following the calculation of the mass balance, equations are the calculation of energy

balance equations that account for the total energy transfer within the process. This was also completed in Chapter 3. Additionally, exergy flows are determined in this phase, together with a graph representation of the process. This is called the *feature space* [5].

The *decision space* follows the feature space by using the energy and exergy values to develop a node signature matrix and subsequently a cost matrix. Finally, the *class space* uses singular value decomposition (SVD) and graph matching to develop a unique fault signature.

Chapter 4 is structured according to the phases shown in Fig. 4.1. In each section, the purpose and methodology of each of the phases will become clear as they are discussed and applied.

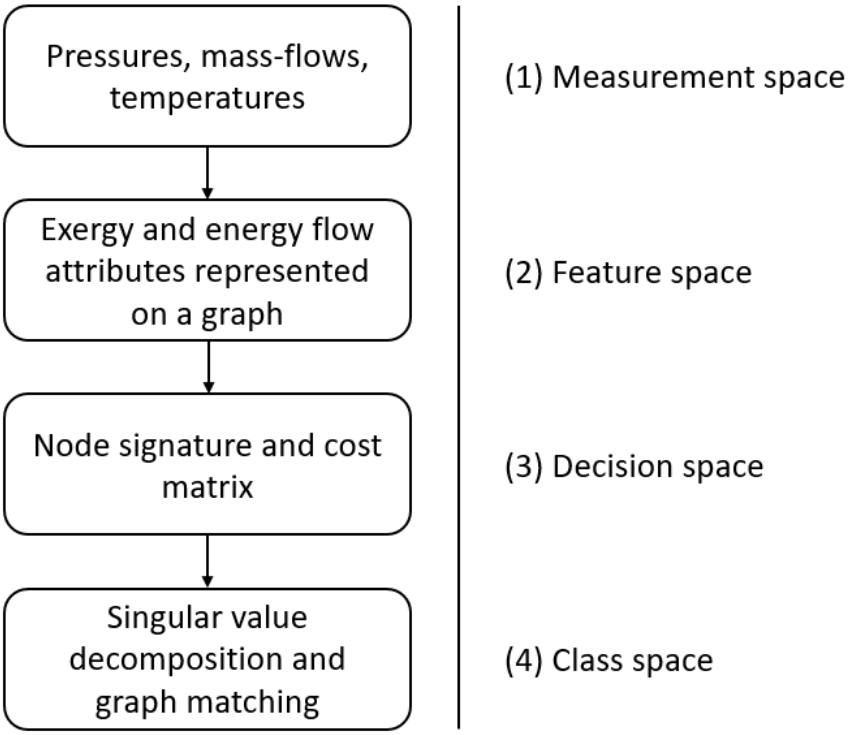


Figure 4.1: Stages of fault signature development [5]

4.2 Feature space

4.2.1 The concept of exergy

Before a graph is developed for the heated two-tank process, the concept of exergy needs to be clarified. Exergy represents the actual amount of work that can be executed by a system

after an energy transfer, i.e. the useful portion of a given energy transfer [45, 69]. This falls within the energy quality postulate [45, 57, 58], which asserts that energy transfers comprise a *quality* component, as well as a *quantity* component. Çengel and Boles [45] explain that both need to be considered to predict the true performance and limitations of a process. Exergy, unlike energy, can be destroyed due to process irreversibilities [45]. The destruction of exergy can therefore simply be described as the loss of energy quality [69].

As with energy, exergy is transferred in a process by mass, heat and work [45]. The heated two-tank process only contains exergy transfer by mass and heat. Exergy transfer by mass occurs within the heated two-tank process in the form of fluid streams entering and exiting various process components. The exergy transfer rate $\dot{B}$ for a fluid stream is defined as [9, 45]:

$$\dot{B}_{stream} = \dot{m}(h - h_0) - \dot{m}T_0(s - s_0), \tag{4.1}$$

with $\dot{m}$ denoting the mass flow rate of the fluid stream considered and T_0 the reference environment temperature. Specific enthalpy and specific entropy of the fluid are denoted by h and s respectively. Since (4.1) describes exergy before a process change occurs, the terms $h - h_0$ and $s - s_0$ are regarded as absolute, meaning a reference temperature of 0 °C is chosen for these terms.

Recall that the rate of enthalpy transfer $\dot{H}$ of a stream was defined by (3.8) in Chapter 3. Due to specific enthalpy being defined as the total enthalpy per unit mass [45], the specific enthalpy term in (4.1) can be related to total enthalpy transfer rate as follows:

$$\dot{H} = \dot{m}(h - h_0). \tag{4.2}$$

Similarly, total entropy transfer rate $\dot{S}$ is related to specific entropy by the equation

$$\dot{S} = \dot{m}(s - s_0). \tag{4.3}$$

Substituting (4.2) and (4.3) into (4.1) yields

$$\dot{B}_{stream} = \dot{H} - T_0\dot{S}. \tag{4.4}$$

The entropy component in (4.4) is significant in that it represents the degree of irreversibility of a process, that is, the amount of energy lost due to disorder throughout a process [57]. In an irreversible process, such as fluid streams, entropy S will always increase and

will have a positive value. As entropy increases, the *quality* of the energy transferred by the process decreases. This principle is accounted for by (4.4) since $\dot{B}$ is understood to mean energy quality [45, 70].

The rate of exergy transfer of heat energy $\dot{Q}$ at process temperature T is given by [45, 70]:

$$\dot{B}_{heat} = \left(1 - \frac{T_0}{T}\right) \times \dot{Q}. \tag{4.5}$$

When considering a control volume (CV), the change in exergy transfer rate across the CV is generally defined as [9, 10, 45]:

$$\Delta\dot{B}_{CV} = \dot{B}_{in} - \dot{B}_{out}, \tag{4.6}$$

and more specifically defined in the case of a tank in the heated two-tank system as:

$$\Delta\dot{B}_{tank} = \dot{B}_{streams,in} - \dot{B}_{streams,out} + \dot{B}_{heat}. \tag{4.7}$$

For the heating coils in the heated two-tank process, (4.6) is specified as:

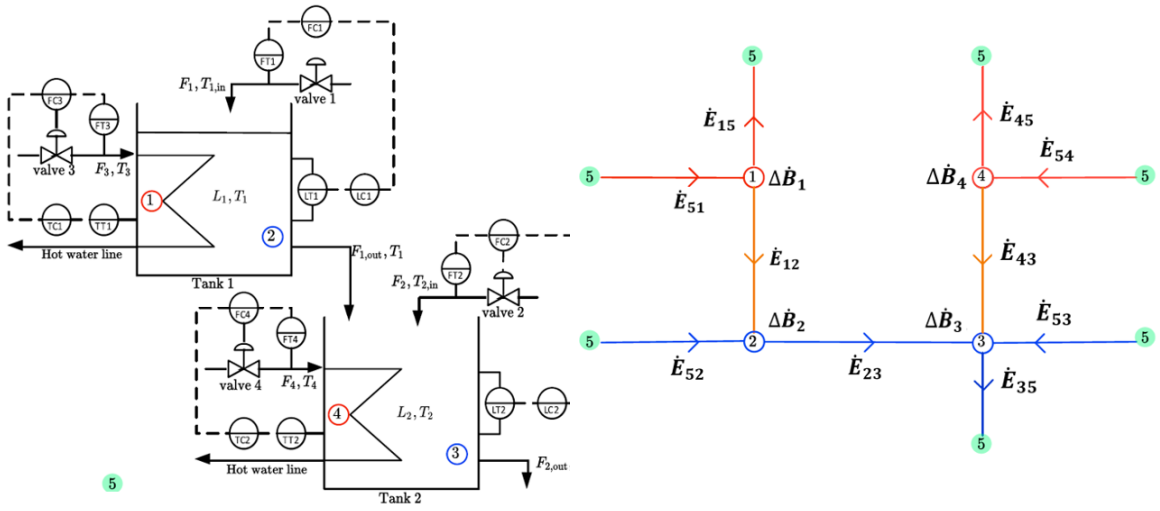
$$\Delta\dot{B}_{coil} = \dot{B}_{stream,in} - \dot{B}_{stream,out} - \dot{B}_{heat}. \tag{4.8}$$

The formulation in (4.7) and (4.8) can now be used in the process of graph construction, as described next.

4.2.2 Graph representation

Wilson [71] argues that graph theory has developed into an important mathematical tool to be used in a variety of sciences. This is supported by Balakrishnan and Ranganathan [72]. He describes a *graph* as a set of dots interconnected by lines, indicating a relationship between the dots. *Directed Graphs* or *digraphs* are graphs indicating the direction of the interconnecting lines [71].

Formally, the dots are defined as nodes (or vertices) and the lines as links (or edges). A graph G is therefore defined in algebraic terms as having a finite set of nodes $\mathcal{N}(G)$ that are non-empty and a link family $\mathcal{L}(G)$ containing multiple, unordered pairs [71, 72]. In this study, a graph approach is used as a tool to logically link the main process components in the heated two-tank system to apply EGBV FDI.



(a) Process diagram of the heated two-tank system

(b) Graph representation of heated two-tank system [9, 10]

Figure 4.2: Derivation of graph G from the heated two-tank process diagram

Figure 4.2 shows the graph representation of the two-tank system, as developed by Uren et al. [9]. In Fig. 4.2a, the original heated two-tank process diagram as described in Chapter 3 is shown, with the addition of node numbers. The exact node description is summarised in Table 4.1. Apart from node five, the nodes are chosen to represent major process components or control volumes, which adequately represent the majority of energy transfers. Node number five represents a fictitious node to which all energy exchange across the system boundary connect. In this case, the cold and hot water supply lines connect to node five.

Table 4.1: Node descriptions

Node number	Node description
1	Heating coil of PU1
2	Tank of PU1
3	Tank of PU2
4	Heating coil of PU2
5	External to system components

In Fig. 4.2b, the nodes are connected by directional arrows or links. Links are assigned to each source of energy transfer. The blue links at the bottom of the graph show the cold streams through the tanks and represent the energy transfer rate by mass flow. Similarly, the red lines at the top of the graph show the hot streams entering and exiting the coils, indicating the mass flow energy transfer rate entering and exiting the coils. Finally, the

orange lines show the heat energy transfer rate from the coils to the tanks.

The links are labelled in the form $\dot{E}_{ij}$, with i denoting the source node and j denoting the destination node. The nodes are labelled with $\Delta\dot{B}_n$, where n indicates the node number. The full list of node and link descriptions is provided in Table 4.2.

Table 4.2: Description of the heated two-tank graph elements

Parameter	Description	Unit
$\Delta\dot{B}_1$	Rate of exergy change in heating coil 1	[kW]
$\Delta\dot{B}_2$	Rate of exergy change in tank 1	[kW]
$\Delta\dot{B}_3$	Rate of exergy change in tank 2	[kW]
$\Delta\dot{B}_4$	Rate of exergy change in heating coil 2	[kW]
$\dot{E}_{12}$	Rate heat energy transfer from coil 1 to tank 1	[kW]
$\dot{E}_{43}$	Rate heat energy transfer from coil 2 to tank 2	[kW]
$\dot{E}_{23}$	Rate of flow energy transfer from tank 1 to tank 2	[kW]
$\dot{E}_{51}$	Rate of flow energy transfer from geyser to coil 1	[kW]
$\dot{E}_{15}$	Rate of flow energy transfer from coil 1 to geyser	[kW]
$\dot{E}_{54}$	Rate of flow energy transfer from geyser to coil 2	[kW]
$\dot{E}_{45}$	Rate of flow energy transfer from coil 2 to geyser	[kW]
$\dot{E}_{52}$	Rate of flow energy transfer from reservoir to tank 1	[kW]
$\dot{E}_{53}$	Rate of flow energy transfer from reservoir to tank 2	[kW]
$\dot{E}_{35}$	Rate of flow energy transfer from tank 2 to reservoir	[kW]

The development of the energy flow graph G concludes the *feature space* phase of the EGBV method.

4.3 Decision space

4.3.1 Node signature matrix development

From the definitions provided by Wilson [71] and Uren et al. [9], a node signature matrix $\mathbf{N}_s$ can be compiled in the following form:

$$\mathbf{N}_s = [\,\mathcal{N}(G)\,|\,\mathcal{L}(G)\,]\,, \quad \mathbf{N}_s \in \mathbb{R}^{n\times(n+1)}, \tag{4.9}$$

where $\mathcal{N}(G) \in \mathbb{R}^n$ is the set containing n nodes and $\mathcal{L}(G) \in \mathbb{R}^{n\times n}$ is the links set. From the graph G in Figure 4.2b it follows that $\Delta\dot{B}_k \in \mathcal{N}(G)$ and $\dot{E}_{ij} \in \mathcal{L}(G)$, allowing the expansion of $\mathbf{N}_s$:

$$\mathbf{N}_s = \left[\begin{array}{c|ccccc} \Delta\dot{B}_1 & \dot{E}_{11} & \dot{E}_{12} & \dot{E}_{13} & \dot{E}_{14} & \dot{E}_{15} \\ \Delta\dot{B}_2 & \dot{E}_{21} & \dot{E}_{22} & \dot{E}_{23} & \dot{E}_{24} & \dot{E}_{25} \\ \Delta\dot{B}_3 & \dot{E}_{31} & \dot{E}_{32} & \dot{E}_{33} & \dot{E}_{34} & \dot{E}_{35} \\ \Delta\dot{B}_4 & \dot{E}_{41} & \dot{E}_{42} & \dot{E}_{43} & \dot{E}_{44} & \dot{E}_{45} \\ \Delta\dot{B}_5 & \dot{E}_{51} & \dot{E}_{52} & \dot{E}_{53} & \dot{E}_{54} & \dot{E}_{55} \end{array}\right]. \tag{4.10}$$

Equation (4.10) can be simplified further by applying the following rules:

1. Where no energy exchange takes place between nodes, the link attribute is simply zero.
2. Since no energy transfers occur from a node to itself, the diagonal entries in $\mathbf{N}_s$ are also equated to zero.
3. The reverse of a link is signed as negative. For example, if an energy transfer exists between node 2 and 3, then $\dot{E}_{23} = -\dot{E}_{32}$.

It should be noted that item 3 may not always be applied. For example, when referring to Fig.4.2b, it is shown that $\dot{E}_{15}$ and $\dot{E}_{51}$ are in fact two separate links. They are indicated as separate links since the temperature of link $\dot{E}_{51}$ will be higher than $\dot{E}_{15}$ as a result of heat transfer. For this reason, it is concluded that $\dot{E}_{15} \neq -\dot{E}_{51}$ and must be computed separately. Item 3 may therefore only be applied if a second link with a reverse notation does not exist on the graph.

With this in mind, $\mathbf{N}_s$ reduces to [9, 73]:

$$\mathbf{N}_s = \left[\begin{array}{c|ccccc} \Delta\dot{B}_1 & 0 & \dot{E}_{12} & 0 & 0 & \dot{E}_{15} \\ \Delta\dot{B}_2 & -\dot{E}_{12} & 0 & \dot{E}_{23} & 0 & -\dot{E}_{52} \\ \Delta\dot{B}_3 & 0 & -\dot{E}_{23} & 0 & -\dot{E}_{43} & \dot{E}_{35} \\ \Delta\dot{B}_4 & 0 & 0 & \dot{E}_{43} & 0 & \dot{E}_{45} \\ 0 & \dot{E}_{51} & \dot{E}_{52} & \dot{E}_{53} & \dot{E}_{54} & 0 \end{array}\right]. \tag{4.11}$$

The fault-free, quantified $\mathbf{N}_s$ of the model is calculated in MATLAB® using (4.6) for $\Delta\dot{B}_k$, as well as (3.8) and (3.9) for $\dot{E}_{ij}$. The mean of each PV for the normal operating conditions (NOC) dataset is used to produce:

$$\mathbf{N}_{s,ref} = \left[\begin{array}{c|ccccc} 0.355 & 0 & 4.192 & 0 & 0 & 27.321 \\ -0.298 & -4.192 & 0 & 41.580 & 0 & -37.396 \\ -0.304 & 0 & -41.580 & 0 & -3.885 & 63.733 \\ 0.343 & 0 & 0 & 3.885 & 0 & 26.749 \\ 0 & 31.513 & 37.396 & 18.283 & 30.635 & 0 \end{array}\right] \tag{4.12}$$

and is regarded as the reference node signature matrix. The values for the energy transfer rates between nodes may be verified by applying the first law of thermodynamics in rate form. This means that the energy transfers to and from a node should accumulate to zero, as energy may only be converted [45, 57, 58].

For node 1:

$$\begin{aligned}\Delta\dot{E}_{coil1} &= \dot{E}_{51} - \dot{E}_{15} - \dot{E}_{12} \\ &= 31.513 - 27.321 - 4.192 \\ &= 0\end{aligned}$$

For node 2:

$$\begin{aligned}\Delta\dot{E}_{tank1} &= \dot{E}_{52} - \dot{E}_{23} + \dot{E}_{12} \\ &= 37.396 - 41.58 + 4.192 \\ &\approx 0\end{aligned}$$

For node 3:

$$\begin{aligned}\Delta\dot{E}_{tank2} &= \dot{E}_{53} + \dot{E}_{23} + \dot{E}_{43} - \dot{E}_{35} \\ &= 18.283 + 41.58 + 3.885 - 63.733 \\ &\approx 0\end{aligned}$$

For node 4:

$$\begin{aligned}\Delta\dot{E}_{coil2} &= \dot{E}_{54} - \dot{E}_{45} - \dot{E}_{43} \\ &= 30.635 - 26.749 - 3.885 \\ &\approx 0\end{aligned}$$

The change in energy transfer rate for all process nodes accumulates to approximately zero, verifying the MATLAB® calculations for energy transfers. The non-exact result may be attributed to the heat transfer approximation given by (3.21) in Chapter 3.

4.3.2 Cost matrix calculation

The same procedure followed in Section 4.3.1 to determine $\mathbf{N}_{s,ref}$ is utilised to calculate the node signature matrix of each sample or sample k in monitored live process data ($\mathbf{N}_k$), which may represent normal or faulty operating conditions. If the monitored process data are revealed to be faulty, then it is expected that a notable and characteristic difference between $\mathbf{N}_{s,ref}$ and the $\mathbf{N}_k$ will be observed. To illustrate this observation, $\mathbf{N}_k$ is calculated using the model process data of the stuck valve fault in PU1, for $k = 600$:

$$\mathbf{N}_{600} = \left[\begin{array}{c|ccccc} 0.287 & 0 & 3.4496 & 0 & 0 & 17.794 \\ -0.238 & -3.449 & 0 & 31.213 & 0 & -27.769 \\ -0.253 & 0 & -31.213 & 0 & -3.1292 & 52.436 \\ 0.277 & 0 & 0 & 3.129 & 0 & 21.613 \\ 0 & 21.243 & 27.769 & 18.050 & 24.7429 & 0 \end{array}\right]. \tag{4.13}$$

Equation (4.13) shows how the node signature matrix results change in the presence of a stuck valve. The values indicated in red are the entries that deviated the most when compared to $\mathbf{N}_{s,ref}$. The highlighted values also correspond to the energy components in PU1, where this fault occurred. Therefore, for a given fault, higher deviations in the matrix entries of $\mathbf{N}_k$ will be observed for the energy and exergy components influenced by said fault. A formal matrix comparison procedure is required to detect these fault-induced shifts for different fault types.

Several methods of matrix comparison exist in literature [74–78]. The Mahalanobis distance is one such comparison method and focuses on the covariance structure between matrices [79]. Most notably, generalized orthogonal procrustes analysis (GOPA) is a matrix comparison method that is useful to compare different matrices to a reference matrix [80] and has been applied in [81] for the purpose of monitoring multiple production processes. However, since the applicable matrices are graphs it is only natural to consider graph matching a means of meaningful comparison of graphs. In the article by Jouili and Tabbone [82] the process of graph matching determines a cost matrix as a basis for comparing two graphs. Three of these methods are discussed by Wilson and Martinez [83] including the Euclidean distance function, the Heterogeneous Euclidean Overlap Metric (HEOM) and the value difference metric (VDM). The Euclidean distance function is well known and has been most frequently used, but is susceptible to input data with large ranges which renders the input of smaller ranged data moot. The VDM method is used for nominal or symbolic data types but may be adapted using discretization to be used on linear continuous data types. However, discretization can have a negative impact on the method's accuracy [83].

The Heterogeneous Euclidean Overlap Metric (HEOM) outperforms the Euclidean dis-

tance function in terms of accuracy and compensates for high-range datasets with a built-in normalization function. It is suited for both nominal and continuous linear data types [83]. Not only has this method been used by Uren et al. [9], but it has been successfully applied on node signature matrices by Jouili & Tabbone [82] for image processing and more recently by De Bruin [73] on a trans-critical CO_2 heat pump cycle process.

The HEOM procedure can therefore be applied to calculate the cost matrix $\mathbf{C}_k \in \mathbb{R}^{n\times n}$, which contains the distances between the nodes of $\mathbf{N}_{s,ref}$ and $\mathbf{N}_k$. Let $n_{ia,ref}$ be the $(i,a)^{th}$ entry of $\mathbf{N}_{s,ref}$ and $n_{ja,k}$ the $(j,a)^{th}$ entry of $\mathbf{N}_k$. Then each entry $c_{ij,k}$ of $\mathbf{C}_k$ is calculated by [82]:

$$c_{ij,k} = \sqrt{\sum_{a=1}^{n+1} \delta\left(n_{ia,ref}, n_{ja,k}\right)^2}, \tag{4.14}$$

thus denoting the distance between node i of $\mathbf{N}_{s,ref}$ and node j of $\mathbf{N}_k$. The delta function in (4.14) is defined as [10, 73]:

$$\delta\left(n_{ia,ref}, n_{ja,k}\right) = \begin{cases} \frac{|n_{ia,ref} - n_{ja,k}|}{\{range\}_a}, & \text{if } \{range\}_a \neq 0 \\ |n_{ia,ref} - n_{ja,k}| & \text{if } \{range\}_a = 0, \end{cases} \tag{4.15}$$

with

$$\{range\}_a = |max_a - min_a|. \tag{4.16}$$

The term max_a is the largest element in column a of $\mathbf{N}_{s,ref}$ and min_a the smallest. Equation (4.15) shows the normalization of matrix values, one of the features that allow HEOM to perform better than the Euclidean distance metric as mentioned previously.

The cost matrix $\mathbf{C}_k$ then reveals the HEOM-determined distances between reference and monitored node matrices. However, a reference cost matrix is still required to evaluate the HEOM distances of monitored behaviour in each $\mathbf{C}_k$. A suitable reference would be the HEOM distances of NOC, which is calculated by matching $\mathbf{N}_{s,ref}$ with itself to produce $\mathbf{C}_{ref} \in \mathbb{R}^{n\times n}$ [21].

For the heated two-tank process NOC, $\mathbf{C}_{ref}$ is calculated based on the results given in (4.12):

$$\mathbf{C}_{ref} = \begin{bmatrix} 0 & 1.552 & 1.215 & 0.109 & 1.516 \\ 1.552 & 0 & 1.517 & 1.478 & 1.633 \\ 1.215 & 1.517 & 0 & 1.181 & 1.892 \\ 0.109 & 1.478 & 1.181 & 0 & 1.500 \\ 1.516 & 1.633 & 1.892 & 1.500 & 0 \end{bmatrix} \tag{4.17}$$

Two key observations are made from $\mathbf{C}_{ref}$ in (4.17). The first is that all diagonal elements in $\mathbf{C}_{ref}$ are zero. This is correct since the distance between two of the same elements within the same matrix is zero. The second observation is that $c_{ij,ref} = c_{ji,ref}$, which is also correct since the distance between any two nodes of the same graph is equal regardless of the direction in which it is measured.

From these observations, it is concluded that equations (4.14) to (4.16) have been verified to be correctly implemented within the MATLAB® environment and may be used for FDI in the following sections.

4.4 Class space

With $\mathbf{C}_{ref}$ and $\mathbf{C}_k$ formulated in the previous section, a procedure is now discussed that will exploit these cost matrices for fault detection and subsequently, fault isolation.

4.4.1 Singular value decomposition

The procedure starts by performing singular value decomposition (SVD) on the cost matrices $\mathbf{C}_{ref}$ and $\mathbf{C}_k$. Singular value decomposition is fundamental in the application of PCA and will therefore be discussed in more detail in Chapter 5. In summary, it can be used to uniquely describe process variation by re-representing $\mathbf{C}_{ref}$ and $\mathbf{C}_k$ in terms of singular values and singular vectors [6]. When faults occur, they can be detected by the change in singular values and vectors of $\mathbf{C}_k$. Singular value decomposition provides superior FDI results when compared to directly monitoring the changes in $\mathbf{C}_k$.

Applying SVD to an $n \times n$ matrix will produce n singular values, each with a matching singular vector of size n [84]. Let $\boldsymbol{\sigma} \in \mathbb{R}^n$ be a vector containing the singular values of $\mathbf{C}$ and let $\mathbf{Z} \in \mathbb{R}^{n \times n}$ be a matrix that contains all corresponding singular vectors, then the SVD result for $\mathbf{C}_{ref}$ in (4.17) is given by:

$$\boldsymbol{\sigma}_{ref} = \begin{bmatrix} 5.5540 & 2.2738 & 1.8233 & 1.3484 & 0.1085 \end{bmatrix} \tag{4.18}$$

and

$$\mathbf{Z}_{ref} = \begin{bmatrix} -0.384 & 0.516 & 0.230 & -0.216 & -0.696 \\ -0.484 & -0.425 & -0.468 & -0.604 & -0.015 \\ -0.469 & 0.179 & -0.544 & 0.671 & 0.002 \\ -0.373 & 0.501 & 0.205 & -0.230 & 0.717 \\ -0.508 & -0.519 & 0.623 & 0.289 & 0.012 \end{bmatrix}. \tag{4.19}$$

The singular values in $\boldsymbol{\sigma}_{ref}$ and vectors in $\mathbf{Z}_{ref}$ therefore form a complete description of the cost matrix $\mathbf{C}_{ref}$. The same is done for each $\mathbf{C}_k$, to produce $\boldsymbol{\sigma}_k$ and $\mathbf{Z}_k$, where k represents the sample number. The SVD values and vectors are both important to evaluate the monitored process state and will henceforth collectively be referred to as SVD *elements*.

The SVD elements of $\mathbf{C}_k$ are normalised using the corresponding elements of $\mathbf{C}_{ref}$, hereby providing a true indication of the deviation from the reference conditions over k samples. The i^{th} normalised singular value of $\boldsymbol{\sigma}_k$ is given by:

$$\tilde{\sigma}_{i,k} = \frac{\sigma_{i,k}}{\sigma_{i,ref}}. \tag{4.20}$$

Likewise, the $(i,j)^{th}$ normalised entry of $\mathbf{Z}_k$ is given by:

$$\tilde{z}_{ij,k} = \frac{z_{ij,k}}{z_{ij,ref}}. \tag{4.21}$$

The normalised SVD elements are plotted and shown in Figure B.1 in Appendix B for the 900 observations in the model NOC dataset. The top row of plots shows the normalised singular values, with the left-most plot showing the first entry of $\tilde{\boldsymbol{\sigma}}_k$ and the right-most plot illustrating the last entry. The first column vector of $\tilde{\mathbf{Z}}_k$ is plotted from rows 2 to 6 on the left side of the figure. Likewise, the last column vector is plotted on the rightmost side of the figure. Figure B.1 essentially illustrates the response and trend of each SVD element when the process is in normal, continuous operation.

It is clear from Fig. B.1 that some SVD element plots exhibit noisier behaviour than others, yet every plot exhibits its own trend that is still visible upon careful inspection, regardless of its noise level. To extract these trends and suppress noise, the use of a filter is appropriate and will be discussed next. Note that since the SVD elements will be referred to in their time-series format, $\tilde{\sigma}_i$ will henceforth be used instead of $\tilde{\sigma}_{i,k}$. Likewise, $\tilde{z}_{ij}$ will be used to refer to all $\tilde{z}_{ij,k}$.

4.4.2 Exponentially weighted moving average

To find an appropriate filtering method, the field of univariate, statistical process monitoring is investigated. Originally, the Shewhart control chart approach to statistical process monitoring was a popular and ground-breaking method. It uses the process mean μ and standard deviation σ to determine whether abnormal behaviour has occurred [6, 85, 86]. It can be argued that an equivalence exists between any given SVD element plot as shown in Fig. B.1 and a Shewhart chart - both are comprised of a single variable (or *univariate*) plot over time that can be evaluated against thresholds such that deviations in the said variable are clear. Thus, the improvements introduced to the Shewhart chart may apply to the SVD element plots as well.

Two prominent Shewhart chart improvements are found in literature, namely the cumulative sum (CUSUM) chart and the exponentially weighted moving average (EWMA) chart. The CUSUM chart was introduced by Page [87] in 1954, to address the lacking sensitivity of the Shewhart chart. The EWMA was developed in the same period by Roberts [88] and is an alternative to CUSUM, providing similar sensitivity improvements [85].

Hunter [86] described the EWMA method as a compromise between the Shewhart chart and CUSUM [86] and is known to be more feasible for use in practical systems [86, 89]. To calculate the EWMA of a data sample k, the following formula is used [85, 88]:

$$y_k = rx_k + (1 - r)y_{k-1}, \tag{4.22}$$

where y_k is the k-th EWMA output calculated from the original raw data sample x_k and $0 \leq r \leq 1$ is the smoothing constant. For $k = 0$, the value of y_{k-1} is set equal to μ_0 [88]. Equation (4.22) reveals the weighted approach of EWMA, whereby the most recent observation's weight is determined by r. If r is set to 1, then (4.22) will be equal to the original data. If r is set close to 0, then (4.22) will resemble CUSUM [86].

Figure 4.3 demonstrates the effect of EWMA. The blue line in the plot shows $\tilde{\sigma}_{1,k}$ during 900 samples of modelled NOC, which is shown to have noisy behaviour. The orange line shows the EWMA-processed version of the blue plot for $r = 0.2$. It exhibits smoother behaviour while still closely following the original trend and serves to filter $\tilde{\sigma}_{1,k}$. Close inspection of the EWMA plot reveals a slight lag in response to the original trend. This is understandable since the most recent sample is weighted by r.

At this point, the author wishes to clarify that while the EWMA chart is described in literature as a Shewhart chart improvement [88] and also a standalone statistical monitoring technique [85], it is only its filtering properties that are of interest in this work and will be used for this purpose.

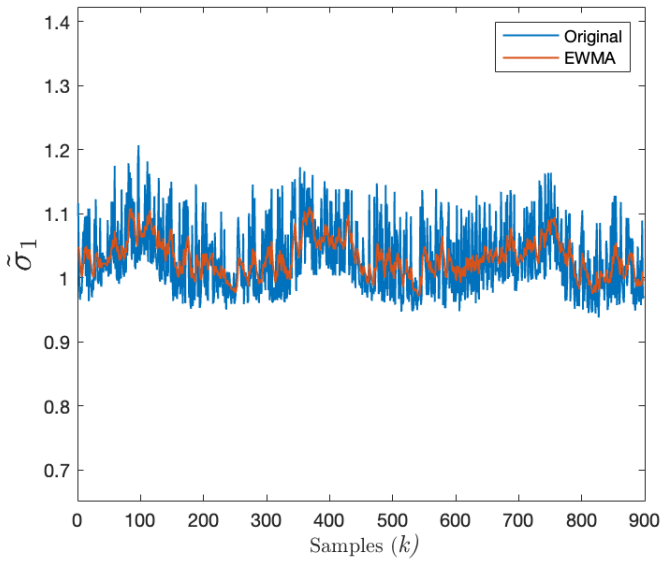


Figure 4.3: Timeseries data of $\tilde{\sigma}_1$ during NOC for EWMA-filtered and original SVD results

4.4.3 Threshold determination

When using EWMA, given that the process has been operational for a long time such that a steady-state is reached, its output may be evaluated against the upper control limit (UCL) or upper threshold (UTh) given by [88]:

$$\text{UTh} = \mu_0 + L\sigma_x\sqrt{\frac{r}{2-r}} \tag{4.23}$$

and the lower control limit (LCL) or lower threshold (LTh) given by [88]:

$$\text{LTh} = \mu_0 - L\sigma_x\sqrt{\frac{r}{2-r}}, \tag{4.24}$$

where μ_0 and σ_x represent the mean and standard deviation respectively of the NOC raw dataset. The L parameter in (4.23) and (4.24) is used to specify the width of the control limits [85]. Note that r is also included in the threshold calculations, meaning a change in r will lead to a change in the threshold.

In [85], it is explained that L and r may be chosen to achieve a specified average run length (ARL) as calculated by Crowder in [90]. The average run length is defined as the average number of observations recorded before a false alarm (ARL_0) or missed detection (ARL_1) is recorded [85, 87]. If the desired ARL_0 and ARL_1 are known, the ARL table in [90] can be used to determine L and r. However, the use of the thresholds in (4.23)

and (4.24) are based on the assumption that the samples being evaluated are *normally distributed* [86]. Inspection of the distribution of the SVD elements reveals that they are *not* normally distributed and will therefore not be evaluated against the UTh and LTh formulas in (4.23) and (4.24). Instead, a simpler approach will be followed, whereby the thresholds of each SVD element will be set empirically such that a total FAR of 5% is achieved using the NOC dataset. The 5% threshold is chosen as a replacement for the standard 2σ threshold used for Gaussian data evaluation. The UTh will be set to achieve an upper FAR of 2.5%, and the LTh to achieve a lower FAR of 2.5%. It should be noted that the generation of critical values from an empirical distribution function [85] may also be a suitable and arguably more objective approach for threshold development.

4.4.4 Fault detection & isolation

The EWMA technique described in Section 4.4.2 and the threshold philosophy given in Section 4.4.3 may now be applied to detect process faults. Each normalised SVD element in $\tilde{\sigma}_k$ and $\tilde{z}_k$ are treated as an EWMA input with its own UTh and LTh. A fault is declared if the EWMA output of *any* SVD element is higher than its UTh or lower than its LTh. With a smoothing constant of $r = 0.2$, the UTh values for the normalised SVD elements of the model are given by:

$$\tilde{\boldsymbol{\sigma}}_{UTh} = \begin{bmatrix} 1.0926 & 0.9933 & 0.9647 & 0.9341 & 0.7417 \end{bmatrix}, \tag{4.25}$$

$$\tilde{\mathbf{Z}}_{UTh} = \begin{bmatrix} 1.0441 & 1.0581 & 1.3104 & 1.0205 & 1.0034 \\ 1.0495 & 1.1589 & 1.0878 & 1.1134 & 1.3467 \\ 1.0249 & 1.2921 & 1.2351 & 1.0202 & 2.5693 \\ 1.0478 & 1.0487 & 1.3157 & 1.0160 & 1.0060 \\ 1.0471 & 1.1518 & 1.0039 & 1.4016 & 1.2435 \end{bmatrix} \tag{4.26}$$

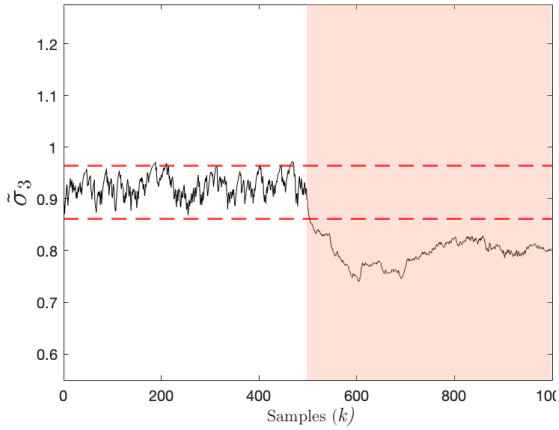
and the LTh is given by:

$$\tilde{\boldsymbol{\sigma}}_{LTh} = \begin{bmatrix} 0.9825 & 0.8936 & 0.8609 & 0.8217 & 0.3967 \end{bmatrix}, \tag{4.27}$$

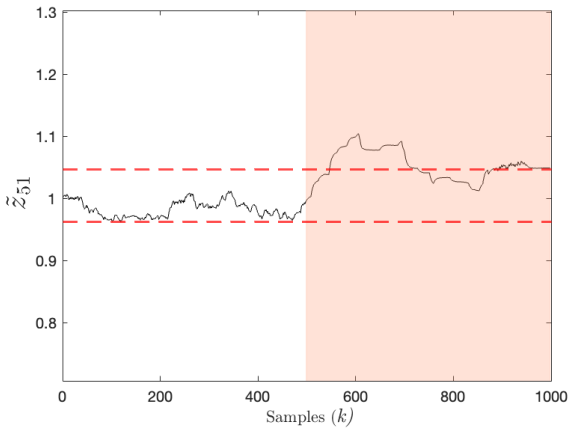
$$\tilde{\mathbf{Z}}_{LTh} = \begin{bmatrix} 0.9414 & 0.9276 & 0.8506 & 0.6970 & 0.9934 \\ 0.9676 & 0.7511 & 0.6932 & 0.9805 & 0.9643 \\ 0.9718 & 0.6666 & 0.9469 & 0.8321 & 0.4301 \\ 0.9414 & 0.9303 & 0.8525 & 0.7383 & 0.9966 \\ 0.9619 & 0.8364 & 0.8786 & 0.9030 & 0.8560 \end{bmatrix}. \tag{4.28}$$

As expected from a normalised dataset with a $\mu_0 \approx 1$, the UTh values tend to be greater than 1 and the LTh values lower than 1. An example of a detection output is given in Fig. 4.4, where four of the eighteen monitored SVD elements are illustrated. The EWMA output of the normalised singular value $\tilde{\sigma}_3$ is illustrated in Fig. 4.4a and the output for $\tilde{z}_{51}$ is shown in Fig. 4.4b. Figures 4.4c and 4.4d show the EWMA of $\tilde{z}_{32}$ and $\tilde{z}_{22}$ respectively. The red lines show the UTh and LTh applicable to each element, as given by (4.25) to (4.28). The first 500 samples of the dataset contain normal behaviour and are correctly reflected as such by all the SVD elements since they mostly remain within the thresholds for this period. Some false alarms are visible - $\tilde{z}_{32}$ shows a clear false alarm event at sample 90, for example.

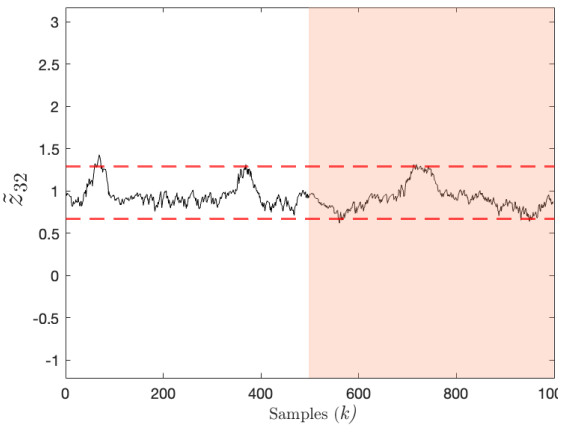
At sample 500, a stuck valve occurred in PU1 and persists, which is indicated by the red region in the plots. The fault is detected by $\tilde{\sigma}_3$, when it crosses the LTh and by $\tilde{z}_{51}$ when crosses the UTh. The plot of $\tilde{z}_{32}$ shows no detection event, while the plot of $\tilde{z}_{22}$ briefly violates the LTh before returning to a normal state.



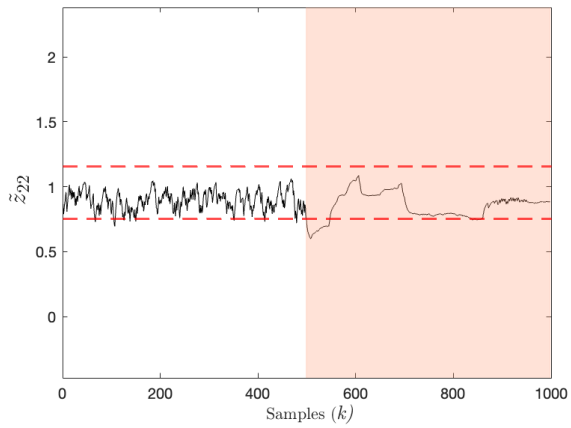
(a) Fault monitoring of $\tilde{\sigma}_3$



(b) Fault monitoring of $\tilde{z}_{51}$



(c) Fault monitoring of $\tilde{z}_{32}$



(d) Fault monitoring of $\tilde{z}_{22}$

Figure 4.4: Detection of a stuck valve in PU1 at sample 500

To isolate a fault, a qualitative fault signature is developed by evaluating the status of the SVD elements and assigning a symbol accordingly, as done in [21], [70] and [73]. The symbols are assigned as follows:

1. If the mean (during fault state) of any EWMA SVD element in $\tilde{\boldsymbol{\sigma}}$ or $\tilde{\mathbf{Z}}$ is lower than its LTh, then a '$-$' symbol is assigned.
2. If the mean of any EWMA SVD element in $\tilde{\boldsymbol{\sigma}}$ or $\tilde{\mathbf{Z}}$ is higher than its UTh, then a '$+$' symbol is assigned.
3. If the mean of any EWMA SVD element in $\tilde{\boldsymbol{\sigma}}$ or $\tilde{\mathbf{Z}}$ is higher than its LTh and lower than its UTh, then a '0' symbol is assigned.

The results from the above procedure can now be tabulated to visually represent the fault signature. Referring to the elements plotted in Fig. 4.4, a '$-$' is assigned to $\tilde{\sigma}_3$, while a '$+$' is assigned to $\tilde{z}_{51}$. SVD elements $\tilde{z}_{32}$ and $\tilde{z}_{22}$ show no clear mean shift to violate the UTh or LTh, so a '0' is assigned. The result displayed in Table 4.3 is therefore the unique signature of the stuck valve fault in PU1 and may be used to isolate this fault from other faults.

Table 4.3: Fault signature for PU1 stuck valve

$\tilde{\boldsymbol{\sigma}}$	$-$	$-$	$-$	$-$	$-$
$\tilde{\mathbf{Z}}$	$-$	0	0	$-$	$+$
	0	0	0	$+$	0
	0	0	0	0	$+$
	$-$	$+$	0	$-$	$-$
	$+$	0	0	0	$+$

It is important to note that the fault signature shown in Table 4.3 should not be thought of as process variable contributions as used in PCA. PCA's fault identification procedure develops numeric values for process variables [42], while with EGBV, the original process variables are obscured by the HEOM and SVD procedures leading to the *latent* variables that represent the original process. The symbols shown in Table 4.3 merely indicate significant directional deviations in these latent variables (or SVD elements).

Considering the numerical and graphical results provided throughout Sections 4.3 to 4.4 for each step in the energy graph-based visualisation procedure, the implementation of this FDI method in MATLAB® is deemed to be correct and verified. The method may now be applied to the practical results for validation.

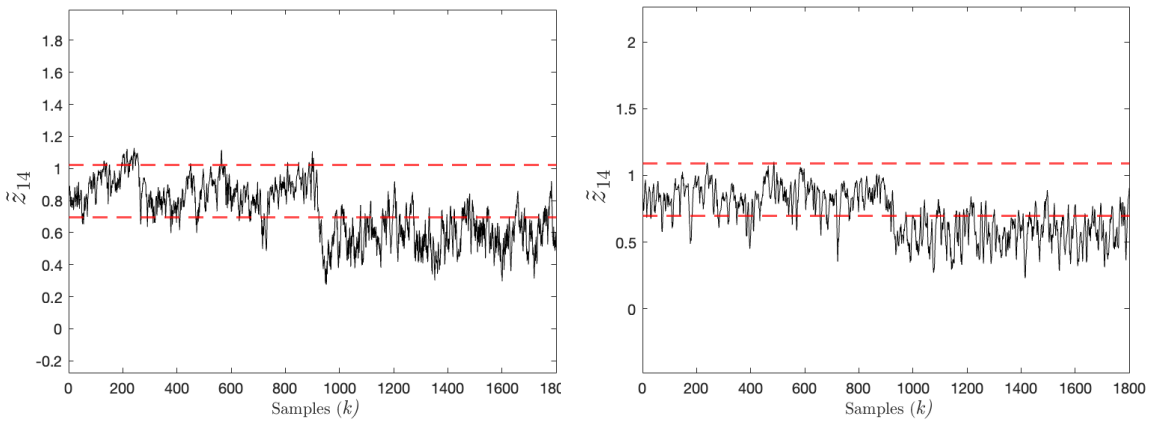
4.5 FDI results & validation

In the sections that follow, the EGBV technique will be applied for fault detection and isolation of the faults from Chapter 3, namely clogging, leakage, stuck valve, sensor drift and fouling. For each fault type and each PU, an arbitrary SVD element is selected from the highest fault magnitude and displayed in this section as proof of detection for the model and practical system. Following the detection of the fault, the model and practical fault signatures are provided for the highest fault magnitude, if multiple magnitudes were tested. The full set of detection plots and fault signatures are provided in Appendix B.

Finally, the detection and isolation results are analysed to make superficial conclusions on the detection, isolation, false alarm and detection speed performance of the EGBV FDI technique for each fault type. An in-depth analysis of these performance outcomes will be provided in Chapter 6.

4.5.1 Fault 1: Clogging

Figure 4.5 shows the EWMA plot of the normalised SVD element $\tilde{z}_{14}$ when a 30% clog in PU1 was created at sample 900. Both plots show a negative mean shift to breach the LTh after sample 900, marking the presence of the process fault. The model and practical output also exhibit false alarm behaviour at the UTh and LTh. For this SVD element, the detection delay is shown to be similar, with both plots providing a clear detection within 100 samples. When comparing the UTh and LTh of the model and practical results, it is observed that the model's thresholds are positioned similarly to the practical thresholds shown in Fig. 4.5b.

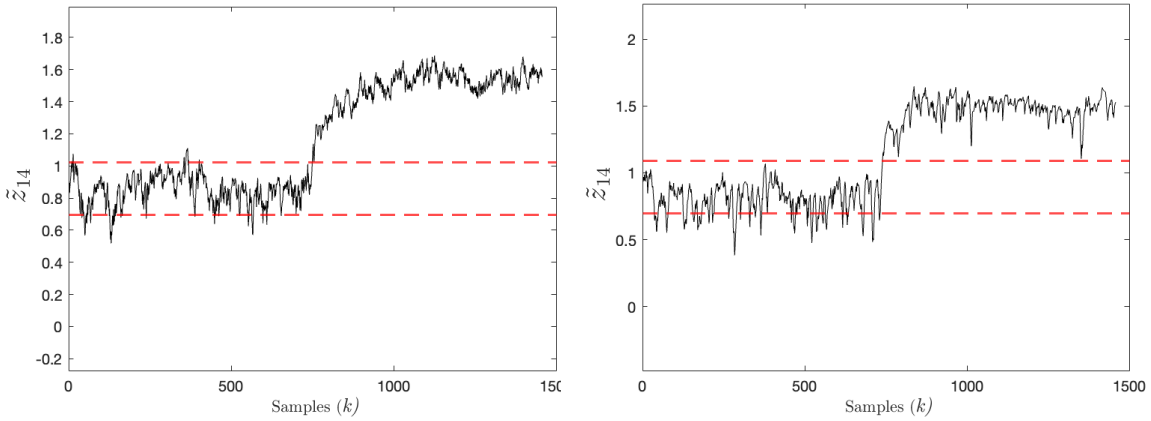


(a) Modelled result of $\tilde{z}_{14}$

(b) Practical result of $\tilde{z}_{14}$

Figure 4.5: SVD detection plots of a model and practical 30% clog in PU1 at sample 900

The detection plots of the same SVD element are shown in Fig. 4.6 when a 30% clog was applied in PU2. Both plots show a distinct positive mean shift, violating the UTh instead of the LTh as in PU1. The same false alarm trend is observed in the normal operation preceding the fault at sample 729, as was seen in PU1 for both systems. Figures 4.6a and 4.6b both show minimal detection delay.



(a) Modelled result of $\tilde{z}_{14}$

(b) Practical result of $\tilde{z}_{14}$

Figure 4.6: SVD detection plots of a model and practical 30% clog in PU2 at sample 729

Figures B.4 to B.7 show the trends of all fault sizes. Analysis of these plots reveals that the PU1 clog faults show little or no deviation. The effect of a PU2 clog is more severe as shown in Fig. B.6 and B.7. For PU1 and PU2, the difference in SVD shift between the fault magnitudes is visible. The model and the practical results show a noticeable false alarm presence for all fault magnitudes. Overall, the results of the model closely resemble that of the practical system.

These figures may now be used to construct the fault signatures. Table 4.4 and 4.5 show the fault signature for the 30% clog in PU1. It is shown that the model result and the practical result differ by two signs. The fault signatures for PU2 are tabulated in Table 4.6 and 4.7. In this case, the fault signatures are shown to differ by three signs. This is expected when considering the performance differences between the model and practical system discussed in Chapter 3. The fact that the PU2 clog has more symbol changes than the PU1 clog supports the earlier observation of the greater effect of the PU2 clog.

Appendix B shows the fault signatures for all tested clogs in the heated two-tank process (Tables B.5 to B.12). The signatures for the PU1 model and practical system show more symbol changes as the fault magnitude increases. For PU2, however, the 20% and 30% clog exhibit nearly the same signature (identical for model result and one symbol difference in the practical signature). Signature differences between the model and practical results are more prevalent in the lower fault magnitudes. Discrepancies may be attributed to the

Table 4.4: Modelled PU1 30% Clog

$\tilde{\sigma}$	0	−	−	−	−
$\tilde{\mathbf{Z}}$	0	0	0	−	+
	0	0	−	+	0
	0	0	+	−	+
	0	0	+	−	−
	+	0	−	+	+

Table 4.5: Practical PU1 30% Clog

$\tilde{\sigma}$	0	−	−	−	−
$\tilde{\mathbf{Z}}$	0	0	+	−	+
	0	0	−	+	0
	0	0	+	−	+
	0	0	+	−	−
	0	0	−	+	+

Table 4.6: Modelled PU2 30% Clog

$\tilde{\sigma}$	0	−	−	−	−
$\tilde{\mathbf{Z}}$	−	0	−	+	−
	0	+	−	−	+
	0	−	0	0	+
	−	0	−	+	+
	+	−	+	0	+

Table 4.7: Practical PU2 30% Clog

$\tilde{\sigma}$	0	−	−	−	−
$\tilde{\mathbf{Z}}$	−	0	−	+	−
	0	+	0	−	+
	0	0	0	0	+
	−	0	−	+	+
	+	−	+	−	+

following contributing factors:

- **Modelling assumptions** - As discussed in Chapter 3, slight differences exist between the process output of the modelled plant behaviour and the practical behaviour due to modelling assumptions. It is then expected that differences will exist between the modelled and practical fault signatures, regardless of fault size.
- **Threshold proximity** - This is an extension of the *modelling assumptions* explanation. Because the mean of the SVD element is used to assign a symbol in the fault signature, the model and practical signatures can have a symbol difference for said SVD element. This is because, even though the model and practical trend of the SVD element are nearly identical, their proximity to or oscillation around the threshold will lead to a mean result that is either slightly above or slightly below the threshold value, leading to a symbol difference between the systems. This effect is more prevalent in smaller fault sizes since larger fault sizes tend to have a more significant deviation across their thresholds.

Regardless, based on the fault signature results of the model and practical system, it is concluded that a clogging fault is isolable to a process unit since the signatures of clogs

in PU1 are different from those in PU2. Furthermore, all clog magnitudes are isolable in PU1 and PU2.

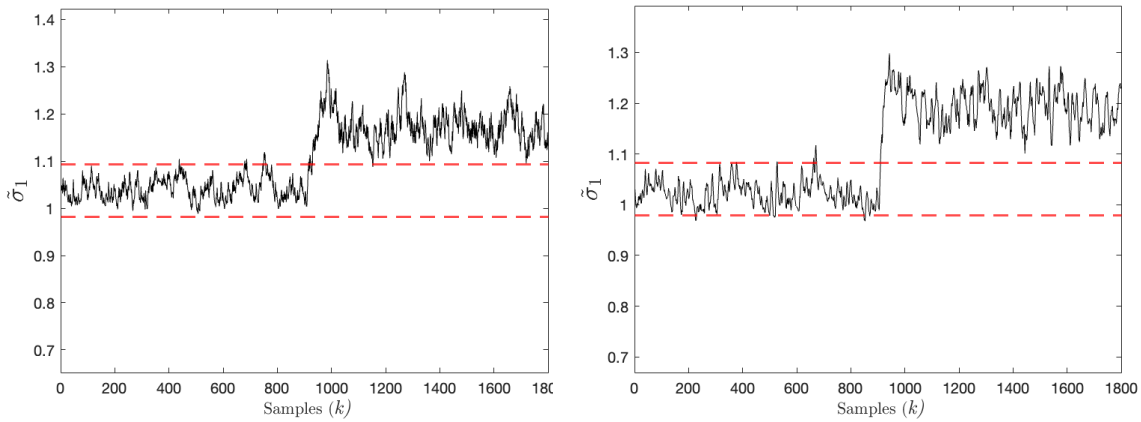
4.5.2 Fault 2: Leakage

Next, the results of the leakage fault are discussed. Figure 4.7 shows the EWMA deviation of the SVD element $\tilde{\sigma}_1$ when a 30% leak occurs in PU1 at sample 900. In Fig. 4.7a and 4.7b, it is shown that the fault is detected when both plots breach their UTh. The model and the practical result show minor false alarm events. The fault was rapidly detected by both systems.

When the same fault is applied to PU2, the energy graph-based FDI was not able to detect it. Figure 4.8 shows the model and practical output of this fault, which shows that the model and the practical system remained within the upper and lower thresholds after the fault was applied at sample 900, thus missing the detection.

Appendix B shows the plots of all SVD elements in Fig. B.8 to B.11. For PU1, it is shown that other SVD elements also show clear detections as in Fig. 4.7 and that all but the 10% fault size were detected. For PU2, it is confirmed that none of the fault magnitudes was successfully detected by the model or practical system.

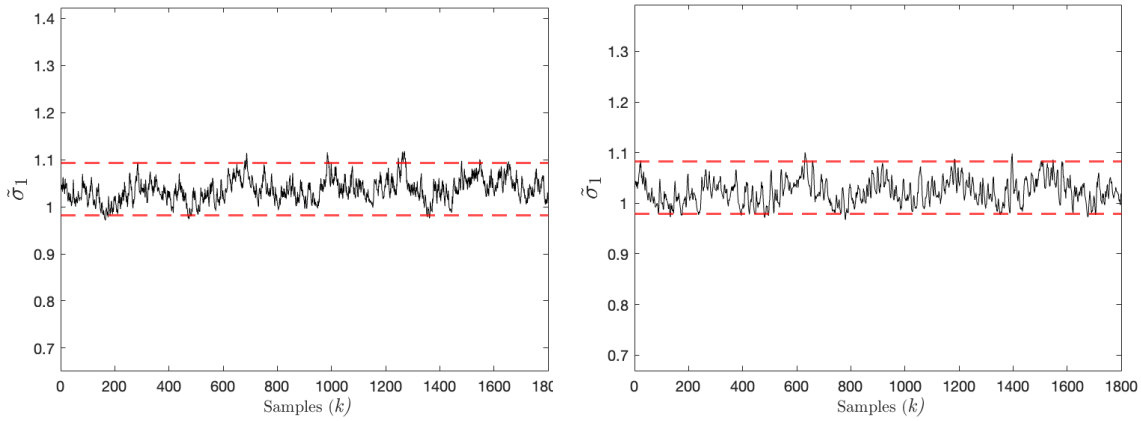
The PU1 fault signature for the 30% leak is tabulated in Table 4.8 for the model and in Table 4.9 for the practical fault. The signatures of the model and the practical plant are identical, confirming the validity of the signature. The fault signatures for the PU2 leak are provided by Tables 4.10 and 4.11 and since no fault was detected, all signature symbols are simply zero.



(a) Modelled result of $\tilde{\sigma}_1$

(b) Practical result of $\tilde{\sigma}_1$

Figure 4.7: SVD detection plots of a model and practical 30% leak in PU1 at sample 900



(a) Modelled result of $\tilde{\sigma}_1$

(b) Practical result of $\tilde{\sigma}_1$

Figure 4.8: SVD detection plots of a model and practical 30% leak in PU2 at sample 900

Table 4.8: Modelled PU1 30% Leak

$\tilde{\boldsymbol{\sigma}}$	+	+	0	0	0
$\tilde{\mathbf{Z}}$	+	0	0	0	0
	−	0	0	0	0
	0	−	0	0	0
	+	0	0	0	0
	0	0	0	0	0

Table 4.9: Practical PU1 30% Leak

$\tilde{\boldsymbol{\sigma}}$	+	+	0	0	0
$\tilde{\mathbf{Z}}$	+	0	0	0	0
	−	0	0	0	0
	0	−	0	0	0
	+	0	0	0	0
	0	0	0	0	0

Table 4.10: Modelled PU2 30% Leak

$\tilde{\boldsymbol{\sigma}}$	0	0	0	0	0
$\tilde{\mathbf{Z}}$	0	0	0	0	0
	0	0	0	0	0
	0	0	0	0	0
	0	0	0	0	0
	0	0	0	0	0

Table 4.11: Practical PU2 30% Leak

$\tilde{\boldsymbol{\sigma}}$	0	0	0	0	0
$\tilde{\mathbf{Z}}$	0	0	0	0	0
	0	0	0	0	0
	0	0	0	0	0
	0	0	0	0	0
	0	0	0	0	0

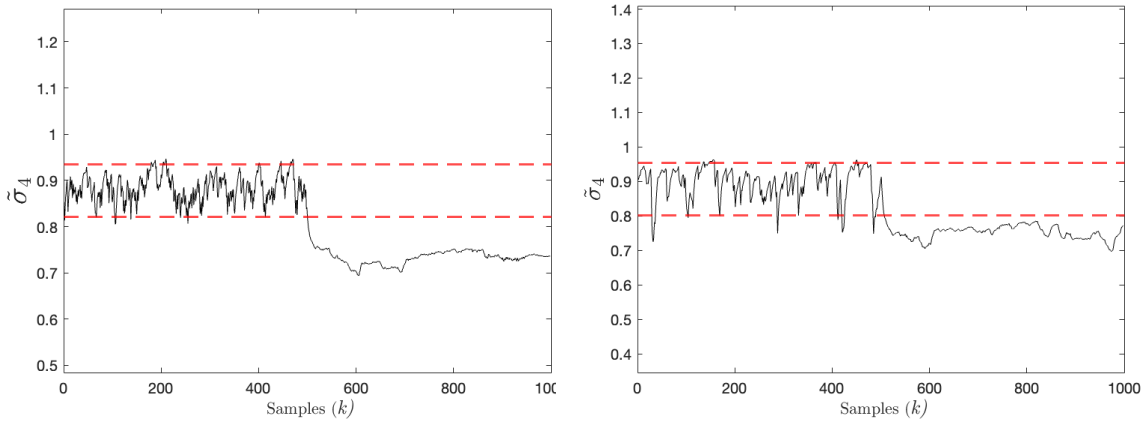
The fault signatures for the different leakage magnitudes are provided in Appendix B (Table B.13 to B.24). The model and practical system have a zero-fault signature for the 10% leak in PU1. The 20% PU1 leak signatures differ by a single symbol, which is shown

to stabilise and converge at the higher fault magnitude of 30%. As described earlier, no detections are recorded for PU2 and therefore all faults have a zero fault signature for Tables B.19 to B.24.

It is concluded that only the 20% and 30% leakage faults in PU1 are detectable. These faults are isolable from PU2 since PU2 leakage detection was not possible. The 20% and 30% leaks exhibit different signatures that may be used for magnitude isolation.

4.5.3 Fault 3: Stuck valve

The stuck valve fault in PU1 is successfully detected in the model and practical result, as shown in Fig. 4.9. Multiple false alarm events are shown in Fig. 4.9a and 4.9b, when $\tilde{\sigma}_4$ violated the UTh and LTh prior to the fault occurrence at sample 500. When the fault occurs, plots cross the LTh, marking the detection with minimal detection delay.



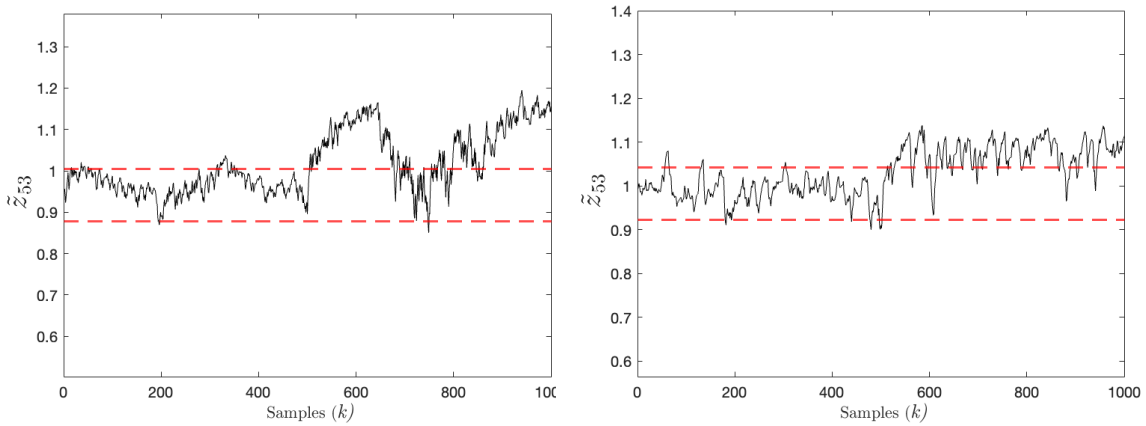
(a) Modelled result of $\tilde{\sigma}_4$

(b) Practical result of $\tilde{\sigma}_4$

Figure 4.9: SVD detection plots of a model and practical stuck valve in PU1 at sample 500

The detection of a stuck valve in PU2 is shown in Fig. 4.10a and 4.10b. The fault occurred at sample 500 and was successfully detected in the model and practical system with minimal delay. The model shows minor false alarm events, whereas the practical plot shows four prominent false alarm events.

Figures B.12 to B.15 in Appendix B show the results of all the extracted SVD elements for the model and practical system. These figures reveal that for the PU1 and PU2 stuck valves, other SVD elements also clearly detected the faults. When considering all SVD elements in these figures, it seems that the PU2 stuck valve has a slower detection response



(a) Modelled result of $\tilde{z}_{53}$

(b) Practical result of $\tilde{z}_{53}$

Figure 4.10: SVD detection plots of a model and practical stuck valve in PU2 at sample 500

than that of PU1. This is not surprising, given that the process variable (PV) disruption in PU2 is not as influential as in PU1, based on the observations from Chapter 3. None of the SVD elements in the figures shows persistent false alarms. A comparison between the model and the practical results reveals similar behaviour.

The fault signature for the PU1 stuck valve is constructed and tabulated in Table 4.12 for the model and Table 4.13 for the practical system. The tables differ by three symbols. The fault signatures for PU2 are given in Table 4.14 and 4.15. In this case, the fault signatures appear to differ significantly, with the model signature showing nine more symbol changes than the practical signature. This is mainly due to the threshold proximity effect explained in Section 4.5.1, since it is revealed that the practical model in Fig. B.15 shows the same response as the model, but its SVD elements' means are not sufficient for a symbol change, hence the limited amount of symbol changes in Table 4.15.

Comparing the fault signatures of PU1 and PU2 for the stuck valve leads to the conclusion that the stuck valve fault may be uniquely isolated with reference to its PU.

4.5.4 Fault 4: Sensor drift

Figure 4.11 shows the detection result of $\tilde{z}_{55}$ when a 5% sensor drift occurred in PU1 at sample 900. Up to sample 900, the model in Fig. 4.11a and the practical system 4.11b correctly show NOC behaviour, with a prominent false alarm event at sample 200 in the modelled system. When the fault occurred, a distinct breach of the UTh occurred. The model and the practical result show immediate detection.

Table 4.12: Modelled PU1 stuck valve

$\tilde{\boldsymbol{\sigma}}$	$-$	$-$	$-$	$-$	$-$
$\tilde{\mathbf{Z}}$	$-$	0	0	$-$	$+$
	0	0	0	$+$	0
	0	0	0	0	$+$
	$-$	$+$	0	$-$	$-$
	$+$	0	0	0	$+$

Table 4.13: Practical PU1 stuck valve

$\tilde{\boldsymbol{\sigma}}$	$-$	$-$	$-$	$-$	$-$
$\tilde{\mathbf{Z}}$	0	0	0	$-$	$+$
	0	0	0	$+$	0
	0	0	0	0	$+$
	$-$	$+$	0	0	$-$
	0	0	$-$	0	$+$

Table 4.14: Modelled PU2 stuck valve

$\tilde{\boldsymbol{\sigma}}$	0	$-$	$-$	$-$	0
$\tilde{\mathbf{Z}}$	0	0	$-$	$+$	$-$
	0	$+$	0	$-$	0
	0	0	0	0	$+$
	0	0	$-$	$+$	$+$
	$+$	$-$	$+$	0	0

Table 4.15: Practical PU2 stuck valve

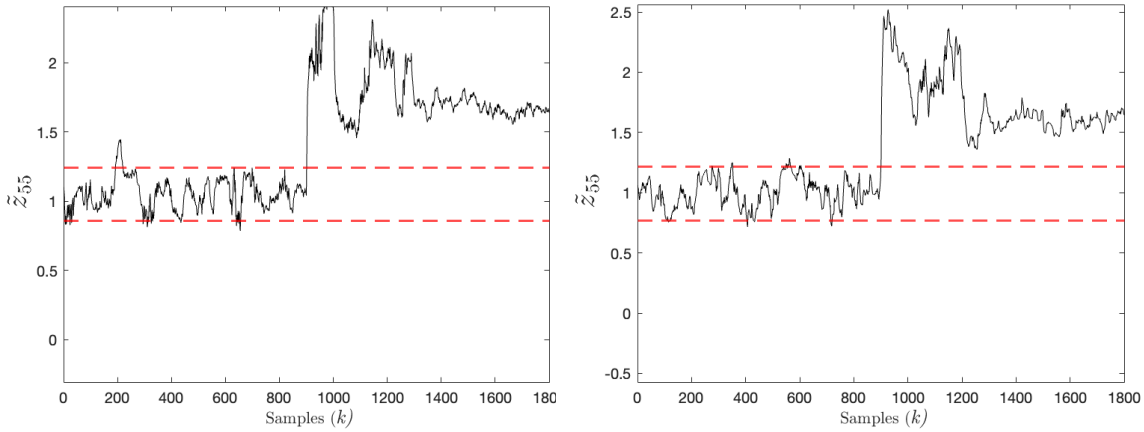
$\tilde{\boldsymbol{\sigma}}$	0	0	$-$	0	0
$\tilde{\mathbf{Z}}$	0	0	$-$	$+$	0
	0	0	0	0	0
	0	0	0	0	0
	0	0	$-$	$+$	0
	0	0	$+$	0	0

The 5% sensor drift fault of PU2 is shown in Figure 4.12 for $\tilde{z}_{31}$. Figures 4.12a and 4.12b show minor false alarms events, including the detection of the fault that occurred at sample 900.

The different magnitudes are plotted together for all SVD elements in Fig. B.16 to B.19. Unlike what is shown in Fig. 4.11b, it can be seen that some SVD elements evaluated here returned to a normal operating state while the fault is still active, specifically for PU1. This is the result of TC1 responding to the temperature upset. For both PUs, the greater process upset of the bigger sensor drift is visible. The trends of the model and practical SVD elements are similar and no persistent false alarm states are observed within this fault type.

For PU1, the fault signatures are tabulated in Tables 4.16 and 4.17 and are shown to be similar, with three symbols difference. The fault signatures for PU2 are given in Tables 4.18 and 4.19 and differ by five symbols.

In Appendix B, the fault signatures of all magnitudes are shown from Table B.29 to B.36. The results show that for both PUs, the fault magnitude of the sensor drift is isolable since both PUs show considerably more symbol changes for a higher fault magnitude.



(a) Modelled result of $\tilde{z}_{55}$

(b) Practical result of $\tilde{z}_{55}$

Figure 4.11: SVD detection plots of a model and practical 5% Sensor drift in PU1 at sample 900

Table 4.16: Modelled PU1 5% sensor drift

$\tilde{\boldsymbol{\sigma}}$	+	−	−	−	−
$\tilde{\mathbf{Z}}$	0	−	0	+	+
	−	+	−	0	0
	−	0	+	−	0
	0	0	0	+	−
	0	−	−	+	+

Table 4.17: Practical PU1 5% sensor drift

$\tilde{\boldsymbol{\sigma}}$	+	−	−	−	−
$\tilde{\mathbf{Z}}$	0	−	0	+	+
	−	+	−	0	0
	−	+	+	−	0
	0	−	0	+	−
	0	0	−	+	+

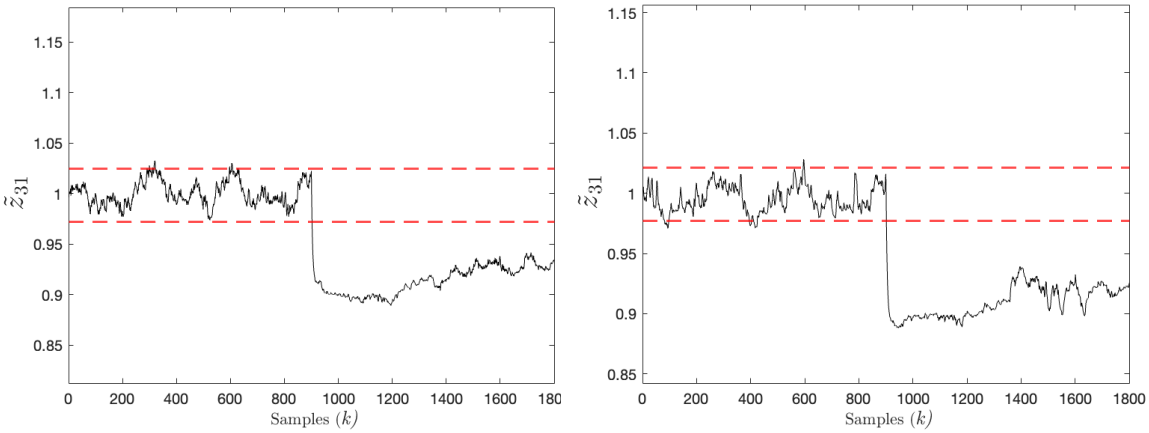
Table 4.18: Modelled PU2 5% sensor drift

$\tilde{\boldsymbol{\sigma}}$	0	−	−	−	−
$\tilde{\mathbf{Z}}$	0	0	−	+	−
	−	+	−	0	+
	−	−	+	−	0
	+	0	−	+	+
	+	−	−	+	−

Table 4.19: Practical PU2 5% sensor drift

$\tilde{\boldsymbol{\sigma}}$	0	−	−	−	−
$\tilde{\mathbf{Z}}$	0	0	0	0	−
	−	+	−	0	+
	−	−	+	−	+
	+	0	0	0	+
	+	−	−	+	−

The overall signatures of the PU1 sensor drifts are different from PU2 sensor drifts and are therefore isolable to its origin PU as well.

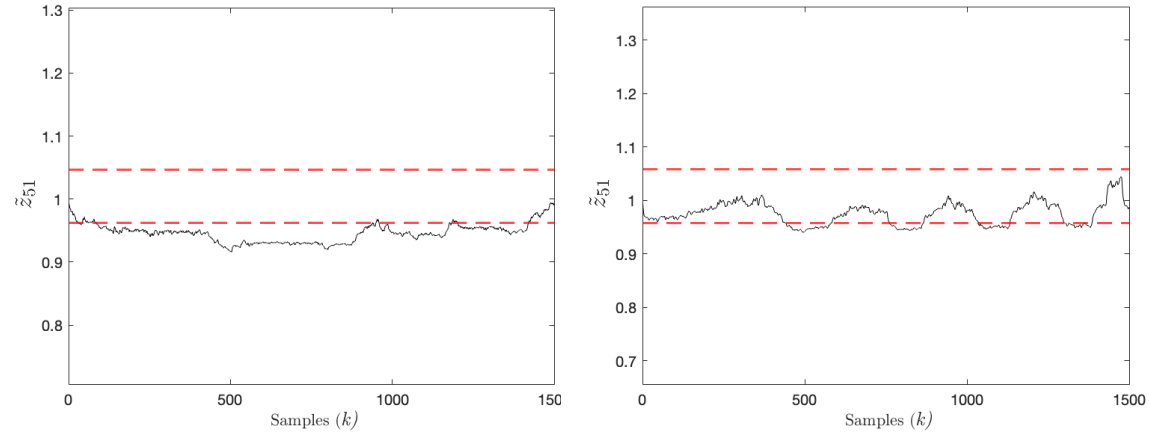


(a) Modelled result of $\tilde{z}_{31}$ (b) Practical result of $\tilde{z}_{31}$

Figure 4.12: SVD detection plots of a model and practical 5% Sensor drift in PU2 at sample 900

4.5.5 Fault 5: Fouling

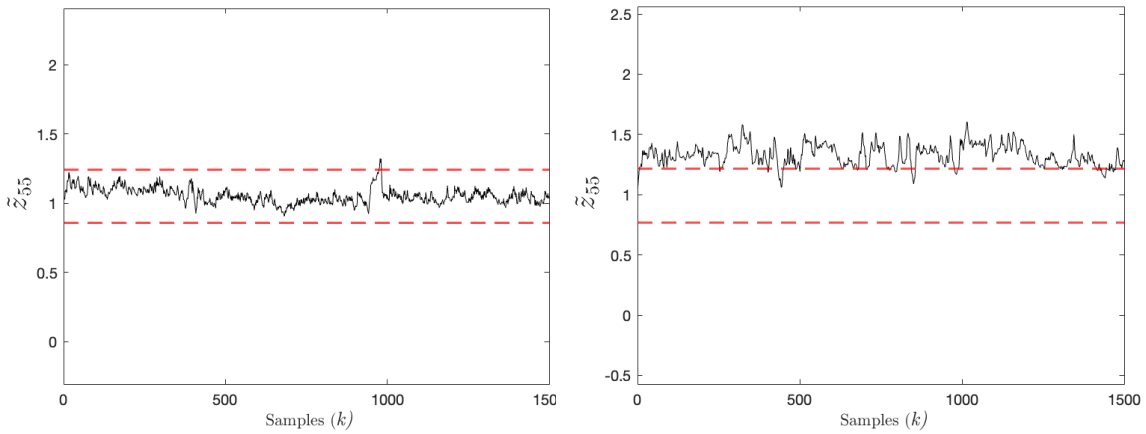
Figure 4.13 shows the detection results of a 20% fouling fault in PU1, which was applied throughout the 1500 samples shown. The SVD element plots in Fig. 4.13a and 4.13b exhibit the most deviation when compared to other SVD elements. The model $\tilde{z}_{51}$ shows a clear and constant breach of the LTh, whereas the practical result cycles in and out of alarm state. False alarms and detection speed are not analysed here, since all samples represent faulty conditions.



(a) Model result of $\tilde{z}_{51}$ (b) Practical result of $\tilde{z}_{51}$

Figure 4.13: SVD detection plots of a model and practical fouling in PU1

When the fouling fault was applied in PU2, the practical system showed that multiple SVD elements successfully detected the fault, while the modelled system showed none. One of these elements is shown in Fig. 4.14b. The model result only shows a momentary breach at sample 1000, while the practical result correctly shows a continuous breach.



(a) Model result of $\tilde{\boldsymbol{\sigma}}_m(2)$

(b) Practical result of $\tilde{\boldsymbol{\sigma}}_m(2)$

Figure 4.14: SVD detection plots of a model and practical fouling in PU2

An overall analysis of the SVD element results given by Fig. B.20 to B.23 reveals that the PU1 fouling fault is barely detected by the model, which shows two clear stray elements. Since the PU1 fouling mostly involves F_3, it is concluded that the model-based EGBV technique is more sensitive to detecting deviations in this PV compared to the practical EGBV system. For PU2, however, F_4 is the deviating PV and is more detectable by the practical-based EGBV configuration.

The model signature is given in Table 4.20 and the practical result is given in Table 4.21. Table 4.22 and 4.23 show the fault signatures for PU2. The fault signatures support the observations made from the detection plots.

In conclusion, the PU1 fouling fault is not practically detectable nor isolable, since the detection of the model may be attributed to hot flow prediction error. Considering the overall fouling results of PU2, it is concluded that the fault is detectable and isolable in practice.

4.6 Conclusion

The EGBV FDI approach was discussed and applied to the tested faults of the heated two-tank process. Throughout Section 4.3 to 4.4, the implementation of the method on model

Table 4.20: Modelled PU1 20% fouling

$\tilde{\boldsymbol{\sigma}}$	+	0	0	0	0
$\tilde{\mathbf{Z}}$	0	0	0	0	0
	0	0	0	0	0
	0	0	0	0	0
	0	0	0	0	0
	−	0	0	0	0

Table 4.21: Practical PU1 20% fouling

$\tilde{\boldsymbol{\sigma}}$	0	0	0	0	0
$\tilde{\mathbf{Z}}$	0	0	0	0	0
	0	0	0	0	0
	0	0	0	0	0
	0	0	0	0	0
	0	0	0	0	0

Table 4.22: Modelled PU2 20% fouling

$\tilde{\boldsymbol{\sigma}}$	0	0	0	0	0
$\tilde{\mathbf{Z}}$	0	0	0	0	0
	0	0	0	0	0
	0	0	0	0	0
	0	0	0	0	0
	0	0	0	0	0

Table 4.23: Practical PU2 20% fouling

$\tilde{\boldsymbol{\sigma}}$	0	0	0	0	0
$\tilde{\mathbf{Z}}$	0	0	0	0	+
	0	0	0	0	−
	0	0	0	0	+
	0	0	0	0	−
	0	0	0	0	+

data was shown and evaluated for verification. In Section 4.5, the detection and isolation results of the model and practical faults were discussed. From the similarities observed between the model and practical results throughout Appendix B, the author concludes that the FDI scheme is sufficiently validated. The cases of dissimilar behaviour were clarified in Section 4.5. The fault signature dissimilarities for the fouling fault specifically may be indicative of unmodelled process behaviour and should be investigated as part of a future study.

The FDI scheme has successfully detected 15 of the 20 tested faults in the practical system. The fault types that were not detected, namely leakage and fouling, have been shown to have minor process disruption in Chapter 3 and will require a more sensitive FDI configuration to be detected. Except for the clogging faults, all tests showed relatively minor and momentary false alarms. Detailed inspection of the false alarm pattern across all tests reveals an interval of 300 samples, which corresponds with the period of the wave-like behaviour observed for the hot water flows in Chapter 3. This suggests that the oscillatory behaviour of the hot water flow is a key contributor to the false alarms observed. Concerning detection speed, the EGBV FDI method has shown prompt response.

It was found that the clogging fault can be isolated from other fault types and within

the origin PU. Its magnitudes may be isolated in PU1, but only partially in PU2. The only leakage faults that may be comprehensively isolated, are in PU1 at 20% and 30% magnitude. The stuck valve faults can be uniquely isolated from other fault types and within their PU. The sensor drift fault can be isolated in type, magnitude and PU. The fouling results showed that, practically, only the PU2 fouling fault is isolable and unique.

The in-depth detection and isolation results will be provided and discussed in Chapter 6 alongside the results of the data-driven PCA approach, which is discussed next in Chapter 5.

CHAPTER

5

PRINCIPAL COMPONENT ANALYSIS

This chapter explains and applies PCA as an FDI method. The theoretical foundation is discussed first and is verified using the Simulink® model. The method is subsequently validated using the practical process data. The chapter is concluded with a brief results discussion.

5.1 Introduction

The EGBV FDI technique from Chapter 4 uses an energy-exergy graph model as a basis to establish a platform on which data-driven techniques, such as SVD may be applied to detect and isolate faults. The principal component analysis (PCA) approach is simpler and purely data-driven. It focuses directly on the PVs, rather than on the energy-exergy interactions of the process.

PCA was introduced by Pearson [91] and developed by Hotelling [40] into its current form. It has been extensively studied and applied in many scientific fields, including chemistry, geology and engineering under various terms [92]. Within the field of industrial process monitoring, it has been the subject of numerous studies and has been applied in practice, which includes DuPont chemical company [6]. Given its presence in the academic environment and its industrial application, PCA may be regarded as a viable FDI method

and a suitable technique for use in this comparative study.

Figure 5.1 provides an overview of the application of the PCA FDI approach. The process of PCA may be divided into two main stages, namely phase I and phase II. During phase I, offline NOC data from a process are used to develop and construct the PCA model using eigenanalysis [85, 93]. Then, a MEWMA detection function is calculated to develop detection thresholds based on NOC. Following phase I, the process is monitored in phase II. Online process data are first captured and standardized using the same mean and standard deviation vectors from phase I. For fault detection, a MEWMA detection function is calculated based on the PCA model and compared to the thresholds from phase I. For fault identification, the process data and the PCA model are used to calculate contribution plots [85, 93]. Finally, the contribution plots are used to derive fault signatures for isolation.

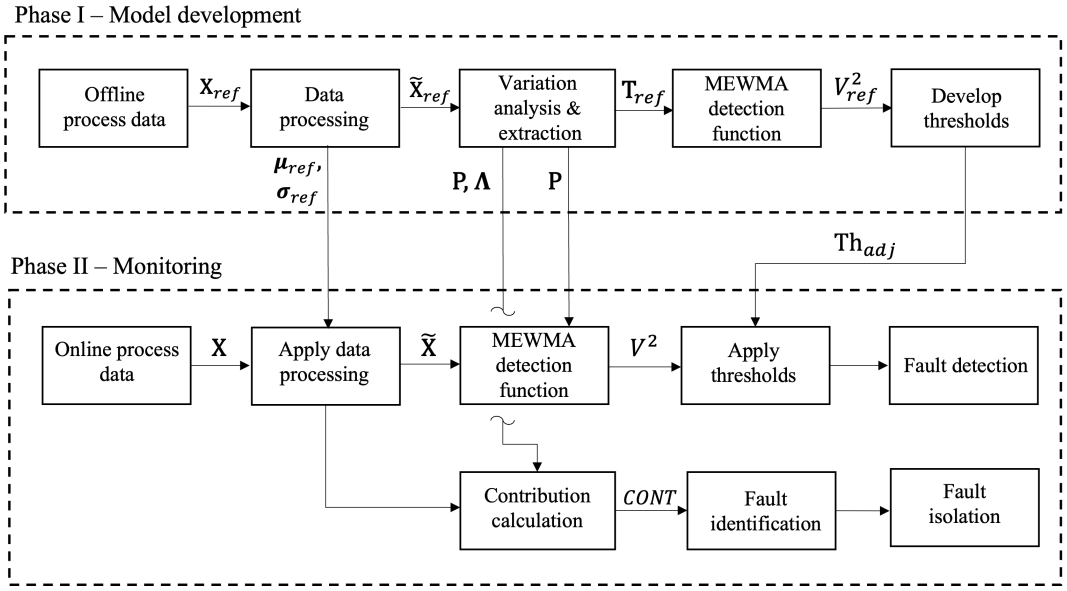


Figure 5.1: A flowchart of PCA FDI adapted from Harrou et al. [93]

In this chapter, the use of PCA as an FDI method is explained and applied to the heated two-tank process model first. The numerical results of each PCA step as it is applied to the model are provided and analysed for verification. Then, the method is validated by its application to the practical process data. Its performance with regard to fault detection and isolation is briefly discussed.

To clarify, the term 'FDI' in this study refers to fault *detection and isolation*, even though some studies and literature use the term for *detection and identification*. While both isolation and identification are applied in this chapter, the term 'FDI' is only used when referring to the former, since the ultimate goal is to *isolate* faults in type, size and location, per the definitions provided in Chapter 2.

5.2 Model development & verification

5.2.1 Data processing

Consider an NOC data matrix $\mathbf{X}_{ref} \in \mathbb{R}^{k \times m}$, where k is the number of samples and m is the number of process variables (PVs). It should be noted that the PVs in $\mathbf{X}_{ref}$ should be selected based on their relevance to the faults within the scope of monitoring [6]. In Chapter 3, it was observed that all measured PVs (apart from the PVs linked to external equipment, such as the hot and cold water reservoirs) were affected at least once throughout the series of faults applied and are therefore used to construct $\mathbf{X}$:

$$\mathbf{X} = \begin{bmatrix} \mathbf{L}_1 & \mathbf{L}_2 & \mathbf{T}_1 & \mathbf{T}_2 & \mathbf{F}_1 & \mathbf{F}_2 & \mathbf{F}_3 & \mathbf{F}_4 \end{bmatrix}. \tag{5.1}$$

The numerical result for the model NOC of (5.1) is given by:

$$\mathbf{X}_{ref} = \begin{bmatrix} 0.497 & 0.501 & 28.0 & 29.0 & 4.6 \times 10^{-4} & 1.7 \times 10^{-4} & 2.4 \times 10^{-4} & 2.4 \times 10^{-4} \\ \vdots & \vdots & \vdots & \vdots & \vdots & \vdots & \vdots & \vdots \\ 0.505 & 0.507 & 28.05 & 29.05 & 3.5 \times 10^{-4} & 1.7 \times 10^{-4} & 2.0 \times 10^{-4} & 2.0 \times 10^{-4} \\ \vdots & \vdots & \vdots & \vdots & \vdots & \vdots & \vdots & \vdots \\ 0.508 & 0.502 & 28.0 & 29 & 3.0 \times 10^{-4} & 1.9 \times 10^{-4} & 2.2 \times 10^{-4} & 2.1 \times 10^{-4} \end{bmatrix}. \tag{5.2}$$

The output in (5.2) shows the PVs in $\mathbf{X}_{ref}$ at $k = 1$, $k = 500$ and $k = 900$. The range of variation within each PV (or column) differs. They also have different magnitudes due to the units in which they are measured. The direct use of these data for PCA will likely cause incorrect variation analysis, due to the domination of the higher ranged process variables [6]. For this reason, the dataset $\mathbf{X}_{ref}$ is standardised to have zero mean and unit variance using the following equation [94]:

$$\tilde{x}_{ij} = \frac{x_{ij} - \mu_j}{\sigma_j}, \tag{5.3}$$

where μ_j and σ_j are the mean and standard deviation of j^{th} column of $\mathbf{X}$ and $\tilde{x}_{ij}$ is the $(i,j)^{th}$ entry of $\mathbf{X}$. The standardisation formula is built into the *normalize()*-function in MATLAB® and was used to standardise $\mathbf{X}$. The numerical result in (5.2) is updated to:

$$\tilde{\mathbf{X}}_{ref} = \begin{bmatrix} -1.61 & -1.10 & -0.11 & -0.21 & 1.41 & -0.38 & 0.52 & 0.84 \\ \vdots & \vdots & \vdots & \vdots & \vdots & \vdots & \vdots & \vdots \\ 0.02 & 0.67 & 1.53 & 1.25 & -0.03 & -0.38 & -1.23 & -0.97 \\ \vdots & \vdots & \vdots & \vdots & \vdots & \vdots & \vdots & \vdots \\ 0.61 & -1.16 & -0.11 & -0.21 & -0.75 & 1.44 & -0.65 & -0.52 \end{bmatrix}. \tag{5.4}$$

It can be seen in (5.4) that each variable has been centred to have a zero mean, as indicated by the presence of negative values and is also shown to have similar scaling. From this result, it is concluded that the matrix $\tilde{\mathbf{X}}_{ref}$ has been correctly prepared for variation analysis, which is discussed in the next section.

5.2.2 Variation analysis

At the core of PCA lies the analysis and extraction of variance from a multidimensional dataset. A basic illustration of the concept by Harrou [38] is shown in Fig. 5.2. The figure shows a three-dimensional scatter plot of dots. Each dot represents a sample containing a value for measured variables 1, 2 and 3. When inspecting the cluster of dots, it is clear that its shape is skewed in the three-dimensional space. If a line-of-closest fit were to be drawn through the skewed cluster, this line would capture the maximum interdimensional variance of the skewed cluster of data. The dots' projection onto the said line is the *first principal component*. Its direction is illustrated in Fig. 5.2 by the purple line appropriately labelled 'PC1'. The scalar length of the PC1 line is described in the figure by σ_1. Likewise, if a second line-of-closest fit were to be drawn through the cluster that is perpendicular to the first line, then it will describe the second most interdimensional variance of the data. In Fig. 5.2, the direction of the second line is shown by the PC2 purple line. If the dots are projected onto this second line, it will represent the *second principal component*. Its length is represented by σ_2, which is shown to be smaller than σ_1.

The procedure may be repeated as many times as the number of variables in the dataset, with each new best-fit line describing less interdimensional variance than the previous line, thus having a smaller σ-description. Therefore, data in an m-dimensional space will have m number of principal components, each with its own σ [38, 91]. The determination of the principal components of multidimensional or multi-variate datasets is significant in that it allows one to view the dataset in terms of its variance, rather than the physical measured values contained in it.

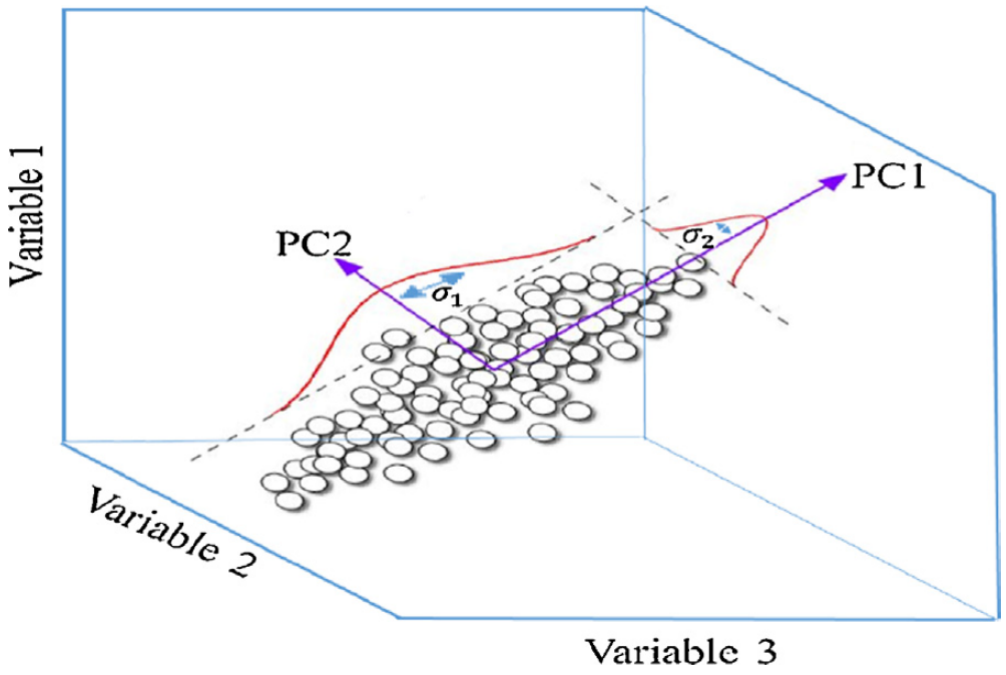


Figure 5.2: Three-dimensional illustration of principal component determination [38]

To determine the principal components and the magnitude descriptors of $\tilde{\mathbf{X}}_{ref}$, singular value decomposition may be used to solve the factorisation equation [6, 84]:

$$\frac{1}{\sqrt{k-1}}\tilde{\mathbf{X}}_{ref} = \mathbf{U}\boldsymbol{\Sigma}\mathbf{V}^T. \tag{5.5}$$

In (5.5), the columns in the matrix $\mathbf{V} \in \mathbb{R}^{\mathbf{m}\times\mathbf{m}}$ are orthonormal and are called *loading vectors*, since they describe the direction of each principal component. The matrix $\boldsymbol{\Sigma} \in \mathbb{R}^{k\times m}$ is made up of the magnitude descriptors, namely *singular values*. The singular values are located along the main diagonal of $\boldsymbol{\Sigma}$ from highest to lowest magnitude ($\sigma_1 \geq \sigma_2 \geq \cdots \geq \sigma_{min(m,k)} \geq 0$). The $\mathbf{U} \in \mathbb{R}^{k\times k}$ matrix, which describes the column space of $\tilde{\mathbf{X}}_{ref}$ [95] satisfies the equation, but is not used further [6]. Alternatively, eigendecomposition may be used to obtain the same results [6, 37]:

$$\mathbf{S} = \frac{1}{k-1}\tilde{\mathbf{X}}_{ref}^T\tilde{\mathbf{X}}_{ref} = \mathbf{V}\boldsymbol{\Lambda}\mathbf{V}^T. \tag{5.6}$$

In this case, the matrix $\mathbf{V}$ in (5.6) is obtained using the covariance matrix $\mathbf{S}$. The loading vectors are therefore given by the *eigenvectors*. The corresponding magnitude descriptors are given by the *eigenvalues*, which are located in the main diagonal of the matrix $\Lambda \in \mathbb{R}^{m\times m}$ and should also be ordered in decreasing magnitude ($\lambda_1 \geq \lambda_2 \geq \cdots \geq \lambda_m \geq 0$).

The eigenvalues given in (5.6) are equated to the singular values in (5.5) by the equation [6]:

$$\lambda_i = \sigma_i^2. \tag{5.7}$$

By applying (5.6) to the model NOC dataset given in (5.4) and subsequently solving (5.6) using the *eig()* -function in MATLAB®, the loading vector matrix $\mathbf{V}$ is calculated as:

$$\mathbf{V} = \begin{bmatrix} -0.011 & 0.703 & 0.072 & -0.019 & 0.029 & -0.043 & -0.113 & -0.696 \\ 0.104 & 0.066 & -0.694 & 0.207 & 0.559 & -0.382 & 0.015 & 0.032 \\ 0.489 & -0.011 & 0.115 & 0.587 & -0.042 & 0.190 & 0.590 & -0.132 \\ 0.496 & 0.004 & 0.094 & -0.248 & 0.508 & 0.567 & -0.318 & 0.052 \\ 0.001 & -0.702 & -0.086 & -0.035 & 0.021 & -0.015 & -0.112 & -0.697 \\ -0.118 & -0.093 & 0.691 & 0.144 & 0.540 & -0.433 & 0.001 & 0.026 \\ -0.515 & 0.013 & -0.070 & -0.287 & 0.356 & 0.370 & 0.613 & -0.087 \\ -0.474 & -0.001 & -0.033 & 0.669 & 0.090 & 0.412 & -0.386 & 0.026 \end{bmatrix}. \tag{5.8}$$

The corresponding matrix $\mathbf{\Lambda}$ containing the eigenvalues is given by:

$$\mathbf{\Lambda} = \begin{bmatrix} 3.263 & 0 & 0 & 0 & 0 & 0 & 0 & 0 \\ 0 & 1.985 & 0 & 0 & 0 & 0 & 0 & 0 \\ 0 & 0 & 1.664 & 0 & 0 & 0 & 0 & 0 \\ 0 & 0 & 0 & 0.505 & 0 & 0 & 0 & 0 \\ 0 & 0 & 0 & 0 & 0.336 & 0 & 0 & 0 \\ 0 & 0 & 0 & 0 & 0 & 0.186 & 0 & 0 \\ 0 & 0 & 0 & 0 & 0 & 0 & 0.043 & 0 \\ 0 & 0 & 0 & 0 & 0 & 0 & 0 & 0.018 \end{bmatrix}. \tag{5.9}$$

The columns in $\mathbf{V}$ give the $m-$dimensional directions of the process variation found in the model NOC, ordered from highest to lowest variance (equivalent to the purple arrows in Fig. 5.2). Matrix $\mathbf{\Lambda}$ in (5.9) shows the corresponding eigenvalues. With $\tilde{\mathbf{X}}_{ref}$ decomposed, one may choose to focus on only a subset of the results in (5.8) and (5.9) that still describes a large portion of $\tilde{\mathbf{X}}_{ref}$. This is referred to as *dimension reduction* and is described next.

5.2.3 Dimension reduction

After determining the loading vectors and corresponding eigenvalues, it is possible to use these results to distinguish between meaningful process variation and noise. Russel,

Chiang and Braatz [6] explain that by extracting and using the loading vectors that describe actual process variation, the effect of erroneous fault detection is reduced. When extracting meaningful variation, the dimension of the dataset at hand is reduced and for this reason, PCA may be referred to as a linear dimensionality reduction technique [6, 34, 38].

Since $\mathbf{V}$ and $\mathbf{\Lambda}$ are ordered according to process variation description, the first a out of m loading vectors are extracted. The selection of a will directly influence the FDI performance. If a is too high or too low, modelling errors will occur which will lead to an increased false alarm rate (FAR) and an increased missed detection rate (MDR) [39, 96].

Several methods exist to optimise the selection of a such that the maximum variance is captured, including the cumulative percent variance (CPV) test [6, 38, 41], scree test [6, 41], parallel analysis [6] and predicted error sum of squares (PRESS) statistic [6, 97]. The variance of reconstruction error (VRE) [97] is proposed by Qin and Dunia [97] as an improved selection method for a, due to the subjectivity of most other methods used throughout literature. In this study, the scree method is used to determine a.

The scree test involves plotting the eigenvalues in $\mathbf{\Lambda}$ in decreasing order of magnitude to look for the point where the biggest change occurs, also referred to as the *elbow* of the plot [98]. This point of gradient transition should provide a clear visual indication of the optimal a, as it will represent the best compromise for maximising process variance captured while minimising the number of loading vectors required for further calculations. In Fig. 5.3, two elbows occur, so to speak, namely $a = 1$ and $a = 3$. Given that each eigenvalue represents a portion of process variance, choosing $a = 1$ may lead to an insufficient representation of the variance of $\tilde{\mathbf{X}}_{ref}$ when considering the values of eigenvalue 2 and 3. For this reason, the value of a is chosen as three.

The corresponding vectors may now be extracted from $\mathbf{V}$ to form a new loading matrix $\mathbf{P} \in \mathbb{R}^{m \times a}$ [6]. Using the results in (5.8), the matrix $\mathbf{P}$ is given by:

$$\mathbf{P} = \begin{bmatrix} -0.011 & 0.703 & 0.072 \\ 0.104 & 0.066 & -0.694 \\ 0.489 & -0.011 & 0.115 \\ 0.496 & 0.004 & 0.094 \\ 0.001 & -0.702 & -0.086 \\ -0.118 & -0.093 & 0.691 \\ -0.515 & 0.013 & -0.070 \\ -0.474 & -0.001 & -0.033 \end{bmatrix}. \tag{5.10}$$

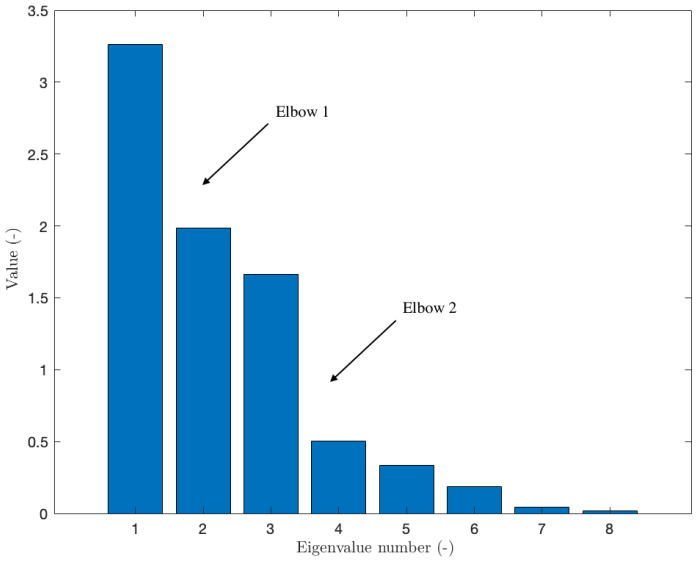


Figure 5.3: Scree plot showing eigenvalues in decreasing order

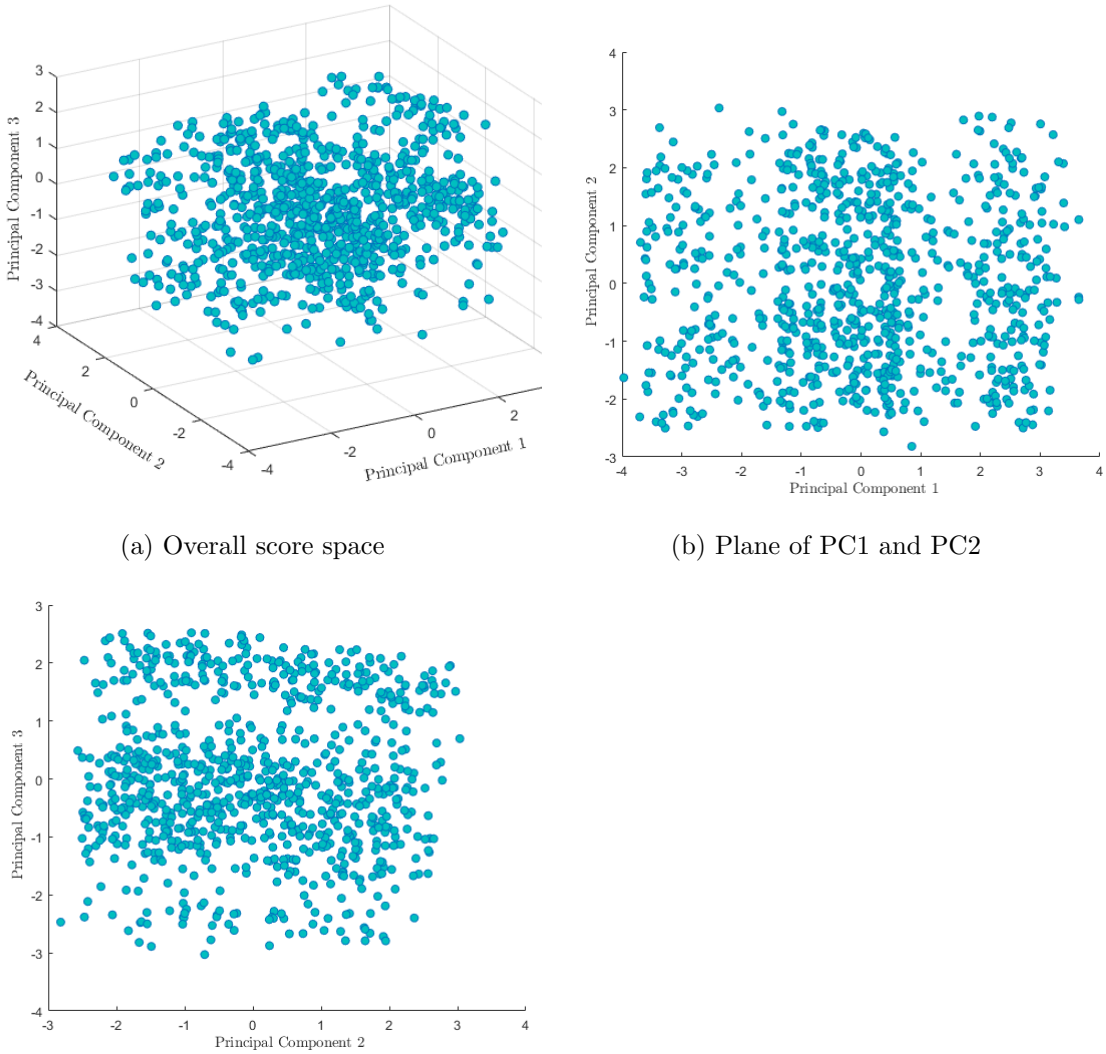
Finally, the *principal components* (PCs) are contained in the matrix $\mathbf{T} \in \mathbb{R}^{k \times a}$ [6, 37]:

$$\mathbf{T}_{ref} = \tilde{\mathbf{X}}_{\mathbf{ref}}\mathbf{P}, \tag{5.11}$$

with the columns in $\mathbf{T}_{ref}$ representing PC 1 to a of $\tilde{\mathbf{X}}_{ref}$. The matrix $\mathbf{T}_{ref}$ is called the *score matrix* of the NOC data, as each sample in $\tilde{\mathbf{X}}_{ref}$ is projected into the lower dimensional *score space* in (5.11) when multiplied by $\mathbf{P}$ [6, 37].

The calculation of $\mathbf{T}_{ref}$ is verified through visual analysis. Since it was determined that $a = 3$ is optimal, the resulting $\mathbf{T}_{ref}$ will contain three PCs in the case of the heated two-tank process and can therefore be visually illustrated. Figure 5.4 provides a visual overview of the score space of the NOC model. The overall result of (5.11) when applied to the model NOC data is plotted in Fig. 5.4a and is representative of 86.4 % of the total variance of $\tilde{\mathbf{X}}_{ref}$. Figures 5.4b and 5.4c provide single plane views of the plot in Fig. 5.4a to aid in its analysis. It can be seen in Fig. 5.4a and more clearly in Fig. 5.4b that the span of PC1 is greater than that of PC2, with the former ranging from -4 to +4 and the latter ranging from -3 to +3. This is expected and visually illustrates how PC1 describes more process variance. Similarly, it is shown in Fig. 5.4c that the span of PC2 is slightly greater than that of PC3. This is also expected since it is shown in (5.9) that λ_2 is only slightly greater than λ_3. It is then concluded that $\mathbf{T}_{ref}$ is correctly calculated.

The formulation of $\mathbf{P}$ and $\mathbf{T}_{ref}$ completes the construction of the PCA model necessary for multivariate FDI and will be used in the sections that follow. For completeness, it should be noted that the same matrix representation can be made for the ignored $m - a$ principal



(a) Overall score space

(b) Plane of PC1 and PC2

(c) Plane of PC2 and PC3

Figure 5.4: Visual illustration of model NOC score space

components to form the *residual space*. The score and the residual space together account for the entire variation description of $\tilde{\mathbf{X}}_{ref}$. This is formulated as [6, 37]:

$$\tilde{\mathbf{X}}_{ref} = \mathbf{T}_{ref}\mathbf{P}^T + \mathbf{E}_{ref}, \tag{5.12}$$

with $\mathbf{E}_{ref} \in \mathbb{R}^{k \times m}$ as the *residual matrix* of the NOC data.

With the process variation analysis and extraction concluded and verified in this section, the PCA detection function is developed in the next section.

5.2.4 Detection function

Although the detection function is mainly applied in the *monitoring phase* (shown in Fig. 5.1), its application to NOC data is a prerequisite for determining the fault detection threshold. For this reason, the detection function is explained next.

A single fault detection function, namely Hotelling's T^2 statistic, may be used to evaluate newly monitored process data to determine whether a fault has occurred. When applied to only the score space developed in Section 5.2.3, its formula is given by [6, 38, 99]:

$$T_k^2 = \tilde{\mathbf{x}}_k^T \mathbf{P} \mathbf{\Lambda}_a^{-1} \mathbf{P}^T \tilde{\mathbf{x}}_k = \sum_{i=1}^{a} \frac{t_i^2}{\lambda_i}, \tag{5.13}$$

where $\tilde{\mathbf{x}}_k \in \mathbb{R}^m$ is the k^{th} sample vector from an online process dataset $\tilde{\mathbf{X}}$ and t_i is the *score* value when $\tilde{\mathbf{x}}_k$ is projected into the score space by the i^{th} principal component. If sample vectors from $\tilde{\mathbf{X}}_{ref}$ is used, then (5.13) results in $T_{ref,k}^2$.

Equation (5.13) can be viewed as a single plot version of the three-dimensional scatter plot in Fig. 5.4a, whereby the T^2 value of every dot in Fig. 5.4a is equal to the sum of its coordinates after every coordinate (t_i) has been divided by the eigenvalue representing the axis. For example, the T^2 value for $k = 1$ is calculated as follows, using (5.13) and the results given in (5.9):

$$T_1^2 = \frac{(-0.870)^2}{3.263} + \frac{(2.157)^2}{1.985} + \frac{(0.169)^2}{1.664} = 2.6 \tag{5.14}$$

where the coordinate for the score space projection of $k = 1$ is (-0.87, 2.16, 0.17) in Fig. 5.4a.

Recall that in Chapter 4, the exponentially weighted moving average (EWMA) technique was implemented to filter each SVD element for fault detection. Since this study aims to compare the PCA FDI approach to the EGBV technique, it is only fair that EWMA is employed for PCA as well. However, the EWMA technique discussed in Section 4.4.2 cannot be directly applied here, because each SVD element was regarded as a standalone variable and as such *univariate* EWMA was used. The *multivariate* EWMA (MEWMA) is applicable here and was first proposed by Lowry et al. [100], expanding (4.22) into vector form:

$$\mathbf{y}_k = r\mathbf{g}_k + (1 - r)\mathbf{y}_{k-1}, \tag{5.15}$$

where $\mathbf{y}_k \in \mathbb{R}^m$ is the k^{th} MEWMA output from an input vector $\mathbf{g}_k \in \mathbb{R}^m$ and $0 \leq r \leq 1$ is

the smoothing constant. Wold [101] then combined the EWMA method with PCA to form exponentially weighted moving principal component analysis (EWM-PCA). Past studies [38, 89, 93] have found that the combination of MEWMA and PCA yields superior FDI results when compared to standalone PCA. It should be noted that even though the term 'EWM-PCA' is used to refer to the combination of MEWMA and PCA, this study will refer to this combination simply as 'PCA'.

When combining MEWMA and PCA, the row vectors $\mathbf{t}_k \in \mathbb{R}^a$ from $\mathbf{T}$ may be used as $\mathbf{g}_k$. Equation (5.15) is then updated to [93, 101]:

$$\mathbf{y}_k = r\mathbf{t}_k + (1-r)\mathbf{y}_{k-1}, \tag{5.16}$$

with $\mathbf{y}_k \in \mathbb{R}^a$ as the MEWMA output of $\mathbf{t}_k$. Naturally, if the offline $\mathbf{T}_{ref}$ were to be used instead of the online $\mathbf{T}$ matrix, then $\mathbf{y}_{ref,k}$ is calculated.

Finally, the online detection function V^2 for the k^{th} sample is given by [38, 100]:

$$V_k^2 = \mathbf{y}_k^T \mathbf{S}_\mathbf{Y}^{-1} \mathbf{y}_k, \tag{5.17}$$

with $\mathbf{S_Y}$ as the covariance matrix of the MEWMA matrix $\mathbf{Y} \in \mathbb{R}^{k \times a}$, containing all $\mathbf{y}_k$ as row vectors. For a large k, matrix $\mathbf{S_Y}$ can be calculated as follows [38, 100]:

$$\mathbf{S_Y} = \left(\frac{r}{2-r}\right) \mathbf{S_T}, \tag{5.18}$$

where $\mathbf{S_T}$ is the covariance matrix of $\mathbf{T}$. Combining (5.17) and (5.18) yields the updated detection function:

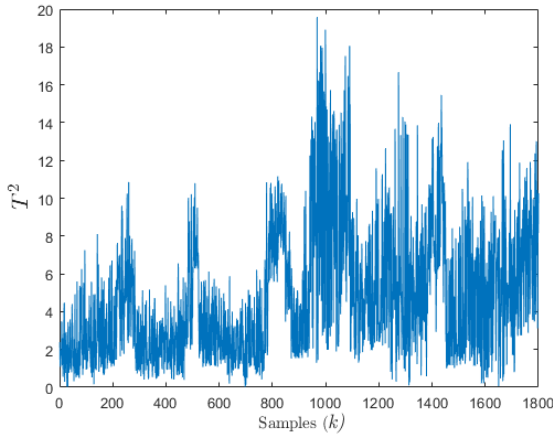
$$V_k^2 = \mathbf{y}_k^T \left(\frac{r}{2-r}\right) \mathbf{S}_\mathbf{T}^{-1} \mathbf{y}_k, \tag{5.19}$$

which will be used for further fault detection in this study. To compare the V^2 function with the traditional T^2 statistic and to verify the correctness of its implementation, the results of (5.13) and (5.19) are plotted in Fig. 5.5 using a modelled 20% clogging fault in PU1 for analysis.

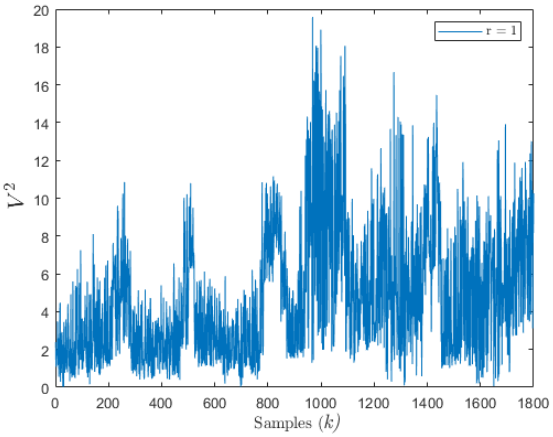
Figure 5.5a shows the monitored T^2 statistic when a clog is applied at sample 900. It is observed that the plot shows lower peaks before the fault was applied, with T^2 varying between 0 and 11. After the fault occurred, higher peaks occur and are more persistent, which correctly shows the presence of a process upset. In Fig. 5.5b, the V^2 result is shown

for a smoothing constant $r = 1$. It is clear that this plot is identical to the T^2 statistic and is correct, since it is expected that (5.13) and (5.19) should be equal when $r = 1$ [100]. Finally, Fig. 5.5c shows V^2 when $r = 0.2$, which is the same smoothing parameter used for EWMA in the EGBV approach. The plot shows the same trend as Fig. 5.5b but is less noisy as a result of the memory effect of MEWMA. It also displays the effect of the clog better with a more distinct mean shift after sample 900.

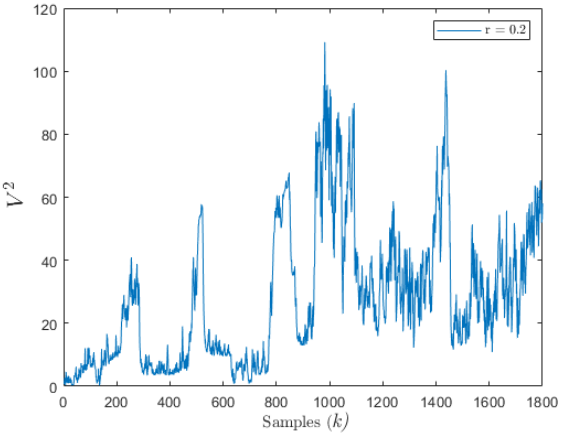
From these results, it is concluded that the detection functions discussed in this section are correctly implemented. It is shown that MEWMA provides superior detection performance and will be implemented with $r = 0.2$ to match the smoothing applied to the EGBV technique. It is now appropriate to discuss the implementation of thresholds for the V^2 detection function.



(a) T^2 statistic



(b) EWMA V^2 with $r = 1$



(c) EWMA V^2 with $r = 0.2$

Figure 5.5: Comparison plots of T^2 and V^2 on a 20% modelled clog in PU1

5.2.5 Threshold determination & fault detection

When using the T^2 statistic from (5.13), its threshold is given by [6]:

$$T_\alpha^2 = \frac{a(k^2-1)}{k(k-a)} F_{a,k-a,\alpha} \tag{5.20}$$

where a is the number of extracted principal components, k is the total number of samples and $F_{a,k-a,\alpha}$ is the $F-$ distribution value for a and $k-a$ degrees of freedom for a given significance level α. The process can be described as normal when [41],

$$T_k^2 \leq T_\alpha^2. \tag{5.21}$$

and faulty when [38]

$$T_k^2 > T_\alpha^2 \tag{5.22}$$

When MEWMA is used with PCA, however, multiple methodologies exist for the determination of a suitable threshold. Chen et al. explained in [89] that when MEWMA is applied in the measurement space, the threshold can be determined by the $F-$distribution. Harrou et al. [38] argue that because MEWMA makes the process samples correlated, the use of a statistical threshold is not appropriate. The widely accepted approach is to use average run lengths (ARLs) as the basis for threshold selection (discussed in Section 4.4.2), with several existing mathematical approaches to calculate and optimise said ARLs and thresholds [38, 100, 102–104]. In this work, an *adjusted threshold* is employed.

An adjusted threshold is used to establish a common ground, as it were, between EGBV and PCA FDI schemes for a fair comparison. Since the MDR, FAR and detection delay benchmarks are all influenced by threshold selection, it is appropriate to select the PCA threshold such that it has equal performance to energy-based visualisation in one of these benchmarks. By selecting the PCA threshold to have an equal FAR to that of EGBV during NOC, this common ground is established.

Recall from Section 4.4.3 that the UTh and LTh of each SVD element were set to achieve a total FAR of 5% for the NOC dataset. The PCA equivalent would therefore be to set its adjusted threshold Th_{adj} such that a FAR of 5% is achieved for the V_{ref}^2 function as calculated from the NOC dataset. Unlike EGBV, PCA only has a single detection function which requires single-sided monitoring, thus only one Th_{adj} value needs to be determined.

By using a MATLAB® script to iteratevly adjust Th_{adj} on the V_{ref}^2 function, it was found

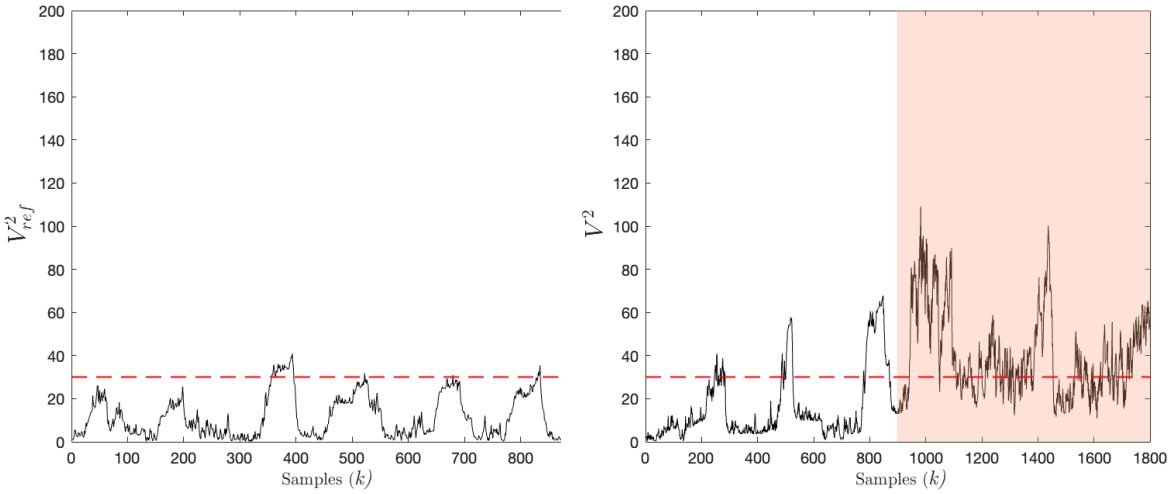
that a $Th_{adj} = 29.87$ achieves the FAR target of 5% using the model results. Equations (5.21) and (5.22) then update to

$$V_k^2 \leq 29.87 \tag{5.23}$$

indicates normal process operation within the model, while

$$V_k^2 > 29.87 \tag{5.24}$$

is regarded as faulty operation. Figure 5.6a displays the model plot of V_{ref}^2 with Th_{adj} added to it. It is illustrated that the majority of samples are below the threshold, while the minority is in a false alarm state. Figure 5.6b shows the same plot as Fig. 5.5c with the addition of Th_{adj}. When the 20% clog is created at $k = 900$, it is shown how the majority of the samples that follow are above the threshold, confirming the presence of the fault. Samples 1 to 900 are faultless, meaning three false alarm events occurred before the fault.



(a) Reference PCA plot with threshold

(b) Faulty PCA plot with threshold

Figure 5.6: Illustration of the threshold for PCA fault detection

Enforcing the detection rules set out in (5.24) may be more theoretically appropriate than practically applicable. Consider Fig. 5.7, which shows a modelled 10% leak fault in PU2 occurring at 900. Three clear false alarm events occurred before sample 900. During the faulty state, a detection spike is observed at approximately $k = 990$ and also at $k = 1750$. According to the rule of (5.24), the fault has been detected, yet the majority of V^2 is below the threshold for the fault period. In fact, more samples are in violation before the

fault occurred than during its occurrence. In this scenario, it is not practically feasible to strictly follow (5.24) for fault detection purposes. To accurately distinguish abnormal from normal behaviour, a simple, objective solution is proposed. To detect a fault, the following rule is applied:

$$\tilde{V}^2_{fault} > 29.87, \tag{5.25}$$

with $\tilde{V}^2_{fault}$ denoting the mean of the V^2 samples during the fault state. This is similar to how the fault signature symbols are determined for EGBV. If (5.25) is applied to the result in Fig. 5.6b, the fault would correctly be detected since most samples violate the threshold. When applied to the scenario in Fig. 5.7, a detection will now not be registered, since the single spike occurring at $k = 990$ is insufficient. The rule in (5.25) will thus be used in this study.

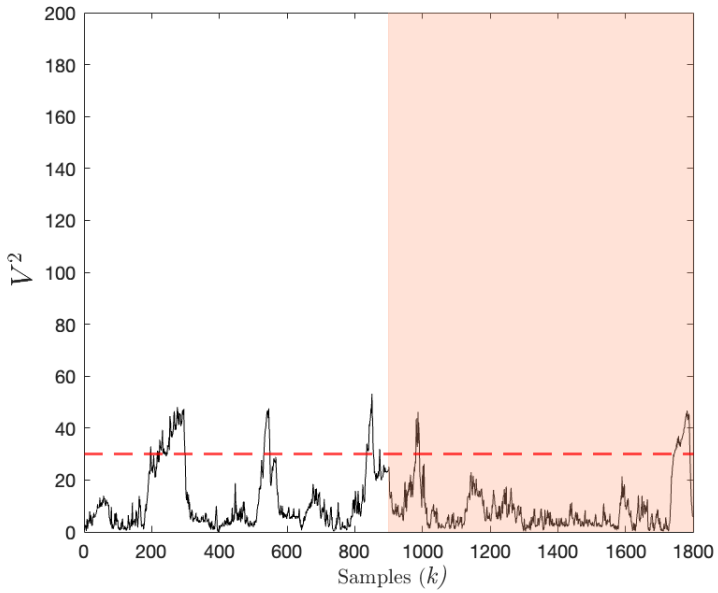


Figure 5.7: PCA V^2-function result for a modelled 10% leak in PU2 at sample 900

5.2.6 Fault identification & isolation

Contribution plots were developed by Miller, Swanson and Heckler [42] to provide plant operators that use multivariate fault monitoring with useful information on identifying the fault. The PVs that constitute the multivariate dataset is displayed on a bar chart which then visually shows how much each PV contributed to the detected process fault. This procedure is known as *fault identification*.

The procedure starts by using the scores $t_{1,k}, t_{2,k}, \ldots, t_{a,k}$ in $\mathbf{t}_k$ (or the coordinates of every

dot in Fig. 5.4a) and calculating a contribution value for every score [6, 105]. Kourti [105] explains that the l highest scores should be selected, where $l \leq a$. In this work, all a scores are considered for the contribution calculation. The contribution value of a score is given by [6, 105, 106]:

$$cont_{ij,k} = \frac{t_{i,k}}{\lambda_i} p_{ij} \tilde{x}_{j,k}, \tag{5.26}$$

where $cont_{ij,k}$ is the contribution value for the i^{th} normalised score t_i/λ_i of the j^{th} PV $\tilde{x}_{j,k}$ for a given sample k. If the contribution value is smaller than zero, it is set to zero [6, 105]. Then, the contributions of the scores are summed to determine the overall contribution value of the j^{th} PV at sample k [6, 105]:

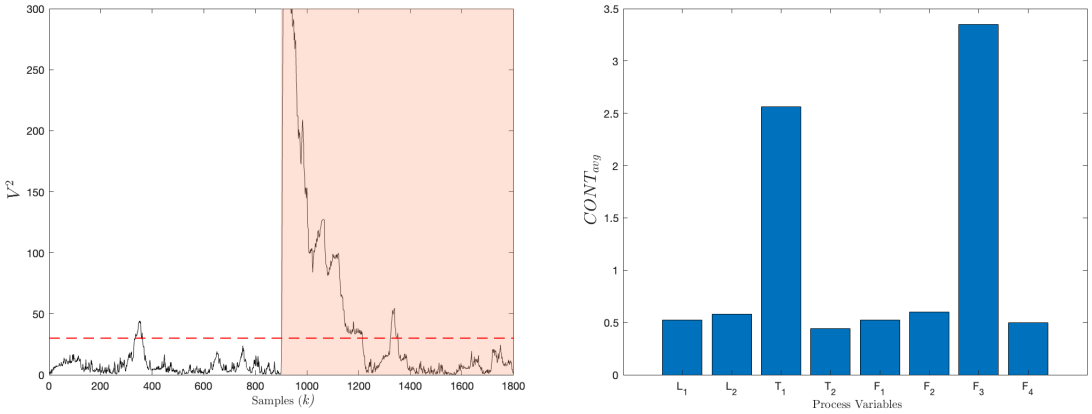
$$CONT_{j,k} = \sum_{i=1}^{a} cont_{ij,k} \tag{5.27}$$

The procedure is repeated for every PV in the dataset, until m-amount of $CONT_{j,k}$ values are calculated, which may now be displayed on a bar chart. A PV with a high value for contribution value relative to the other PV's contributions is considered a top contributor to the fault [6, 105].

Before continuing to the application of these equations, two matters need to be clarified on the approach taken in this work. Firstly, it should be noted that the original score space values $\mathbf{t}_k$ will be used for the contribution calculation and not the MEWMA enhanced $\mathbf{y}_k$ values calculated in (5.16), as the former is well researched within the academic community and has been successfully used in multiple studies [26, 106–108]. Secondly, similar to the fault isolation approach in Chapter 4, the mean contribution value of each PV across all samples in fault state will be used as the final contribution plot value for said PV.

To verify the application of (5.26) and (5.27), the modelled 2% sensor drift fault in PU1 is tested. The V^2 detection plot is shown in Fig. 5.8a, while the contribution plot for the fault is shown in Fig. 5.8b. In Fig. 5.8a, it is shown how the fault is detected when occurring at sample 900. From the results in Chapter 3, it is known that the PVs that exhibit the largest change during the fault are the PU1 temperature variable T_1, as well as the hot water flow F_3 to PU1. Figure 5.8b shows how these PVs have a higher contribution value relative to the other PVs. Thus, the PVs that were influenced the most by the fault have been correctly identified.

Finally, all contribution values are tabulated to form the fault isolation signature and are given by Table 5.1. The primary purpose of the fault signature is to capture the fault identification results in such a way that the location, size and type of the fault are easily distinguishable and isolable. The PVs with the highest contributions relative to the others



(a) V^2 detection plot

(b) Mean contribution plot of PVs

Figure 5.8: Illustration of fault detection and identification of a 2% sensor drift in PU1 at sample 900

are shown in red to ease reader inspection. It should be noted that the red colouring serves no additional purpose than to highlight the author's observations in this regard.

Table 5.1: Contribution values for a modelled PU1 20% clog

L_1	L_2	T_1	T_2	F_1	F_2	F_3	F_4
0.52	0.58	2.56	0.44	0.52	0.60	3.35	0.50

Thresholds are not applied here to form the fault signature as was done in Chapter 4. For EGBV, thresholds were required to assign symbols that form the fault signature and were determined using NOC data. This procedure cannot be applied to the NOC PCA contribution values, due to the *contribution plot smearing* effect. Westerhuis, Gurden and Smilde [109] first explained that during a fault, contributions of PVs that are unaffected by a fault are also influenced or *smeared*, which may lead to false identifications if thresholds were to be enforced. This phenomenon is studied and explained in depth by Van den Kerkhof et al. [110]. Liu [111] has proposed a solution to the smearing effect, but is beyond the scope of this study.

Up to now, the theoretical foundation of fault detection, identification and isolation of PCA has been explained and verified using the Simulink® model. The practical validation of this FDI method is now in order.

5.3 FDI results & validation

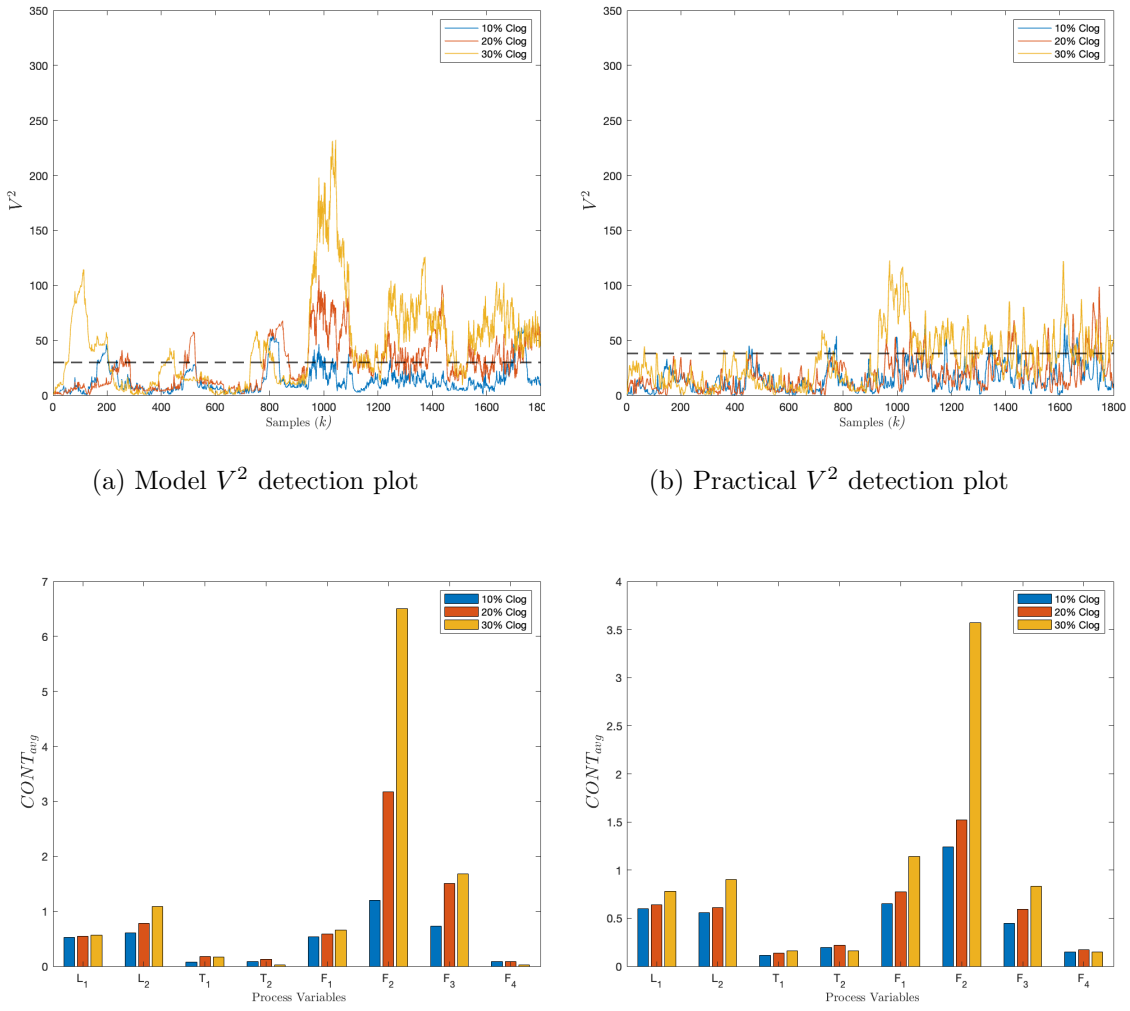
In this section, the PCA technique will be applied to the practical process data of the heated two-tank process. The detection and isolation results of the model and practical results are compared for validation. A brief comparison of false alarms and detection delay characteristics is discussed but will be analysed in detail in Chapter 6.

The section outline follows that of Chapter 3 and Chapter 4, where the results of every fault type are discussed and analysed separately. The V^2 detection and contribution plots for *all* faults are presented in this section. If more than one fault size was tested, the V^2 and $CONT$ results of each fault size are displayed in the same figure to illustrate the effect of the fault magnitude, even though each fault size was tested independently. The fault signatures compiled from the contribution plots are given in Appendix C.

5.3.1 Fault 1: Clogging

Figure 5.9 shows the detection and identification results for all clog faults in PU1. The threshold of the practical system was calculated to be 37.9, which is reasonably similar to the model threshold of 29.87. From Fig. 5.9a and 5.9b, it is clear that the 10 % fault is not detected in the model or the practical system, since the blue line remained below the threshold with single spikes that are indistinguishable from the false alarm behaviour. The 20% fault was detected in the model, but in the practical system, a fault cannot be declared with confidence. Both systems show a near immediate detection of a 30% fault (yellow plot) when it occurred at sample 900. False alarm events are present in the model and practical system but are more prominent in the model results.

The contribution plots are displayed in Fig. 5.9c and 5.9d for the model and practical system, respectively. It is observed in both systems that the average contribution of the process variables tends to increase with fault size, especially in the case of the highest contributors. For the 10% clog, the model and practical system's highest contributors are not clear. This is expected since these faults remained undetected in Fig. 5.9a and 5.9b. At 20% fault size, outlier contributors become clear in Fig. 5.9a and even clearer at 30% fault size, namely F_2 and F_3. This corresponds with the detection results of the model. A distinctly high contributor (F_2) is only visible at 30% fault level for the practical system, corresponding to the results of Fig. 5.9b.



(a) Model V^2 detection plot

(b) Practical V^2 detection plot

(c) Model contribution plot

(d) Practical contribution plot

Figure 5.9: Plots of FDI results of all clogs in PU1 at sample 900 for the model and practical process

Considering the process results from Chapter 3, these findings are valid. Both systems showed increased F_2 contribution, but the model identified F_3 to be a significant contributor as well. This is because the model predicted a reduced F_3, while the practical F_3 showed no change in Fig. A.4. The fault signatures are compiled from the contribution plots and shown in Tables C.1 and C.2.

While both detection plots have the same trend, the model plot appears to have overall more sensitive behaviour when comparing the peaks during false alarms and fault occurrence. The contribution values for each PV also differ to varying degrees. The following factors are the main contributors to these discrepancies:

- **Model deficiencies** - The model discrepancies discussed in Chapter 3 will lead to a model matrix $\mathbf{X}$ that is slightly different from that of the practical system, which in turn leads to dissimilarities in the FDI results.

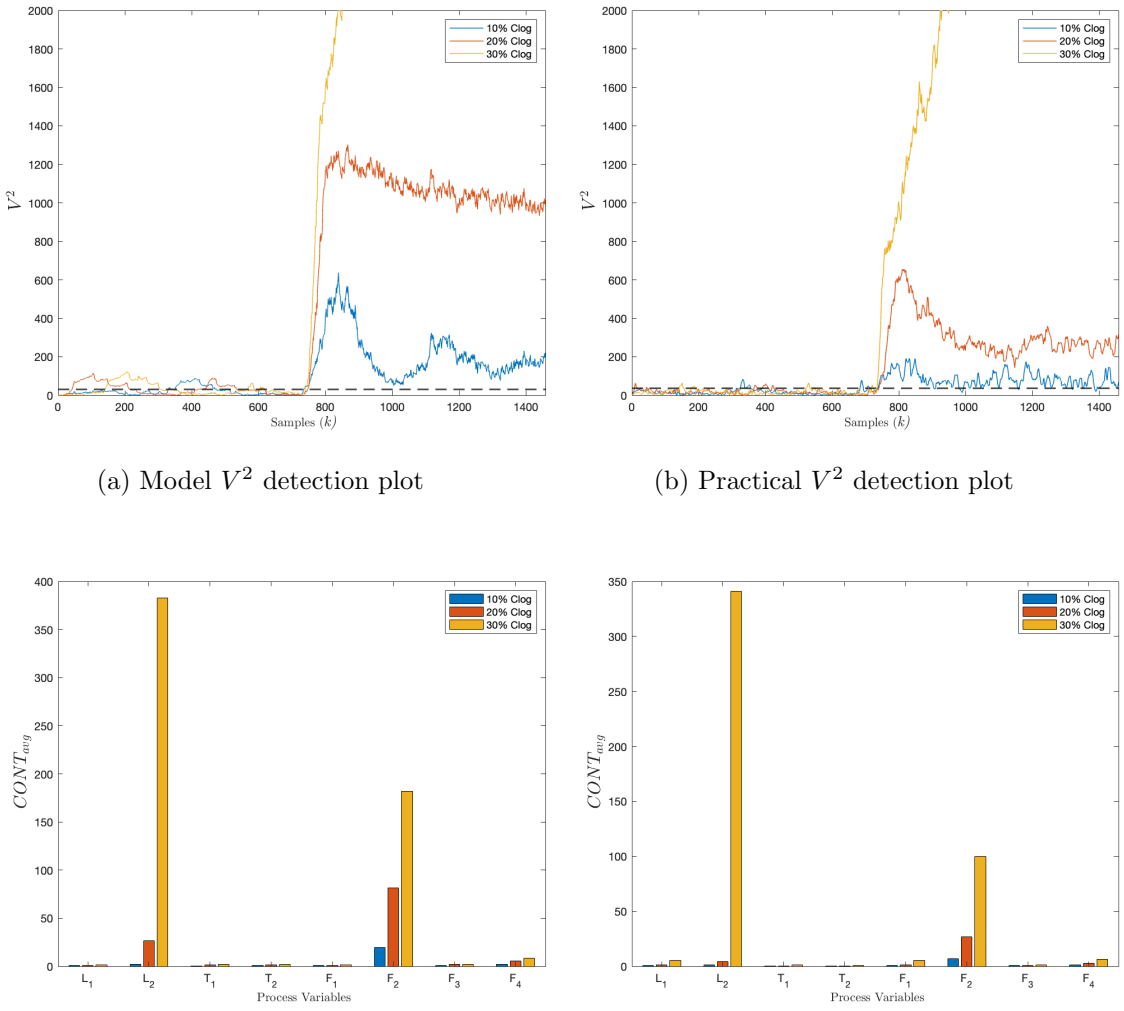
- **Score space coverage** - The PCA model for the practical system, which also shows an optimal PC count of 3, only provides 74% variance coverage compared to the 86% coverage of the Simulink® model. The practical system is, therefore, less likely to detect faults of smaller influence, but will also be less prone to process noise, consequently leading to fewer false alarms.

- **Score space distribution** - The selection of the first three PCs, in this case, means that the first three interdimensional directions of most variance (contained in the $\mathbf{P}$ matrix) are used to construct the PCs (contained in $\mathbf{T}$). With discrepancies occurring in the training dataset $\mathbf{X}_{ref}$, the directions in $\mathbf{P}$ will also differ slightly as a result. Ultimately, the model and practical detection plots may show dissimilar behaviour (indicated in Fig. 5.9a and 5.9b) and the contribution values calculated for the model and practical system may differ as well (as shown in Fig. 5.9c and 5.9d).

The clogging results of PU2 are given in Fig. 5.10. All fault sizes are definitively detected in both systems as shown in Fig. 5.10a and 5.10b, with minimal detection delay. Both systems also show false alarm events prior to the fault, with the model showing major false alarm events during the NOC stage of every fault size.

The contribution plots in Fig. 5.10c and 5.10d show that at 10% clog size, only F_2 is identified to be a significant contributor. The model shows that L_2 is also significant in addition to F_2 at 20% clog size. Finally, at 30% clog size, both systems illustrate L_2 to be the top contributor, followed by F_2. These identified process variables correspond to trends observed in the process results given in Fig. A.5 to A.7. Tables C.3 and C.4 contain the fault signatures of the PU2 clogs.

For the clogging fault type it is concluded that for PU1, only the 30% clog is truly detectable, given its detection in both systems. The 20% clog in PU1 is detected by the model, but not by the practical system. All clog sizes are detectable in PU2. Fault size isolation is possible when considering the contribution increase with fault size. Low confidence isolation of fault location is expected, since it is observed that overlapping of high contributing PVs occurs between PU1 and PU2, specifically F_2.



(a) Model V^2 detection plot

(b) Practical V^2 detection plot

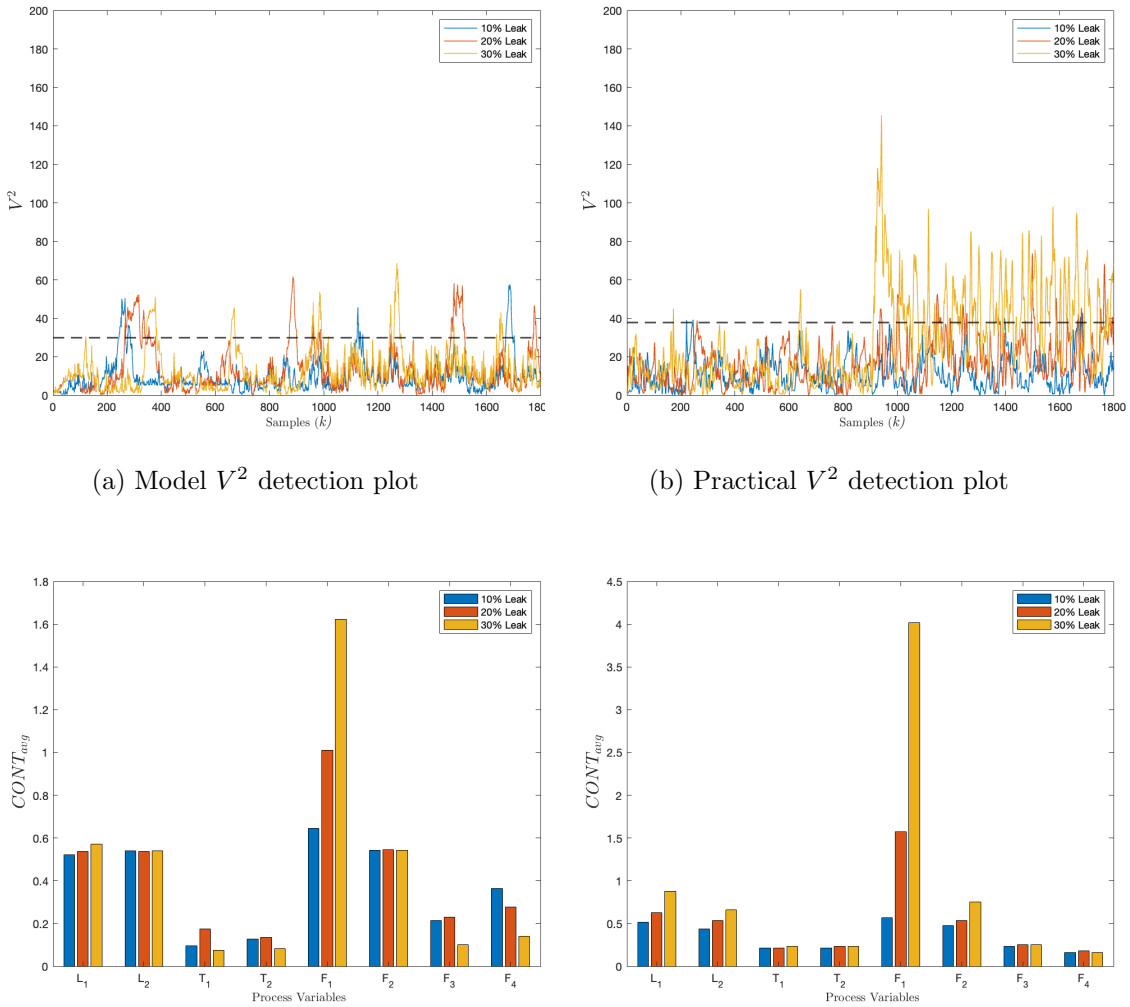
(c) Model contribution plot

(d) Practical contribution plot

Figure 5.10: Plots of FDI results of all clogs in PU2 at sample 729 for the model and practical process

5.3.2 Fault 2: Leakage

The V^2 detection results, as well as the contribution plots for the leak faults in PU1, are provided in Fig. 5.11. No clear detection is made in the model V^2 plots given in Fig. 5.11a, which only indicate momentary breaches that are indistinguishable from the false alarm behaviour before the faults occurred at sample 900. Additionally, $\tilde{V}^2_{fault} < 29.87$ for all three fault sizes. The practical system only shows a clear detection of a 30% leak, illustrated in Fig. 5.11b, with minimal detection delay. Both systems have false alarm events. However, the model's false alarms appear to be more distinct, as expected from the *score space coverage* explanation given in Section 5.3.1.



(a) Model V^2 detection plot

(b) Practical V^2 detection plot

(c) Model contribution plot

(d) Practical contribution plot

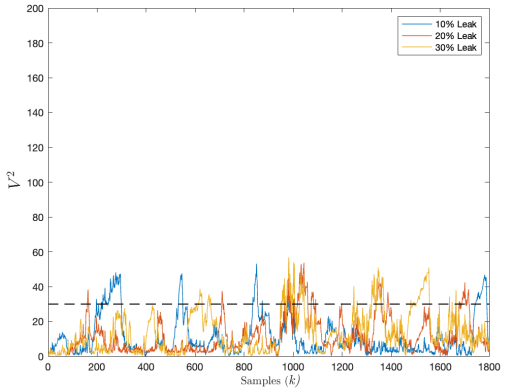
Figure 5.11: Plots of FDI results of all leaks in PU1 at sample 900 for the model and practical process

The contribution plots for these faults are provided in Fig. 5.11c and 5.11d. With no clear detection, the contribution of the PVs at each fault level remains fairly constant in the model results, except for F_1. The highest contribution of F_1, understandably, remains low relative to previously observed contribution values linked to successful detections. The practical system displays the same outcome, but has a higher F_1 contribution relative to other PVs at 30% fault size and compared to its model counterpart, which supports the successful detection of this fault in Fig. 5.11b. The fault signatures for these faults are captured in Table C.5 and C.6.

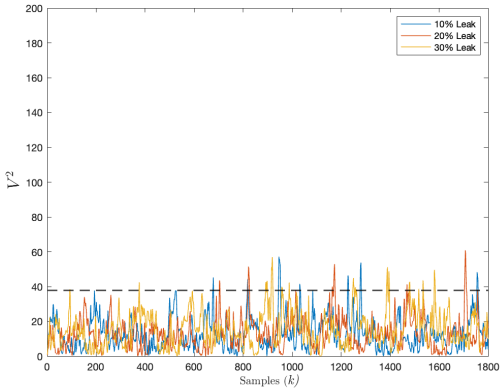
Figure 5.12 shows the results of leak detection and identification in PU2. Inspection of

the V^2 plot in Fig. 5.12a and 5.12b reveal that neither system was able to detect any leak, since $\tilde{V}^2_{fault}$ of the plots were not higher than their thresholds. Even though the model and practical system do show an increase in spikes after fault occurrence, this behaviour cannot be distinguished from the false alarm behaviour. The contribution values for both systems unsurprisingly show minimal change across fault sizes, apart from F_2 at 30% fault size. The contribution value of F_2, however, remains relatively low. Tables C.7 and C.8 in Appendix C contains the fault signatures.

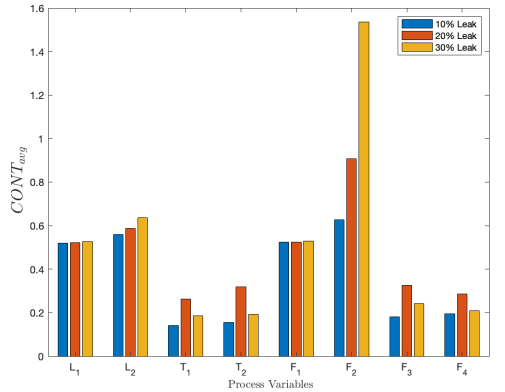
For the leakage fault type, it is concluded that only the 30% leak in PU1 is detectable as shown by the practical system. The model was unable to predict this detection, owing to the discrepancy explanations provided in Section 5.3.1, but was still able to support the conclusion of F_1 being the highest contributor to the fault. With only the 30% leak in PU1 detectable, it is the only leak that is isolable in location and size.



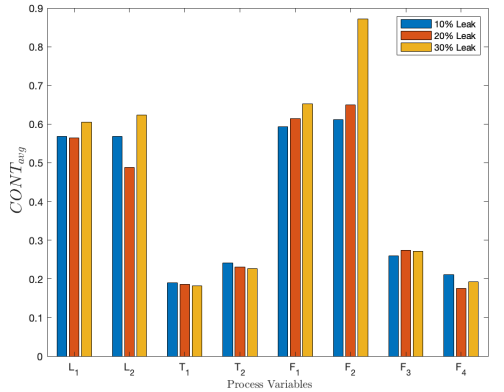
(a) Model V^2 detection plot



(b) Practical V^2 detection plot



(c) Model contribution plot

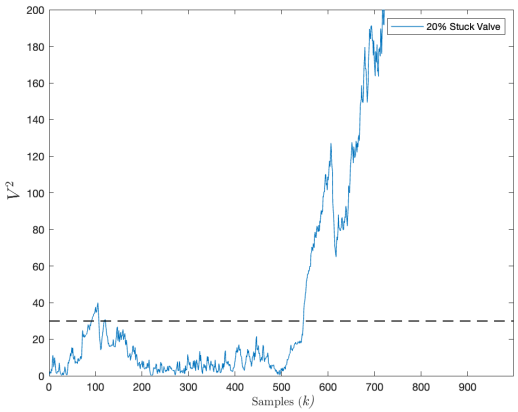


(d) Practical contribution plot

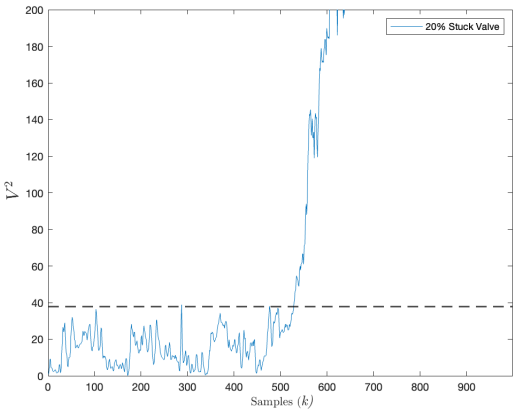
Figure 5.12: Plots of FDI results of all leaks in PU2 at sample 900 for the model and practical process

5.3.3 Fault 3: Stuck valve

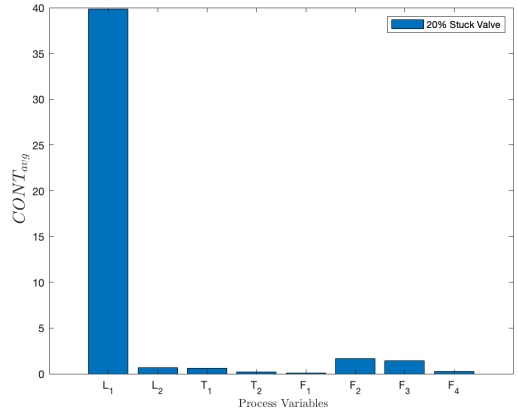
The stuck valve fault in PU1 is detected in the model (Fig. 5.13a) and in the practical system (Fig. 5.13b) when it occurred at sample 500. The model and practical V^2 plots show a clear threshold breach after minimal delay. Only the model exhibits a false alarm event, occurring at sample 100. When considering the contribution plots in the presence of the fault given provided in Fig. 5.13c and 5.13d, it is clear that L_1 is the highest contributor. Regarding the process result in Fig. A.14, this result is true and correct. The constructed fault signatures are given in Table C.9 and C.10.



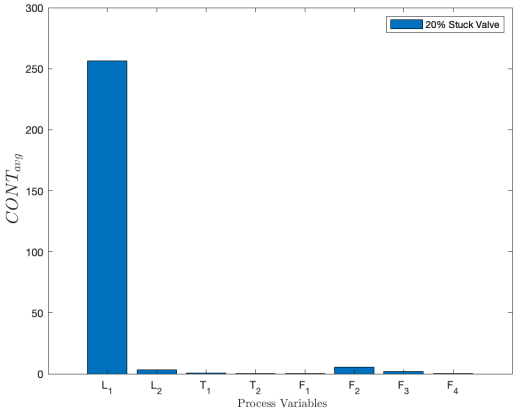
(a) Model V^2 detection plot



(b) Practical V^2 detection plot



(c) Model contribution plot

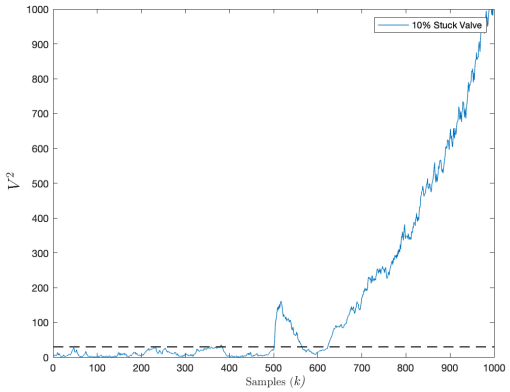


(d) Practical contribution plot

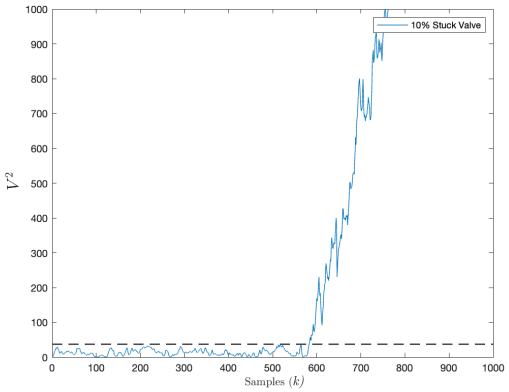
Figure 5.13: Plots of FDI results of a stuck valve in PU1 at sample 500 for the model and practical process

Figure 5.14 shows how the stuck valve fault in PU2 is detected and identified when the

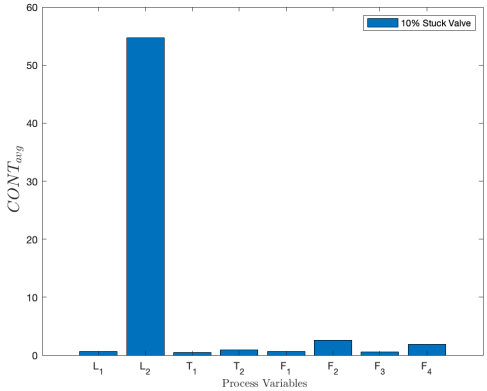
fault occurred at sample 500. Both systems show no false alarm behaviour. It is observed that the V^2 detection plot of the model (Fig. 5.14a) shows dissimilar behaviour than that of the practical system (5.14b) and needs to be clarified.



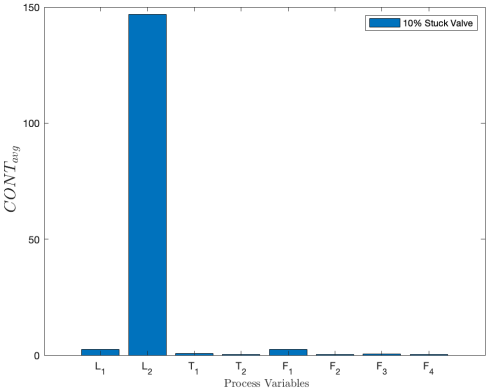
(a) Model V^2 detection plot



(b) Practical V^2 detection plot



(c) Model contribution plot



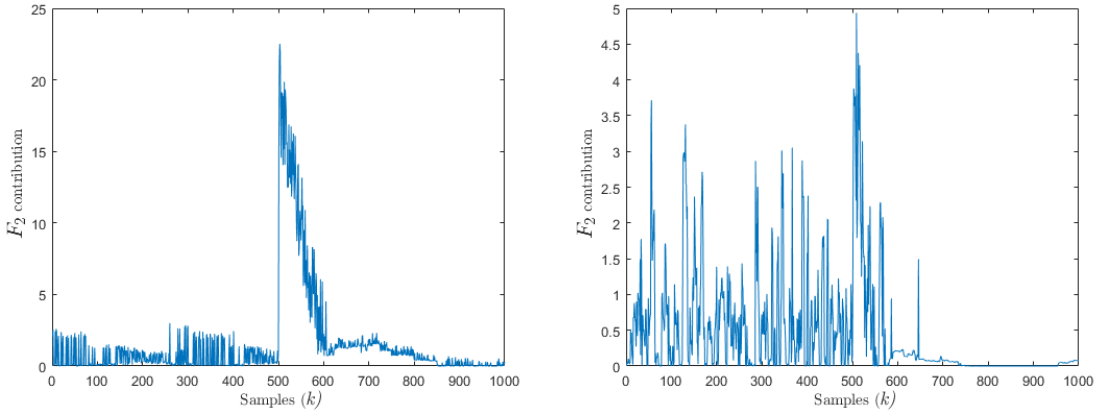
(d) Practical contribution plot

Figure 5.14: Plots of FDI results of a stuck valve in PU2 at sample 500 for the model and practical process

The model plot shows a significant 'bump' at sample 500 that is not present in the practical result. Both plots, however, display a steep increase from sample 600 onward. It is important to understand this occurrence, to determine the correct detection delay. The process results, combined with the PV contribution per sample were analysed to find the root cause of this dissimilarity. In the process results (Fig. A.15), the sequence of events is as follows. First, the valve (controlling F_2) freezes at a 10% open position at sample 500. Soon after, the level maintained by F_2 (L_2) starts to decline. Analysis of the sample-by-sample contributions showed how L_2 is responsible for the steep increase at sample 600 in Fig. 5.14a and 5.14b. Figure 5.15 shows the sample-by-sample contribution of F_2 for

both systems. The same 'bump' is observed for the model contribution in Fig. 5.15a and is absent in Fig. 5.15b, which proves that the model's F_2 response to the fault causes this anomaly. Further analysis showed that the root cause of this discrepancy is unmodelled valve behaviour and is particularly visible in this instance, due to the inherent low flow volume of F_2 (as discussed in Section 3.4.6). Therefore, the correct detection delay is 124 samples in the case of the model and 83 samples for the practical system.

The fault identification results are provided in Fig. 5.14c and 5.14d. The model and practical results show that L_2 is the main contributor to this fault. This correctly correlates with the process observation in Fig. A.15.



(a) Model F_2 contribution plot

(b) Practical F_2 contribution plot

Figure 5.15: Model and practical contribution plots of F_2 for the PU2 stuck valve fault

It is concluded that isolation of the stuck valve fault location within the heated two-tank process is possible since the highest contributors of PU1 and PU2 differ. The fault isolation results are given in Table C.11 and C.12.

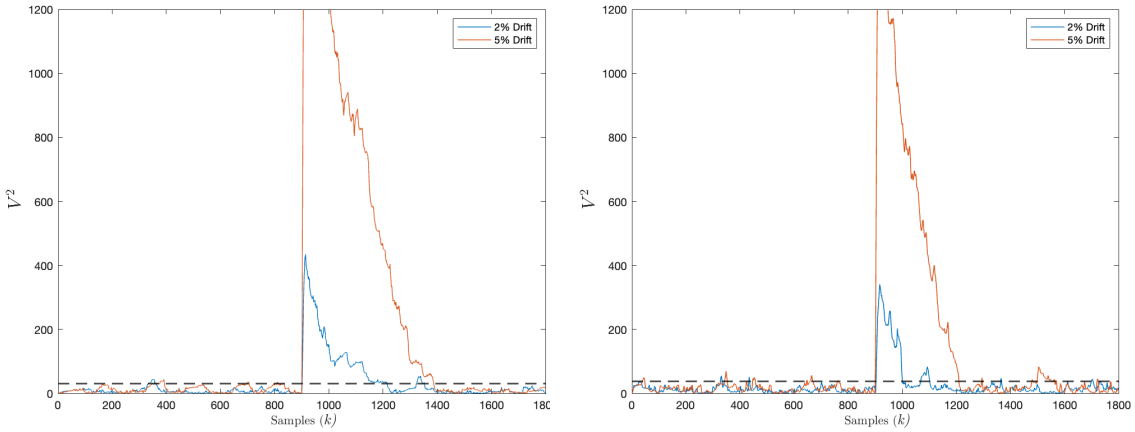
5.3.4 Fault 4: Sensor drift

The detection and identification results of the 2% and 5% sensor drift faults in PU1 are provided in Fig. 5.16. Both systems show how a larger sensor drift fault leads to a greater process upset and by extension, a more prominent V^2 plot.

It should be noted that while the plots breach their thresholds, all detection plots return to a fault-free state after some time. This phenomenon may be attributed to the temperature controller's response to lower the T_1 to normal range, by lowering hot water flow F_3. Even though F_3 is lower throughout the fault state, its deviation from the fault-free state is not

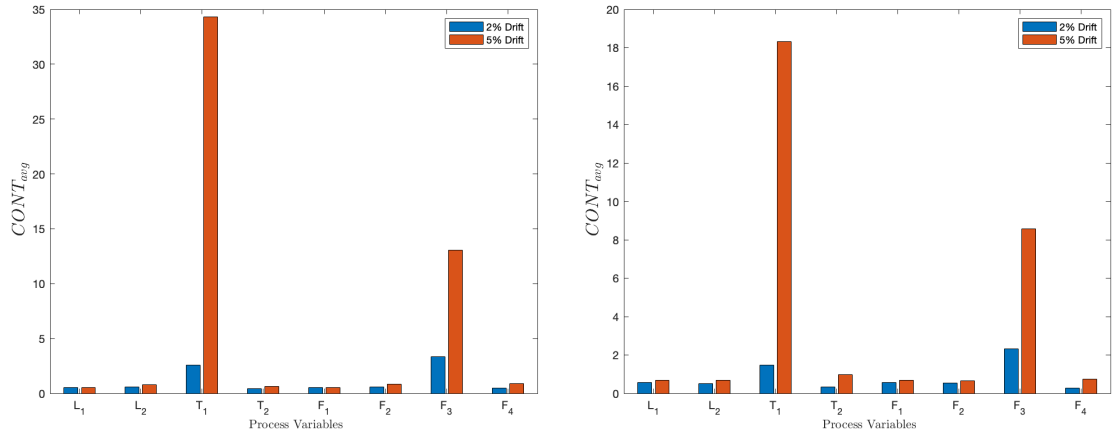
sufficient to maintain the fault detection condition. The model's 2% and 5% drift have a $\tilde{V}^2_{fault}$ that is greater than its threshold and may be regarded as successful detections. Only the 5% drift of the practical process may be regarded as a detection, since the 2% drift's $\tilde{V}^2_{fault} = 36.9$, which is less than its threshold. Regardless, the fault response is nearly instantaneous and minimal false alarms are observed before the fault.

Figure 5.16c and 5.16d show how the previously referenced PVs, namely T_1 and F_3, are indicated to be the highest contributors to the fault. This is true for the 2% and 5% fault size but is understandably more distinctive with reference to other PVs at 5% fault size. Tables C.13 and C.14 provide the fault signatures.



(a) Model V^2 detection plot

(b) Practical V^2 detection plot

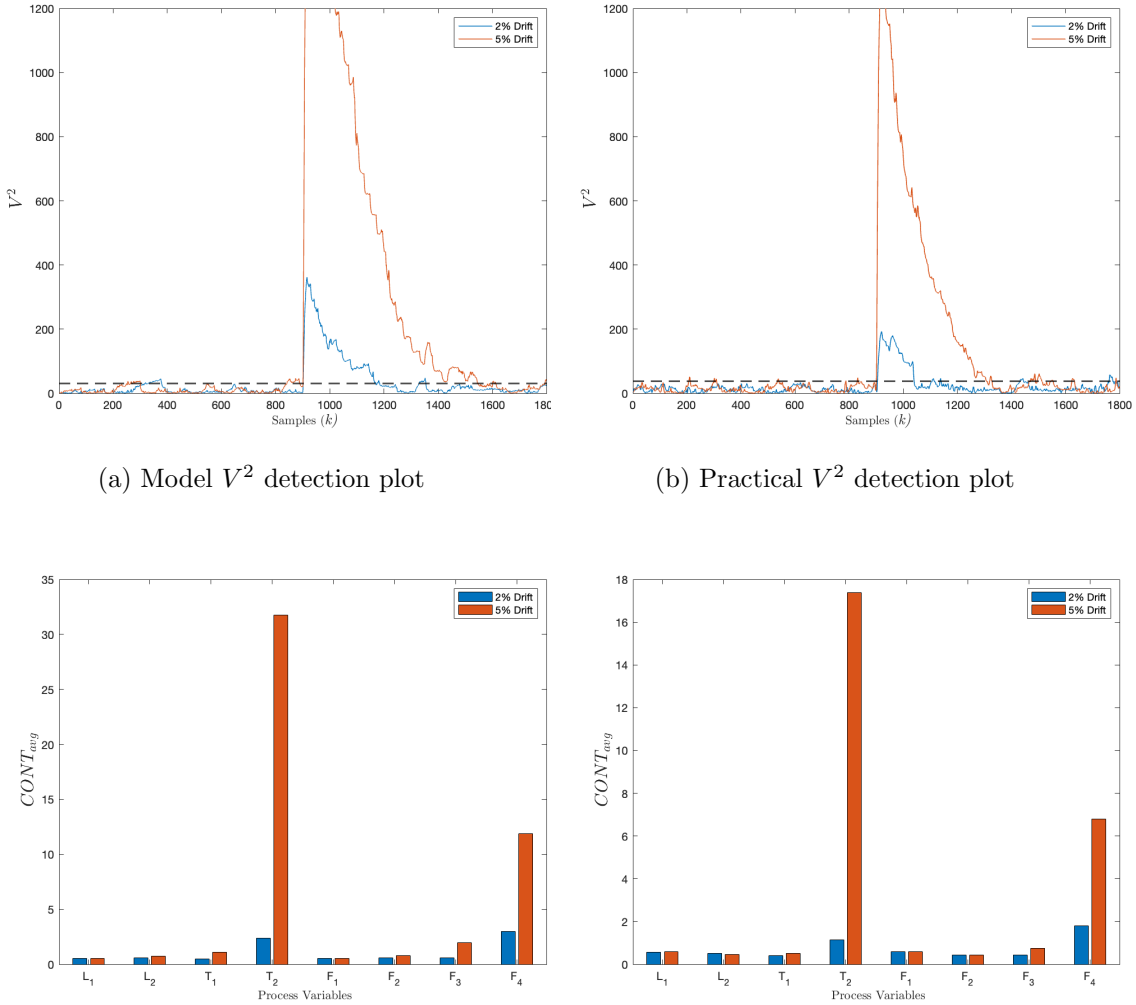


(c) Model contribution plot

(d) Practical contribution plot

Figure 5.16: Plots of FDI results of sensor drifts in PU1 at sample 900 for the model and practical process

The 2% and 5% sensor fault response in PU2 are illustrated in Fig. 5.17a and 5.17b, respectively. Similar to the detection results of the faults in PU1, the response is almost immediate, but eventually returns to a normal state even though the fault persists. Both systems indicate false alarm events, with those of the model being more prominent. While both model faults have a sufficient $\tilde{V}^2_{fault}$, only the 5% practical drift qualifies as a detection. The contribution plots in Fig. 5.17c and 5.17d illustrate how T_2 and F_4 are top contributors. Once more, the higher fault size is more prominent.



(a) Model V^2 detection plot

(b) Practical V^2 detection plot

(c) Model contribution plot

(d) Practical contribution plot

Figure 5.17: Plots of FDI results of sensor drifts in PU2 at sample 900 for the model and practical process

For the sensor drift fault, it is concluded that only the 5% drift is practically detectable by PCA according to the rule set out in (5.25). The faults are isolable in size by displaying higher contributions at 5% than at 2%. The sensor drifts are also isolable in location since

each PU involves a different combination of the highest contributing PVs. These fault signatures are given in Tables C.15 and C.16.

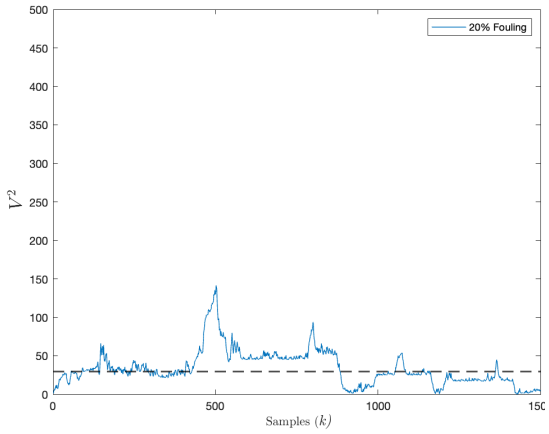
5.3.5 Fault 5: Fouling

Figure 5.18 illustrates the PU1 fouling results for detection and identification. Since the entire dataset contains fouling data, then ideally, the entire V^2 plot should be above the threshold. This is not the case in the model result, nor the practical result. The model V^2 plot in Fig. 5.18a does show detection, albeit with low confidence since approximately 50% of the samples are observed to be in a fault condition. It is found that its $\tilde{V}^2_{fault} = 33.7$, which is greater than the threshold, thus qualifying as a detection. The practical result in Fig. 5.18b displays momentary threshold breaches. However, its $V^2_{fault} = 24.66$. This is lower than the practical threshold and for this reason, the fault is not detectable in practice.

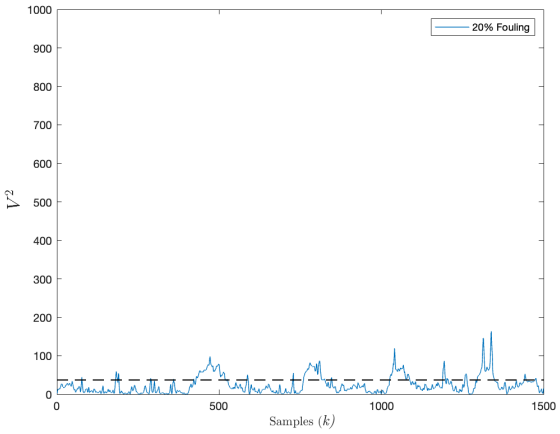
The contribution plots in Fig. 5.18c and 5.18d support the detection results by displaying low contribution values overall. The model result correctly shows that F_3 is affected by the fouling, while the practical contribution plot in Fig. 5.18d does not display the same outcome. Tables C.17 and C.18 show the fault signature result.

When fouling is applied in PU2, it is apparent in Fig. 5.19a and 5.19b that the fault is not detected in the model, nor the practical system. Unlike the results of PU1, the detection plots show little to no threshold violations. The contribution plots in Fig. 5.19c and 5.19d also show that the main PV influenced by the fault, F_4, does not exhibit a high fault contribution in either system. Regardless, the PU2 fouling fault signatures are provided in Tables C.19 and C.20.

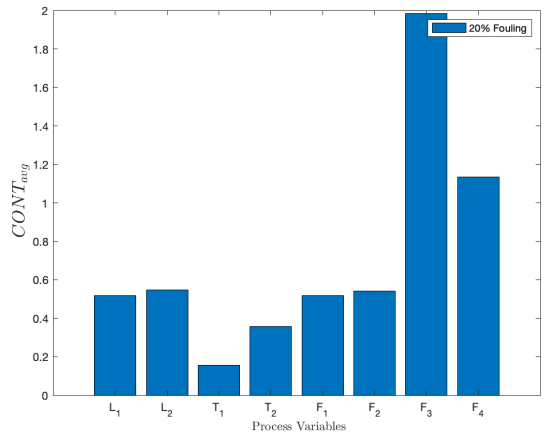
Overall, it is concluded that fouling in PU1 is not practically detectable. The PU2 fault is also not detectable, as shown by both the model and the practical system. Practically, neither of these faults are identifiable and by extension, not isolable.



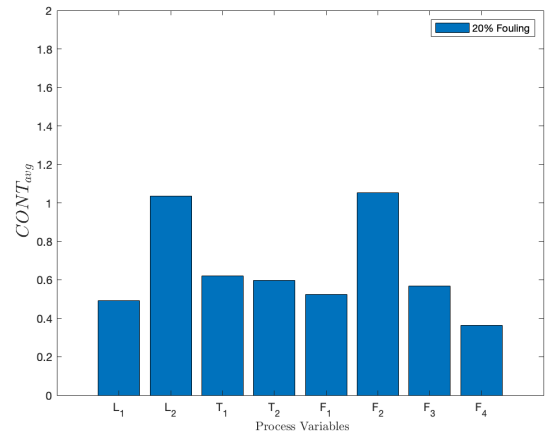
(a) Model V^2 detection plot



(b) Practical V^2 detection plot

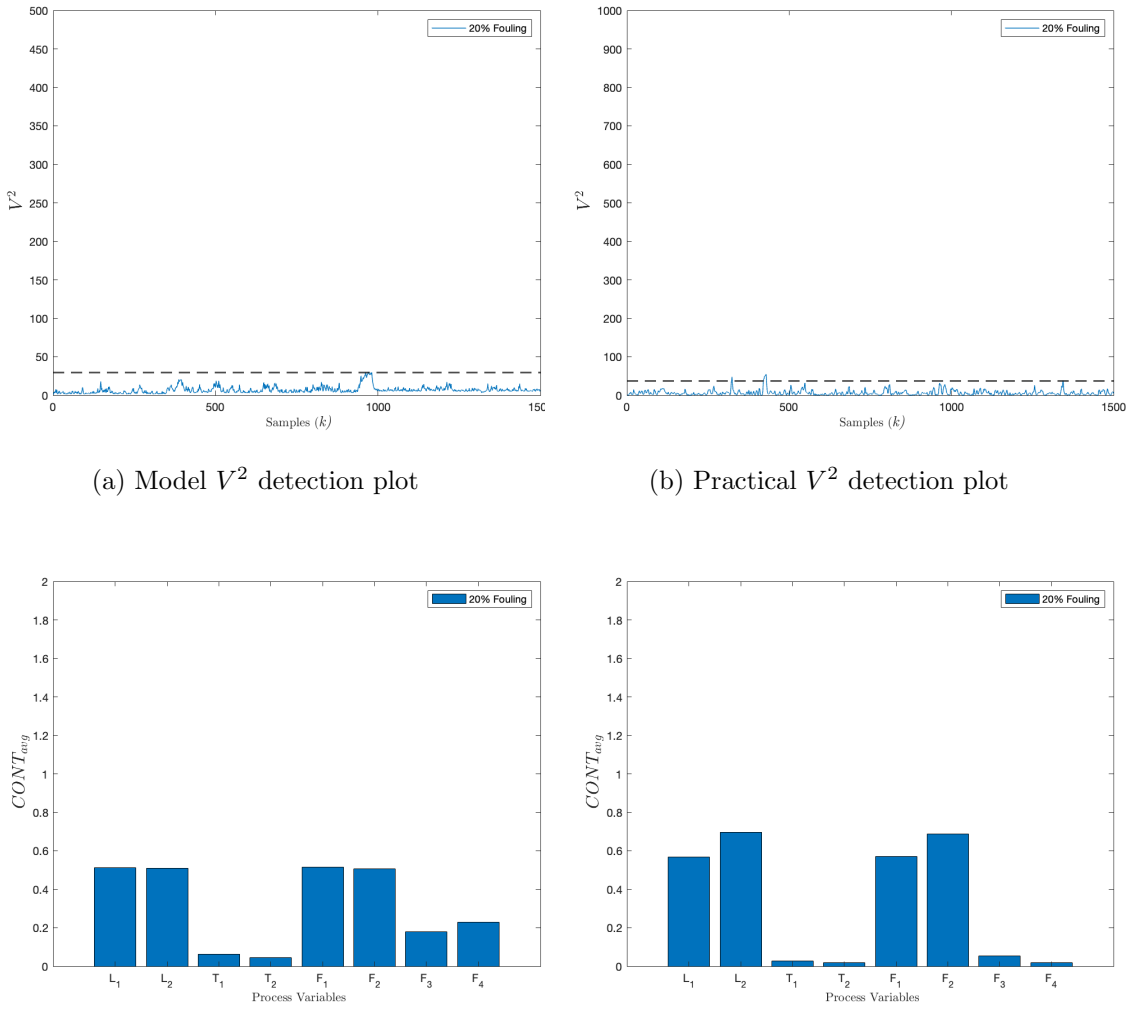


(c) Model contribution plot



(d) Practical contribution plot

Figure 5.18: Plots of FDI results of fouling in PU1 for the model and practical process



(a) Model V^2 detection plot

(b) Practical V^2 detection plot

(c) Model contribution plot

(d) Practical contribution plot

Figure 5.19: Plots of FDI results of fouling in PU2 for the model and practical process

5.4 Conclusion

The data-driven PCA approach for FDI was explained and applied in this chapter. Its theoretical foundation was discussed and verified using the Simulink® model in Section 5.2. The MEWMA method was utilised, such that the detection results of this chapter are more comparable to the EWMA detections of the EGBV approach from Chapter 4. Validation was achieved when the model and practical systems showed similar detection, identification and isolation results in Section 5.3. The discrepancies between the model and practical results were explained throughout the latter section.

It was found that twelve out of the twenty faults were detectable in the model, while only nine were detectable in the practical process. The fault that was missed by the model but is detectable in the practical system is the 30% leak in PU1. This discrepancy may be contributed to the unmodelled characteristics of the heated two-tank process. Additionally, with the model having a greater score space coverage, it showed more sensitive behaviour overall, which in turn leads to more detections, especially when enforcing the detection philosophy defined in Section 5.2.5.

With regard to identification and isolation, it is found that the stuck valve and sensor drift faults are isolable in type, size and location with high confidence, due to their unique combinations of high contributing PVs. The clogging faults exhibit fault signatures that are less distinctive, with overlapping high-contributors between PU1 and PU2. The single detected leakage fault is isolable in location and size, but with low confidence. The fouling faults were shown to be practically non-isolable.

In the following chapter, detailed comparisons are made between these results and those of energy-based visualisation, based on key FDI benchmarks.

CHAPTER

6

EGBV & PCA COMPARISON

The EGBV FDI method of Chapter 4 and the PCA FDI approach of Chapter 5 are compared in this chapter. The detection and isolation abilities are evaluated using established performance metrics. Additional comparisons are made according to Venkatasubramanian's [5] ideal FDI attributes. The chapter is concluded with a comparison summary and insights.

6.1 Introduction

Throughout this work, FDI performance metrics have been briefly named and discussed. In Section 2.3, a summary was provided of the key performance requirements of FDI methods as observed within the surveyed studies. Three requirements, in particular, were found to be key performance metrics for fault detection, namely robustness, sensitivity and promptness. In Chapters 4 and 5, brief insights into the FDI results concerning the latter metrics were given.

Additionally, fault isolation was applied for both methods. The author made superficial conclusions regarding the isolability of the tested faults. It was noted that the *degree* of isolation should be considered, as this would provide clarity on how well each FDI method can isolate faults.

This chapter aims to provide a detailed comparison between the EGBV and PCA FDI methods and is divided into two main sections, namely fault detection comparison and fault isolation comparison. The fault detection comparison section will provide an analysis of each method's performance for each metric. Subsequently, the fault isolation comparison section will analyse how unique each method's fault signatures are. Throughout the chapter, the model and practical results are considered simultaneously, to ensure that final comparisons and conclusions may be made with confidence. For convenience and ease of comparison, this chapter will numerically refer to each tested fault as designated in Table 6.1.

Table 6.1: Numeric designations for process faults

Fault ID	Fault description
$\mathcal{F}_1$	10% clog in PU1
$\mathcal{F}_2$	20% clog in PU1
$\mathcal{F}_3$	30% clog in PU1
$\mathcal{F}_4$	10% clog in PU2
$\mathcal{F}_5$	20% clog in PU2
$\mathcal{F}_6$	30% clog in PU2
$\mathcal{F}_7$	10% leakage in PU1
$\mathcal{F}_8$	20% leakage in PU1
$\mathcal{F}_9$	30% leakage in PU1
$\mathcal{F}_{10}$	10% leakage in PU2
$\mathcal{F}_{11}$	20% leakage in PU2
$\mathcal{F}_{12}$	30% leakage in PU2
$\mathcal{F}_{13}$	Stuck valve in PU1
$\mathcal{F}_{14}$	Stuck valve in PU2
$\mathcal{F}_{15}$	2% sensor drift in PU1
$\mathcal{F}_{16}$	5% sensor drift in PU1
$\mathcal{F}_{17}$	2% sensor drift in PU2
$\mathcal{F}_{18}$	5% sensor drift in PU2
$\mathcal{F}_{19}$	20% Fouling in PU1
$\mathcal{F}_{20}$	20% Fouling in PU2

Before providing detailed results, it is appropriate to summarise the configuration choices made for EGBV and PCA, such that a fair comparison is possible.

1. **Detection plot filtering** - Both FDI methods were enhanced using the same filtering technique, namely exponentially weighted moving average (EWMA) for improved detection performance and plot smoothing. Recall from Section 4.4.2 that each SVD element of the EGBV technique was filtered to remove noisy behaviour. This was

done using the EWMA method. For the sake of fair comparison, PCA must then also be enhanced by this method. Since PCA is a multivariate FDI technique, the multivariate version of EWMA (MEWMA), was applied to PCA for this purpose.

2. **EWMA/MEWMA filtering constant** - The same smoothing constant was selected for both systems ($r = 0.2$).

3. **Adjusted threshold** - The detection thresholds for both methods were calibrated to achieve a 5% FAR on the same reference NOC dataset. This will ensure that all detection-related performance metrics are fairly compared.

6.2 Fault detection comparison

6.2.1 Robustness

First, the robustness of each FDI method is evaluated. As explained in Chapter 2, an FDI system's robustness is a measure of its capability to reject false alarms, thus having a low false alarm rate (FAR) is ideal [6, 16]. To evaluate the methods' performance in this regard, the FAR is calculated for each fault-free operation period preceding the process fault. For example, consider the 30% clogging fault in PU1. The dataset contains 1800 samples, with the fault state occurring from sample 900 to 1800 (Fig. A.4). In this dataset, samples 1 to 900 contain NOC data and will thus be considered for FAR calculation. This is done for each fault experiment so that the FAR may be calculated for every fault experiment dataset that is initiated with NOC state, namely $\mathcal{F}_1$ to $\mathcal{F}_{18}$. Faults $\mathcal{F}_{19}$ and $\mathcal{F}_{20}$ consist entirely of faulty data and are therefore not considered for the FAR metric.

The FAR for EGBV is calculated using the formula:

$$\text{FAR} = \frac{\text{Number of samples in violation}}{\text{Number of samples in NOC}} \times 100\% \tag{6.1}$$

and tabulated in Table 6.2. The table shows the results for the model, as well as the practical system regarding the minimum (FAR_{min}), the average (FAR_{avg}) and maximum (FAR_{max}) false alarm rates. Recall that the EGBV FDI technique consists of thirty SVD elements that are individually monitored to detect a process fault. The FAR_{avg} columns show the average of the thirty SVD elements' FAR for $\mathcal{F}_1$ to $\mathcal{F}_{18}$. The FAR_{min} column shows the lowest FAR achieved by a single SVD element. Likewise, FAR_{max} is the highest FAR of a single element.

From Table 6.2 it is clear that the model and practical systems performed similarly. A noticeable increase in all FAR metrics is visible for $\mathcal{F}_1$ to $\mathcal{F}_6$ when compared to their

respective reference NOC results. This increase is ascribed to the heated two-tank process's non-optimal valve configuration, which is particularly visible within the clogging fault datasets (explained in Chapter 3). However, $\mathcal{F}_7$ to $\mathcal{F}_{18}$ show results that are approximate to that of the reference NOC and were not influenced by this issue.

Table 6.2: False alarm rates for EGBV [%]

	Model			Practical		
Fault number	FAR_{min}	FAR_{avg}	FAR_{max}	FAR_{min}	FAR_{avg}	FAR_{max}
Reference NOC	5.1	5.14	5.3	5.1	5.17	6.0
$\mathcal{F}_1$	3.2	25.0	70.7	3.3	20.9	68.8
$\mathcal{F}_2$	6.0	31.9	77.3	3.9	23.3	76.0
$\mathcal{F}_3$	2.6	44.0	89.0	9.2	30.6	87.1
$\mathcal{F}_4$	11.4	40.3	88.8	8.2	33.3	92.6
$\mathcal{F}_5$	13.3	55.7	95.1	6.2	37.1	97.4
$\mathcal{F}_6$	9.2	47.8	92.7	11.0	34.4	96.6
$\mathcal{F}_7$	0.2	5.8	30.3	0.0	5.2	30.0
$\mathcal{F}_8$	0.1	6.8	23.2	0.4	4.6	23.1
$\mathcal{F}_9$	1.7	7.2	36.3	0.9	8.1	28.1
$\mathcal{F}_{10}$	1.4	7.8	17.7	0.0	9.0	27.0
$\mathcal{F}_{11}$	0.2	6.0	48.2	0.0	7.7	26.8
$\mathcal{F}_{12}$	2.7	6.0	23.8	1.0	8.5	25.0
$\mathcal{F}_{13}$	0.0	5.0	14.8	0.8	9.0	34.3
$\mathcal{F}_{14}$	0.2	4.3	9.6	0.6	6.3	18.4
$\mathcal{F}_{15}$	0.4	5.8	19.7	0.8	6.0	26.2
$\mathcal{F}_{16}$	3.2	6.9	10.2	5.1	5.2	6.1
$\mathcal{F}_{17}$	1.1	6.2	30.0	0.1	7.5	24.2
$\mathcal{F}_{18}$	1.1	6.6	18.1	0.2	7.8	32.9

Table 6.3 shows the FAR results of the PCA method. Having only one detection plot, a single FAR value is calculated for each fault test. The reference NOC FAR values show the 5% FAR calibration result. It is observed that most model FAR values are close to their practical counterparts, while some differ substantially, especially for $\mathcal{F}_1$ to $\mathcal{F}_6$. This discrepancy stems from the variance coverage difference between the model and the practical system. With the model covering a wider variance space (86.4%) than the practical system (74%), it will also include more process noise, leading to the model having higher FAR values in some cases. As was found in Table 6.2, faults $\mathcal{F}_1$ to $\mathcal{F}_6$ show higher FAR values than the other datasets.

For a visual comparison of the FAR performance of the methods, consider Fig. 6.1. The figure shows a comparison between the FDI methods for the model in Fig. 6.1a, as well

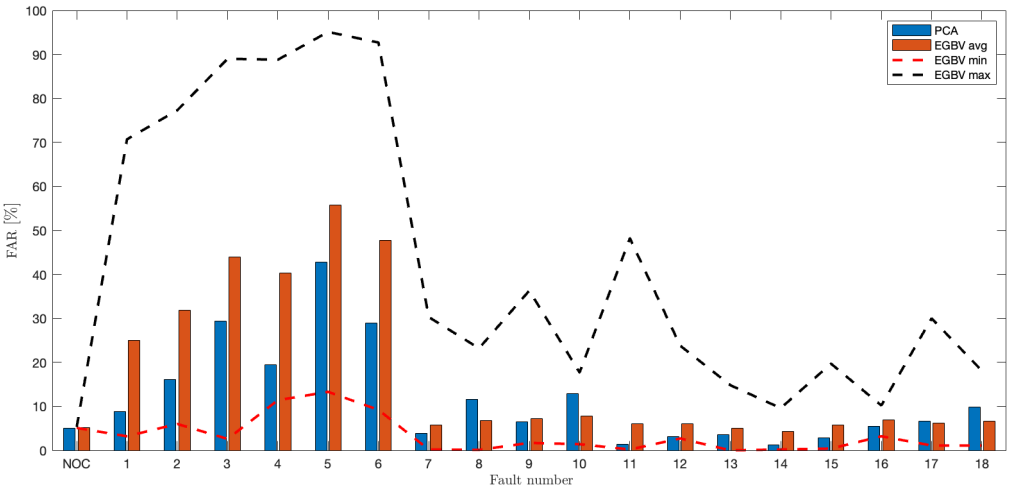
Table 6.3: False alarm rates for PCA [%]

Fault number	Model FAR	Practical FAR
Reference NOC	5.01	5.01
$\mathcal{F}_1$	8.88	2.44
$\mathcal{F}_2$	16.11	0.11
$\mathcal{F}_3$	29.44	4.67
$\mathcal{F}_4$	19.48	6.86
$\mathcal{F}_5$	42.79	6.30
$\mathcal{F}_6$	28.94	6.17
$\mathcal{F}_7$	3.89	0.33
$\mathcal{F}_8$	11.56	0.11
$\mathcal{F}_9$	6.44	1.00
$\mathcal{F}_{10}$	12.89	0.78
$\mathcal{F}_{11}$	1.33	1.00
$\mathcal{F}_{12}$	3.11	1.00
$\mathcal{F}_{13}$	3.60	0.40
$\mathcal{F}_{14}$	1.20	0.00
$\mathcal{F}_{15}$	2.89	1.11
$\mathcal{F}_{16}$	5.44	5.00
$\mathcal{F}_{17}$	6.56	0.00
$\mathcal{F}_{18}$	9.77	2.44

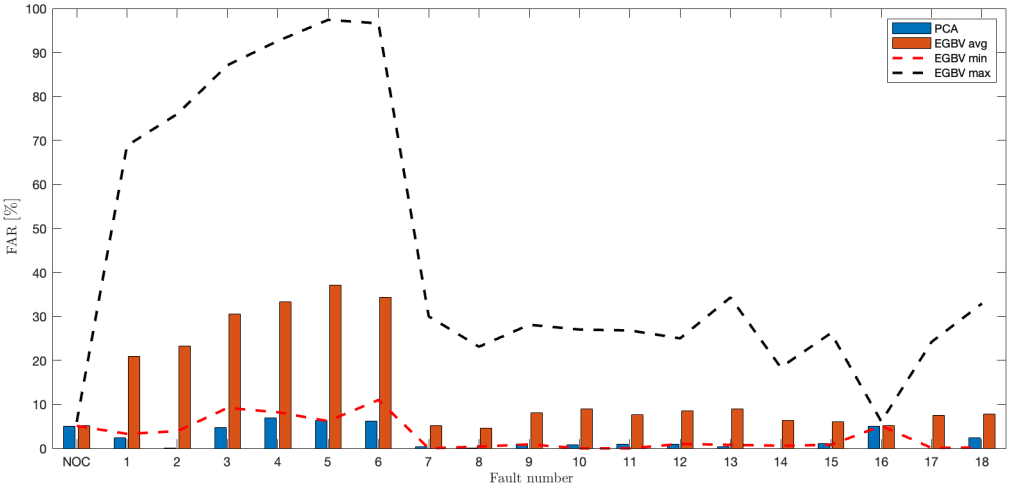
as for the practical results in Fig. 6.1b. The blue bars show the FAR results from Table 6.3 and the orange bars the results from Table 6.2. The red and black striped lines show the minimum and maximum FAR achieved by a single SVD element respectively within EGBV. In Fig. 6.1a, mixed results are observed for the bar plots. However, in most cases, it is shown that PCA exhibited a lower FAR. The FAR_{max} results of EGBV are consistently higher than the PCA result, while the FAR_{min} values are lower or match the PCA performance. The practical FAR results in Fig. 6.1b show a clear difference in FAR performance between the two methods, indicating that in practice, PCA had fewer false alarm events.

Based on the results given in Tables 6.2 and 6.3, as well as Fig. 6.1, it is concluded that PCA is more robust than EGBV. The two FDI methods appear to follow the same trend in the model and practice (as seen in Fig. 6.1b), meaning both FDI systems respond similarly to changes occurring in the normal process state, yet the PCA plot features consistently lower FAR values. The author argues that this improved FAR performance stems from the dimension reduction of PCA. Recall from Section 5.2.3, that only the principal components that are descriptive of true process variation were retained, that is,

the principal components corresponding to the highest eigenvalues. EGBV does not have an equivalent procedure wherein process noise is eliminated - process noise introduced in the energy-exergy graph will persist in the SVD element plots. As a result, the EGBV detection system will exhibit more false alarms.



(a) Model FAR comparison (lower is better)



(b) Practical FAR comparison (lower is better)

Figure 6.1: False alarm rate comparison plots of PCA and EGBV

Furthermore, a fundamental disadvantage of EGBV with regard to FAR performance is the monitoring of several SVD elements (or detection plots). With each element having its own false alarms, it is likely that in practice, the monitoring system will suffer from false alarm flooding, should its thresholds be too sensitive or when applied to an unoptimized process. To avoid alarm flooding, all SVD elements' thresholds may be set to be overly robust, but this will limit the FDI method's ability to detect small faults. If the thresholds of the

elements are set to be sensitive to small faults, the process will require perfect optimization to avoid alarm flooding, which is not feasible. Additionally, the false alarm problem will be worse for larger processes, as larger processes will have more SVD elements that require monitoring. The author, therefore, recommends that a single detection parameter method be developed as part of a future study.

6.2.2 Sensitivity

To compare and evaluate the FDI methods' sensitivity, the true alarm rate (TAR) [112] is calculated for each fault that was tested. Sensitivity may also be evaluated through missed detection rate (MDR) [6], but the TAR metric will be used in this study. A higher TAR is better and calculated by:

$$\text{TAR} = \frac{\text{Number of samples in violation}}{\text{Number of samples in fault state}} \times 100\%. \tag{6.2}$$

First, the TAR values of the EGBV technique are discussed. The results in Table 6.4, show the minimum, average and maximum achieved TAR. It should be noted that the TAR values of *all* faults are given, with the non-detected faults from Chapter 4 shown in red. As expected, these faults show lower TAR values overall. In most cases, the TAR_{max} of the model is above 90%. Similarly, the practical system's TAR_{max} is mostly above 80%. The TAR_{avg} shows a wider range of results, since some faults lead to a significant amount of SVD element detections which causes a higher TAR_{avg}, while other faults cause a limited amount and as a result, a lower TAR_{avg}. When the definition of Section 4.4.4 is strictly followed for fault detection, which states that *any* SVD element in violation during the fault period may be regarded as a detection, then the TAR_{max} metric is of most significance here. Effectively, this a univariate TAR consideration. However, it is also valid to consider the TAR_{avg} as important, which is a single value representing the collective result and perhaps more appropriate to use in a comparison with the multivariate PCA method.

Interestingly, the magnitude of process influence of every fault can be seen in Table 6.4. For example, it is observed that the PU1 clogs ($\mathcal{F}_1$ to $\mathcal{F}_3$), have a TAR_{avg} ranging from 36.0% to 60.4% in the model. The PU2 clogs range from 62.8% to 75.5%, which suggests that clogs in PU2 are more disruptive to this particular process than clogs in PU1. The leakages ($\mathcal{F}_7$ to $\mathcal{F}_{12}$) are shown to have minor disruption, except for $\mathcal{F}_8$ and $\mathcal{F}_9$. The stuck valves ($\mathcal{F}_{13}$ to $\mathcal{F}_{14}$) are shown to be of significant disruption and the 5% sensor drift faults ($\mathcal{F}_{16}$ and $\mathcal{F}_{18}$) are among the highest.

Table 6.5 shows the TAR results of the PCA approach. Once more, the eight undetected faults in the model and eleven undetected faults in the practical system as observed in

Table 6.4: True alarm rates for EGBV [%]

	Model			Practical		
Fault number	TAR_{min}	TAR_{avg}	TAR_{max}	TAR_{min}	TAR_{avg}	TAR_{max}
$\mathcal{F}_1$	2.33	36.0	90.3	4.22	27.21	92.1
$\mathcal{F}_2$	1.89	55.4	99.8	5.67	36.2	98.2
$\mathcal{F}_3$	1.11	60.4	99.8	3.67	51.4	99.8
$\mathcal{F}_4$	8.50	62.8	99.8	7.00	48.9	90.7
$\mathcal{F}_5$	11.66	74.0	99.6	2.74	69.0	99.8
$\mathcal{F}_6$	12.62	75.5	99.7	7.41	72.9	99.0
$\mathcal{F}_7$	0.00	10.4	42.7	0.00	5.8	33.3
$\mathcal{F}_8$	0.00	22.4	87.4	0.22	18.4	83.3
$\mathcal{F}_9$	0.00	26.2	98.1	0.00	28.7	99.0
$\mathcal{F}_{10}$	0.89	6.2	37.6	0.56	6.3	17.9
$\mathcal{F}_{11}$	0.00	4.5	15.6	0.00	7.9	22.4
$\mathcal{F}_{12}$	0.22	5.9	31.7	0.00	9.5	28.7
$\mathcal{F}_{13}$	2.61	54.1	99.8	4.21	54.2	98.6
$\mathcal{F}_{14}$	12.20	63.0	95.8	4.20	39.7	86.4
$\mathcal{F}_{15}$	3.44	41.0	99.4	0.22	32.5	98.1
$\mathcal{F}_{16}$	3.56	68.1	99.8	1.67	65.3	99.8
$\mathcal{F}_{17}$	4.33	54.6	85.4	3.11	47.5	91.9
$\mathcal{F}_{18}$	0.22	78.8	99.9	9.33	74.5	99.8
$\mathcal{F}_{19}$	0.00	12.4	87.7	0.00	7.2	46.9
$\mathcal{F}_{20}$	0.00	3.5	19.3	0.00	16.4	92.3

Chapter 5 are shown in red. The red values clearly show the lowest TAR results.

Similar to the EGBV results, PCA performed poorly in the detection of process leaks ($\mathcal{F}_7$ to $\mathcal{F}_{12}$). Most clogging faults ($\mathcal{F}_2$ to $\mathcal{F}_6$) were well detected, which have a TAR of up to 99.30% in the model and practical system. The stuck valve faults ($\mathcal{F}_{13}$ to $\mathcal{F}_{14}$) are also easily detectable, having TAR values ranging from 83.60% to 94.19% in the practical system. The fouling faults ($\mathcal{F}_{19}$ to $\mathcal{F}_{20}$) have lower TAR results - $\mathcal{F}_{20}$ in particular.

To compare the TAR performance, the model and practical results are plotted in Fig. 6.2. The blue bars represent the TAR result of the PCA method, while the orange bars display the TAR_{avg} of the EGBV approach. The red and black striped lines additionally indicate the minimum and maximum logged TAR results of EGBV, respectively. For $\mathcal{F}_1$ to $\mathcal{F}_6$, PCA generally shows higher TAR values compared to the EGBV average, particularly at higher fault magnitudes. In the PU1 leak tests ($\mathcal{F}_7$ to $\mathcal{F}_9$), the model differs from the practical results in that the model displays better EGBV performance, while in practice

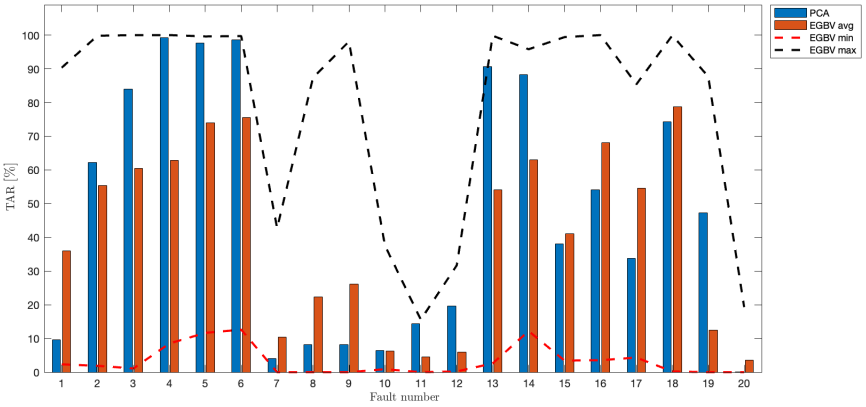
Table 6.5: True alarm rates [%] for PCA

Fault number	Model TAR	Practical TAR
$\mathcal{F}_1$	9.56	7.56
$\mathcal{F}_2$	62.22	16.78
$\mathcal{F}_3$	84.00	64.78
$\mathcal{F}_4$	99.30	93.00
$\mathcal{F}_5$	97.67	98.49
$\mathcal{F}_6$	98.62	99.31
$\mathcal{F}_7$	4.11	1.00
$\mathcal{F}_8$	8.22	10.00
$\mathcal{F}_9$	8.11	57.77
$\mathcal{F}_{10}$	6.44	2.67
$\mathcal{F}_{11}$	14.33	2.22
$\mathcal{F}_{12}$	19.67	4.56
$\mathcal{F}_{13}$	90.58	94.19
$\mathcal{F}_{14}$	88.20	83.60
$\mathcal{F}_{15}$	38.11	15.89
$\mathcal{F}_{16}$	54.11	42.44
$\mathcal{F}_{17}$	33.78	19.44
$\mathcal{F}_{18}$	74.22	52.89
$\mathcal{F}_{19}$	47.33	20.80
$\mathcal{F}_{20}$	0.07	0.87

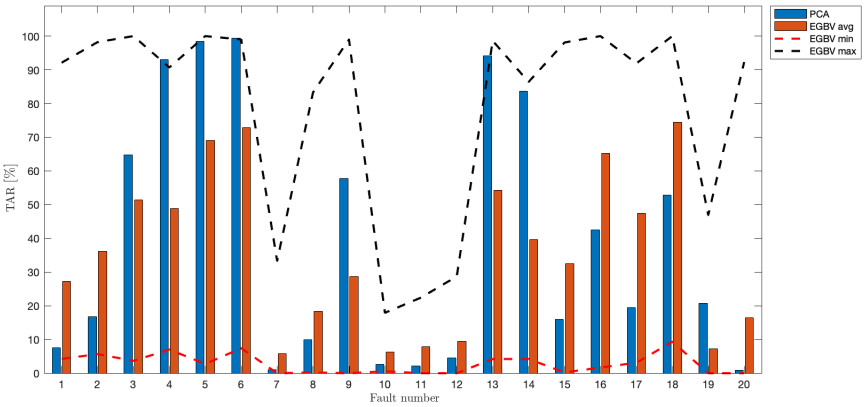
the latter is only true for 10% and 20% fault sizes. This is likely due to the PCA score space coverage difference as described in Section 5.3.1. The PU2 leaks ($\mathcal{F}_{10}$ to $\mathcal{F}_{12}$) are closely matched in practice and show that the average EGBV results have a higher TAR for these faults. The stuck valves ($\mathcal{F}_{13}$ to $\mathcal{F}_{14}$) are better detected by PCA in both systems. The sensor drifts ($\mathcal{F}_{15}$ to $\mathcal{F}_{18}$) are better detected by EGBV, since unlike PCA, EGBV's SVD elements were able to remain in fault state (Fig. B.16 to B.19). Finally, PCA was able to show superior detection results for PU1 fouling ($\mathcal{F}_{19}$), but not for PU2 fouling.

It is concluded that the more sensitive FDI approach is dependent on the chosen detection philosophy of EGBV. The results discussed in the previous paragraph mainly compared the EGBV TAR_{avg} results to the TAR of PCA. This comparison is valid if the EGBV elements are regarded as a collective detection system, hereby using the TAR_{avg} as a multivariate summary of EGBV. In this case, the more sensitive FDI method is fault dependent. PCA shows better detection results for the clogs and stuck valves, whereas EGBV shows superior detection performance for leaks and sensor drifts. However, if the detection philosophy defined in Section 4.4.4 is followed (a univariate view of EGBV),

then the EGBV TAR_{max} must be considered. It is clear from Fig. 6.2 that for any fault, EGBV always has an SVD element with a TAR_{max} that is higher than the PCA TAR. In this case, EGBV may be considered as the more sensitive detection method.



(a) Model TAR comparison (higher is better)



(b) Practical TAR comparison (higher is better)

Figure 6.2: True alarm rate comparison plots of PCA and EGBV

6.2.3 Promptness

The last key benchmark evaluated with regard to fault detection is promptness. Also referred to as *detection speed*, it is defined as the time lag before a fault is detected [6, 35, 112]. Naturally, a lower time lag is better. This section will use the term *detection delay* (DD) as the measure of how prompt the method is to detect faults.

In [112], a sample buffer of three samples was implemented before the fault was officially registered. For example, if a fault occurred at sample 900 and the detection plot violates the threshold at sample 920 but returns to normal at sample 922, a fault is not registered.

If the plot then violates the threshold at sample 950 and is still in fault state at sample 953, then the fault is registered with a DD of 53 samples. The buffer acts as a filter for sporadic behaviour that is not linked to the fault. Russel, Chiang and Braatz [6] employed a six-sample buffer in their work. Given the high frequency of false alarms within the tested heated two-tank process, this study will follow the six-sample buffer approach.

The DD of every fault is provided in Table 6.6 for EGBV. As was done in the previous sections, the minimum, average and maximum results are provided for the Simulink® model and practical systems. The fouling faults ($\mathcal{F}_{19}$ to $\mathcal{F}_{20}$) are not applicable for detection delay evaluation, since the entire fouling datasets are in a fault state. As the detection delay can only be determined for a successful detection, the non-detected faults are also not applicable and are marked as 'N/A'.

Table 6.6: Detection delay for EGBV [samples]

	Model			Practical		
Fault number	DD_{min}	DD_{avg}	DD_{max}	DD_{min}	DD_{avg}	DD_{max}
$\mathcal{F}_1$	6	169	900	6	191	900
$\mathcal{F}_2$	6	150	900	6	114	516
$\mathcal{F}_3$	6	86	900	6	63	180
$\mathcal{F}_4$	6	65	368	6	64	313
$\mathcal{F}_5$	6	44	132	6	68	432
$\mathcal{F}_6$	6	37	176	6	37	120
$\mathcal{F}_7$	N/A	N/A	N/A	N/A	N/A	N/A
$\mathcal{F}_8$	17	397	900	7	365	900
$\mathcal{F}_9$	22	343	900	16	380	900
$\mathcal{F}_{10}$	N/A	N/A	N/A	N/A	N/A	N/A
$\mathcal{F}_{11}$	N/A	N/A	N/A	N/A	N/A	N/A
$\mathcal{F}_{12}$	N/A	N/A	N/A	N/A	N/A	N/A
$\mathcal{F}_{13}$	6	120	498	9	58	249
$\mathcal{F}_{14}$	7	10	196	16	113	499
$\mathcal{F}_{15}$	6	53	331	6	66	900
$\mathcal{F}_{16}$	7	96	513	6	100	900
$\mathcal{F}_{17}$	6	45	539	9	41	238
$\mathcal{F}_{18}$	7	66	900	6	67	482
$\mathcal{F}_{19}$	N/A	N/A	N/A	N/A	N/A	N/A
$\mathcal{F}_{20}$	N/A	N/A	N/A	N/A	N/A	N/A

In both the model and practical system, the lowest DD_{min} is six samples. The highest DD_{max} is 900 samples, which implies that some SVD elements within EGBV remained

unresponsive to some faults. From the full set of EGBV results in Appendix B, this result is valid. Similar to the TAR_{avg} results, a wide range of DD_{avg} is observed and for the same reason - not all SVD elements respond to a given fault and as such, the DD_{avg} is dependent on the amount of SVD elements that indicated a fault state.

The detection delay results of PCA are provided in Table 6.7, with the non-detected faults from Chapter 5 marked as not applicable. Faults $\mathcal{F}_{15}$ to $\mathcal{F}_{18}$ are observed to have the shortest DD in the model. In the practical system, $\mathcal{F}_{16}$ and $\mathcal{F}_{18}$ have the shortest DD. This is expected given the sudden deviation caused by the sensor faults. The detected clogging faults ($\mathcal{F}_2$ to $\mathcal{F}_6$) have detection delays slower than that of the sensor faults. The leakage fault ($\mathcal{F}_9$) that was detected in the practical system has a DD similar to the clogging faults. The PU2 stuck valve has a slow response in the model and practical system, and may be attributed to the slow decline in tank level that eventually triggers the fault detection.

Table 6.7: Detection delay for PCA [samples]

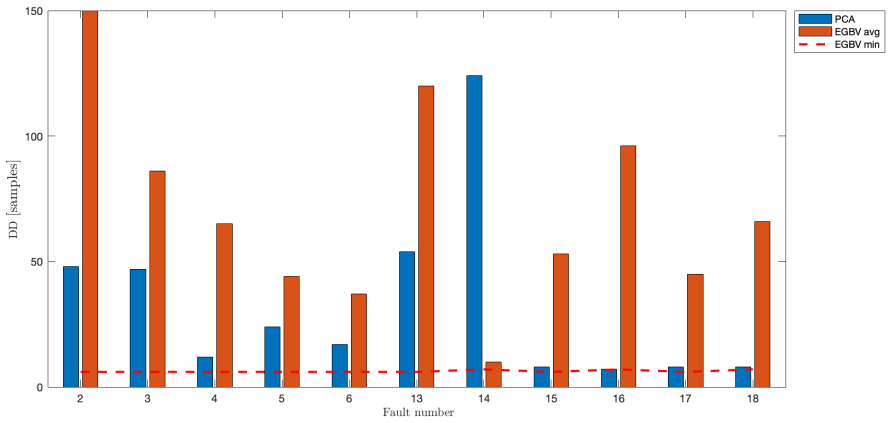
Fault number	Model DD	Practical DD
$\mathcal{F}_1$	N/A	N/A
$\mathcal{F}_2$	48	N/A
$\mathcal{F}_3$	47	36
$\mathcal{F}_4$	12	15
$\mathcal{F}_5$	24	18
$\mathcal{F}_6$	17	12
$\mathcal{F}_7$	N/A	N/A
$\mathcal{F}_8$	N/A	N/A
$\mathcal{F}_9$	N/A	18
$\mathcal{F}_{10}$	N/A	N/A
$\mathcal{F}_{11}$	N/A	N/A
$\mathcal{F}_{12}$	N/A	N/A
$\mathcal{F}_{13}$	54	36
$\mathcal{F}_{14}$	124	83
$\mathcal{F}_{15}$	8	N/A
$\mathcal{F}_{16}$	7	7
$\mathcal{F}_{17}$	8	N/A
$\mathcal{F}_{18}$	8	7
$\mathcal{F}_{19}$	N/A	N/A
$\mathcal{F}_{20}$	N/A	N/A

A discrepancy is observed for the PU2 stuck valve $\mathcal{F}_{14}$ with the model showing a DD of 124 samples, while the practical system reports an 83-sample delay. This discrepancy was

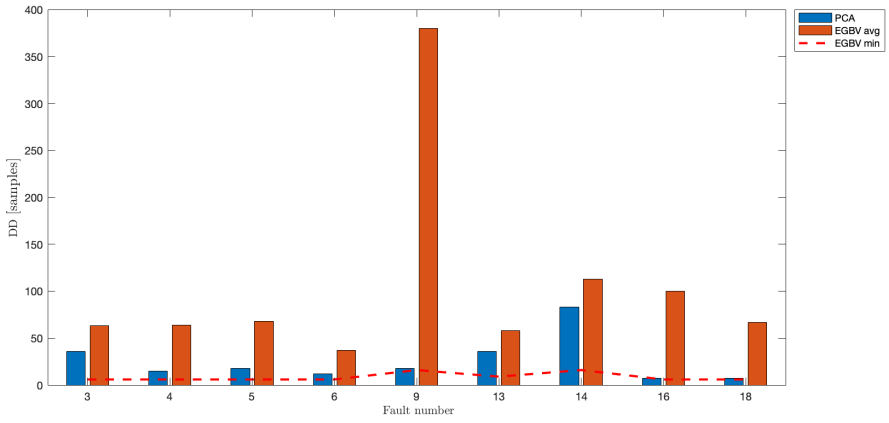
clarified in Section 5.3.3 to be caused by valve modelling limitations.

In light of the results shown in Fig. 6.3, PCA may be regarded as the more prompt FDI technique *if* EGBV is regarded as a collective detection system. Should each EGBV SVD element be monitored independently (according to the original detection philosophy in Section 4.4.4), then it is accepted that EGBV is more prompt than PCA.

To compare the detection delay results of the FDI methods, the results of Tables 6.6 and 6.7 are plotted in Fig. 6.3. The blue bars show the PCA DD and the orange bars show the DD_{avg} of the EGBV FDI technique. The short-stripe line shows the quickest possible response time achieved by a single EGBV element. Note that only the faults there were successfully detected by *both* methods are considered for comparison. In the model results shown in Fig. 6.3a and the practical results shown in Fig. 6.3b, it is clear that PCA is more prompt than the average response of EGBV. However, the DD_{min} is shown to be lower or equal to the PCA DD for both systems.



(a) Model DD comparison (lower is better)



(b) Practical DD comparison (lower is better)

Figure 6.3: Detection delay comparison plot of PCA and EGBV

6.3 Fault isolation comparison

In this section, the degree to which each fault can be isolated is evaluated and compared. This is done by calculating the scalar distances between the elements of one fault signature and another fault signature. For EGBV, the qualitative signatures need to be converted to quantitative signatures first. A simple transformation procedure is followed: a '+' symbol becomes '+1', while '−' symbols are converted to '-1' and the '0' symbols are simply regarded as zero in value. Then, the distance d_{xy} is calculated by [113]:

$$d_{xy} = \sum_{i=1}^{6} \sum_{j=1}^{5} |\mathcal{F}_{x,ij} - \mathcal{F}_{y,ij}|. \tag{6.3}$$

For the PCA fault signatures, (6.3) is adapted as follows:

$$d_{xy} = \sum_{i=1}^{8} |\mathcal{F}_{x,i} - \mathcal{F}_{y,i}|. \tag{6.4}$$

Equations (6.3) and (6.4) explain how the distance d is calculated between fault signature $\mathcal{F}_x$ of fault number x and $\mathcal{F}_y$ of fault number y. A higher d therefore implies that $\mathcal{F}_x$ and $\mathcal{F}_y$ are 'further' away from each other and are for this reason highly isolable. Alternatively, a lower d indicates close similarity and poor isolability. Given that the fault signature structure of EGBV consists of thirty elements with discrete values ranging from -1 to +1, while the signatures of PCA are made up of eight analogue values, it is expected that the results of (6.3) and (6.4) will differ in range. Consequently, the results of the former and the latter are not directly comparable. This problem is addressed by normalising (6.3) and (6.4) using the formula:

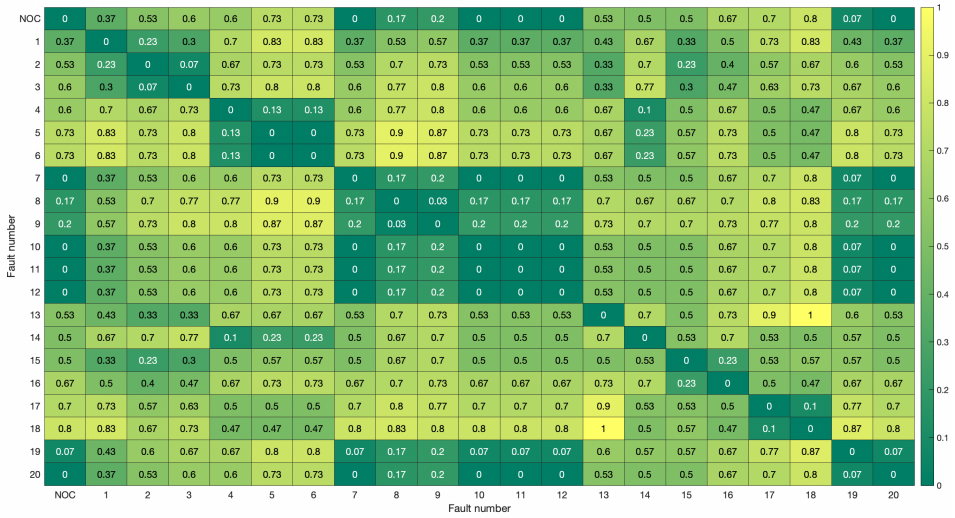
$$\tilde{d}_{xy} = \frac{d_{xy}}{d_{max} - d_{min}}, \tag{6.5}$$

where d_{min} and d_{max} are the minimum and maximum distances respectively of all d_{xy} for a given FDI technique. The normalised distances calculated with (6.5) will result in the original distances being scaled between zero and one, thus enabling a fair comparison between the isolation results of PCA and EGBV.

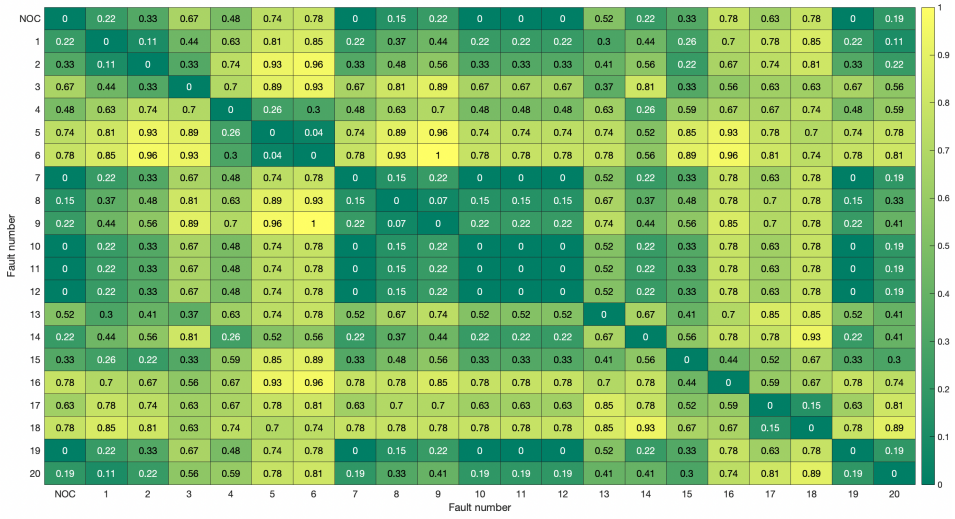
The author wishes to clarify that by calculating $\tilde{d}_{xy}$, it is not assumed that the same process variables cannot contribute to more than one fault and in the same magnitude. In fact, it is expected that a subset of different faults will lead to overlapping process variable disruptions. This was observed in the results of Chapters 3, 4 and 5, which will be indicated by a low $\tilde{d}_{xy}$ value. A good fault isolation structure should be able

to produce a unique fault signature, even when the affected process variables overlap, hereby producing a higher $\tilde{d}_{xy}$. Therefore, the use of the $\tilde{d}_{xy}$ metric is a valid approach for isolation performance evaluation.

Figure 6.4 shows the results of (6.3) and (6.5) in the form a coloured heat map. The figures are shaded from green to yellow, with green indicating lower isolability and yellow indicating higher isolability. Overall, it can be seen that the model and practical systems exhibit a similar isolation distribution, as Fig. 6.4a and 6.4b have similar shading. The main diagonal on both figures contains zeros since the distance between a given fault signature and itself is zero. When considering the first row of each figure (the distance from NOC), faults $\mathcal{F}_5$, $\mathcal{F}_6$, $\mathcal{F}_{16}$ and $\mathcal{F}_{18}$ are the most isolable, that is, the 20% and 30% PU2 clogs, and 5% sensor drifts.



(a) Heat map of the isolability of the model EGBV faults



(b) Heat map of the isolability of the practical EGBV faults

Figure 6.4: Heat maps of the isolability of EGBV

The PU1 clogs ($\mathcal{F}_1$ to $\mathcal{F}_3$) are well distanced from other faults, but not well distanced from one another in fault size. The PU2 clogs are also well distanced from other fault types (better than PU1 clogs), yet it also exhibits low isolability between their fault sizes. It can be seen that the 20% and 30% clogs of PU2 ($\mathcal{F}_5$ to $\mathcal{F}_6$) are isolable from one another in practice. Furthermore, the 10% PU2 clog ($\mathcal{F}_4$) is revealed to be similar to the PU2 stuck valve ($\mathcal{F}_{14}$). The detected PU1 leaks ($\mathcal{F}_7$ to $\mathcal{F}_9$) are shown to be similar to the fouling faults ($\mathcal{F}_{19}$ and $\mathcal{F}_{20}$). The PU2 leaks ($\mathcal{F}_{10}$ to $\mathcal{F}_{12}$) are included for completeness but are not evaluated since they were not detected. The PU1 and PU2 stuck valves ($\mathcal{F}_{13}$ and $\mathcal{F}_{14}$) are isolable from one another and generally well distanced from other fault types with the only exception being $\mathcal{F}_{14}$'s similarity to the leakage faults in practice. Most sensor drifts ($\mathcal{F}_{16}$ to $\mathcal{F}_{18}$) are well distanced from other fault types, except for the 2% practical sensor drift in PU1 ($\mathcal{F}_{15}$). While the 2% and 5% sensor drifts in PU1 ($\mathcal{F}_{15}$ to $\mathcal{F}_{16}$) can be isolated from each other with confidence, the same is not true for PU2 ($\mathcal{F}_{17}$ to $\mathcal{F}_{18}$). PU1 fouling ($\mathcal{F}_{19}$) in the model can be isolated with low confidence from NOC but cannot be isolated in practice. Fouling in PU2 is shown to be non-isolable from NOC in the model, but may be isolated with low confidence in practice.

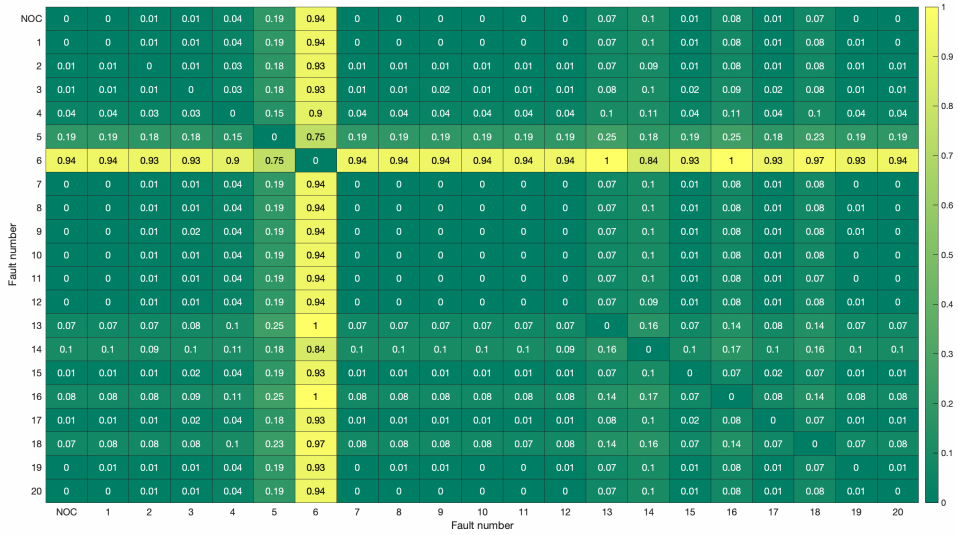
The PCA results of (6.4) and (6.5) are provided in Fig. 6.5. Figures 6.5a and 6.5b show that the distances between the fault signatures are not uniform across fault types, location and sizes. For the model result, the 30% clog in PU2 ($\mathcal{F}_6$) is distinctly the most isolable fault within the scope of the tested faults, with its 20% variant as the second most isolable. The practical results in Fig. 6.5b also show that $\mathcal{F}_6$ is the most isolable, while the stuck valves faults ($\mathcal{F}_{13}$ and $\mathcal{F}_{14}$) are also shown to be distinguishable. The rest of the faults all have low $\tilde{d}$-values relative to the most isolable faults.

It is concluded that for the given scope of tested faults within the heated two-tank process, the EGBV FDI approach provides superior isolation capability compared to PCA. The former has shown that its fault signatures are uniformly distanced, allowing for confident fault *type* isolation. Fault *size* isolation is also possible in most cases but is limited due to the low $\tilde{d}$-values between the fault sizes. Additionally, it is possible to isolate the fault *location*, but the degree of location isolation is dependent on the fault type. The non-uniform distribution of the PCA $\tilde{d}$-values show that only a subset of faults can be well isolated and most of its $\tilde{d}$-values are significantly lower than the corresponding EGBV $\tilde{d}$-values.

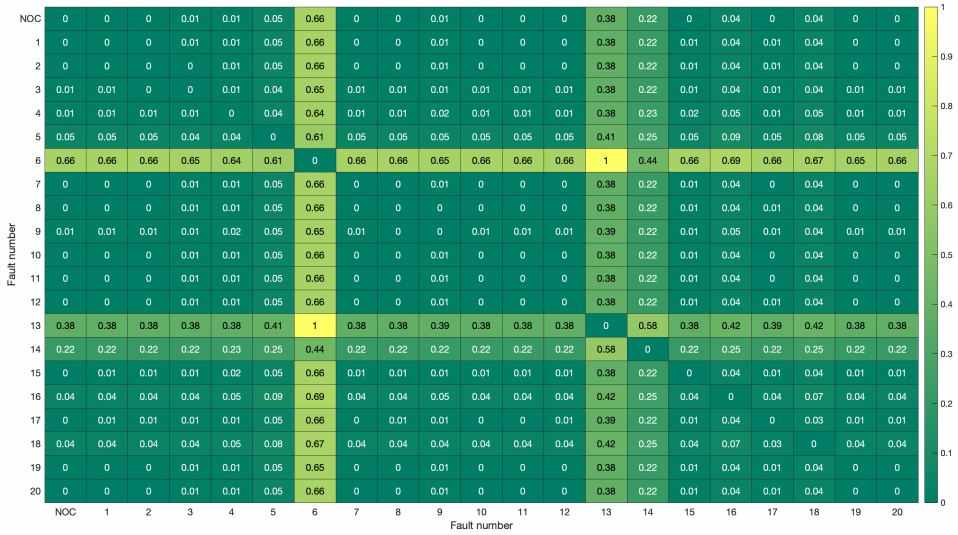
Two notable insights are gained from the isolability results. The first deals with the EGBV isolation performance. Recall that the EGBV FDI method uses the SVD values and vectors as individual elements that comprise its fault signature. These individual elements, when examined together, create an *expanded view* of the process, resulting in good isolation performance even if faults have similar process effects.

The second deals with PCA isolation performance. For PCA faults, the contribution of

each process variable was used to make up its fault signature. It is revealed that the use of process variable contributions as a platform for fault isolation is ineffective for the scope of faults studied and within the chosen process. The isolability performance of this method will be highly dependent on the number of process variables available, as well as how unique the monitored variables respond to the faults.



(a) Heat map of the isolability of the model PCA faults



(b) Heat map of the isolability of the practical PCA faults

Figure 6.5: Heat maps of the isolability of PCA

6.3.1 Detection & isolation comparison summary

To summarise Sections 6.2 and 6.3, the fault detection and isolation comparison conclusions are presented Table 6.8. As described throughout this chapter, the EGBV approach

is indicated in its collective and single-element philosophies regarding fault detection. The numbers in the table represent a rank from one to three, with one meaning best method and three meaning least desirable method. It is shown that PCA is the most robust, while the best sensitivity and promptness are given by EGBV if the single element detection philosophy is followed. For fault isolation, EGBV is the best approach.

Table 6.8: Ranking of FDI methods according to benchmarks

	EGBV		PCA
Benchmark	Single element (Section 4.4.4)	Collective system	-
Robustness	3	2	1
Sensitivity	1	3	2
Promptness	1	3	2
Isolation	-	1	2

6.4 Comparison of ideal attributes

As described in Section 2.3, ten ideal FDI characteristics are defined by Venkatasubramanian et al. [5, 16]. In [16], the authors have evaluated PCA in light of these characteristics. Likewise, Neser [70] performed this evaluation for EGBV after its application on a Brayton cycle power conversion process. This section aims to compare and comment on PCA's and EGBV's compliance with the ideal characteristics as observed from the findings of this study.

6.4.1 Quick detection & diagnosis

Section 6.2.3 elaborated on how quickly PCA and EGBV can detect faults. However, the speed of isolation was not evaluated here, as the fault signatures were compiled from the mean of the entire fault state. Therefore, this comparison may be done only if the fault signatures are constructed and evaluated in real time. The true speed at which EGBV can generate a fault signature would then be determined by the slowest responding symbol change, assuming all symbol changes persist once triggered and that the fault signature is known before the fault occurrence. For PCA, isolation speed evaluation may be performed only if thresholds have been applied to the contribution plots, such that the time-to-isolation (or isolation delay) can be captured.

6.4.2 Isolability

The isolability was evaluated in detail in Section 6.3, which showed that EGBV provides better isolability than PCA when using the PCA contribution plots as a platform for fault signatures.

6.4.3 Robustness

The robustness of EGBV and PCA regarding fault detection was clarified in Section 6.2.1. It was found that PCA is more robust, regardless of the detection philosophy followed for EGBV.

6.4.4 Novelty identifiability

The novelty identifiability criterion is defined in two parts. First, the FDI technique must be able to distinguish NOC from faulty operating conditions. Secondly, the technique should be able to distinguish between a novel fault and a known fault [5]. Throughout the study, it has been shown that EGBV is at least able to detect all fault types within the scope of the study, but not all fault sizes. Neser [70] also found that not all fault magnitudes were detectable and for this reason, concluded that EGBV does not possess novelty identifiability. PCA showed that in practice, all fault types were detectable but not all sizes, yet Venkatasubramanian [16] indicated that PCA *does* possess novelty identifiability. The author argues that both EGBV and PCA have novelty identifiability, since a novel fault that sufficiently disrupts the process, will be detectable by methods. Given the uniqueness of the EGBV fault signatures produced by the wide range of tested faults, it is likely that novel faults will also produce unique signatures, albeit to varying degrees. For PCA, the novelty of the fault will be visible within its contribution plot when an unusual combination of high-contributing process variables is shown.

6.4.5 Classification error estimate

The classification error attribute is the FDI method's ability to provide a priori estimate of how reliable the fault diagnosis (or fault isolation in the case of this study) of the FDI method is [5]. In this regard, this study employed a distance calculation method to quantify how well the fault signatures of EGBV and PCA can be isolated, but this calculation is not part of the methods' output and was only used in this work as an analysis tool. The author argues that the same procedure may be used to compare online, monitored fault signatures of EGBV with a list of known fault signatures to produce a classification error estimate.

Based on the approach of PCA isolation in this work and its isolation results, however, the implementation of such an error estimate would be challenging. In conclusion, EGBV has the potential to gain the classification error estimation criterion, while PCA does not have this ability.

6.4.6 Adaptability

Adaptability is defined as the FDI technique's ability to recognise shifts in normal process operation and adjust to them, rather than registering that a fault condition has occurred [5]. The results of this study suggest that neither EGBV nor PCA possess this attribute. Consider the FAR results of the clogging fault datasets ($\mathcal{F}_1$ to $\mathcal{F}_6$) shown in Fig. 6.1. Higher FAR values were logged on these process datasets, which are verified to be NOC, meaning both techniques failed to recognise the shift that occurred in the process's NOC. This may in part be attributed to the implementation of static thresholds.

6.4.7 Explanation facility

The FDI technique's ability to explain the origin and propagation of a fault through the process is called *explanation facility* [5]. In [5], it is further explained that this criterion requires the FDI system to provide a cause-and-effect explanation of the fault occurrence. EGBV is able to detect and isolate faults but is not able to explain its propagation. Similarly, PCA is set up well to detect and identify faults, but also cannot explain fault origin and propagation.

6.4.8 Modelling requirements

Ideally, the modelling necessary for an FDI system to function should be minimal [5]. This is understandable since complex modelling would increase the computational load of the FDI system and will be difficult to maintain if the process is regularly expanded and upgraded. In Chapter 4, it was shown that EGBV requires a basic, qualitative model upon which fault detection and isolation are based. Additionally, a reference NOC dataset is required to establish the normal energy-exergy conditions of the model. PCA on the other hand only requires a reference NOC dataset from which a data model is derived for online fault monitoring, and for this reason, has fewer modelling requirements than EGBV. Both methods, however, require low modelling input when compared to a fully analytical modelling approach.

6.4.9 Storage & computation

Similar to the modelling requirements attribute, the ideal FDI system should have low storage requirements and should be computationally efficient to facilitate prompt, real-time fault detection [5].

To evaluate the computational requirements of each method, the stages of calculation are considered here, rather than their detailed numerical implementation. According to Fig. 4.1, EGBV undergoes four stages of transformation before detection and isolation can be completed, namely the measurement space, feature space, decision space and class space. This process is repeated for every process sample. PCA progresses through the same stages, but only once, to construct a data model. Thereafter, PCA detections are made directly from the measurement space, making it computationally more efficient for online monitoring. However, it can be argued that with larger processes that have more PVs, EGBV might be more efficient. This is because its energy and exergy calculations require only a subset of the PVs that PCA requires, and only of key parts of the process, which can be accepted as a form of data reduction [53], thereby lowering the overall computational load.

Concerning storage requirements, EGBV may be slightly more efficient. Both methods require historic process data to be stored, but as discussed in the previous section, EGBV may use fewer PVs, leading to smaller datasets when compared to PCA.

6.4.10 Multiple fault identifiability

The ability to isolate, identify or diagnose multiple process faults that occur simultaneously is challenging [5, 18]. Russel et al. [18] note that this may be achieved by constructing models of each fault combination. For EGBV, this would entail constructing additional fault signatures based on tested fault combinations. While this is an attainable prospect for the heated two-tank process, this approach may not be feasible for larger processes. If the PCA contribution plots are used as was done in this work, multiple faults may not be visible, especially when the different faults influence the same PVs. While this study did not test multiple fault isolation, the author concludes that neither EGBV nor PCA have the multiple fault isolability attribute.

6.4.11 Ideal attribute comparison summary

Table 6.9 shows a summary of the ideal attributes comparison of this section. A '$\checkmark$' means the FDI method has the attribute or performs well in it. Alternatively, a '$\times$' indicates the method does not have the ability or performs poorly in the given attribute with reference

to the other method. EGBV conforms to six of the ideal attributes, while PCA conforms to five. Regardless, the best method, in this case, will be the method that satisfies most of the plant practitioner's FDI goals, and not necessarily the method with the most ideal attributes.

Table 6.9: Summary of ideal attributes comparison

Attribute	EGBV	PCA
Quick detection	✓	✓
Isolability	✓	×
Robustness	×	✓
Novel identifiability	✓	✓
Classification error estimate	✓	×
Adaptability	×	×
Explanation facility	×	×
Modelling requirements	✓	✓
Storage & computation	✓	✓
Multiple fault identifiability	×	×

6.5 Conclusion

This chapter served to fulfil the purpose of this study, namely the comparison of EGBV and PCA as fault detection and isolation methods. Two main areas of comparison were considered, namely *fault detection* and *fault isolation*. Additionally, each method was evaluated according to the ideal FDI attributes as established by Venkatasubramanian [5]. To support the final comparison conclusions, both the model and practical results were considered.

It was found that the superior method regarding fault detection is heavily dependent on the detection philosophy followed for EGBV. If the SVD elements of EGBV are considered as a collective detection group with the expectation that as many SVD elements as possible must react to a fault condition, then the PCA approach is regarded to be superior by showing better robustness and promptness. The most sensitive method is dependent on the fault type. Conversely, if the detection philosophy of Section 4.4.4 is followed, where only a single SVD element detection is required within the group of SVD elements for a fault to be declared, then EGBV is more sensitive and prompt than PCA. This detection philosophy will likely lead to false alarm flooding for EGBV and therefore, PCA is still regarded as the more robust method.

EGBV has shown superior fault isolation performance overall when compared to PCA.

The heatmaps of the methods visually showed how well the fault signatures were separated from each other and by extension, how unique each fault signature is with reference to others. The EGBV results showed that if the fault is detected, the type of fault can be isolated with high confidence, while the size of the fault can be isolated in most cases, but with low confidence. Fault location isolation is possible, but the confidence with which the location can be isolated was shown to be dependent on the fault type. For PCA, it was found that only three of the twelve detected faults are truly isolable in practice. The author predicts that an analogue, quantitative fault signature approach in EGBV will likely lead to improved fault size isolation and should be investigated.

Additionally, it is found that neither EGBV nor PCA possesses the ability to adapt to normal process shifts (*adaptability*) or explain the cause-and-effect of faults (*explanation facility*). The methods are also not able to isolate multiple simultaneous faults without extensively modelled combinations of said faults (*multiple fault identifiability*). They do, however, have the ability to detect novel faults (*novel identifiability*), given that the fault is of sufficient magnitude. EGBV is more likely to show novel fault signatures in this regard. PCA is regarded to be the more efficient method when considering the *modelling* requirement of the FDI technique. Regarding *computational and storage requirements*, valid arguments exist for both techniques' superiority.

In conclusion, the better FDI method depends on the need of the plant operator. Since EGBV currently functions with multiple detection plots, PCA with its single detection plot might be more attractive and simpler to implement in practice. If fault isolation is of more interest than its detection, then EGBV is the better solution. Given the current state of computational capability and storage, this attribute is of less importance when deciding between these two FDI methods. The attributes that are of more importance, apart from robustness, sensitivity and promptness, are arguably adaptability and explanation facility, which these techniques do not possess. EGBV and PCA, each having their advantages and disadvantages, cannot be regarded as perfect FDI methods. Nevertheless, both are shown to be competent FDI techniques in their own right.

CHAPTER

7

CONCLUSION

7.1 Summary & conclusions

The energy graph-based visualisation (EGBV) FDI method was compared to the more established principal component analysis (PCA) method to gain insight into the performance and shortcomings of each, using the heated two-tank process. The five research objectives set out in Chapter 1 have been achieved, thus answering the research question:

1. **Literature survey of relevant concepts** - A survey of the relevant fault monitoring literature has been conducted in Chapter 2. The survey clarified the nomenclature of fault monitoring, as well as the main performance metrics to be used for the objective evaluation of FDI methods in this study. Example case studies were presented to illustrate the abilities of EGBV and PCA. Additionally, the benefits of FDI enhancement techniques, such as EWMA, were noted.

2. **Verification and validation of the Simulink® model** - In Chapter 3, the Simulink® model of the process was successfully adapted to match a practical pilot plant version of the process provided by the NWU Faculty of Engineering. It was also modified to correctly simulate the faults in the scope of the study, namely clogging, leakage, stuck valve, sensor drift and fouling. The model modifications were verified and validated against the practical process's data, which include normal operating conditions and twenty different process faults. This established the

Simulink® model as a sufficiently accurate reference system to be used in the comparison.

3. **EGBV application, verification and validation** - The EGBV method was explained and verified using the model, and subsequently validated using the practical data in Chapter 4. The EWMA method noted in Chapter 2 was applied for improved performance.

4. **PCA application, verification and validation** - Chapter 5 explained the mathematical structure of PCA and verified its application using the model. Its application to the practical data proved its validity. Throughout its configuration, care was taken to configure PCA such that a scientifically fair comparison would be possible. This included using the MEWMA enhancement for PCA, which is equal to the EWMA enhancement of EGBV.

5. **Comparison of EGBV and PCA** - An objective comparison was made in Chapter 6 between EGBV and PCA based on the key FDI performance metrics discussed in Chapter 2. Both the model and practical results were considered. The comparison revealed that PCA is the more robust FDI method. If the original detection philosophy of EGBV is followed, then EGBV is more sensitive and prompt than PCA, but at the cost of alarm flooding. If EGBV is regarded as a collective system, then the best method for optimized sensitivity is dependent on fault type. Owing to its unique fault representation platform, EGBV is the superior fault isolation technique. Nevertheless, the most suitable FDI method is still dependent on the priorities of the plant practitioner.

7.2 Future work & recommendations

Several aspects were identified in this study that warrant further research and improvement.

7.2.1 Practical pilot plant improvements

While the practical plant sufficiently achieves its purpose as a test bench for process faults, two main areas will significantly improve the system. Firstly, the sizes of the valves in the process need to be reconsidered. It was shown in Chapter 3, Fig. 3.6 that the valves are

operating at a low %-open range. This is non-ideal, as this limits the valve's ability to exercise fine control. This in return limits the fault testing abilities of the system.

The second consideration is the stability of the external utilities, specifically the external temperature regulation of the hot water reservoir. As the name suggests, the utilities are regarded as *external* to the main process, which comprises the heated two-tank system. It is therefore required that these external systems remain unaffected by the tests conducted on the main process. However, it was found that some faults did affect the externally regulated hot water temperatures T_3 and T_4. It is recommended that these utilities be revised for improved stability.

7.2.2 Model improvements

The author recommends further improvements to the Simulink® model. The first recommendation involves improved valve modelling. In this work, basic linear approximations were used to model the valve behaviour, but it is clear from Fig. 3.6 that other unmodelled valve dynamics are present. These include valve stiction, hysteresis, deadband and dead zones.

The second recommendation is an extension of the first - inclusion of line pressure modelling. As explained in Section 3.4.4, the line pressure upstream and downstream of valves affect their performance and produces an *installed* characteristic as opposed to the *inherent* characteristic. Modelling of process pressure will also introduce new PVs to use for FDI.

Addressing these aspects will allow for a more robust reference system upon which fault testing may be conducted.

7.2.3 EGBV enhancements

The use of EGBV in this study has revealed several aspects that may be improved upon. The development of a single parameter detection system is arguably the most important. As discussed in Chapter 6, EGBV will suffer from false alarm flooding if multiple SVD elements are required to be monitored simultaneously. Reducing the detection system to a single parameter may address this issue, such as multidimensional scaling [114]. An equally important improvement is the reduction of process noise. EGBV currently does not have a method of reducing process noise entering the measurement phase.

Investigating methods of matrix comparison other than the HEOM method may prove useful. Notable methods include the Mahalanobis method [79] and generalised orthogonal

procrustes analysis (GOPA) [80].

It may be beneficial to investigate real-time, analogue fault signatures, rather than using qualitative, symbol-based signatures. This will add more resolution to the fault signatures such that the distinction between fault sizes is improved.

7.2.4 Additional comparisons

In Chapter 2, other prominent FDI methods were surveyed, which include FDA, PLS, DPCA and CVA. These methods were shown to have better performance in some cases, making them ideal options to use in future comparison studies. Independent component analysis (ICA) is another potential method for FDI comparison and may be more relevant since it focuses on non-gaussian distributions [115].

7.3 Closure

The objective of comparing EGBV and PCA using the heated two-tank process was achieved in this study. PCA provides a more robust platform, while EGBV may be regarded as more sensitive and prompt than PCA if the original univariate approach of EGBV is used. If EGBV is viewed from a collective, multivariate perspective, it is less prompt than PCA and the best method for sensitivity then becomes fault dependent. Due to false alarm flooding, PCA may still be the most practically viable method for fault detection, but EGBV is the better approach for fault isolation. While both methods were shown to be competent fault monitoring platforms, the priorities of the plant practitioner will be the determining factor of the preferred method.

BIBLIOGRAPHY

[1] M. A. Fahim, T. A. Al-Sahhaf, and A. S. Elkilani, *Fundamentals of Petroleum Refining*, 1st ed. Oxford: Elsevier B.V., 2010.

[2] T. F. Edgar and J. Hahn, "Process Automation," in *Springer handbook of automation*. Berlin, Heidelberg: Springer Berlin Heidelberg, 2009, pp. 529–543. [Online]. Available: http://link.springer.com/10.1007/978-3-540-78831-7{_}31

[3] R. Isermann and P. Ballé, "Trends in the application of model-based fault detection and diagnosis of technical proceses," *Control Engineering Practice*, vol. 5, no. 5, pp. 709 – 719, 1997.

[4] G. K. McMillan and D. M. Considine, *Process / Industrial Instruments and Controls*, 5th ed. McGraw-Hill, 1999.

[5] V. Venkatasubramanian, R. Rengaswamy, K. Yin, and S. N. Kavuri, "A review of process fault detection and diagnosis part I: Quantitative model-based methods," *Computers and Chemical Engineering*, vol. 27, no. 3, pp. 293–311, 2003.

[6] E. Russel, L. H. Chiang, and R. D. Braatz, *Data-driven Techniques for Fault Detection and Diagnosis in Chemical Processes*, 2000.

[7] S. F. Alan, A. W. Leonard, A. C. Curtis, M. Louis, and L. B. Andersen, *Principles of Unit Operation*, 2nd ed. Wiley, 1980.

[8] B. Jiang, D. Huang, Z. Xiaoxiang, F. Yang, and R. D. Braatz, "Canonical variate analysis-based contributions for fault identification," *Journal of Process Control*, vol. 26, pp. 17–25, 2015.

[9] K. R. Uren, G. van Schoor, and L. Auret, "An energy-attributed graph approach for the purposes of FDI in a heated two-tank system," *IFAC-PapersOnLine*, vol. 1, no. 1, 2018.

[10] G. van Schoor and K. R. Uren, "A vision of energy-based visualisation of large scale industrial systems for the purposes of condition monitoring," *31st Conference on Condition Monitoring and Diagnostic Engineering Management*, pp. 1–10, 2018.

[11] Z. Chen, K. Zhang, Y. A. W. Shardt, S. X. Ding, X. Yang, C. Yang, and T. Peng, "Comparison of two basic statistics for fault detection and process monitoring," *IFAC-PapersOnLine*, vol. 50, no. 1, pp. 14 776–14 781, 2017. [Online]. Available: https://doi.org/10.1016/j.ifacol.2017.08.2586

[12] W. Chen, "Fault detection and isolation in nonlinear systems: observer and energy-balance based approaches," Dr-Ing. Thesis, Universität Duisburg-Essen, 2011.

[13] I. Izadi, S. L. Shah, D. S. Shook, and T. Chen, "An introduction to alarm analysis and design," *IFAC Proceedings Volumes*, vol. 42, no. 8, pp. 645–650, 2009.

[14] S. J. Qin, "Data-driven fault detection and diagnosis for complex industrial processes," in *IFAC Proceedings Volumes*, vol. 42, no. 8. IFAC, 2009, pp. 1115–1125. [Online]. Available: http://dx.doi.org/10.3182/20090630-4-ES-2003.00184

[15] T. Downes, "The abnormal situation management consortium: Past and future of abnormal situation management," in *The Abnormal Situation Management Consortium*, 2017, pp. 1 – 26. [Online]. Available: https://www.asmconsortium.net/Documents/ASMAmmoniaSafetyConference20170911V7clean.pdf

[16] V. Venkatasubramanian, R. Rengaswamy, S. N. Kavuri, and K. Yin, "A review of process fault detection and diagnosis Part III: Process history based methods," *Computer and Chemical Engineering*, vol. 27, pp. 327–346, 2003.

[17] K. Juslin, "A companion model approach to modelling and simulation of industrial processes," 2005.

[18] E. L. Russell, L. H. Chiang, and R. D. Braatz, "Fault detection in industrial processes using canonical variate analysis and dynamic principal component analysis," *Chemometrics and Intelligent Laboratory Systems*, vol. 51, no. 1, pp. 81–93, 2000.

[19] N. M. N., C. R. C. Hassan, and M. A. Hussain, "A review of data-driven fault detection and diagnosis methods: Applications in chemical process systems," *Reviews in Chemical Engineering*, vol. 36, pp. 513–553, 2020.

[20] G. Zhiwei, C. Cecati, and X. S. Ding, "A survey of fault diagnosis and fault-tolerant techniques-part ii: Fault diagnosis with knowledge-based and hybrid/active approaches," *IEEE Transactions on Industrial Electronics*, vol. 62, pp. 3768–3774, 6 2015.

[21] K. R. Uren, G. Van Schoor, M. Van Eldik, and J. J. A. De Bruin, "An energy graph-based approach to fault diagnosis of a transcritical CO2 heat pump," *Energies*, vol. 13, no. 1789, pp. 1–34, 2020.

[22] H. Neser, G. van Schoor, and K. R. Uren, "Energy-based fault detection and isolation of a brayton cycle-based htgr power conversion unit – a comparative study," *Annals of Nuclear Energy*, vol. 164, p. 108616, 2021. [Online]. Available: https://doi.org/10.1016/j.anucene.2021.108616

[23] C. Ji and W. Sun, "A review on data-driven process monitoring methods: Characterization and mining of industrial data," 2 2022.

[24] A. Asokan and D. Sivakumar, "Fault detection and diagnosis for a three-tank system using structured residual approach," *ICGST-ACSE*, vol. 7, no. 2, pp. 1–8, 2007.

[25] H. J. Marais, G. V. Schoor, and K. R. Uren, "An energy-based approach to condition monitoring of industrial processes," vol. 28, 9 2015, pp. 772–777.

[26] M. Adil, M. Abid, A. Q. Khan, and G. Mustafa, "Comparison of PCA and FDA of coupled liquid tank system," in *13th International Bhurban Conference on Applied Sciences & Technology*. Islamabad: IEEE, 2016, pp. 225–230.

[27] S. Yin, S. X. Ding, A. Haghani, H. Hao, and P. Zhang, "A comparison study of basic data-driven fault diagnosis and process monitoring methods on the benchmark tennessee eastman process," *Journal of Process Control*, vol. 22, pp. 1567–1581, 2012. [Online]. Available: http://dx.doi.org/10.1016/j.jprocont.2012.06.009

[28] B. S. Lindner and L. Auret, "Exploiting process topology for optimal process monitoring," pp. 1–288, 2014.

[29] W. Y. Svrcek, D. P. Mahoney, and B. R. Young, *A Real-time Approach to Process Control*, 3rd ed. John Wiley & Sons, 2014.

[30] J. Berge, "Transmitters: smart, multivariable and fieldbus," in *Instrument Engineer's Handbook Volume Two: Process Control and Optimization*, 4th ed., B. Lipták, Ed. Taylor & Francis, 2005, ch. 3.10, pp. 567 – 574.

[31] B. A. Jensen, "Batch control description, terminology, and Standard S88," in *Instrument Engineer's Handbook Volume Two: Process Control and Optimization*, 4th ed., B. Lipták, Ed., 2004, ch. 8.3, pp. 1528 – 1543.

[32] G. Vachtsevanos, F. Lewis, M. Roemer, A. Hess, and B. Wu, *Intelligent Fault Diagnosis and Prognosis for Engineering Systems*, 1st ed. John Wiley & Sons, 2006.

[33] G. M. Garcia and C. J. Munaro, "Isolation of plant-wide faults using causality detection methods," *IFAC-PapersOnLine*, vol. 49, no. 7, pp. 13–18, 2016. [Online]. Available: http://dx.doi.org/10.1016/j.ifacol.2016.07.209

[34] T. Villegas, M. J. Fuente, and M. Rodríguez, "Principal component analysis for fault detection and diagnosis. Experience with a pilot plant," *International Conference on Computational Intelligence, Man-Machine Systems and Cybernetics - Proceedings*, pp. 147–152, 2010.

[35] J. J. Gertler, *Fault Detection and Diagnosis in Engineering Systems.* CRC press, 1998.

[36] Y. Peng, M. Dong, and M. J. Zuo, "Current status of machine prognostics in condition-based maintenance: A review," *International Journal of Advanced Manufacturing Technology*, vol. 50, pp. 297–313, 9 2010.

[37] M. Mansouri, M. Harkat, H. N. Nounou, and M. N. Nounou, *Data-driven and Model-based Methods for Fault Detection and Diagnosis.* Elsevier, 2020.

[38] F. Harrou, F. Kadri, S. Khadraoui, and Y. Sun, "Ozone measurements monitoring using data-based approach," *Process Safety and Environmental Protection*, vol. 100, pp. 220–231, 2016. [Online]. Available: http://dx.doi.org/10.1016/j.psep.2016.01.015

[39] R. Fazia, O. Taouali, I. Elaissi, and N. Bouguila, "Online fault detection methods and fault detection indices based on PCA Approach," *Recent Researches in Electrical Engineering*, pp. 69–78, 2014. [Online]. Available: http://www.wseas.us/e-library/conferences/2014/Lisbon/ELEL/ELEL-08.pdf

[40] H. Hotelling, "Analysis of a complex of statistical variables into principal components," *The Journal of Educational Psychology*, vol. 24, no. 6, pp. 417 – 441, 1933.

[41] D. Garcia-Alvarez, "Fault detection using principal component qnalysis (PCA) in a wastewater treatment plant (WWTP)," *62-th International Student's Scientific Conference, 2009*, no. January 2009, p. 6, 2009. [Online]. Available: http://sntk09en.guap.ru/sntk09en/main/docs/Alvarezisa.pdf

[42] P. Miller, R. E. Swanson, and C. E. Heckler, "Contribution plots: A missing link in multivariate quality control," *Applied Mathematics and Computer Science*, vol. 8, no. 4, pp. 775 – 792, 1998.

[43] A. Chen, H. Zhou, Y. An, and W. Sun, "PCA and PLS monitoring approaches for fault detection of wastewater treatment process," *IEEE International Symposium on Industrial Electronics*, vol. 2016-November, pp. 1022–1027, 2016.

[44] D. J. H. Wilson and G. W. Irwin, "PLS modelling and fault detection on the Tennessee Eastman benchmark," *International Journal of Systems Science*, vol. 31, no. 11, pp. 1449–1457, 2000.

[45] Y. A. Çengel and M. A. Boles, *Thermodynamics: An Engineering Approach*, 5th ed. McGraw-Hill, 2004.

[46] C. P. Du Rand, G. Van Schoor, and C. Nieuwoudt, "Enthalpy – entropy graph approach for the classification of faults in the main power system of a closed Brayton cycle HTGR," *Annals of Nuclear Energy*, vol. 36, pp. 703–711, 2009. [Online]. Available: http://dx.doi.org/10.1016/j.anucene.2009.02.012

[47] C. P. D. Rand and G. V. Schoor, "Fault diagnosis of generation iv nuclear htgr components - part i: The error enthalpy-entropy graph approach," *Annals of Nuclear Energy*, vol. 40, pp. 14–24, 2012. [Online]. Available: http://dx.doi.org/10.1016/j.anucene.2011.09.013

[48] ——, "Fault diagnosis of generation iv nuclear htgr components - part ii: The area error enthalpy-entropy graph approach," *Annals of Nuclear Energy*, vol. 41, pp. 79–86, 2012. [Online]. Available: http://dx.doi.org/10.1016/j.anucene.2011.11.009

[49] G. V. Schoor, K. R. Uren, M. A. V. Wyk, P. A. V. Vuuren, and C. P. D. Rand, "An energy perspective on modelling, supervision, and control of large-scale industrial systems: Survey and framework," *IFAC Proceedings Volumes (IFAC-PapersOnline)*, vol. 19, pp. 6692–6703, 2014.

[50] J. W. Chinneck and M. Chandrashekar, "Models of large-scale industrial energy systems ii - optimizationa and synthesis," *Energy*, vol. 9, pp. 679–692, 1984.

[51] V. Nikulshin, C. Wu, and V. Nikulshina, "Exergy efficiency calculation of energy intensive systems by graphs," *International Journal of Applied Thermodynamics*, vol. 5, pp. 67–74, 2002.

[52] W. Chen, S. X. Ding, A. Q. Khan, and M. Abid, "Energy-based fault detection for dissipative systems," 2010, pp. 517–521.

[53] H. Marais, G. van Schoor, and K. R. Uren, "The merits of exergy-based fault detection in petrochemical processes," *Journal of Process Control*, vol. 74, pp. 110–119, 2019. [Online]. Available: http://dx.doi.org/10.1016/j.jprocont.2017.11.005

[54] V. Venkatasubramanian, R. Rengaswamy, and S. N. Kavuri, "A review of process fault detection and diagnosis Part II : Qualitative models and search strategies," *Computers and Chemical Engineering*, vol. 27, pp. 313–326, 2003.

[55] T. E. Marlin, "Mathematical Modelling Principles," in *Process control: Designing processes and control systems for dynamic performance*, 2nd ed. International: McGraw-Hill Science/Engineering/Math, 2000, ch. 3, pp. 49 – 95.

[56] K. M. Hangos and I. T. Cameron, "A formal representation of assumptions in process modelling," *Computers and Chemical Engineering*, vol. 25, no. 2-3, pp. 237–255, 2001.

[57] D. E. Winterbone and A. Turan, *Advanced Thermodynamics*, 2nd ed. Elsevier, 2015.

[58] T. . J. Kotas, *The Exergy Method of Thermal Plant Analysis*, 1st ed. Essex: Butterworths, 1985.

[59] J. R. Hansman, "Characteristics of instrumentation," in *The Measurement, Instrumentation and Sensors Handbook*, J. G. Webster, Ed. CRC press, 1999, ch. 1, pp. 25 – 31.

[60] T. R. Kuphaldt, *Lessons in Industrial Instrumentation*, 2nd ed., San Francisco, 2019. [Online]. Available: https://control.com/uploads/Lessons-In-Industrial-Instrumentation-Control.pdf

[61] M. A. A. Shoukat Choudhury, N. F. Thornhill, and S. L. Shah, "Modelling valve stiction," *Control Engineering Practice*, vol. 13, no. 5, pp. 641–658, 2005.

[62] J. J. Yamé and L. El-Bahir, "Teaching control valve friction using modeling and simulation," in *American Society for Engineering Education Annual Conference and Exposition*, 2005, pp. 1 – 11.

[63] A. Kaiyhan and F. J. Doyle III, "Friction compensation for a process control valve," *Control Engineering Practice*, vol. 8, no. 7, pp. 799–812, 2000.

[64] R. A. Romano and C. Garcia, "Valve friction and nonlinear process model closed-loop identification," *Journal of Process Control*, vol. 21, no. 4, pp. 667–677, 2011. [Online]. Available: http://dx.doi.org/10.1016/j.jprocont.2010.11.009

[65] W. Yu, D. I. Wilson, and B. R. Young, "Nonlinear control performance assessment in the presence of valve stiction," *Journal of Process Control*, vol. 20, no. 6, pp. 754–761, 2010. [Online]. Available: http://dx.doi.org/10.1016/j.jprocont.2010.04.004

[66] J. F. Monsen, "An insider's guide to valve sizing and selection," *Flow Control Magazine*, pp. 28 – 32, February 2015. [Online]. Available: https://www.piprocessinstrumentation.com/instrumentation/flow-measurement/article/15562033/part-i-an-insiders-guide-to-valve-sizing-selection

[67] J. S. Carson, "Model verification and validation," in *Proceedings of the 2002 Winter Simulation Conference*, 2002, pp. 52–58.

[68] R. G. Sargent, "Verification and validation of simulation models," in *Proceedings of the 2011 Winter Simulation Conference*, 2011, pp. 183–198. [Online]. Available: https://www.informs-sim.org/wsc11papers/016.pdf

[69] I. Dincer and M. A. Rosen, *Exergy: Energy, Environment and Sustainable Development*, 1st ed. Elsevier Science, 2007. [Online]. Available: https://www.scribd.com/book/282478235/Exergy-Energy-Environment-and-Sustainable-Development

[70] H. Neser, "Energy based visualisation of a Brayton cycle power conversion unit for the purpose of condition monitoring," Doctoral thesis, North-West University, 2019.

[71] R. J. Wilson, *Introduction to Graph Theory*, 4th ed. Essex: Longman Group Ltd, 1996.

[72] R. Balakrishnan and K. Ranganathan, *A Textbook of Graph Theory*, 2nd ed., S. Axler, V. Capasso, C. Casacuberta, A. J. MacIntyre, K. Ribet, C. Sabbah, E. Süli, and W. A. Woyczynski, Eds. New York: Springer, 2012.

[73] J. J. A. de Bruin, "Energy-based visualisation of a transcritical CO 2 heat pump cycle," 2018.

[74] U. G. Indahl, T. Næs, and K. H. Liland, "A similarity index for comparing coupled matrices," *Journal of Chemometrics*, vol. 32, no. 10, pp. 1–18, 2018.

[75] P. Robert and Y. Escoufier, "A unifying tool for linear multivariate statistical methods : The RV- coefficient," *Journal of the Royal Statistical Society*, vol. 25, no. 3, pp. 257–265, 1976. [Online]. Available: https://www.jstor.org/stable/2347233

[76] R. Sibson, "Studies in the robustness of multidimensional scaling: Procrustes statistics," *Journal of the Royal Statistical Society*, vol. 40, no. 2, pp. 234–238, 1978. [Online]. Available: https://www.jstor.org/stable/2984761

[77] A. K. Smilde, H. A. L. Kiers, S. Bijlsma, C. M. Rubingh, and M. J. Van Erk, "Matrix correlations for high-dimensional data: The modified RV-coefficient," *Bioinformatics*, vol. 25, no. 3, pp. 401–405, 2009.

[78] A. El Ghaziri and E. Qannari, "Measures of association between two datasets: Application to sensory data," *Food Quality and Preference*, vol. 40, no. PA, pp. 116–124, 2015.

[79] P. C. Mahalanobis, "On the generalised distance in statisics," in *Proceedings of the National Institute of Science of India 12*, 1936, pp. 49 – 55.

[80] J. C. Gower, "Generalized procrustes analysis," *Psychometrika*, vol. 40, no. 1, pp. 33 – 51, 1975.

[81] R. L. Coetzer, R. F. Rossouw, and N. J. Le Roux, "Reference set selection with generalized orthogonal Procrustes analysis for multivariate statistical process monitoring of multiple production processes," *Chemometrics and Intelligent Laboratory Systems*, vol. 132, pp. 52–62, 2014. [Online]. Available: http://dx.doi.org/10.1016/j.chemolab.2014.01.006

[82] S. Jouili and S. Tabbone, "Attributed graph matching using local descriptions," in *Advanced Concepts for Intelligent Vision Systems*, Bordeaux, 2009, pp. 1–13.

[83] D. R. Wilson and T. R. Martinez, "Improved heterogeneous distance functions," *Journal of Artificial Intelligence Research*, vol. 6, pp. 1– 34, 1997.

[84] L. Han and M. Neumann, "Inner products spaces, orthogonal projection, least squares, and singular value decomposition," in *Handbook of Linear Algebra*, K. H. Rosen, Ed. New York: CRC press, 2007, ch. 5, pp. 95 – 97.

[85] D. C. Montgomery, *Introduction to Statistical Quality Control*, 8th ed. John Wiley & Sons, 2013.

[86] J. Hunter, "The exponentially weighted average," *Journal of Quality Control*, vol. 18, no. 4, pp. 203 – 210, 1986.

[87] E. S. Page, "Cumulative sum charts," *Technometrics*, vol. 3, no. 1, pp. 1–9, 1961. [Online]. Available: https://www.jstor.org/stable/1266472

[88] S. W. Roberts, "Control chart tests based on geometric moving averages," *Technometrics*, vol. 1, no. 3, pp. 239–250, 1959.

[89] J. Chen, C. Laio, F. R. J. Lin, and M. Lu, "Principal component analysis based control charts with memory effect for process monitoring," *Industrial and Engineering Chemistry Research*, vol. 40, pp. 1516–1527, 2001.

[90] S. V. Crowder, "A simple method for studying run-length distributions of exponentially weighted moving average charts," *Technometrics*, vol. 29, no. 4, pp. 401 – 407, 1987. [Online]. Available: https://www.jstor.org/stable/1269450

[91] K. Pearson, "LIII. On lines and planes of closest fit to systems of points in space," *The London, Edinburgh, and Dublin Philosophical Magazine and Journal of Science*, vol. 2, no. 11, pp. 559–572, 1901.

[92] S. Wold, K. Esbensen, and P. Geladi, "Principal component analysis," *Chemometrics and intelligent laboratory systems*, vol. 2, no. 1-3, pp. 37–52, 1987.

[93] F. Harrou, M. Madakyaru, Y. Sun, and S. Khadraoui, "Improved detection of incipient anomalies via multivariate memory monitoring charts: Application to an air flow heating system," *Applied Thermal Engineering*, vol. 109, pp. 65–74, oct 2016. [Online]. Available: https://linkinghub.elsevier.com/retrieve/pii/S135943111631393X

[94] J. Devore and N. Farnum, *Applied Statistics for Engineers and Scientists*, 2nd ed., C. Crockett, Ed. Belmont, CA: Brooks/Cole, 2005.

[95] G. Strang, *Introduction to Linear Algebra*, 4th ed. Wellesley-Cambridge Press, 2009.

[96] M. Tamura and S. Tsujita, "A study on the number of principal components and sensitivity of fault detection using PCA," *Computers and Chemical Engineering*, vol. 31, no. 9, pp. 1035–1046, 2007.

[97] S. J. Qin and R. Dunia, "Determining the number of principal components for best reconstruction," *Journal of Process Control*, vol. 10, no. 2, pp. 245–250, 2000.

[98] M. Zhu and A. Ghodsi, "Automatic dimensionality selection from the scree plot via the use of profile likelihood," *Computational Statistics and Data Analysis*, vol. 51, pp. 918–930, 11 2006.

[99] J. E. Jackson, "Quality control methods for several related variables," *Technometrics*, vol. 1, no. 4, pp. 359–377, 1959. [Online]. Available: https://www.jstor.org/stable/1266717

[100] C. A. Lowry, W. H. Woodall, C. W. Champ, and S. E. Rigdon, "A multivariate exponentially weighted moving average control chart," *Technometrics*, vol. 34, no. 1, pp. 46–53, 1992. [Online]. Available: https://www.jstor.org/stable/1269551

[101] S. Wold, "Exponentially weighted moving principal components analysis and projections to latent structures," *Chemometrics and intelligent laboratory systems*, vol. 23, pp. 149–161, 1994.

[102] K. M. Bodden and S. E. Rigdon, "A Program for approximating the in-control ARL for the MEWMA chart," *Journal of Quality Technology*, vol. 31, no. 1, pp. 120–123, 1999.

[103] S. E. Rigdon, "An integral equation for the in-control average run length of a multivariate exponentially weighted moving average control chart," *Journal of Statistical Computation and Simulation*, vol. 52, no. 4, pp. 351 –365, 1995. [Online]. Available: http://dx.doi.org/10.1080/00949659508811685

[104] G. C. Runger and S. S. Prabhu, "A Markov chain model for the multivariate exponentially weighted moving averages control chart," *Journal of the American Statistical Association*, vol. 91, no. 436, pp. 1701 – 1706, 1996. [Online]. Available: https://www.jstor.org/stable/2291599?seq=1&cid=pdf-reference#references_tab_contents

[105] T. Kourti, "Application of latent variable methods to process control in industry," *International Journal of Adaptive Control and Signal Processing*, vol. 19, pp. 213 – 246, 2005.

[106] B. Mnassri, E. M. E. Adel, B. Ananou, and M. Ouladsine, "Fault detection and diagnosis based on PCA and a new contribution plot," in *IFAC Proceedings Volumes*, vol. 42, no. 8. IFAC, 2009, pp. 834–839. [Online]. Available: http://dx.doi.org/10.3182/20090630-4-ES-2003.00137

[107] A. Ferrer, "Multivariate statistical process control based on principal component analysis (MSPC-PCA): Some Reflections and a Case Study in an Autobody Assembly Process," *Quality Engineering*, vol. 19, no. 4, pp. 311–325, 2007.

[108] R. Tan and C. Yi, "Contribution plots based fault diagnosis of a multiphase flow facility with PCA-enhanced canonical variate analysis," in *IEEE International Conference on Automation and Computing*, Huddersfield, 2017, pp. 1 – 6.

[109] J. A. Westerhuis, S. P. Gurden, and A. K. Smilde, "Generalized contribution plots in multivariate statistical process monitoring," *Chemometrics and intelligent laboratory systems*, vol. 51, pp. 95–114, 2000.

[110] P. Van Den Kerkhof, J. Vanlaer, G. Gins, and J. F. M. Van Impe, "Analysis of smearing-out in contribution plot based fault isolation for Statistical Process Control," *Chemical Engineering Science*, vol. 104, pp. 285–293, 2013. [Online]. Available: http://dx.doi.org/10.1016/j.ces.2013.08.007

[111] J. Liu, "Fault diagnosis using contribution plots without smearing effect on non-faulty variables," *Journal of Process Control*, vol. 22, no. 9, pp. 1609–1623, 2012. [Online]. Available: http://dx.doi.org/10.1016/j.jprocont.2012.06.016

[112] C. Aldrich and L. Auret, *Unsupervised Process Monitoring and Fault Diagnosis with Machine Learning Methods*. Springer, 2013.

[113] S. Greyling, H. Marais, G. van Schoor, and K. R. Uren, "Application of exergy-based fault detection in a gas-to-liquids process plant," *Entropy*, vol. 21, no. 6, pp. 1–19, 2019.

[114] M. Yunus and J. Zhang, "Multivariate Process Monitoring Using Classical Multidimensional Scaling and Procrustes Analysis," in *9th International Symposium on Dynamics and Control of Process Systems*. IFAC, 2010, pp. 165–170. [Online]. Available: http://dx.doi.org/10.3182/20100705-3-BE-2011.00027

[115] M. Kano, S. Tanaka, S. Hasebe, I. Hashimoto, and H. Ohno, "Monitoring independent components for fault detection," *American Institute for Chemical Engineers*, vol. 49, pp. 969–976, 2003.

[116] P. Z. Oberholzer, "A benchmark two-tank heated system emulating typical fault conditions," pp. 1–218, 2022.

[117] B. G. Liptak, *Instrumentation Engineer's Handbook: Process Measurement and analysis*, 4th ed. CRC Press, 2003, vol. 1.

[118] IEC, "Iec 61131-9:2022: Programmable controllers - part 9: Single-drop digital communication interface for small sensors and actuators (sdci)," pp. 1–677, 5 2022.

APPENDIX

A

MODEL & PRACTICAL PROCESS RESULTS

A.1 Introduction

This appendix serves as supplementary to Chapter 3, by providing the complete set of process results from the model and practical plant. This includes the different magnitudes of faults tested. Appendix A has two main goals. The first goal is to provide a process data overview such that process trends become visible. The second goal is to support the conclusions made in Chapter 3 on the performance and accuracy of the model.

The appendix is structured in sections and subsections, where each section is a fault type and each subsection is a fault magnitude, if applicable. The figures provided in each subsection will contain twelve sub-figures to show the results of the fault across the entire plant. Each sub-figure provides the model and practical result of a process variable (PV).

The figures are structured such that the PVs from process unit 1 (PU1) are provided by the top eight sub-figures. The PVs from PU2 are provided in the bottom eight sub-figures. The left column of sub-figures shows all controlled variables across PU1 and PU2. The middle column shows the manipulated variables across PU1 and PU2. Finally, the right column shows the externally controlled temperatures of the cold water and hot water streams to each PU.

A.2 Normal steady-state operation

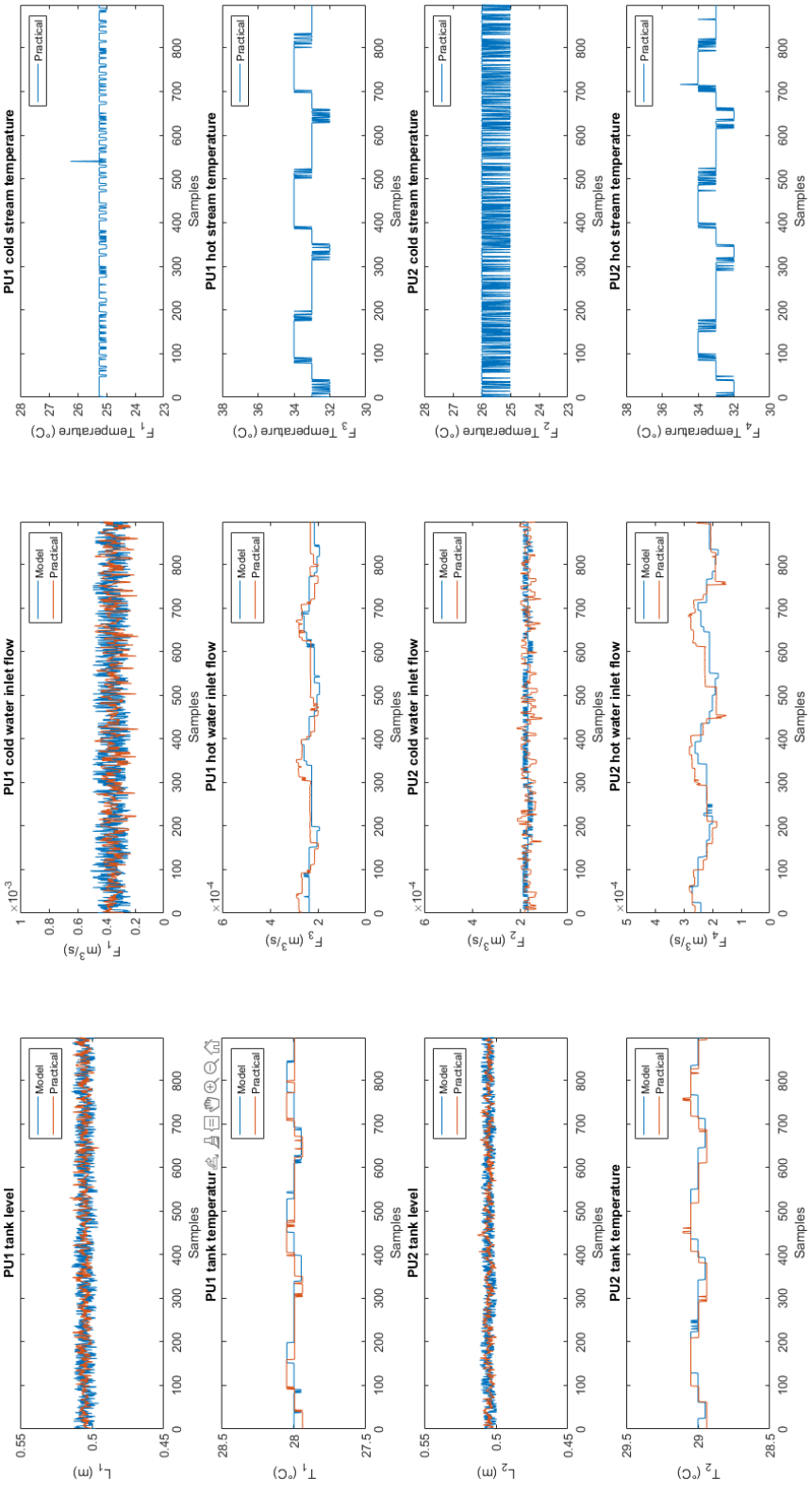


Figure A.1: Normal steady-state results

A.3 Clogging fault data

A.3.1 Process Unit 1 - 10% Clog

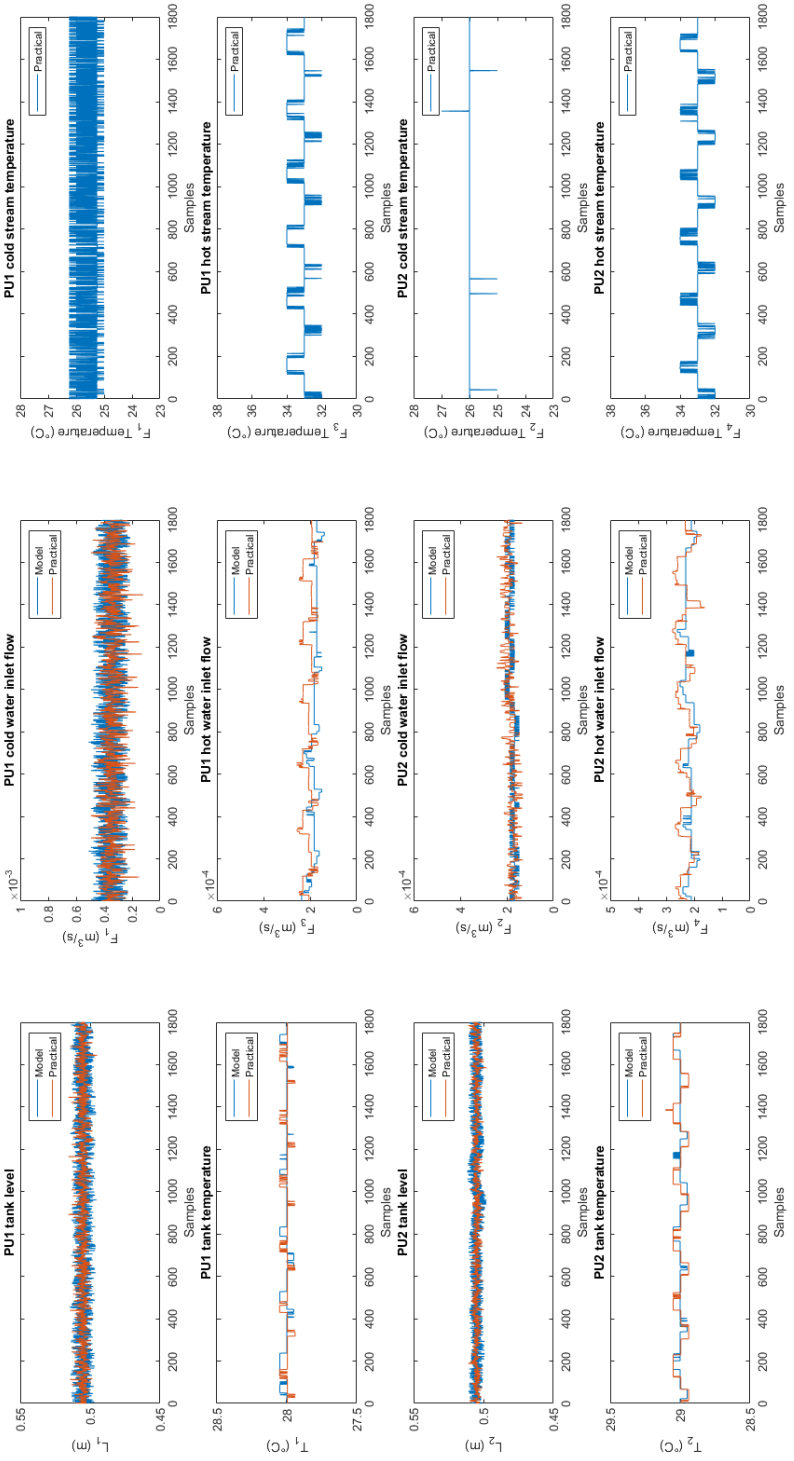


Figure A.2: Process results for 10% clog at sample 900

A.3.2 Process Unit 1 - 20% Clog

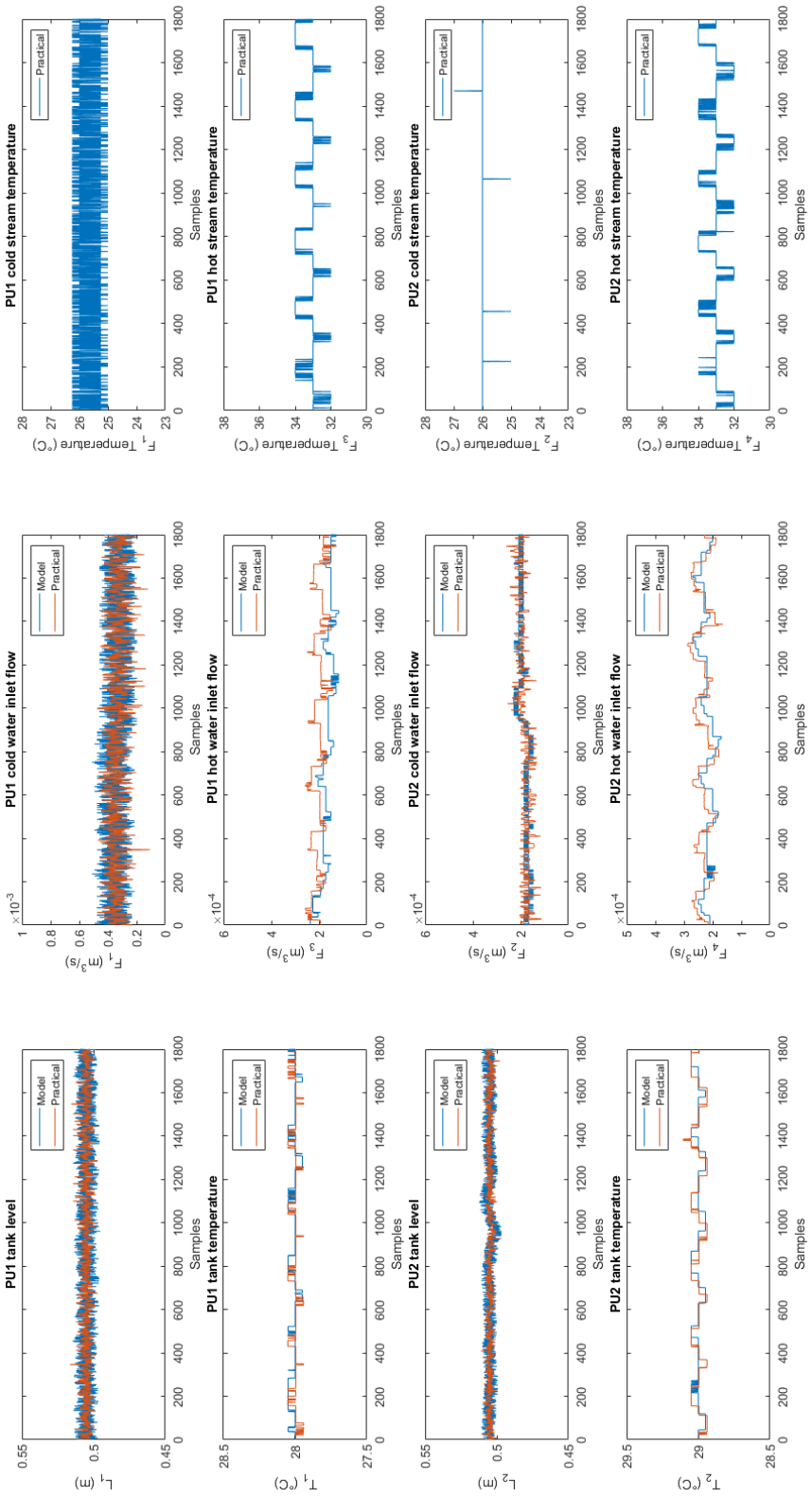


Figure A.3: Process results for 20% clog at sample 900

A.3.3 Process Unit 1 - 30% Clog

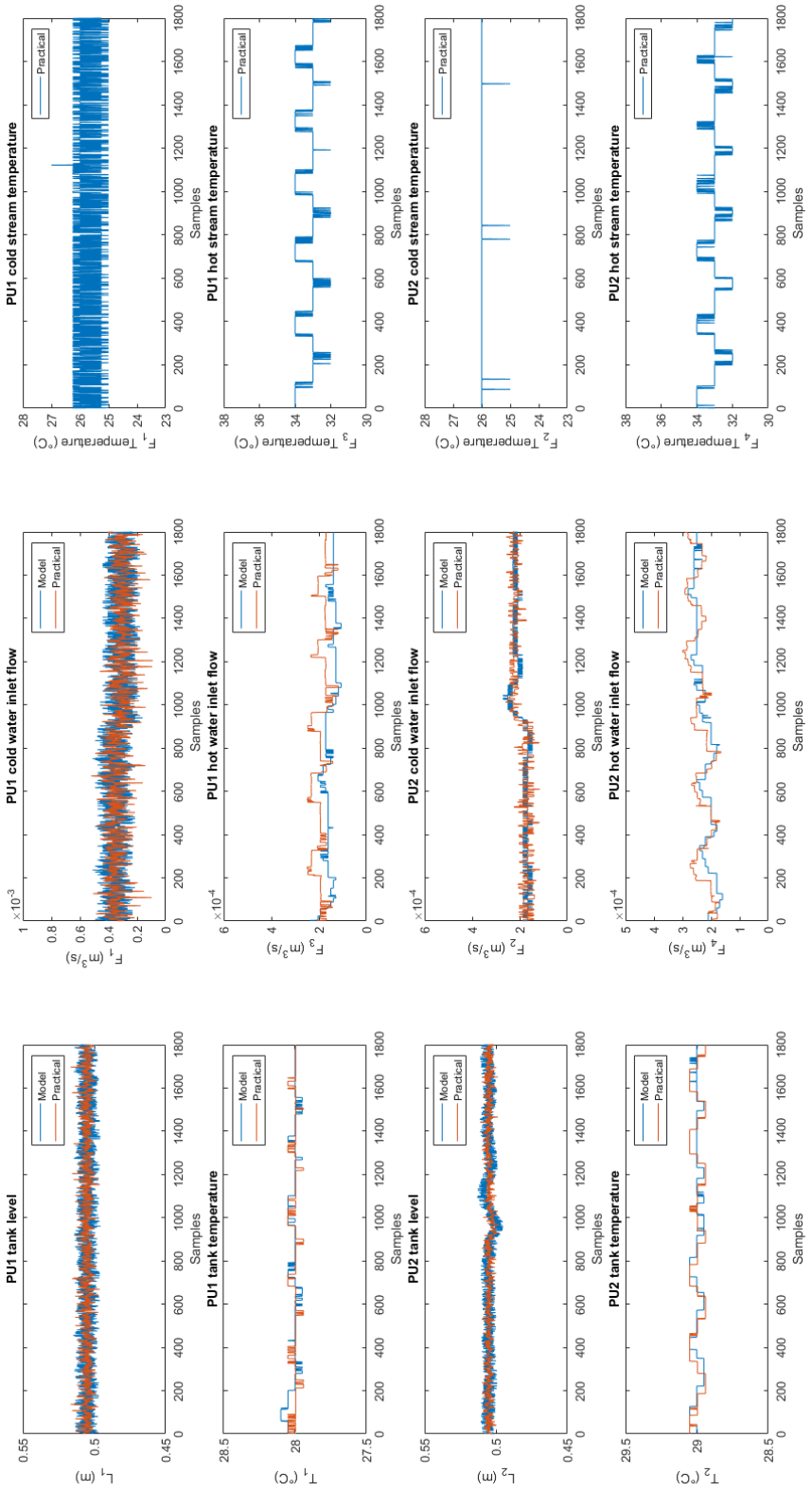


Figure A.4: Process results for 30% clog at sample 900

A.3.4 Process Unit 2 - 10% Clog

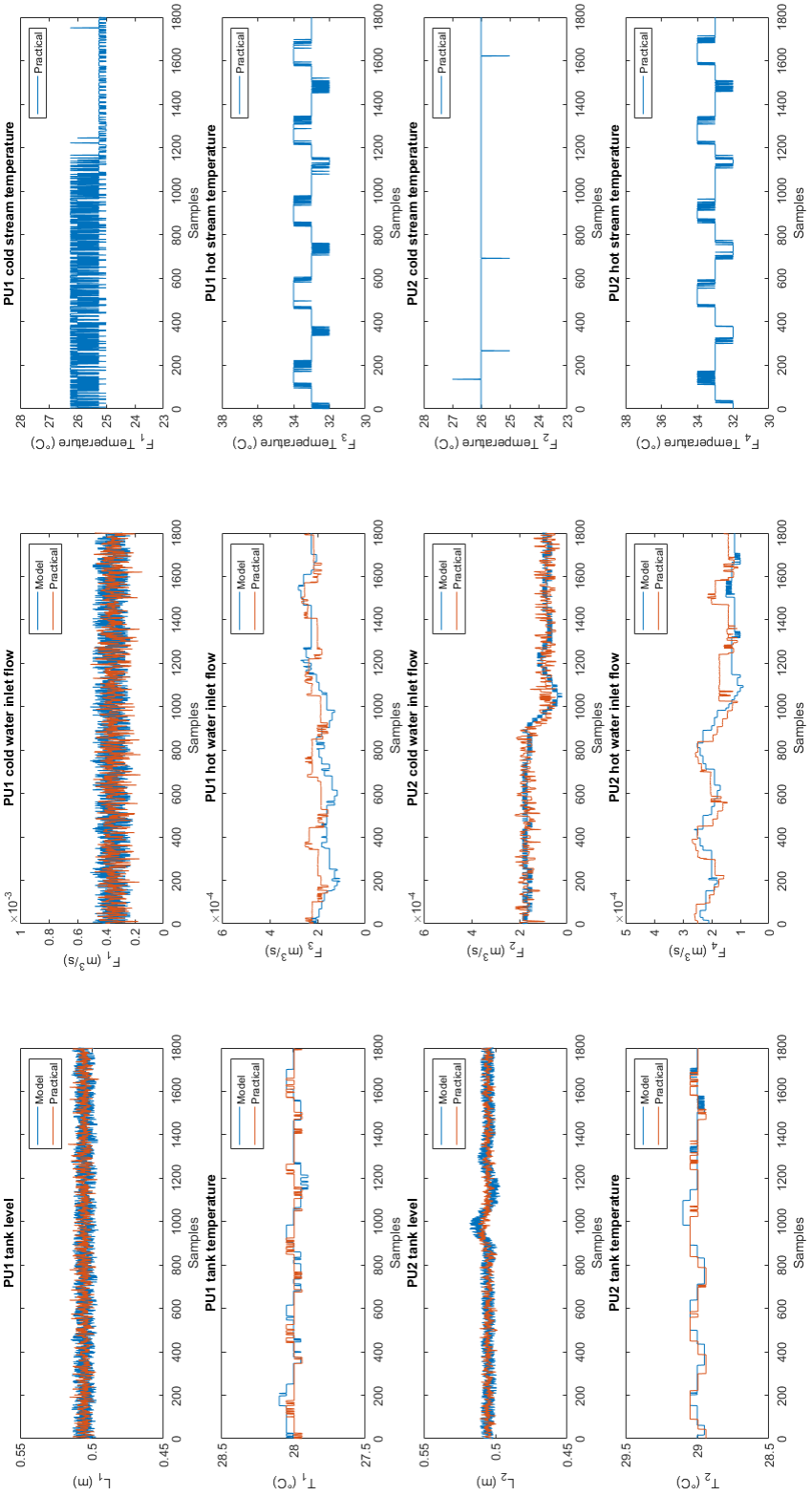


Figure A.5: Process results for 10% clog at sample 900

A.3.5 Process Unit 2 - 20% Clog

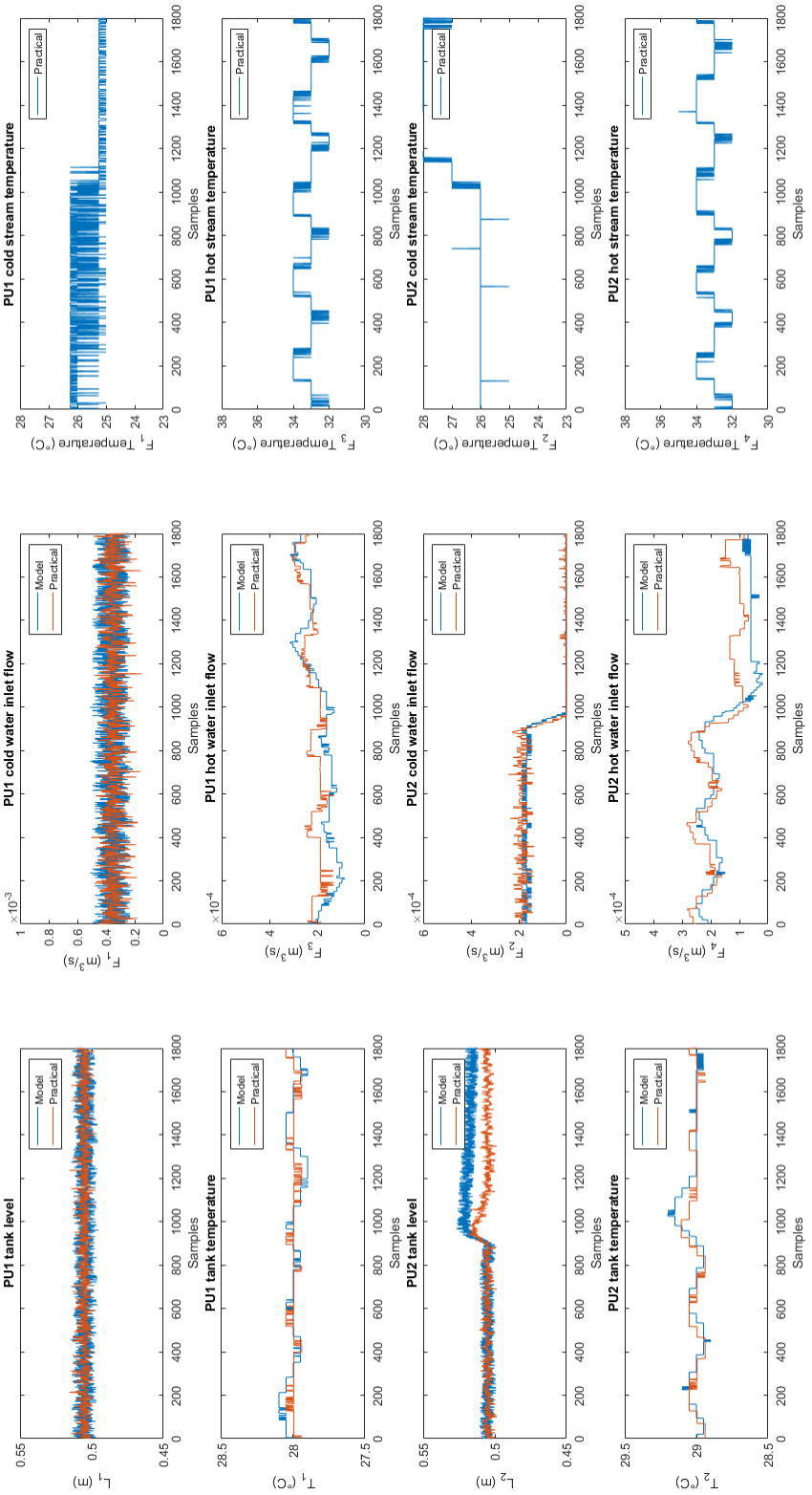


Figure A.6: Process results for 20% clog at sample 900

A.3.6 Process Unit 2 - 30% Clog

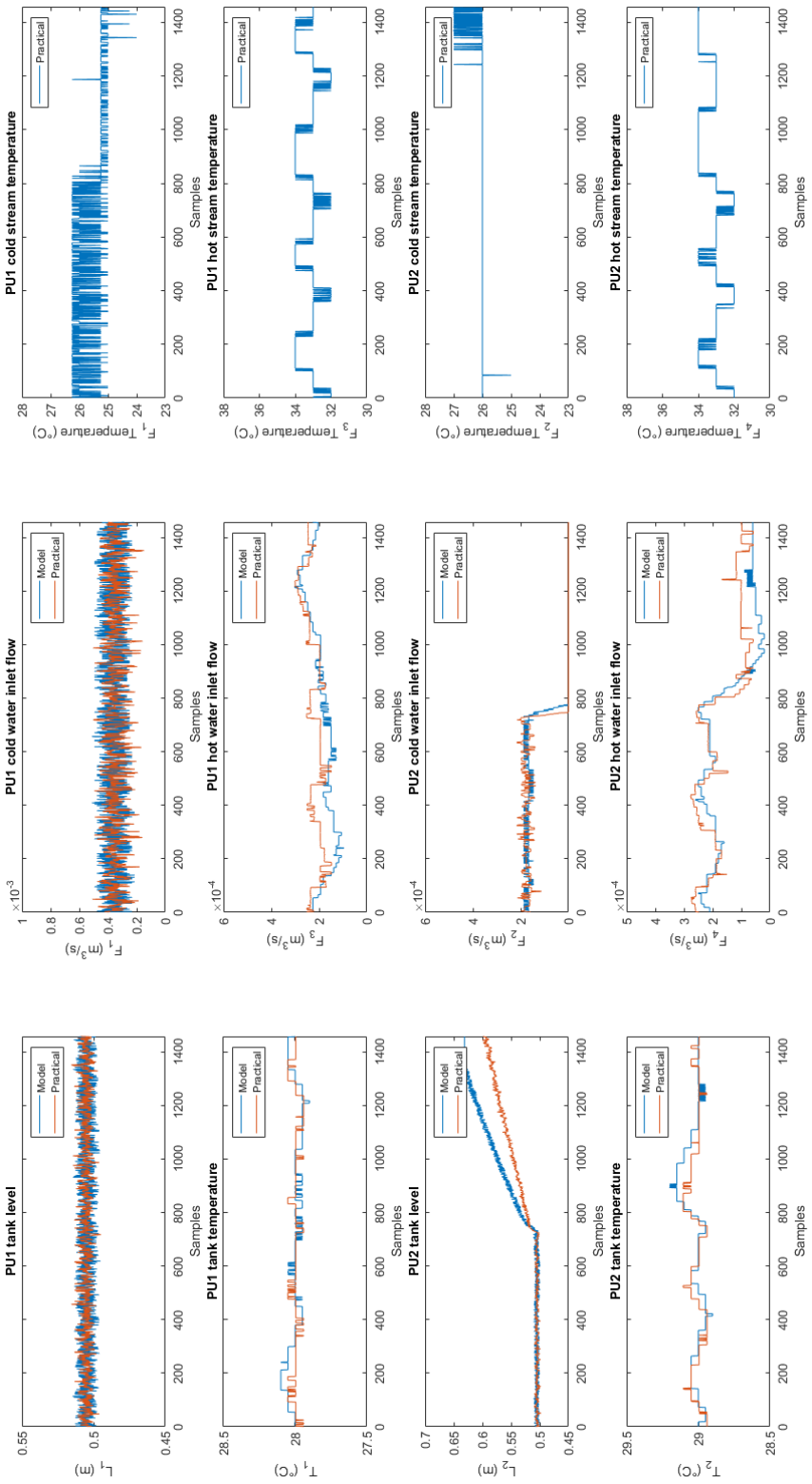


Figure A.7: Process results for 30% clog at sample 729

A.4 Leakage fault data

A.4.1 Process Unit 1 - 10% Leak

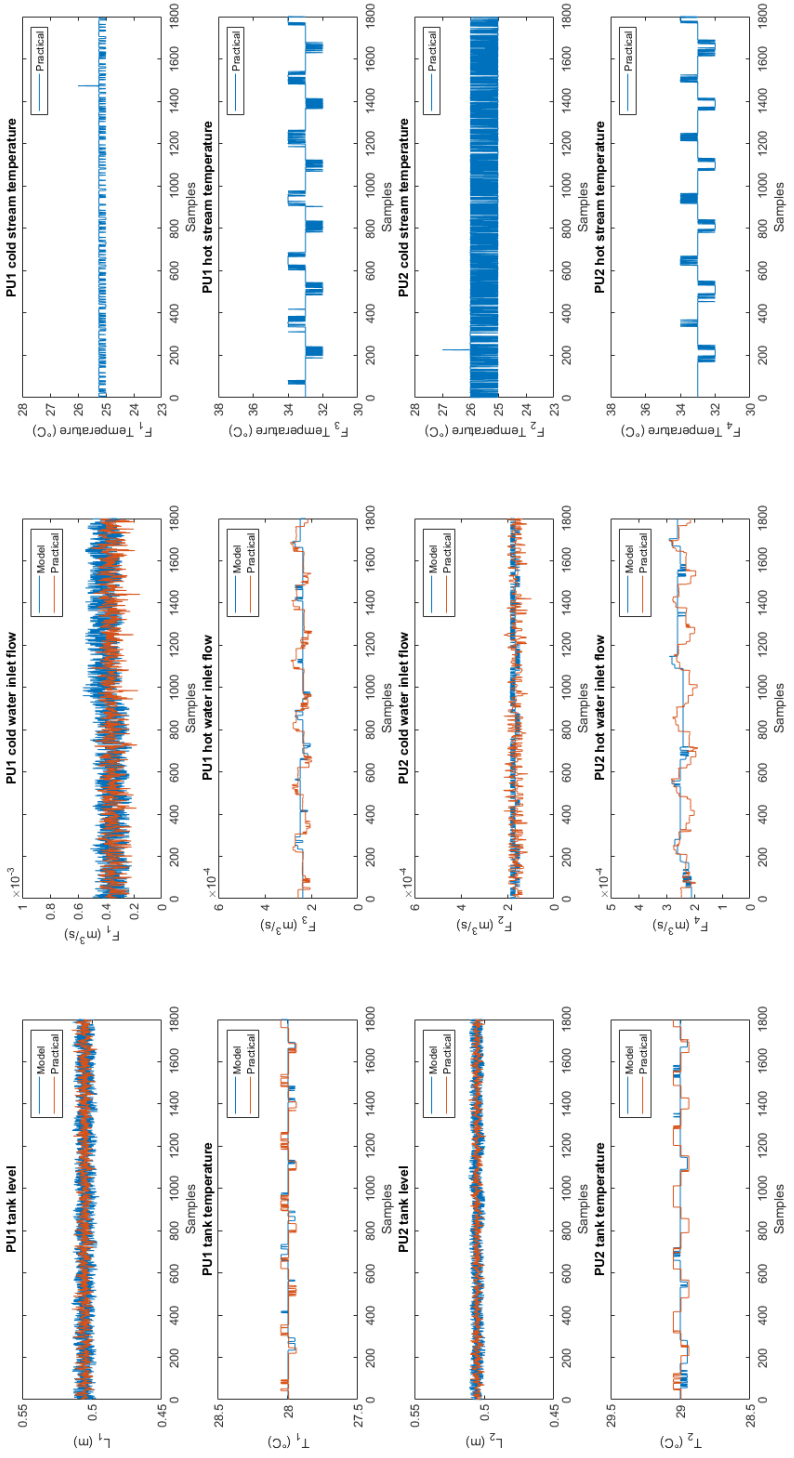


Figure A.8: Process results for 10% leak at sample 900

A.4.2 Process Unit 1 - 20% Leak

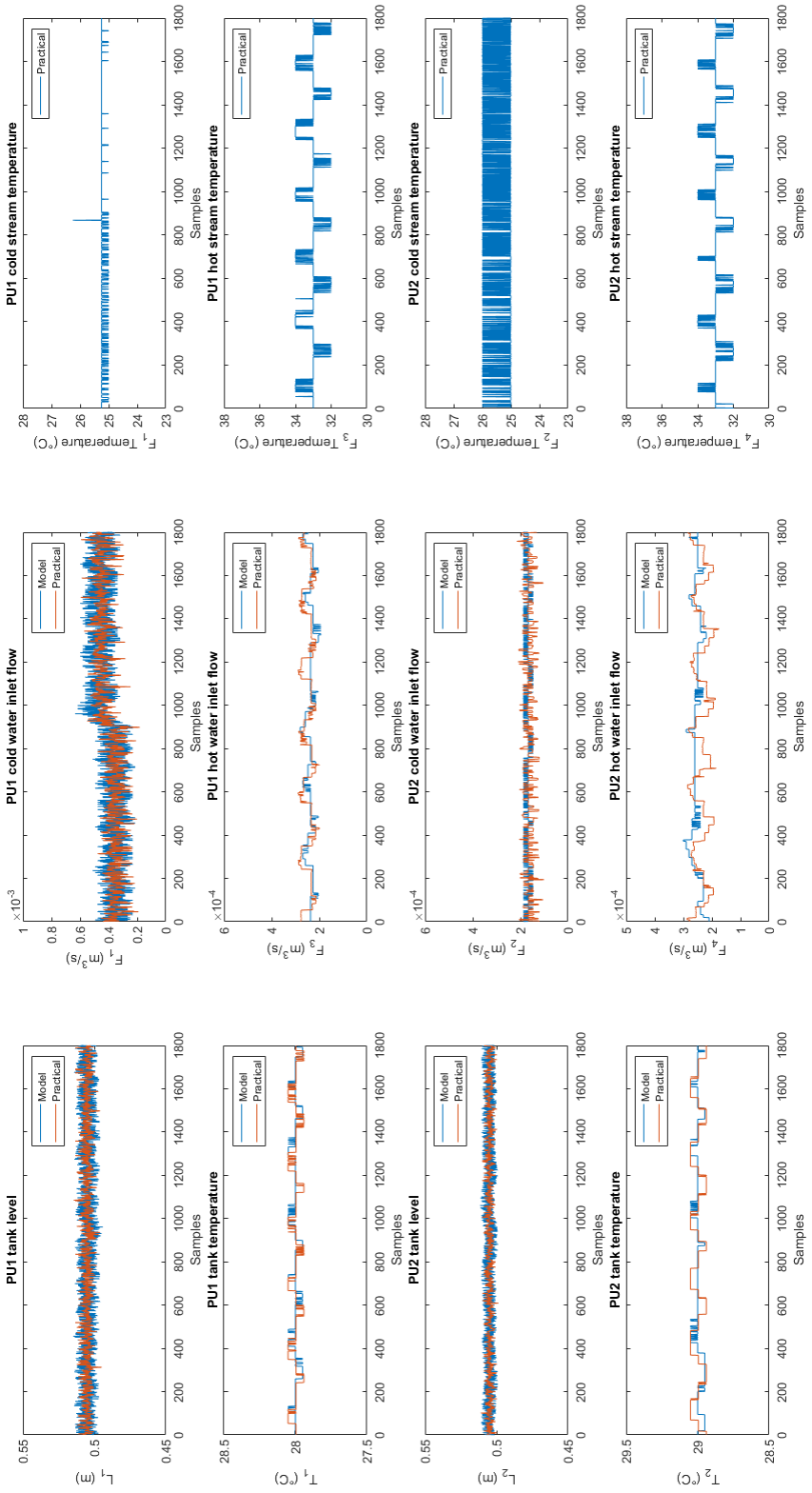


Figure A.9: Process results for 20% leak at sample 900

A.4.3 Process Unit 1 - 30% Leak

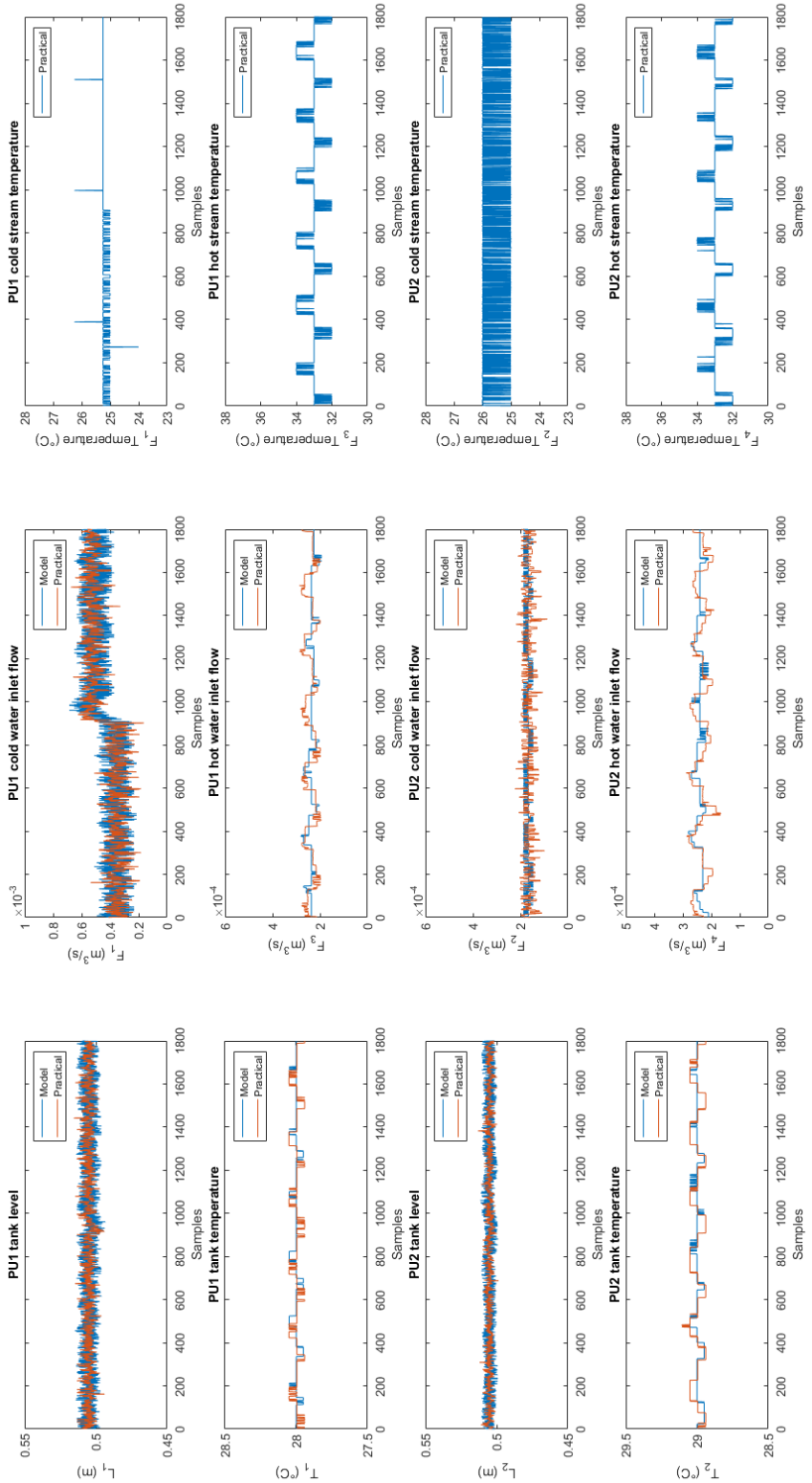


Figure A.10: Process results for 30% leak at sample 900

A.4.4 Process Unit 2 - 10% Leak

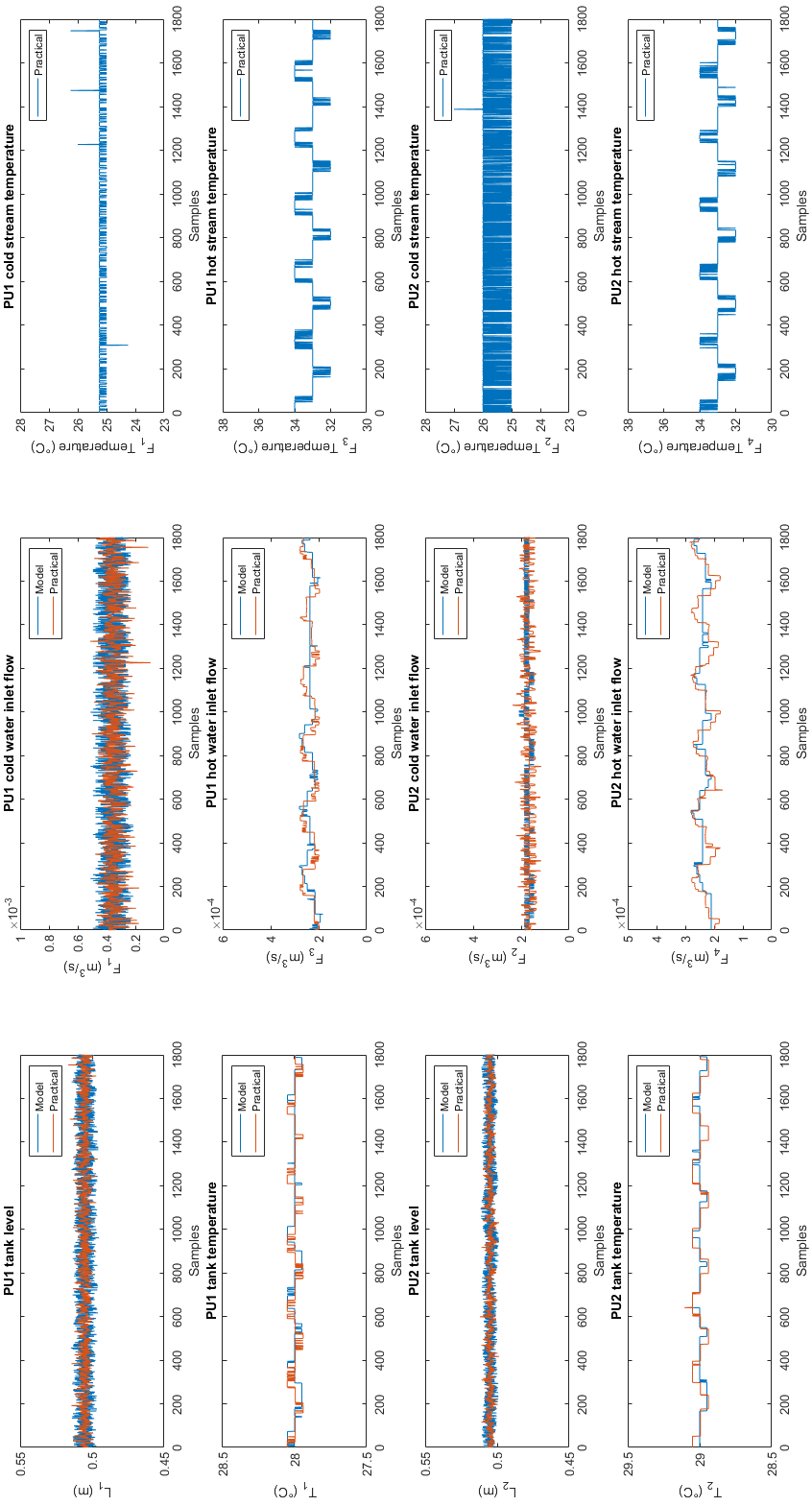


Figure A.11: Process results for 10% leak at sample 900

A.4.5 Process Unit 2 - 20% Leak

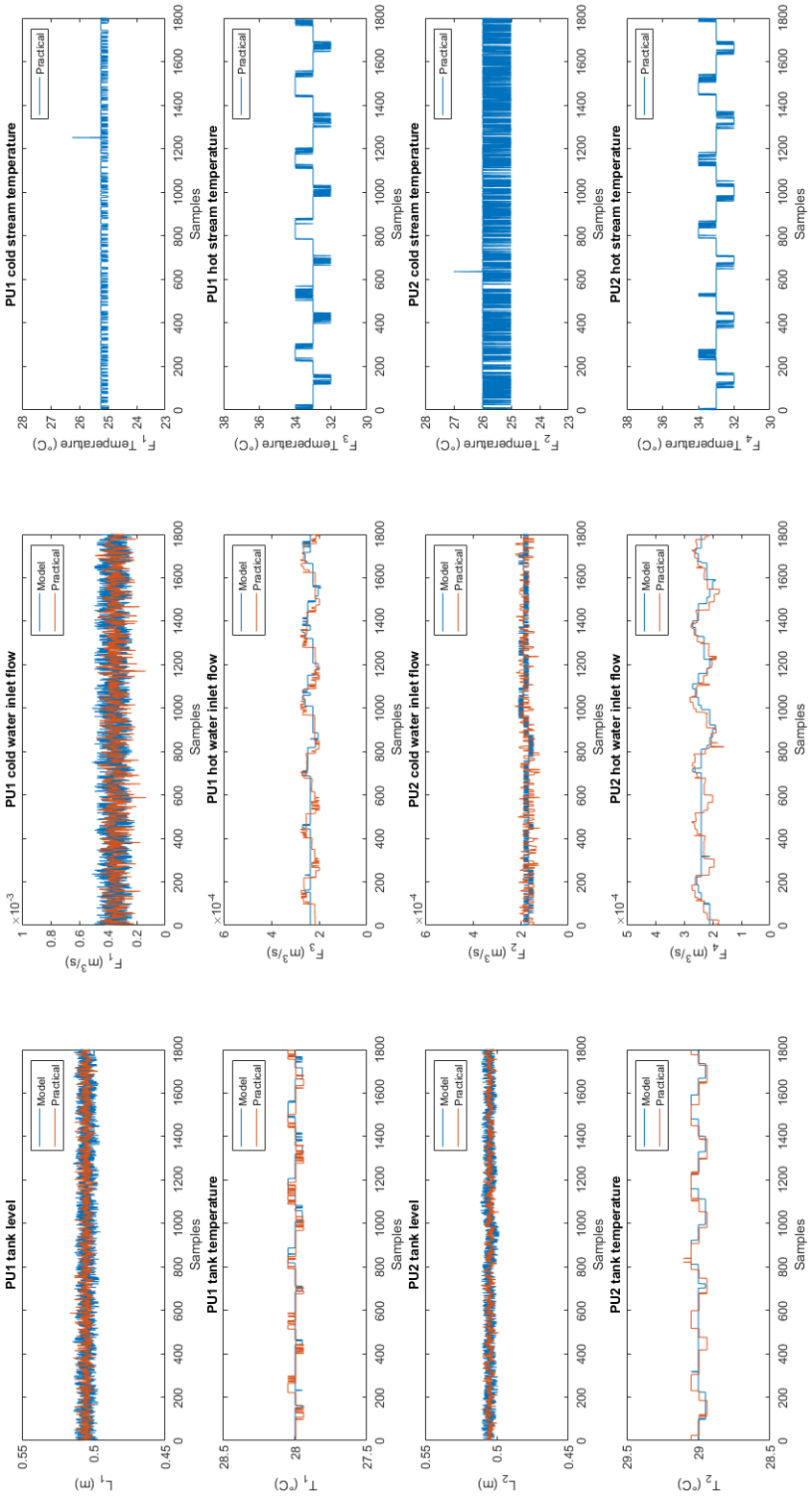


Figure A.12: Process results for 10% leak at sample 900

A.4.6 Process Unit 2 - 30% Leak

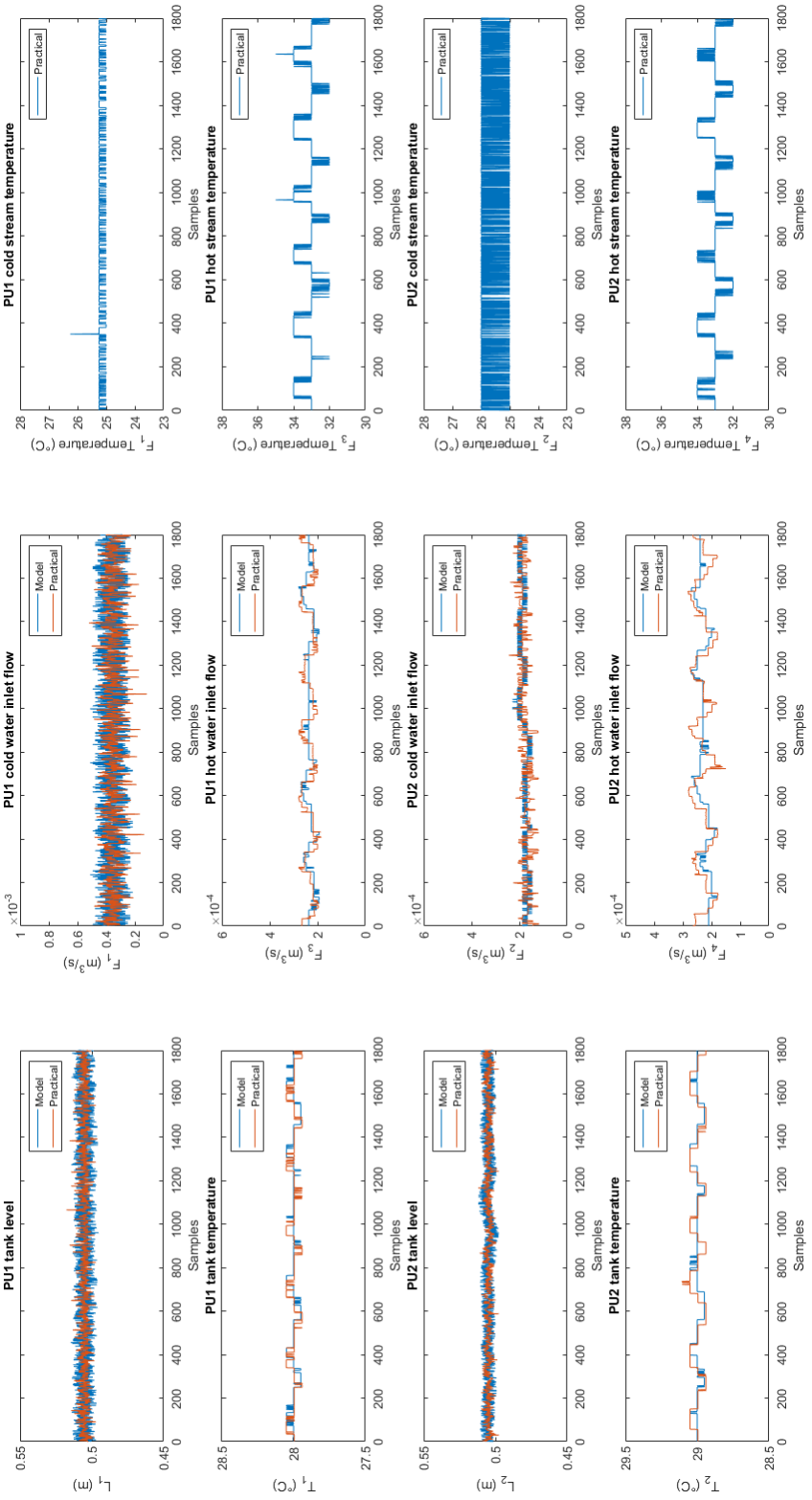


Figure A.13: Process results for 30% leak at sample 900

A.5 Stuck valve fault data

A.5.1 Process Unit 1 - stuck valve

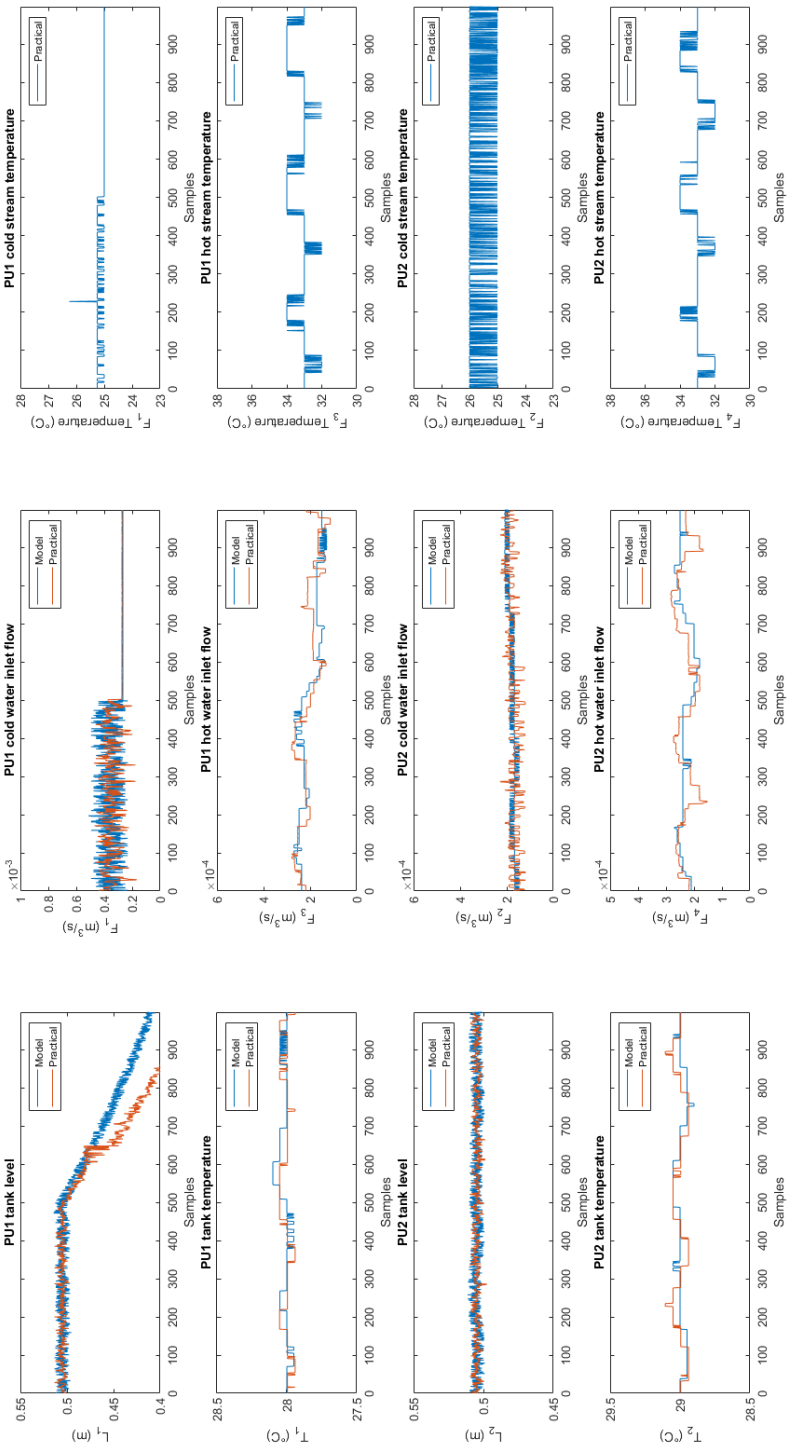


Figure A.14: Process results for a 20% open stuck valve at sample 500

A.5.2 Process Unit 2 - stuck valve

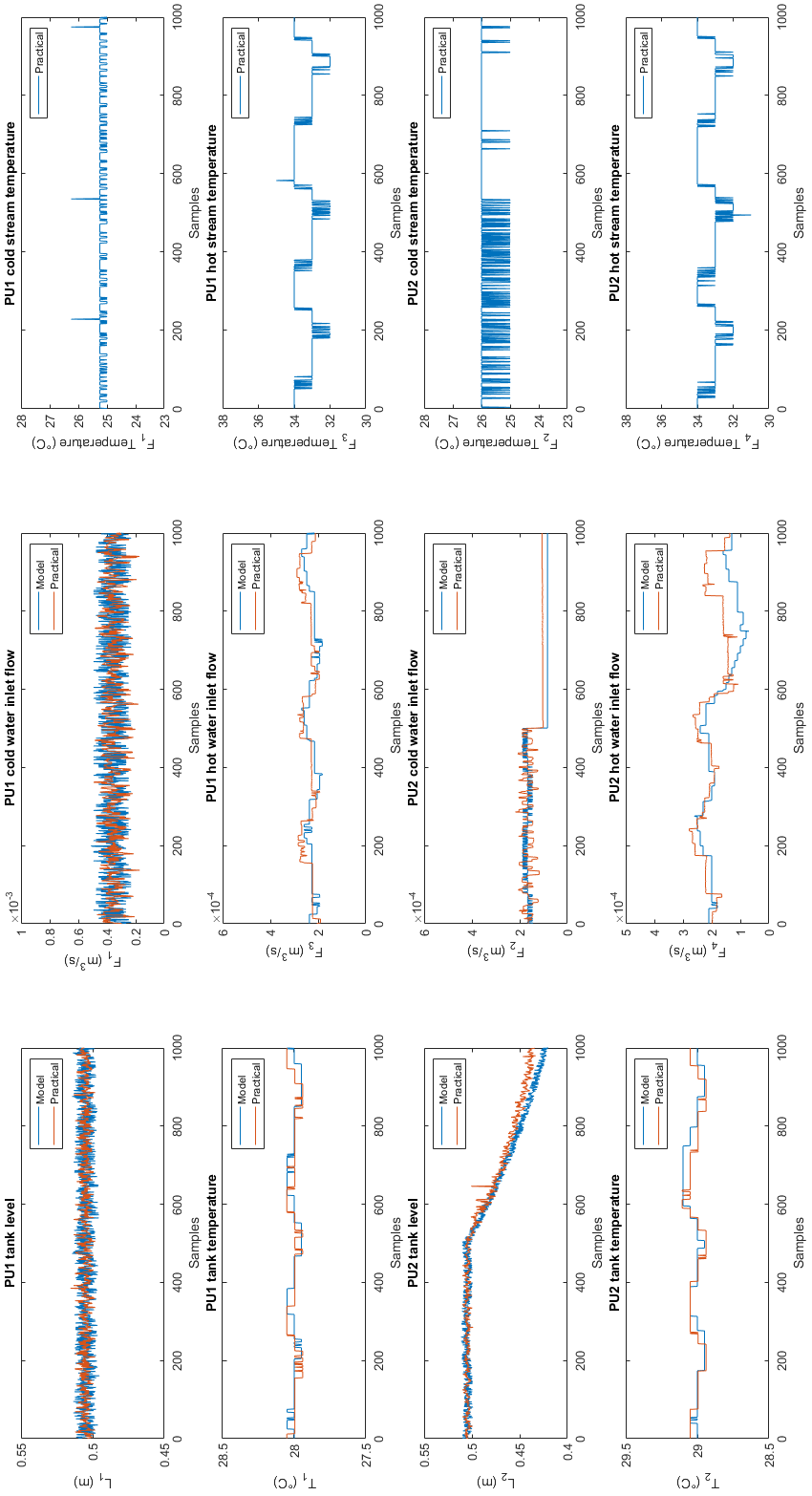


Figure A.15: Process results for a 10% open stuck valve at sample 500

A.6 Sensor drift fault data

A.6.1 Process Unit 1 - 2% sensor drift

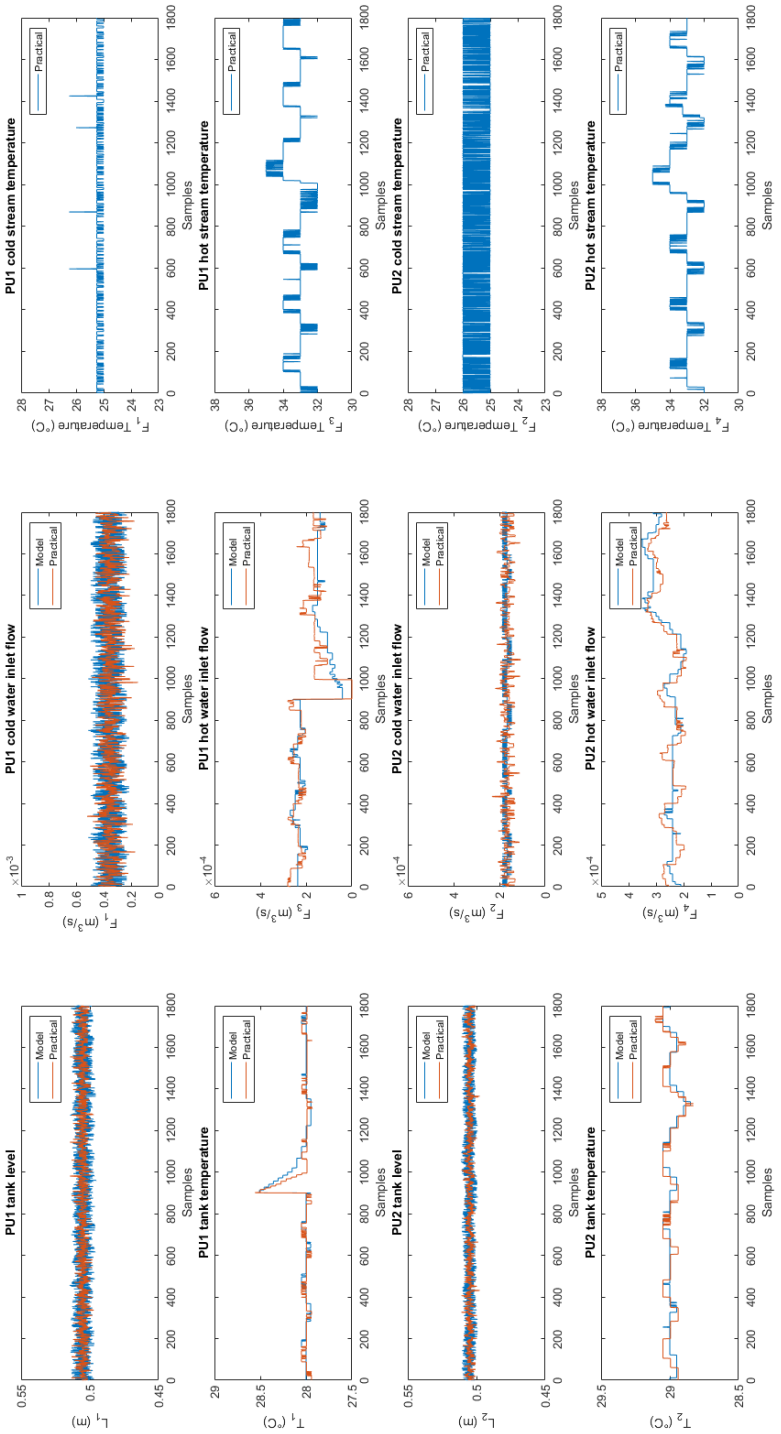


Figure A.16: Process results for a 2% sensor drift at sample 900

A.6.2 Process Unit 1 - 5% sensor drift

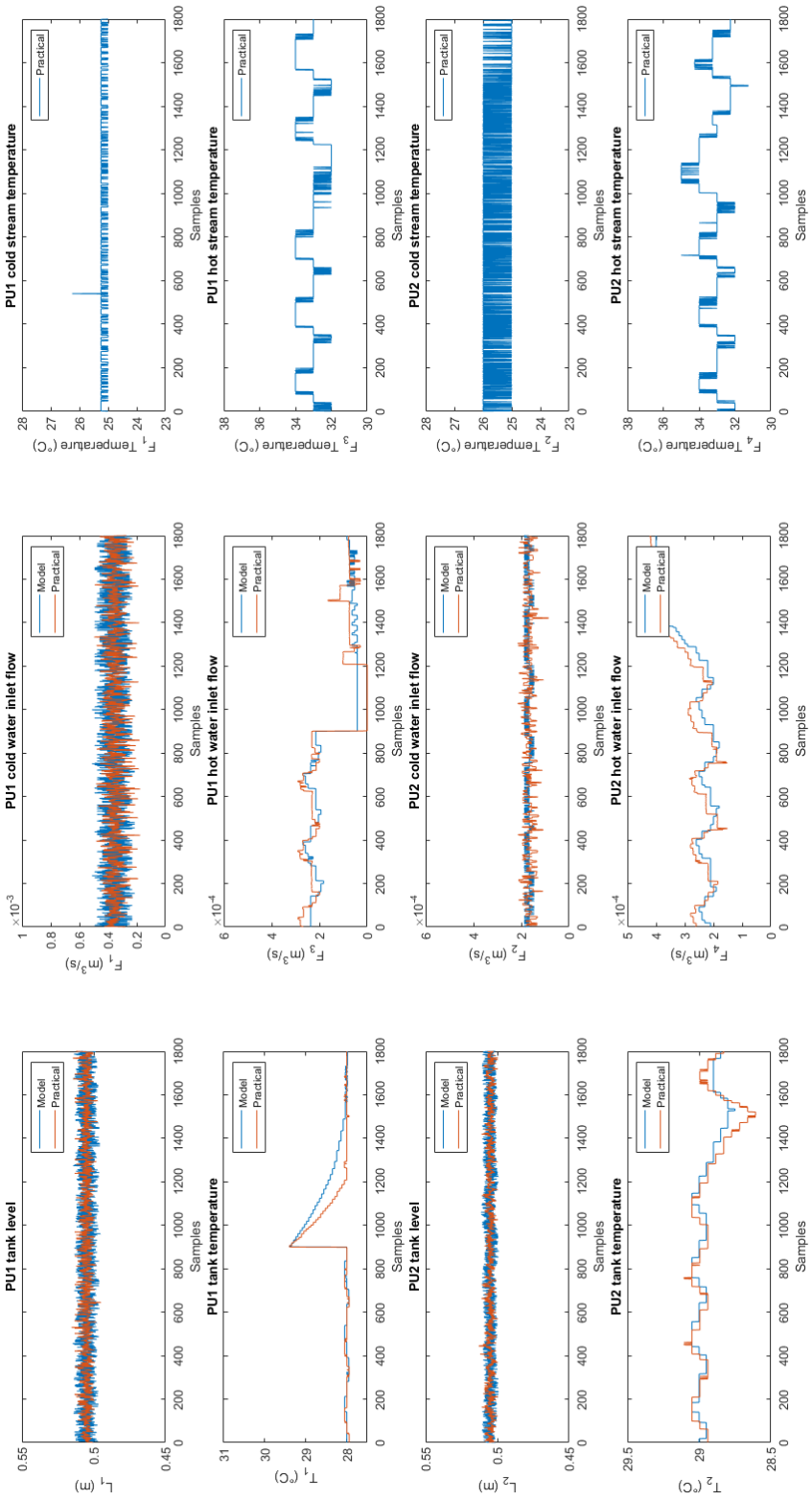


Figure A.17: Process results for a 5% sensor drift at sample 900

A.6.3 Process Unit 2 - 2% sensor drift

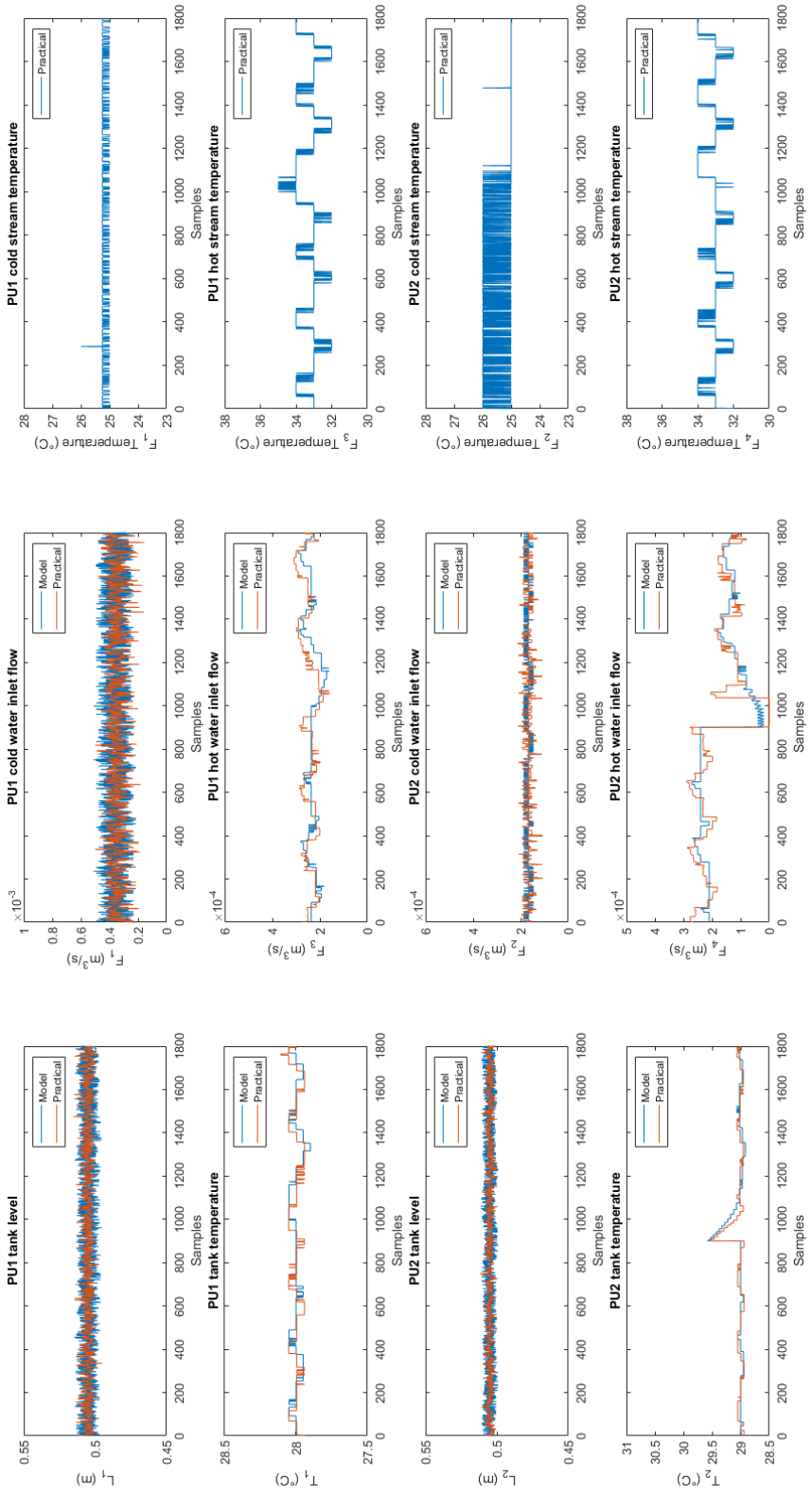


Figure A.18: Process results for a 2% sensor drift at sample 900

A.6.4 Process Unit 2 - 5% sensor drift

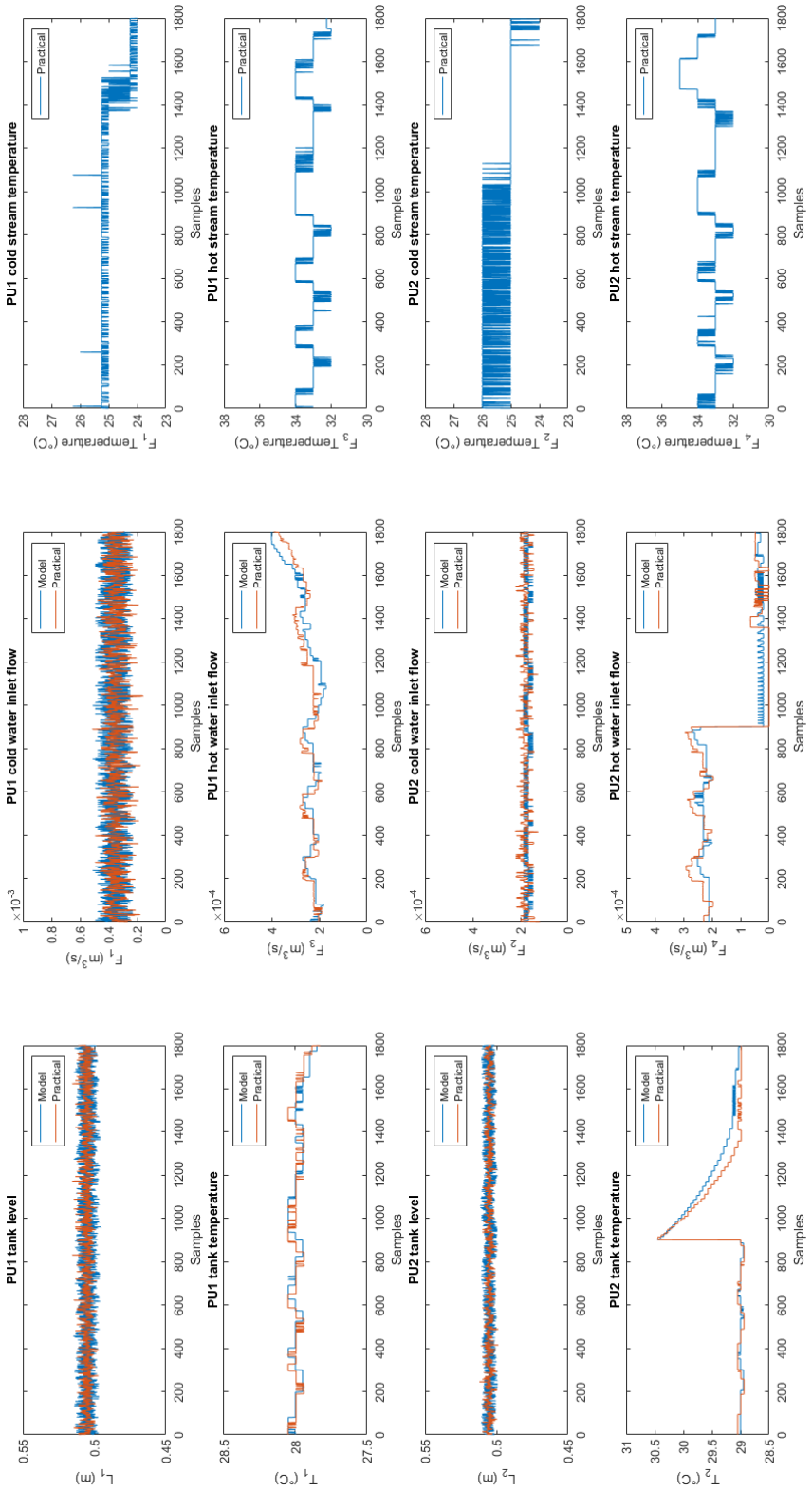


Figure A.19: Process results for a 5% sensor drift at sample 900

A.7 Fouling fault data

A.7.1 Process Unit 1 - 20% fouling

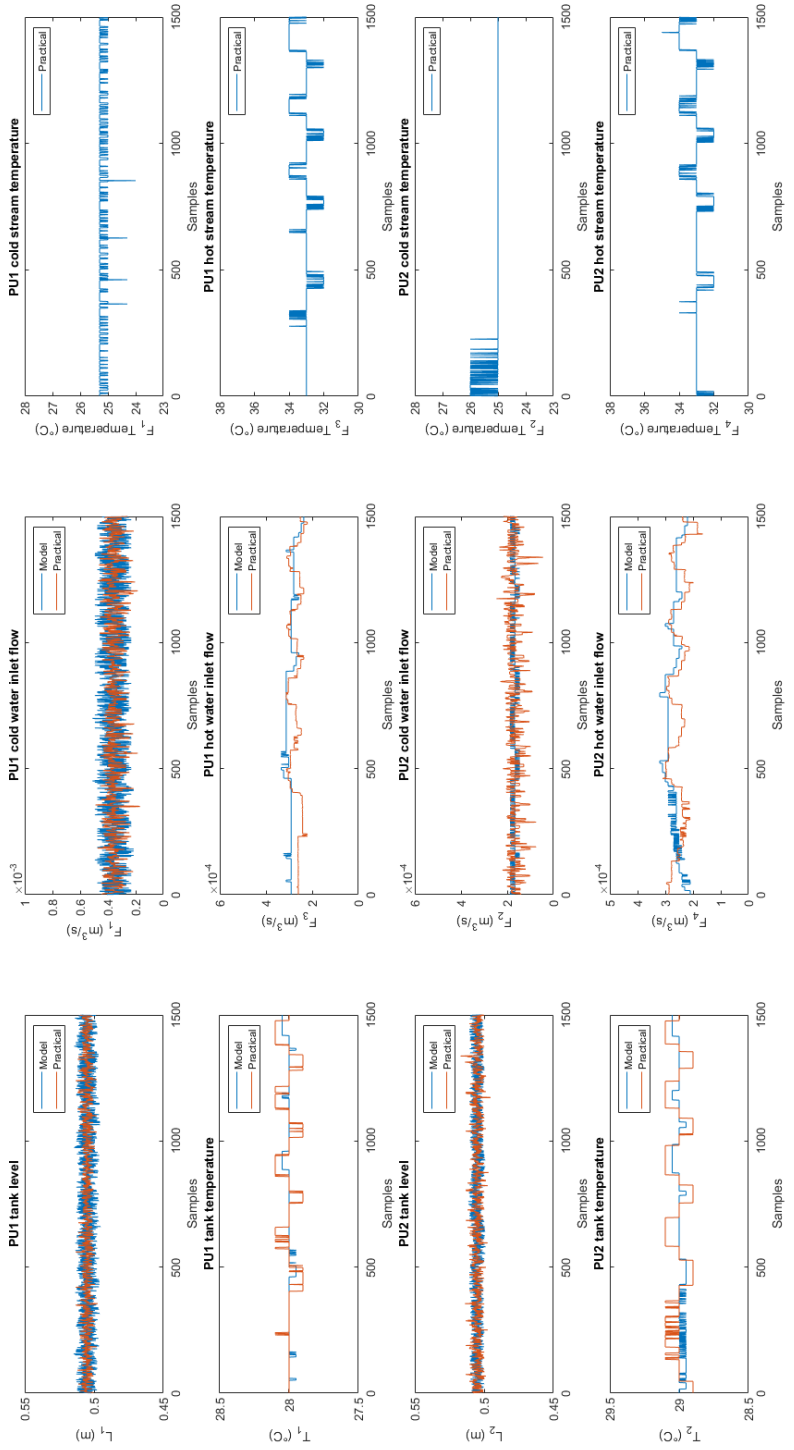


Figure A.20: Process results for a 20% fouling in PU1

A.7.2 Process Unit 2 - 20% fouling

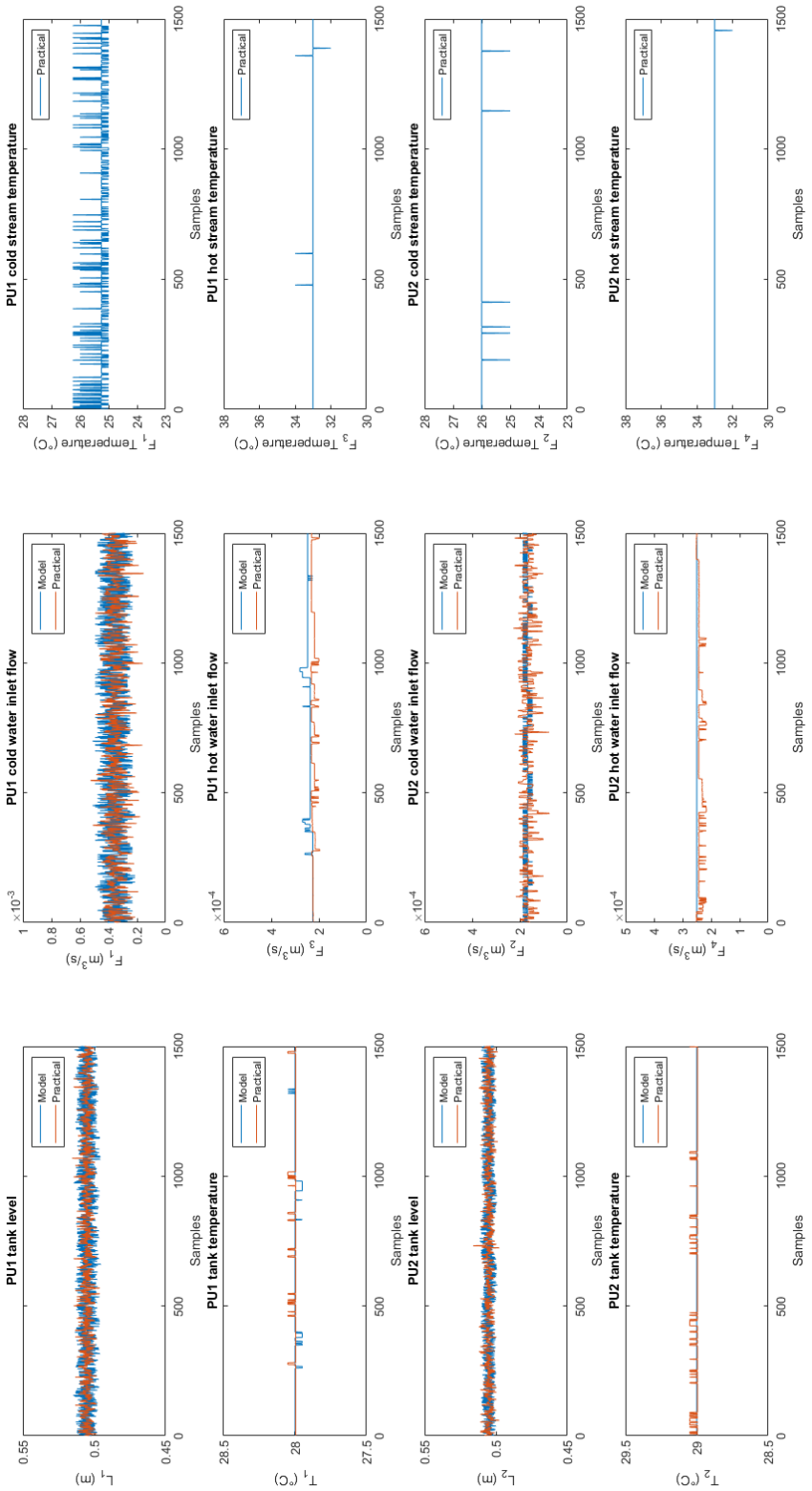


Figure A.21: Process results for a 20% fouling in PU2

APPENDIX

B

EGBV RESULTS

B.1 Introduction

The content in this appendix is supplementary to Chapter 4 in that all EGBV fault detection and isolation (FDI) results are supplied.

First, the EWMA detection plots are supplied for each fault from the model and practical system. Due to separately calculated control limits, the model and practical results are provided in separate figures. The model detection result will be directly followed by the practical test result for comparison. The fault-free, reference plots are also provided to illustrate normal behaviour. Each figure contains thirty plots, which illustrate the behaviour of each SVD element over time. The first row of plots shows the singular values (refer to Section 4.4.1). Each column of plots from row two to row six are the SVD elements contained in the singular vector that corresponds with the singular value in the top row. For example, the second plot in the first row will show the second singular value $\tilde{\sigma}_2$ and the plots beneath it represent the entries of the second singular vector.

Finally, the EGBV signature for each tested fault is provided. The model and practical fault signatures are given side-by-side for comparison. The trends and observations made from the results in this appendix are summarised in Section 4.5.

B.2 Fault detection results

B.2.1 Pre-EWMA normal operation - Model

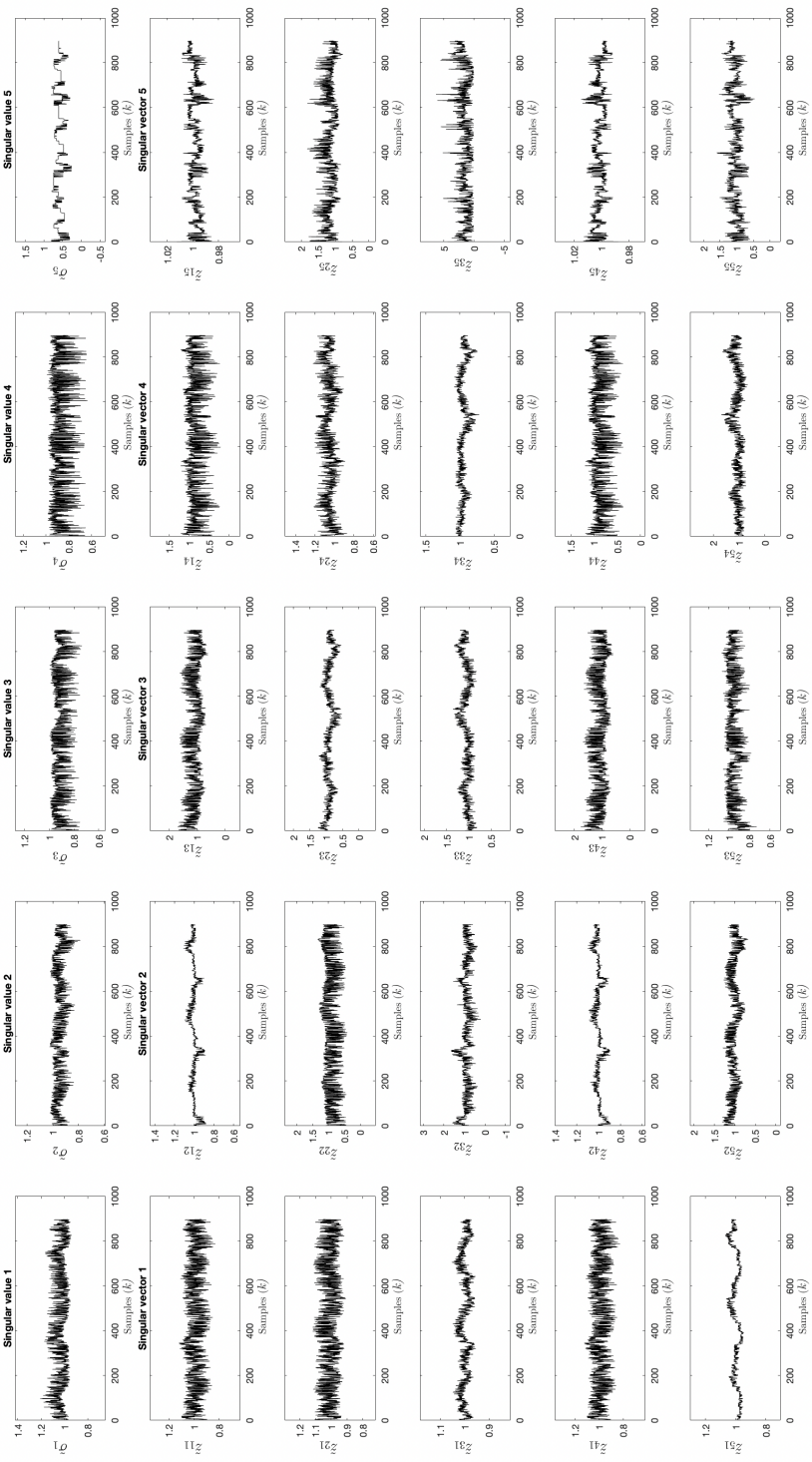


Figure B.1: Normalised SVD results for model NOC

B.2.2 Normal operation - Model

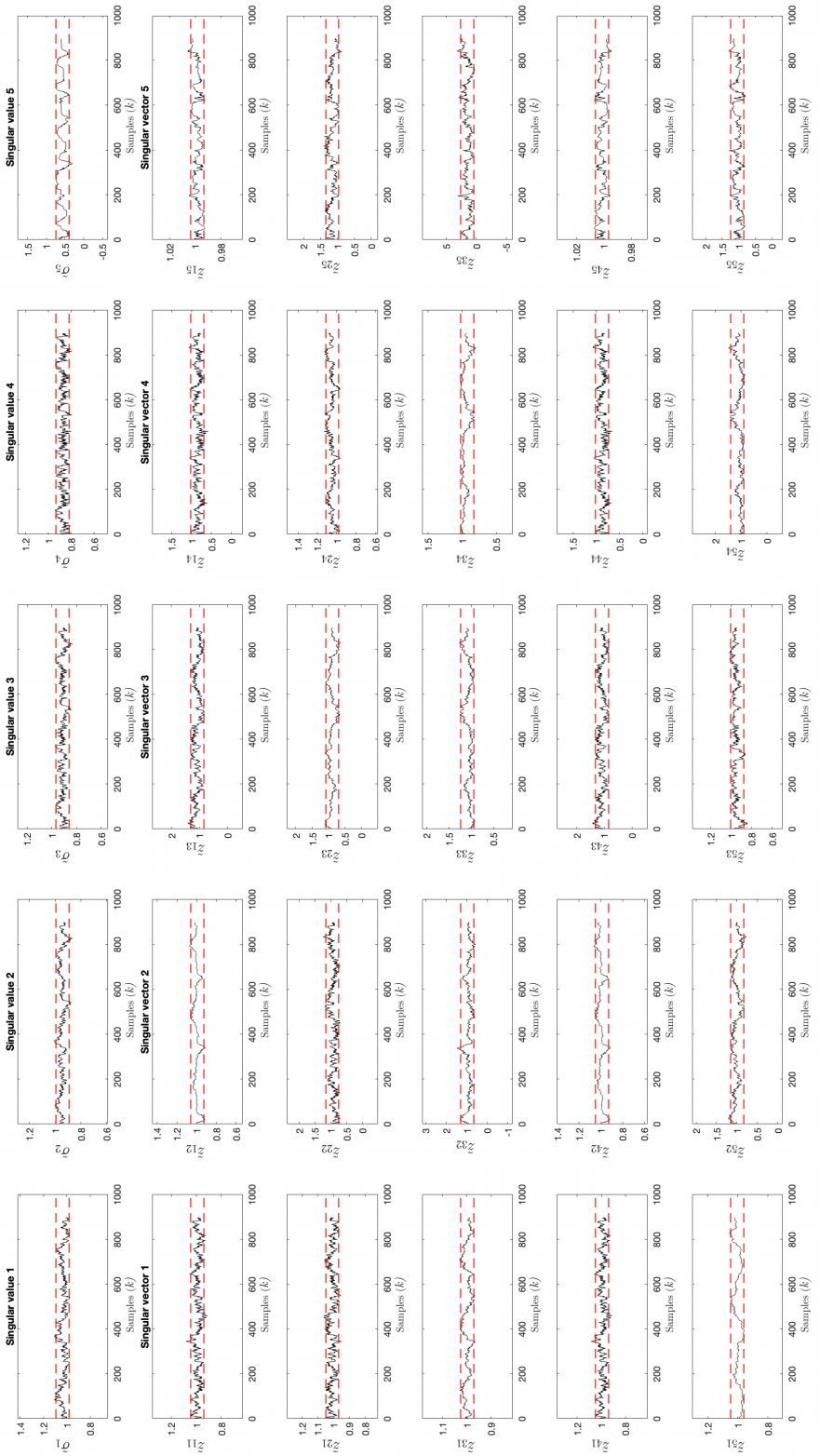


Figure B.2: EWMA SVD results for model NOC

B.2.3 Normal operation - Practical

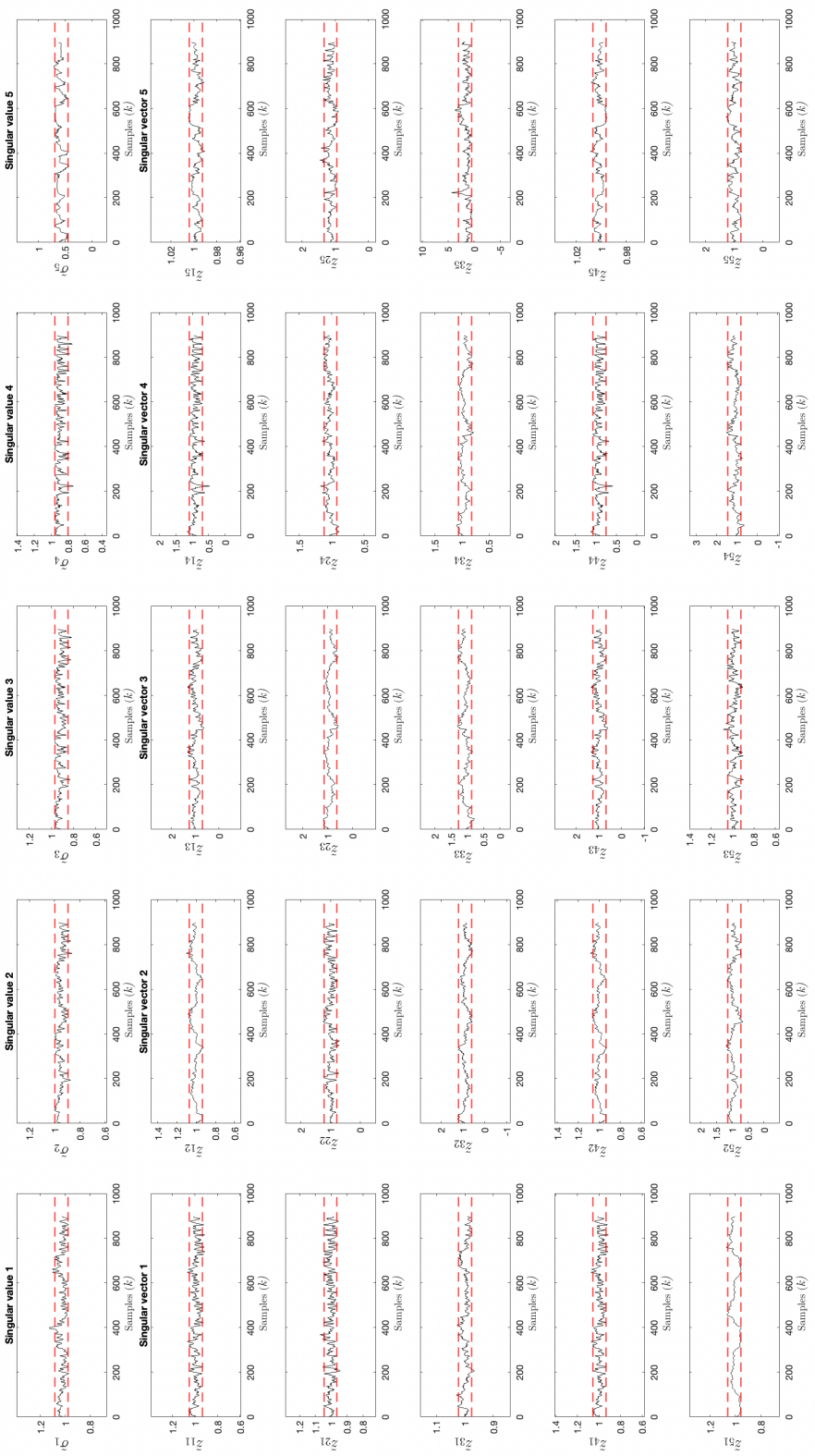


Figure B.3: EWMA SVD results for practical NOC

B.2.4 Process Unit 1 Clogs - Model

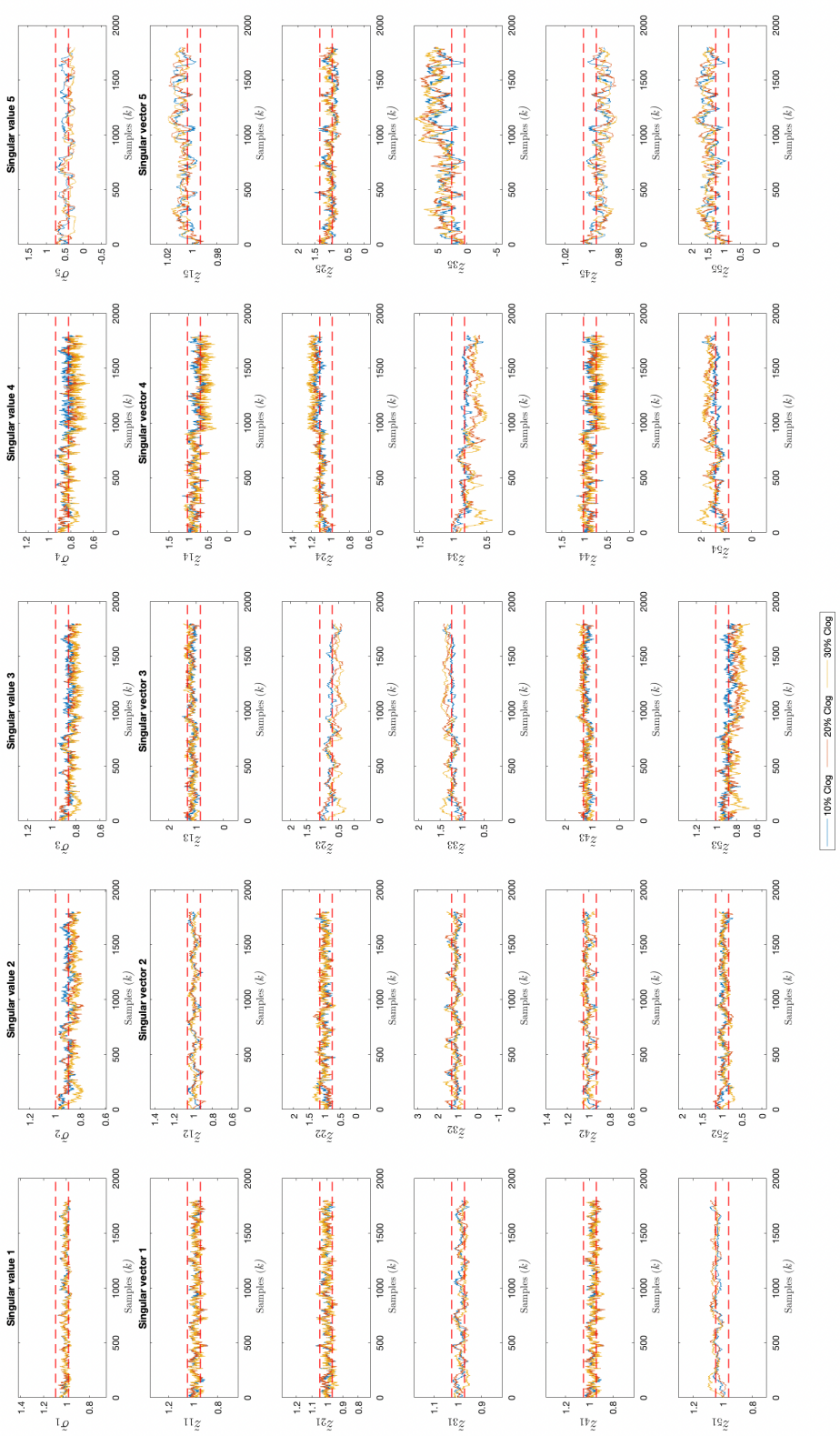


Figure B.4: EWMA SVD results for PU1 clogging at sample 900

B.2.5 Process Unit 1 Clogs - Practical

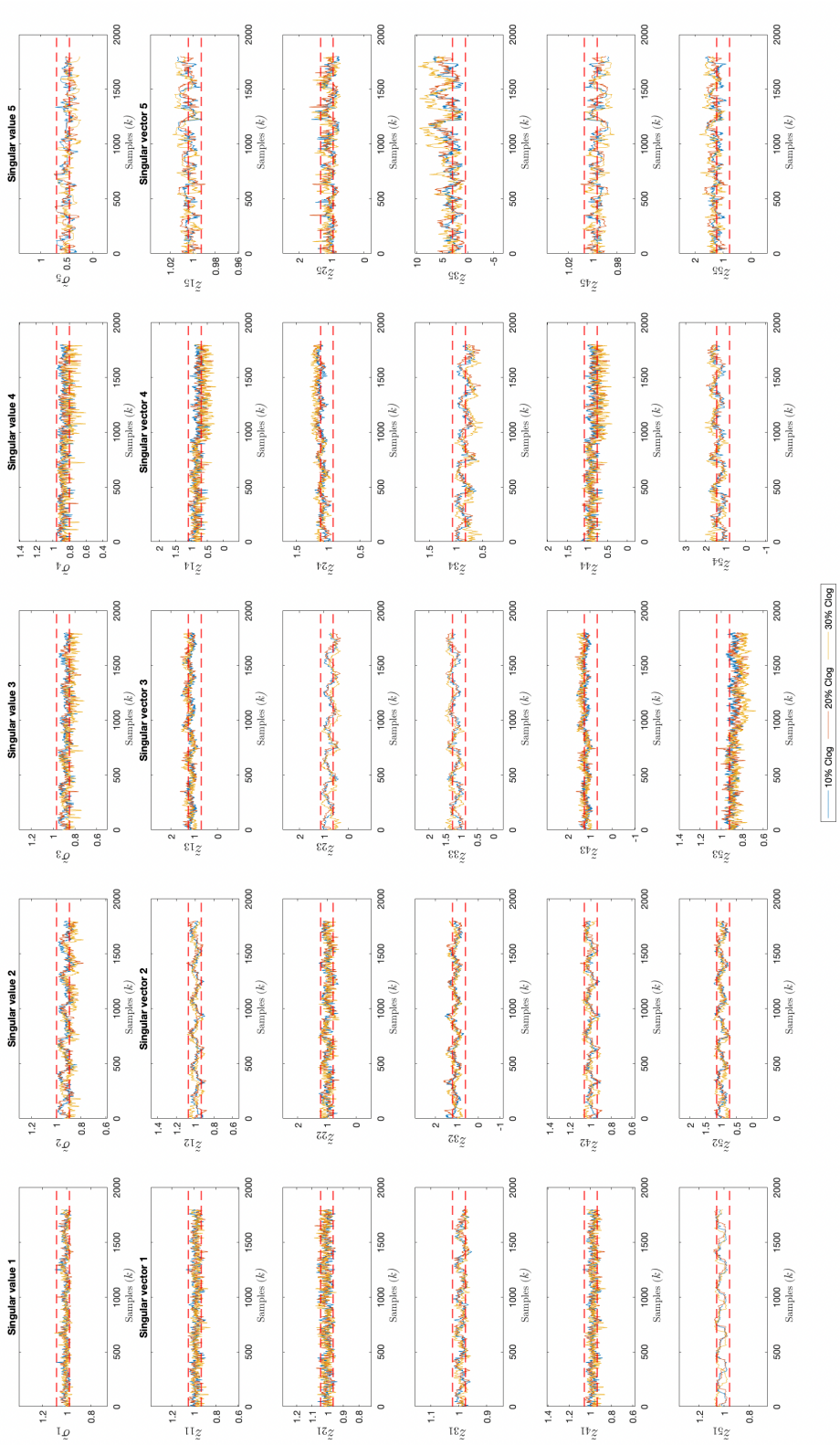


Figure B.5: EWMA SVD results for PU1 clogging at sample 900

B.2.6 Process Unit 2 Clogs - Model

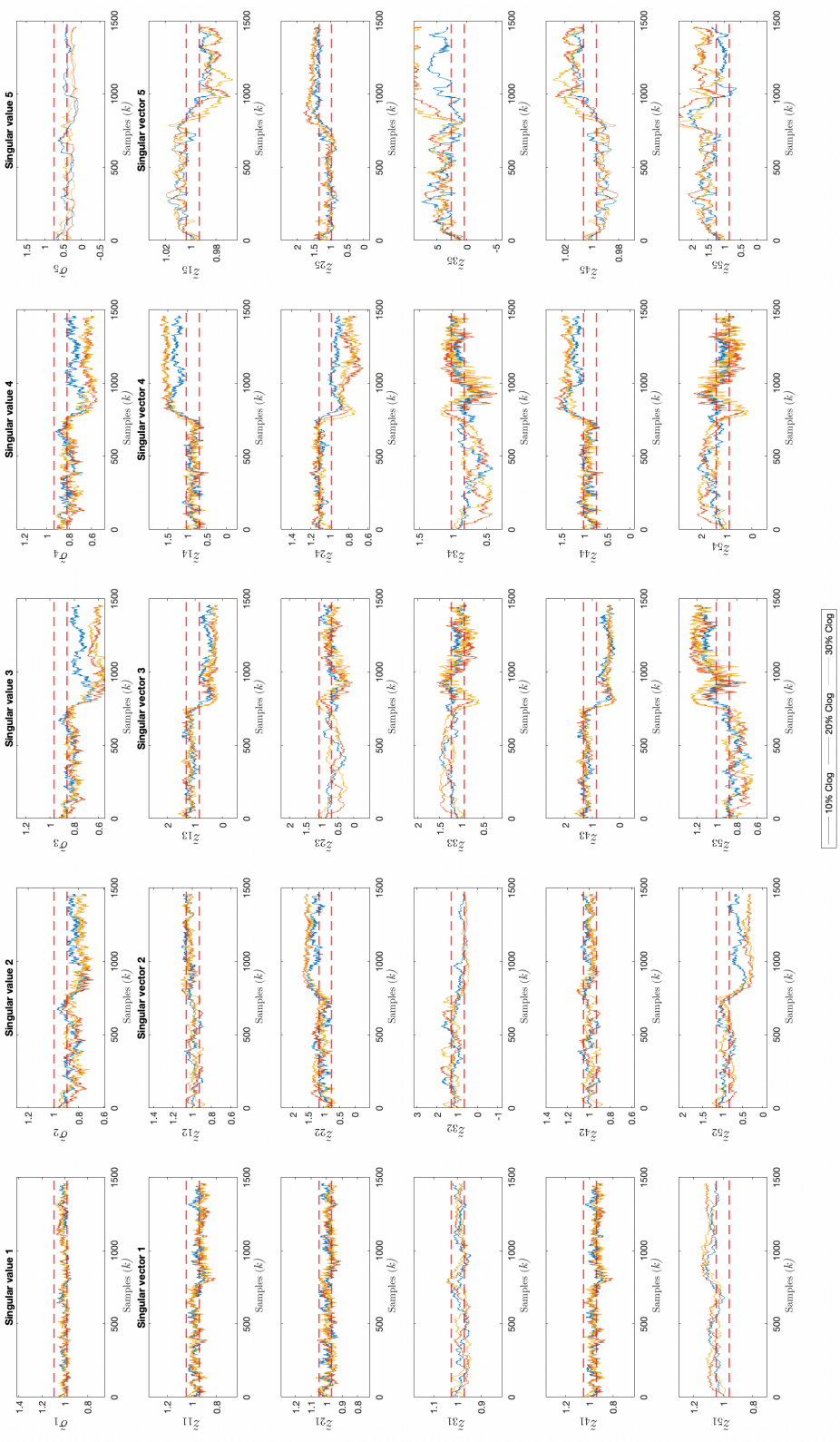


Figure B.6: EWMA SVD results for PU2 clogging at sample 729

B.2.7 Process Unit 2 Clogs - Practical

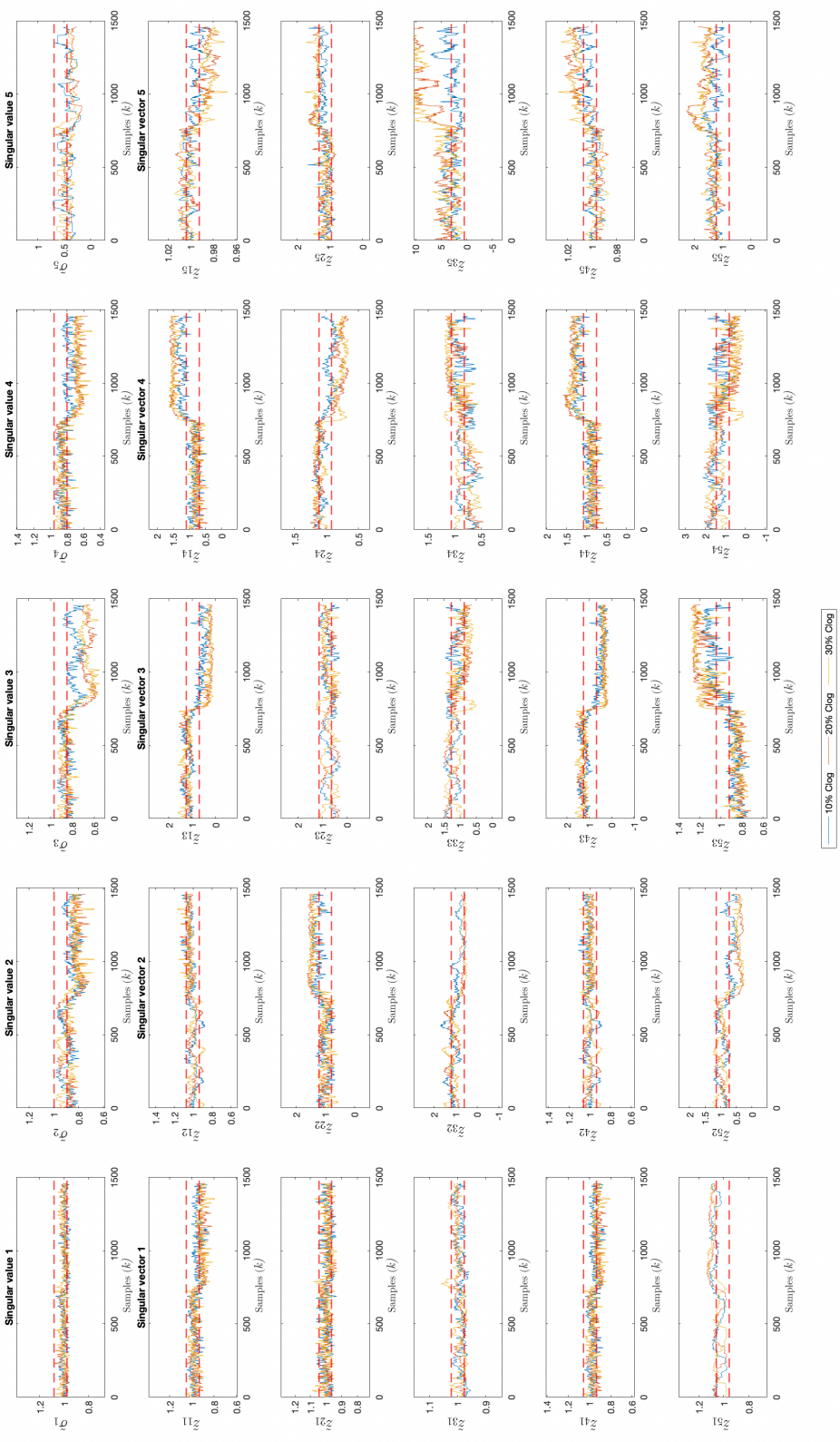


Figure B.7: EWMA SVD results for PU2 clogging at sample 729

B.2.8 Process Unit 1 Leaks - Model

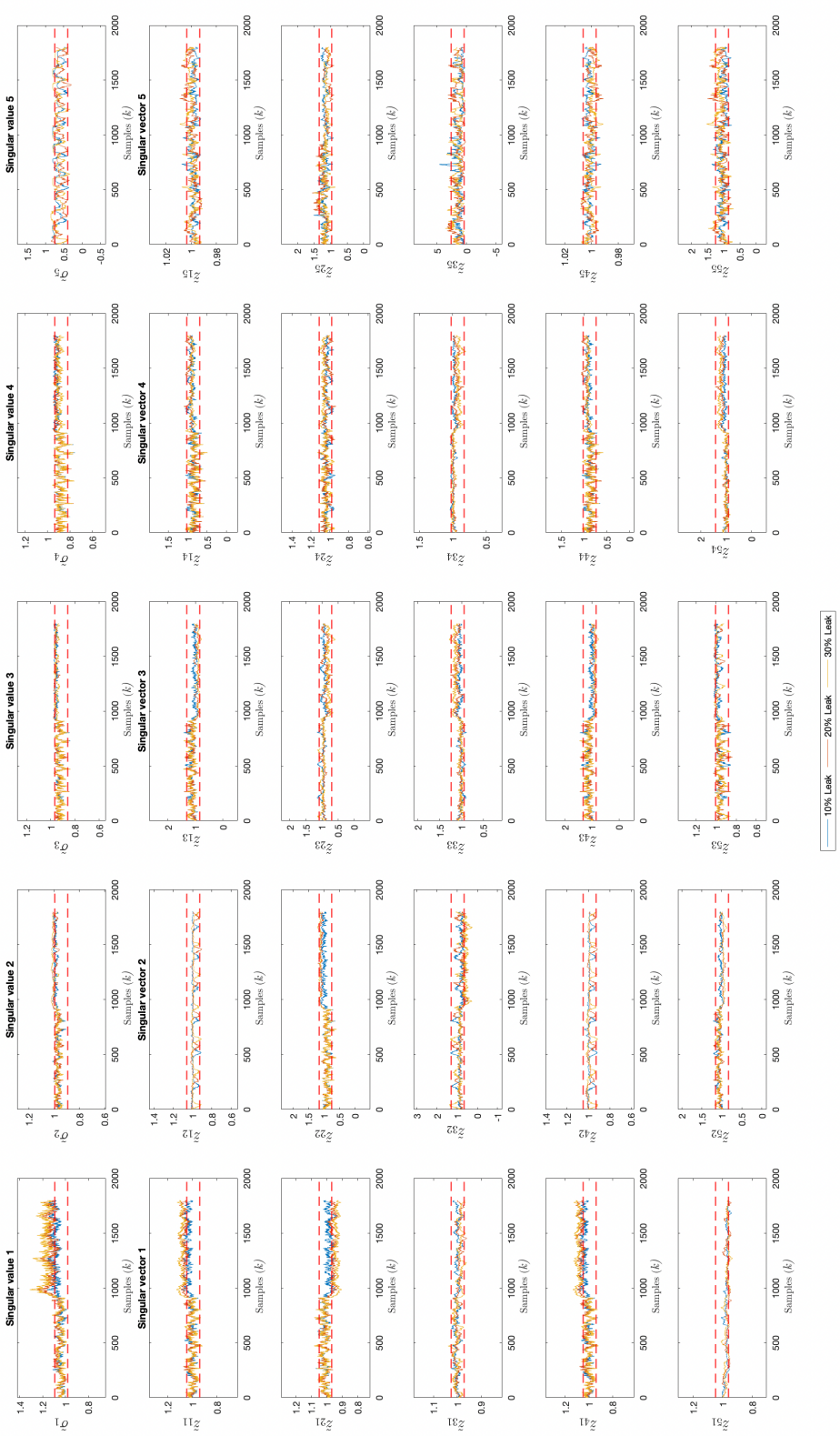


Figure B.8: EWMA SVD results for PU1 leakage at sample 900

B.2.9 Process Unit 1 Leaks - Practical

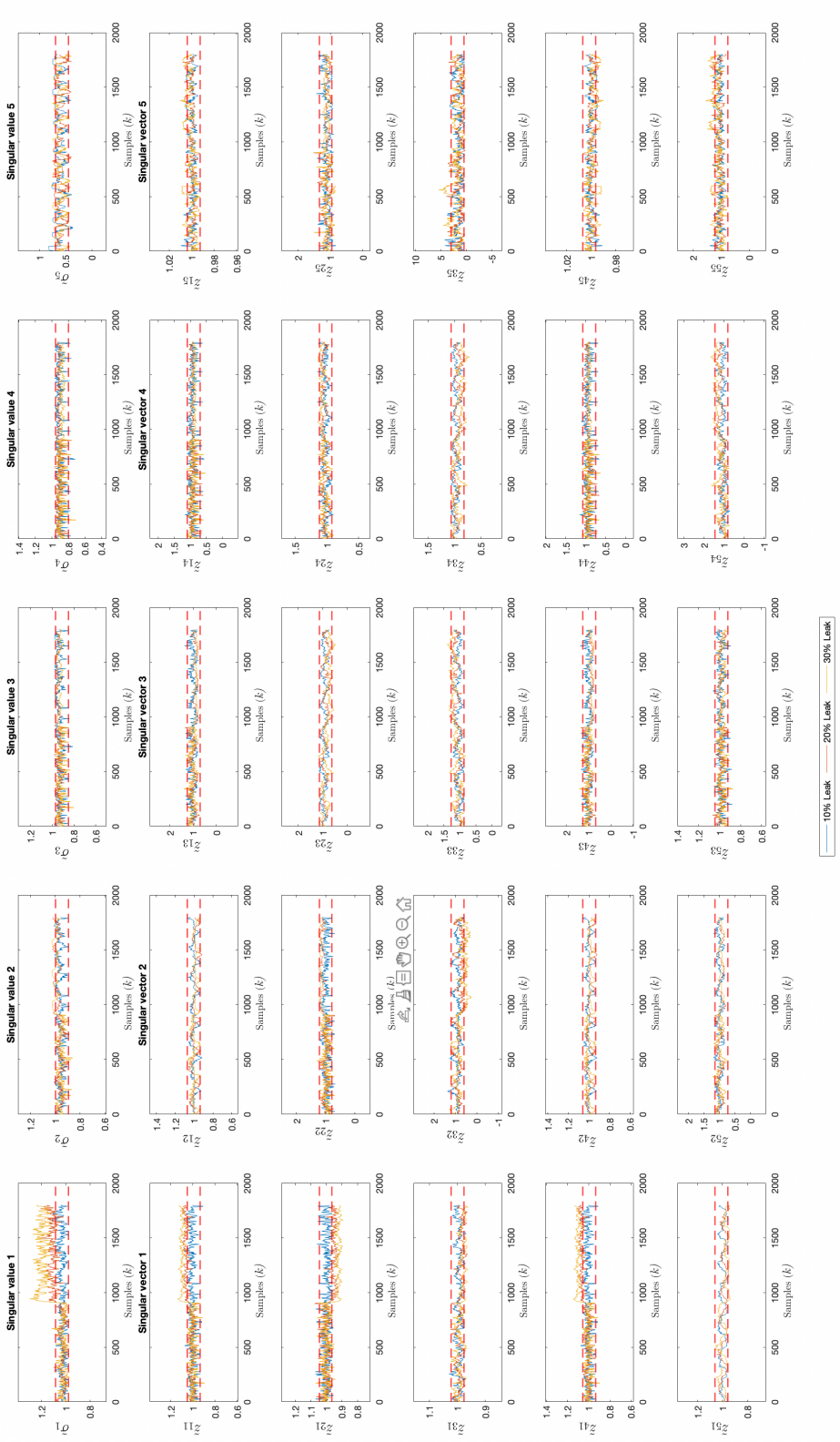


Figure B.9: EWMA SVD results for PU1 leakage at sample 900

B.2.10 Process Unit 2 Leaks - Model

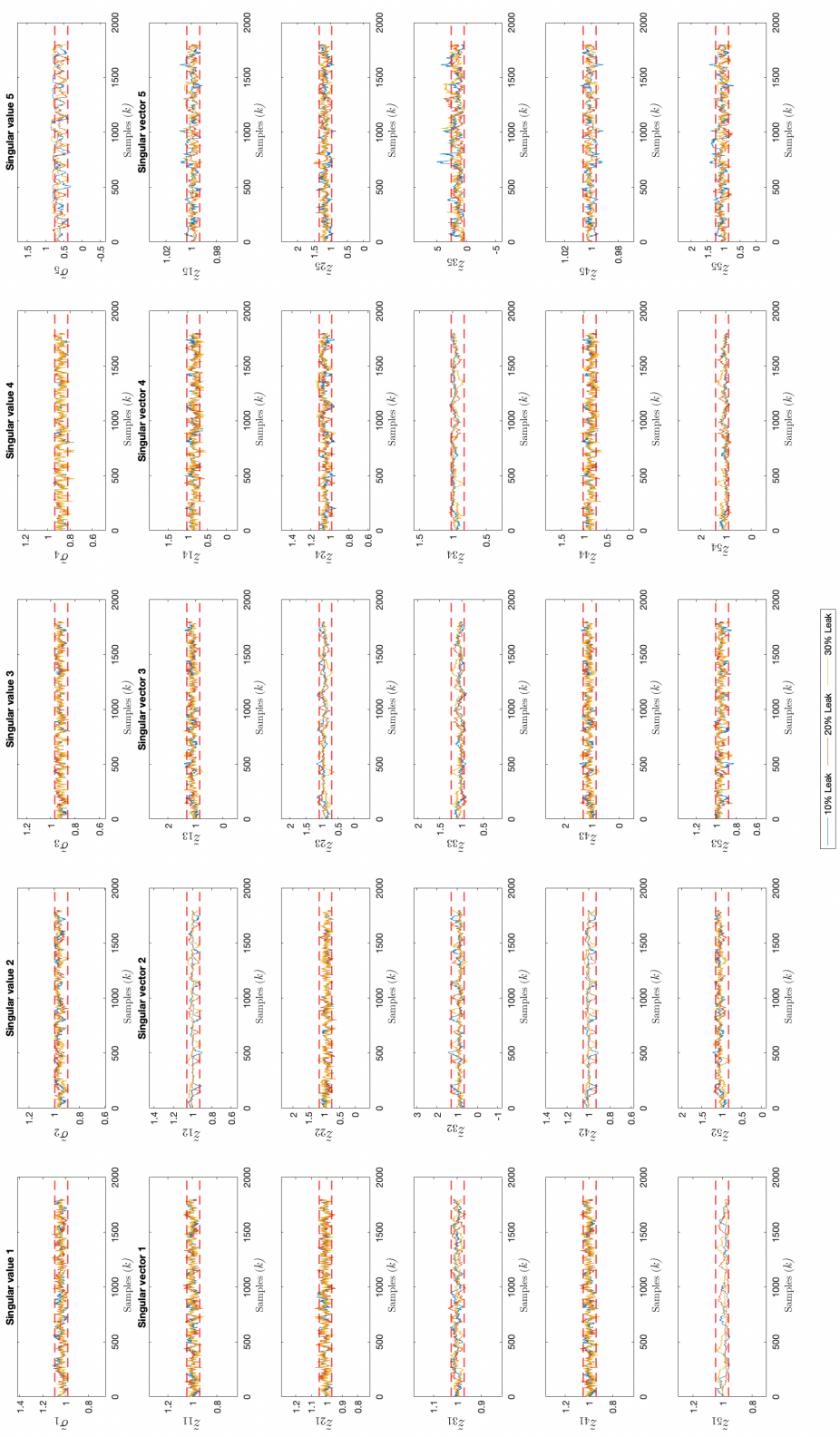


Figure B.10: EWMA SVD results for PU2 leakage at sample 900

B.2.11 Process Unit 2 Leaks - Practical

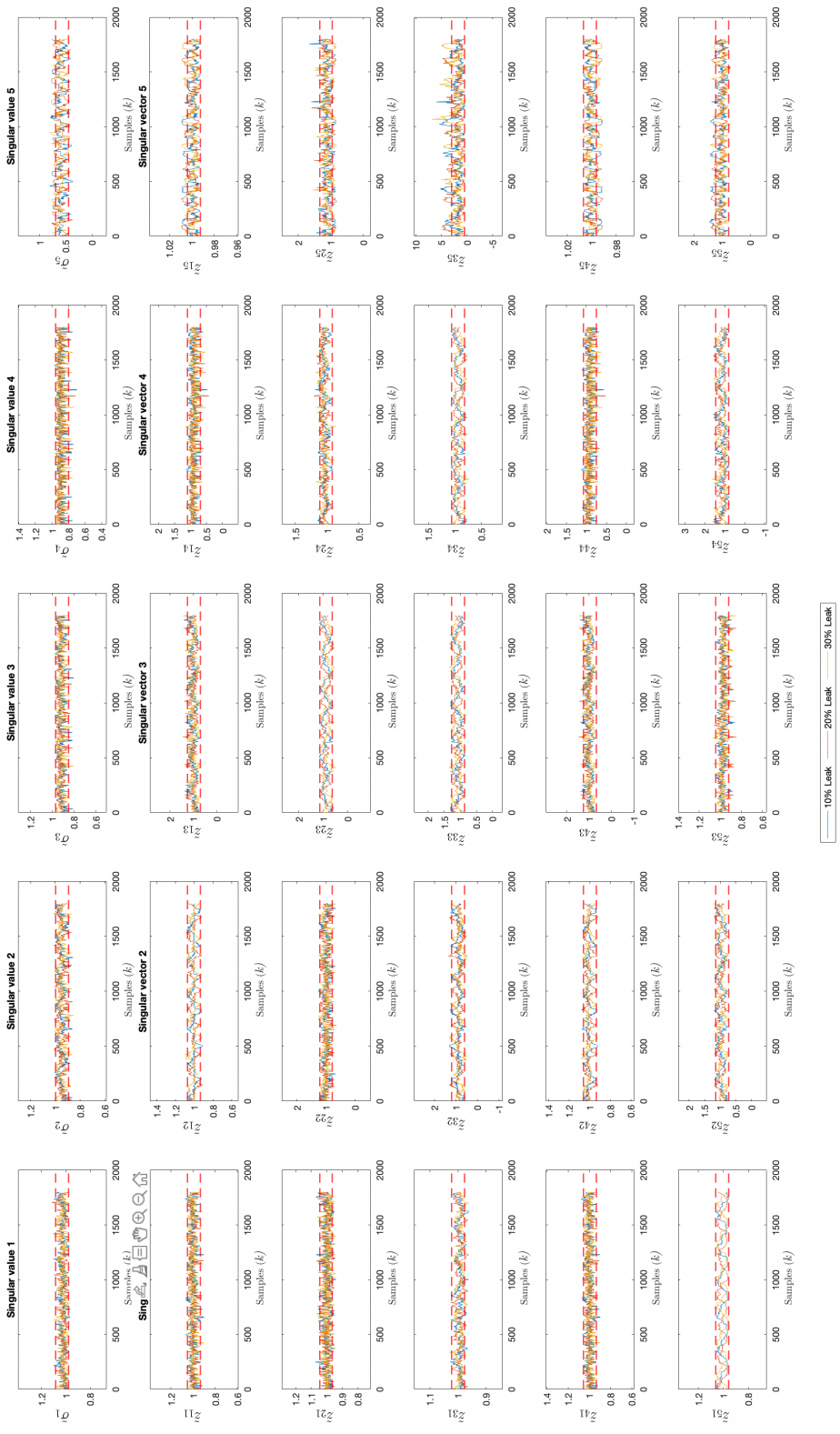


Figure B.11: EWMA SVD results for PU2 leakage at sample 900

B.2.12 Process Unit 1 stuck valve - Model

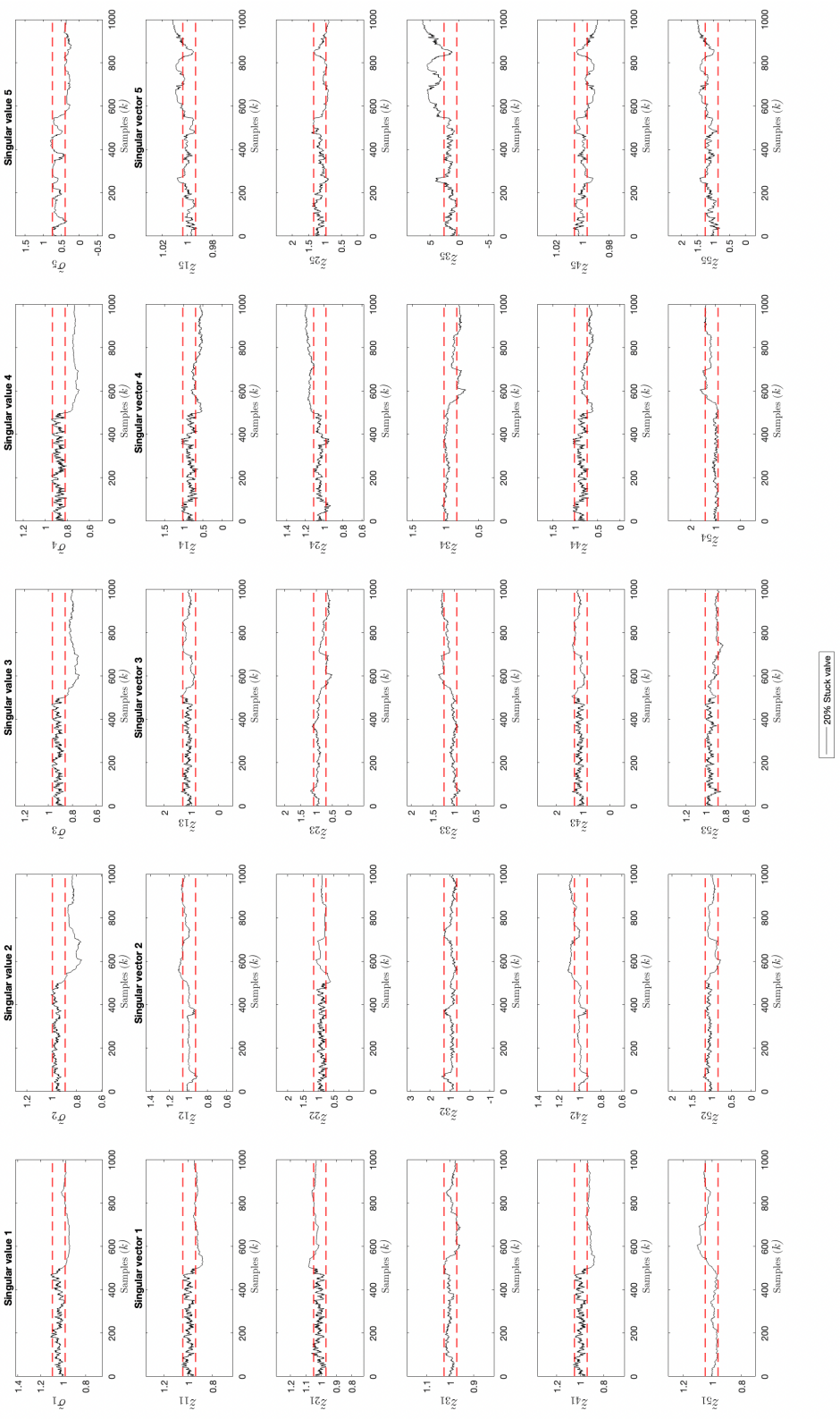


Figure B.12: EWMA SVD results for PU1 stuck valve at sample 500

B.2.13 Process Unit 1 stuck valve - Practical

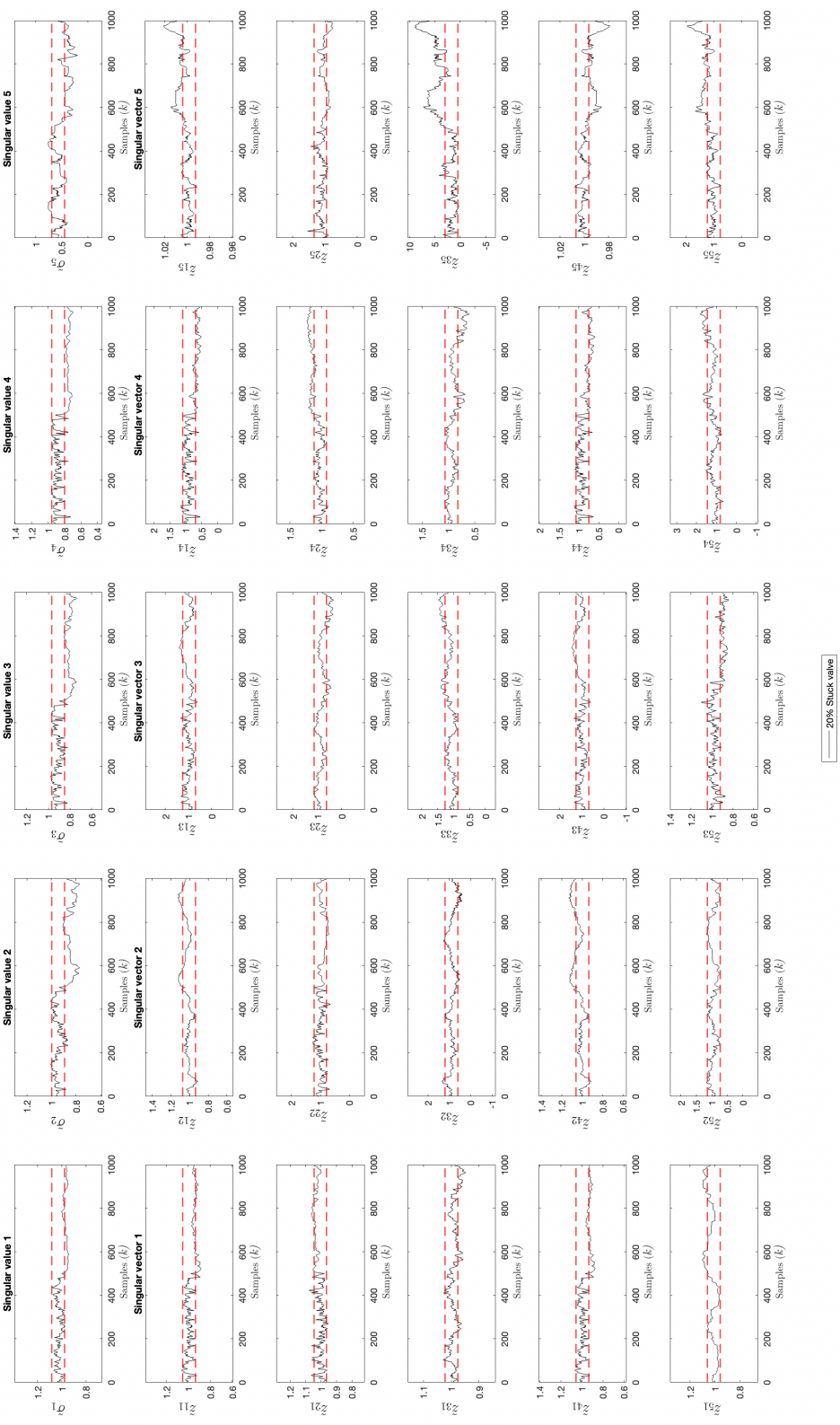


Figure B.13: EWMA SVD results for PU1 stuck valve at sample 500

B.2.14 Process Unit 2 stuck valve - Model

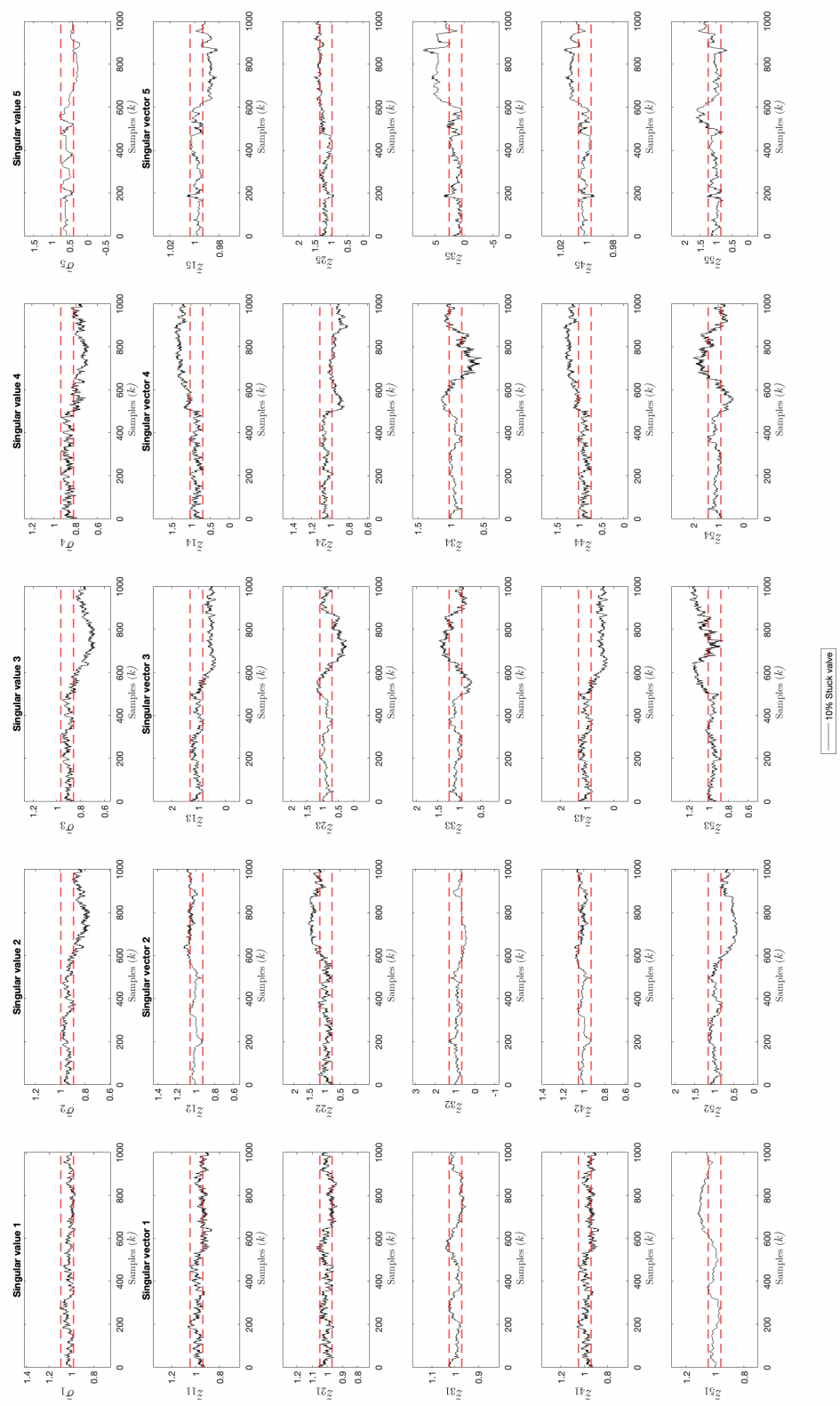


Figure B.14: EWMA SVD results for PU2 stuck valve at sample 500

B.2.15 Process Unit 2 stuck valve - Practical

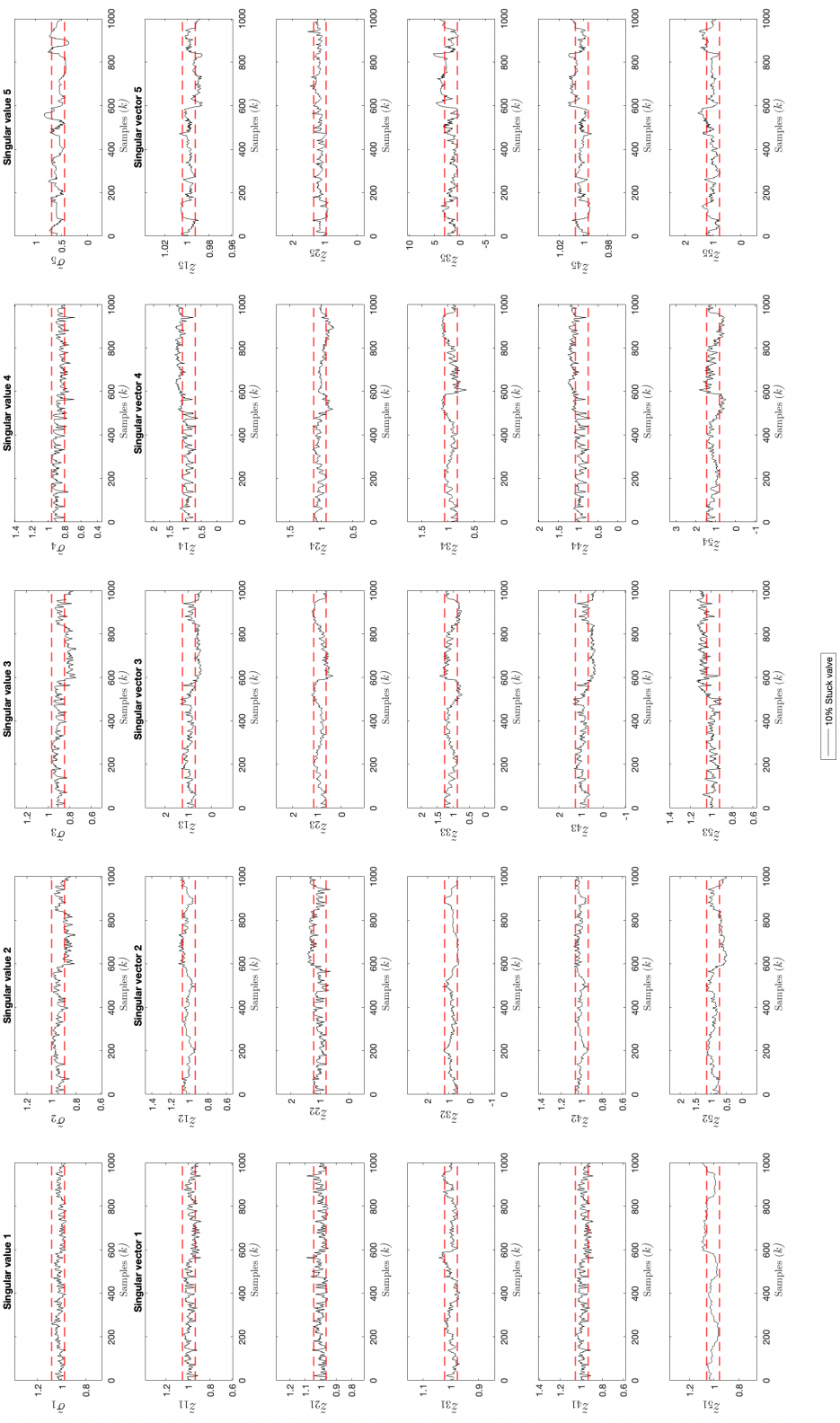


Figure B.15: EWMA SVD results for PU2 stuck valve at sample 500

B.2.16 Process Unit 1 sensor drifts - Model

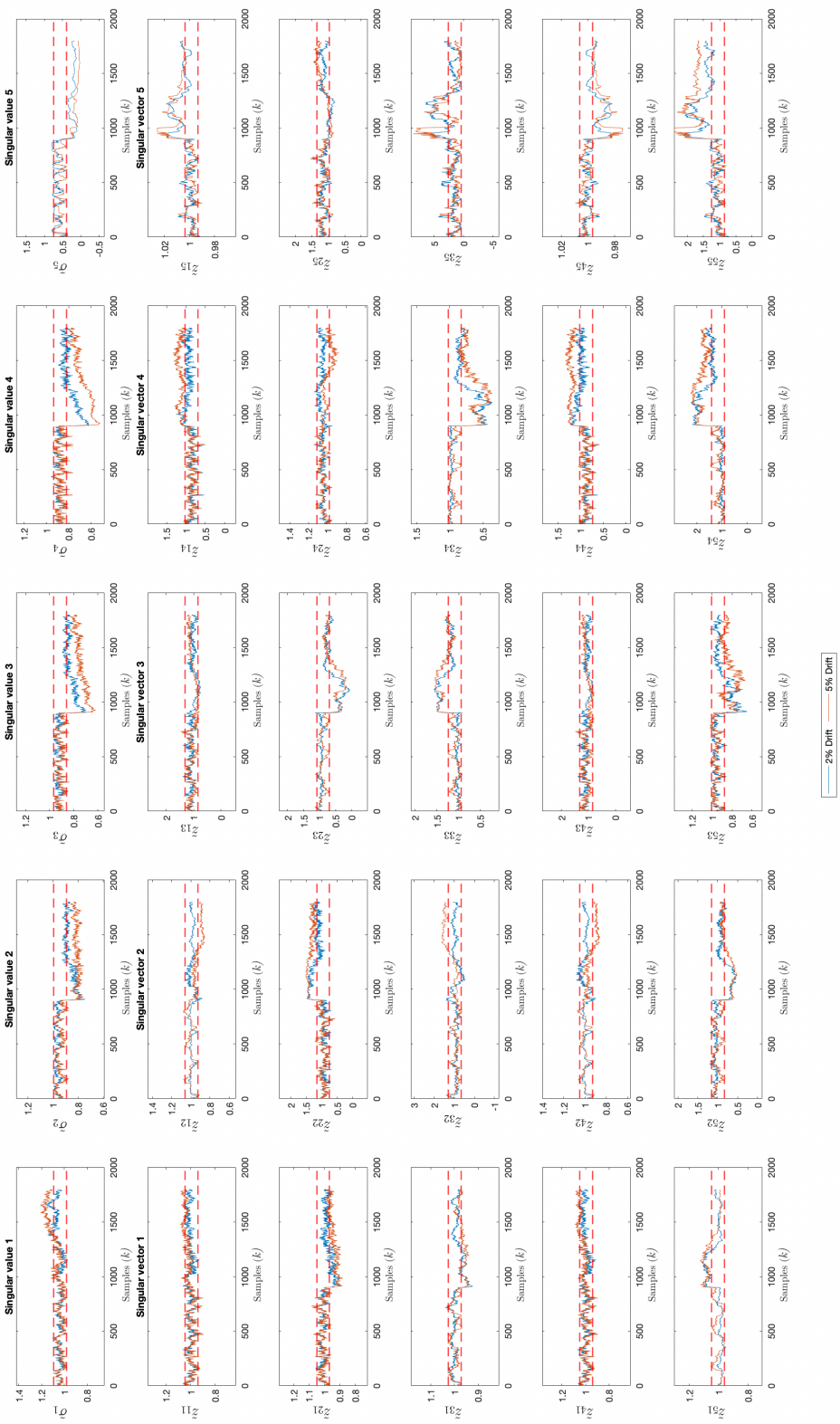


Figure B.16: EWMA SVD results for PU1 sensor drifts at sample 900

B.2.17 Process Unit 1 sensor drifts - Practical

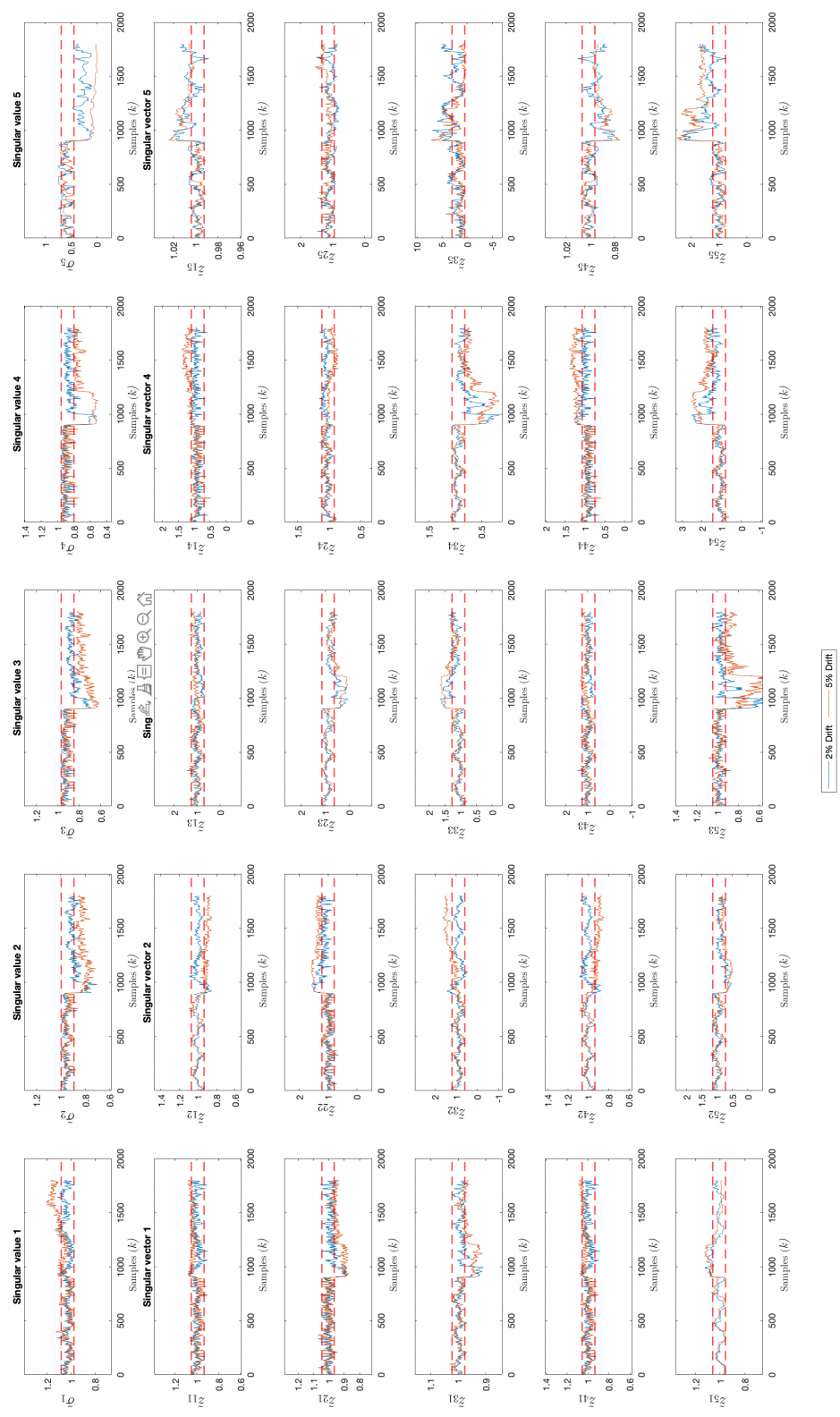


Figure B.17: EWMA SVD results for PU1 sensor drifts at sample 900

B.2.18 Process Unit 2 sensor drifts - Model

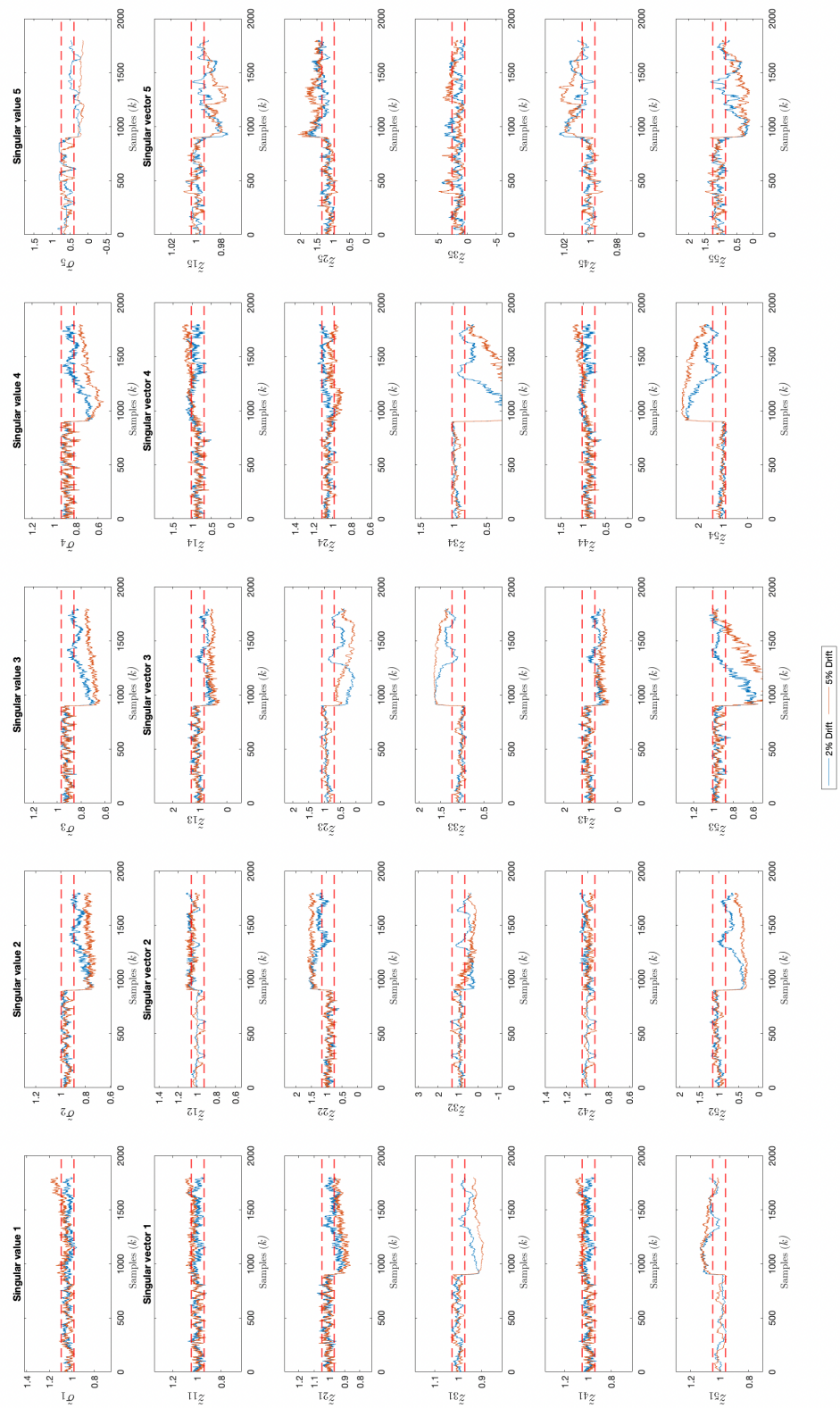


Figure B.18: EWMA SVD results for PU2 sensor drifts at sample 900

B.2.19 Process Unit 2 sensor drifts - Practical

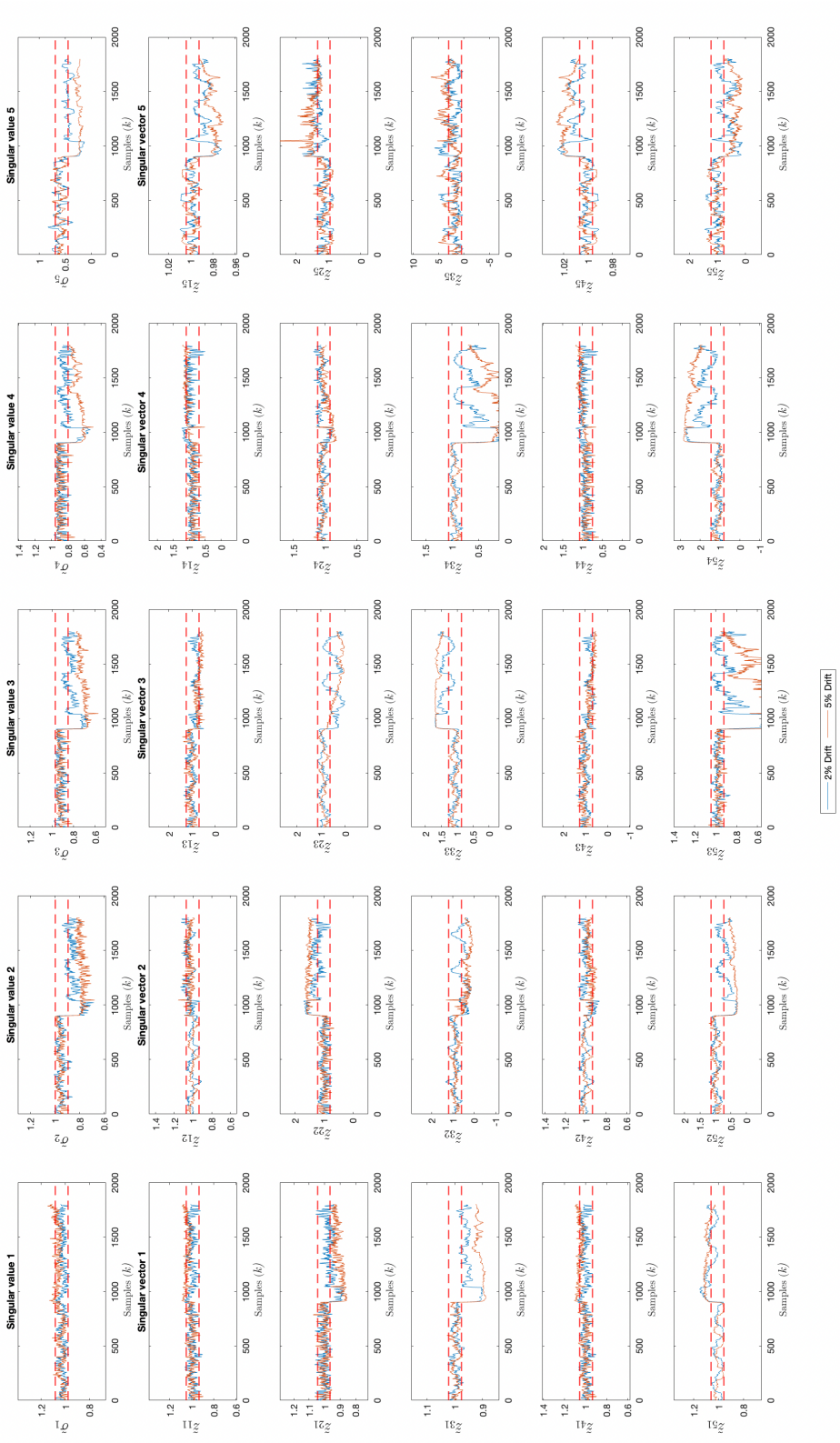


Figure B.19: EWMA SVD results for PU2 sensor drifts at sample 900

B.2.20 Process Unit 1 fouling - Model

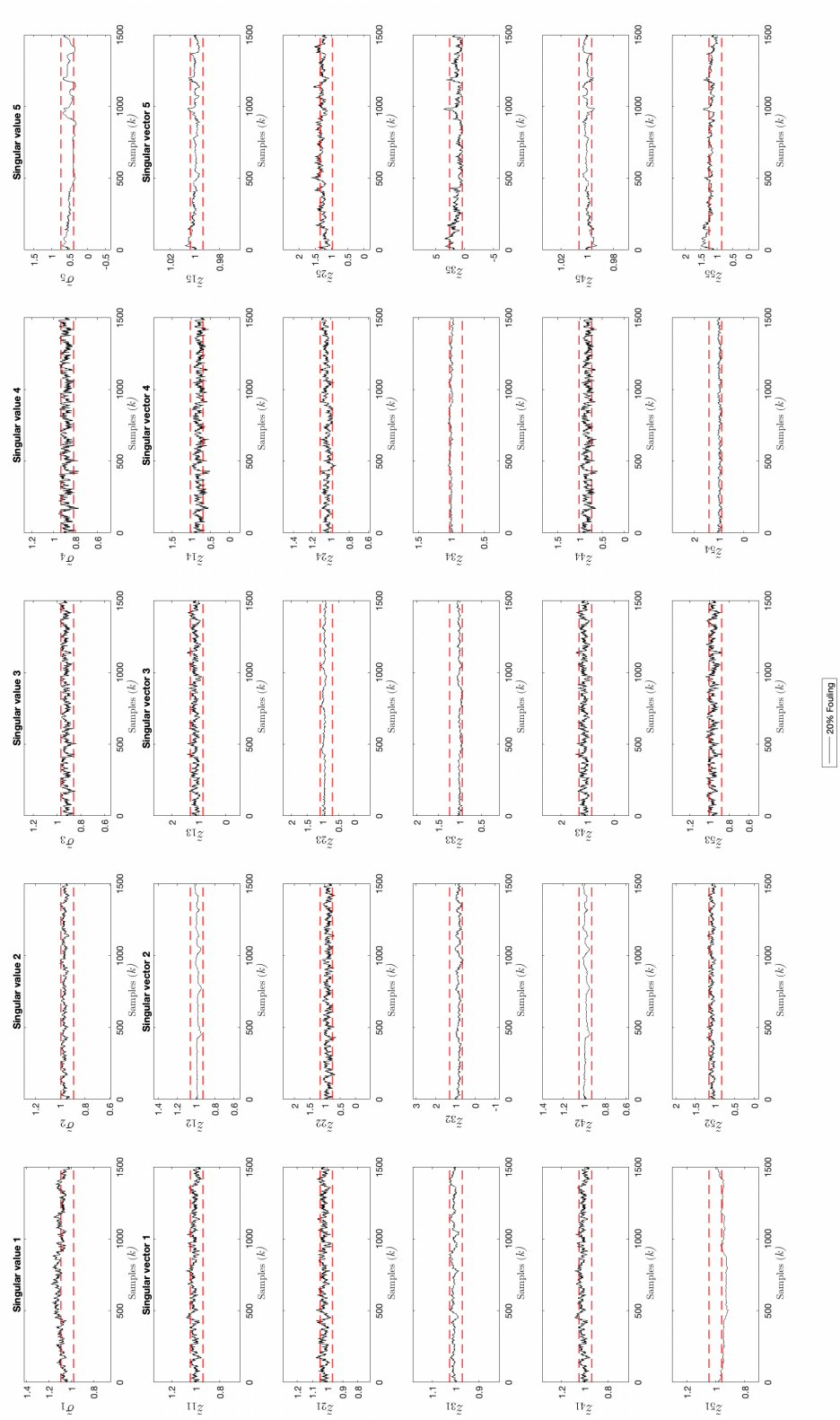


Figure B.20: EWMA SVD results for PU1 fouling

B.2.21 Process Unit 1 fouling - Practical

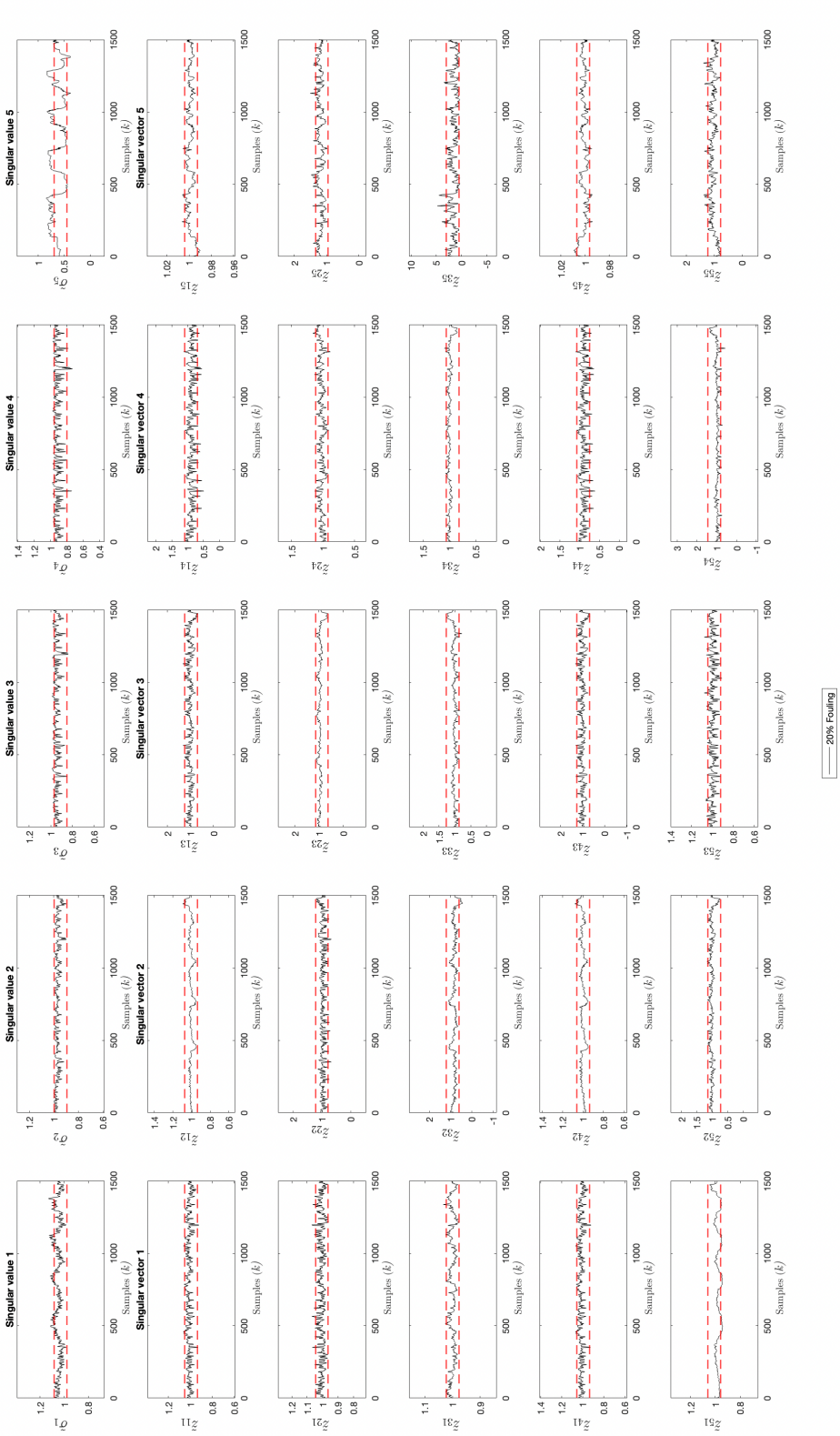


Figure B.21: EWMA SVD results for PU1 fouling

B.2.22 Process Unit 2 fouling - Model

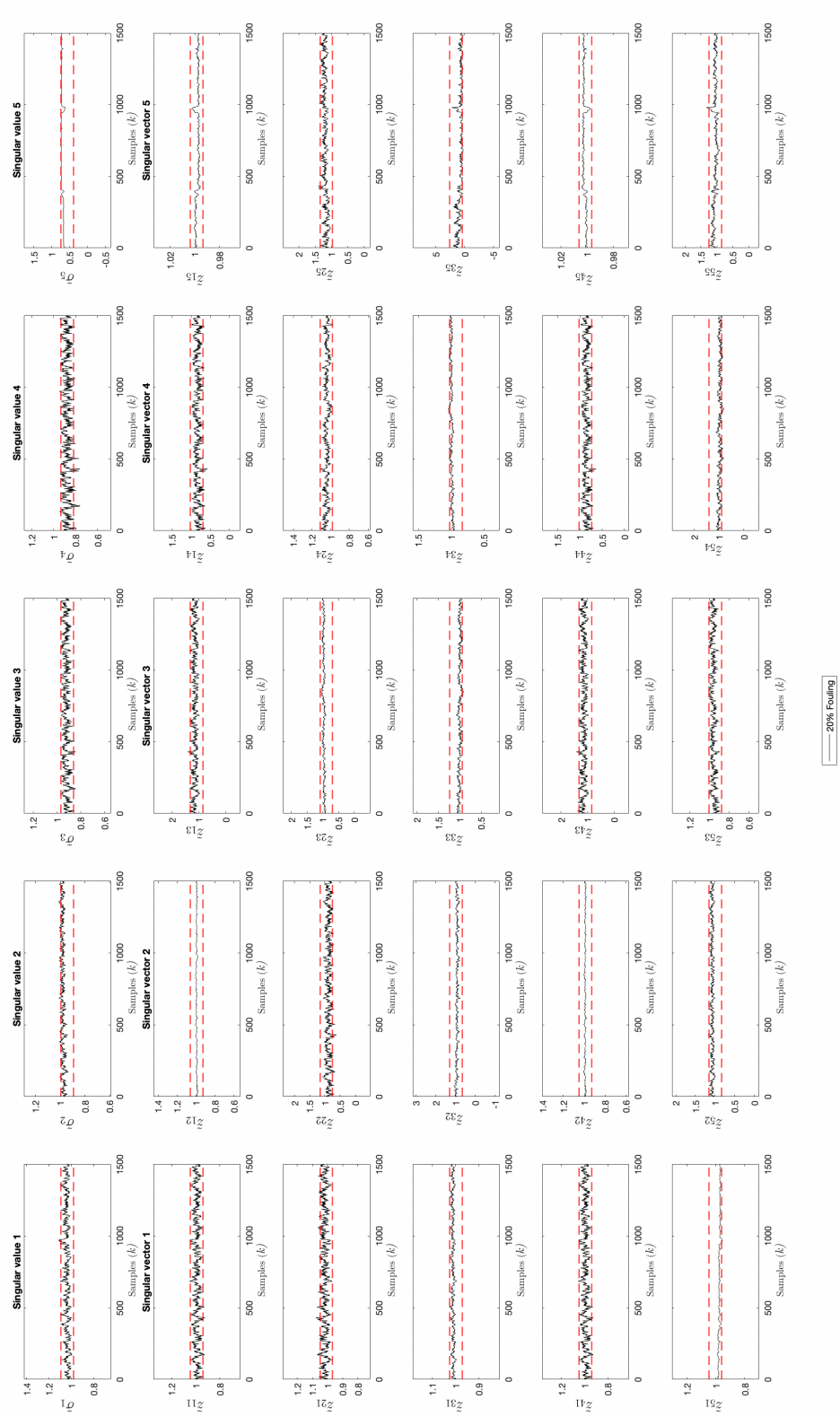


Figure B.22: EWMA SVD results for PU2 fouling

B.2.23 Process Unit 2 fouling - Practical

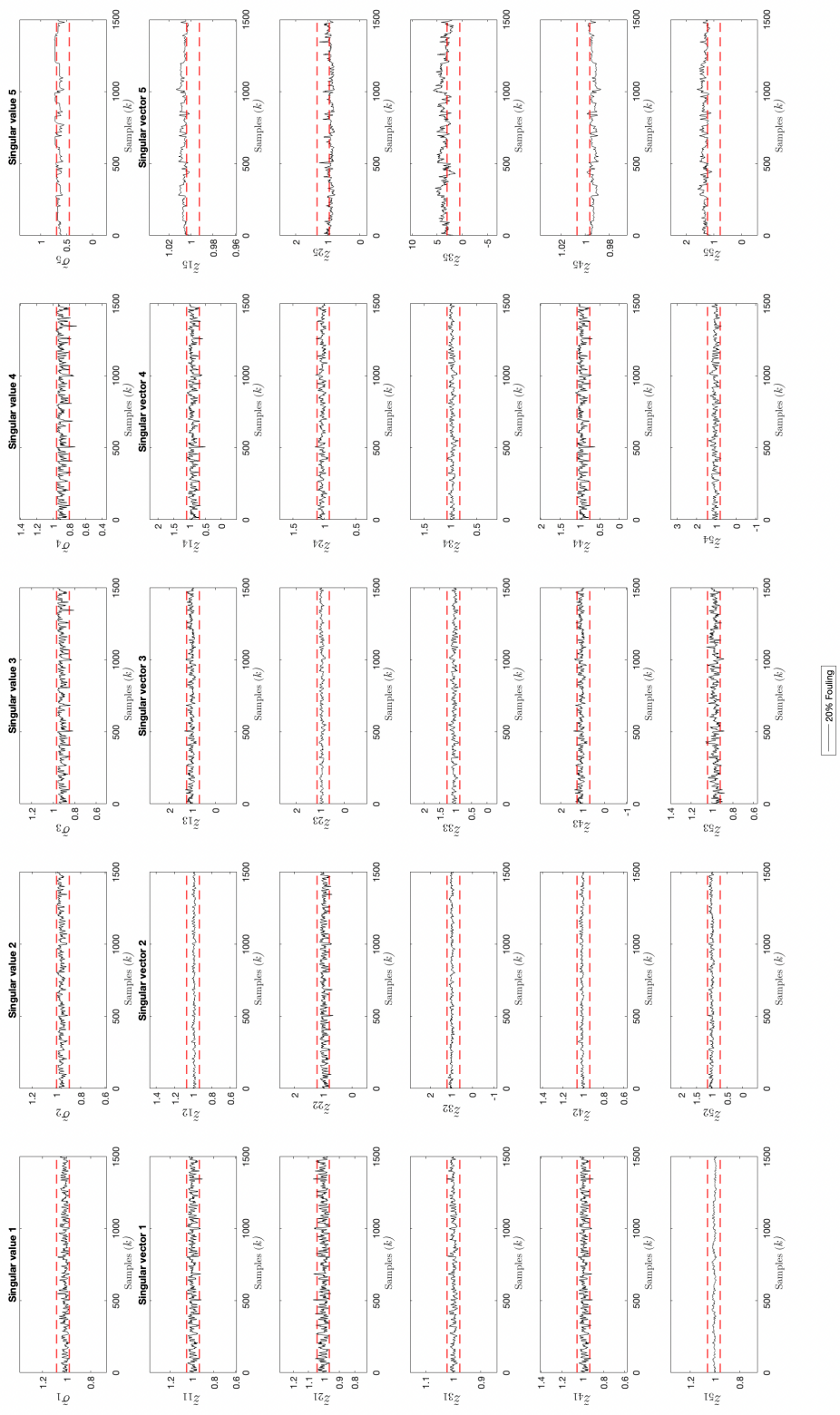


Figure B.23: EWMA SVD results for PU2 fouling

B.3 Fault signature results

B.3.1 Process Unit 1 Clogs

Table B.1: Modelled PU1 10% Clog

$\tilde{\boldsymbol{\sigma}}$	0	−	−	0	0
$\tilde{\mathbf{Z}}$	0	0	0	0	+
	0	0	0	+	−
	0	0	0	+	+
	0	0	0	0	−
	0	0	−	+	+

Table B.2: Practical PU1 10% Clog

$\tilde{\boldsymbol{\sigma}}$	0	0	0	0	0
$\tilde{\mathbf{Z}}$	0	0	0	0	+
	0	0	0	+	0
	0	0	0	0	+
	0	0	0	0	−
	0	0	−	0	+

Table B.3: Modelled PU1 20% Clog

$\tilde{\boldsymbol{\sigma}}$	0	−	−	−	−
$\tilde{\mathbf{Z}}$	0	0	0	−	+
	0	0	−	+	0
	0	0	+	−	+
	0	0	0	0	−
	+	0	−	+	+

Table B.4: Practical PU1 20% Clog

$\tilde{\boldsymbol{\sigma}}$	0	0	0	0	0
$\tilde{\mathbf{Z}}$	0	0	0	0	+
	0	0	0	+	0
	0	0	0	−	+
	0	0	+	0	−
	0	0	−	+	+

Table B.5: Modelled PU1 30% Clog

$\tilde{\boldsymbol{\sigma}}$	0	−	−	−	−
$\tilde{\mathbf{Z}}$	0	0	0	−	+
	0	0	−	+	0
	0	0	+	−	+
	0	0	+	−	−
	+	0	−	+	+

Table B.6: Practical PU1 30% Clog

$\tilde{\boldsymbol{\sigma}}$	0	−	−	−	−
$\tilde{\mathbf{Z}}$	0	0	+	−	+
	0	0	−	+	0
	0	0	+	−	+
	0	0	+	−	−
	0	0	−	+	+

B.3.2 Process Unit 2 Clogs

Table B.7: Modelled PU2 10% Clog

$\tilde{\boldsymbol{\sigma}}$	0	−	−	−	−
$\tilde{\mathbf{Z}}$	0	0	−	+	−
	0	+	0	−	+
	0	0	0	0	+
	0	0	−	+	+
	+	−	+	0	+

Table B.8: Practical PU2 10% Clog

$\tilde{\boldsymbol{\sigma}}$	0	−	−	−	−
$\tilde{\mathbf{Z}}$	0	0	−	+	0
	0	+	0	0	0
	0	0	0	0	0
	0	0	−	+	0
	+	−	+	0	+

Table B.9: Modelled PU2 20% Clog

$\tilde{\boldsymbol{\sigma}}$	0	−	−	−	−
$\tilde{\mathbf{Z}}$	−	0	−	+	−
	0	+	−	−	+
	0	−	0	0	+
	−	0	−	+	+
	+	−	+	0	+

Table B.10: Practical PU2 20% Clog

$\tilde{\boldsymbol{\sigma}}$	0	−	−	−	−
$\tilde{\mathbf{Z}}$	−	0	−	+	−
	0	+	0	−	+
	0	0	0	0	+
	−	0	−	+	+
	+	−	+	0	+

Table B.11: Modelled PU2 30% Clog

$\tilde{\boldsymbol{\sigma}}$	0	−	−	−	−
$\tilde{\mathbf{Z}}$	−	0	−	+	−
	0	+	−	−	+
	0	−	0	0	+
	−	0	−	+	+
	+	−	+	0	+

Table B.12: Practical PU2 30% Clog

$\tilde{\boldsymbol{\sigma}}$	0	−	−	−	−
$\tilde{\mathbf{Z}}$	−	0	−	+	−
	0	+	0	−	+
	0	0	0	0	+
	−	0	−	+	+
	+	−	+	−	+

B.3.3 Process Unit 1 Leaks

Table B.13: Modelled PU1 10% Leak

$\tilde{\boldsymbol{\sigma}}$	0	0	0	0	0
$\tilde{\mathbf{Z}}$	0	0	0	0	0
	0	0	0	0	0
	0	0	0	0	0
	0	0	0	0	0
	0	0	0	0	0

Table B.14: Practical PU1 10% Leak

$\tilde{\boldsymbol{\sigma}}$	0	0	0	0	0
$\tilde{\mathbf{Z}}$	0	0	0	0	0
	0	0	0	0	0
	0	0	0	0	0
	0	0	0	0	0
	0	0	0	0	0

Table B.15: Modelled PU1 20% Leak

$\tilde{\boldsymbol{\sigma}}$	+	+	0	0	0
$\tilde{\mathbf{Z}}$	+	0	0	0	0
	−	0	0	0	0
	0	0	0	0	0
	+	0	0	0	0
	0	0	0	0	0

Table B.16: Practical PU1 20% Leak

$\tilde{\boldsymbol{\sigma}}$	+	0	0	0	0
$\tilde{\mathbf{Z}}$	+	0	0	0	0
	−	0	0	0	0
	0	0	0	0	0
	+	0	0	0	0
	0	0	0	0	0

Table B.17: Modelled PU1 30% Leak

$\tilde{\boldsymbol{\sigma}}$	+	+	0	0	0
$\tilde{\mathbf{Z}}$	+	0	0	0	0
	−	0	0	0	0
	0	−	0	0	0
	+	0	0	0	0
	0	0	0	0	0

Table B.18: Practical PU1 30% Leak

$\tilde{\boldsymbol{\sigma}}$	+	+	0	0	0
$\tilde{\mathbf{Z}}$	+	0	0	0	0
	−	0	0	0	0
	0	−	0	0	0
	+	0	0	0	0
	0	0	0	0	0

B.3.4 Process Unit 2 Leaks

Table B.19: Modelled PU2 10% Leak

$\tilde{\boldsymbol{\sigma}}$	0	0	0	0	0
$\tilde{\mathbf{Z}}$	0	0	0	0	0
	0	0	0	0	0
	0	0	0	0	0
	0	0	0	0	0
	0	0	0	0	0

Table B.20: Practical PU2 10% Leak

$\tilde{\boldsymbol{\sigma}}$	0	0	0	0	0
$\tilde{\mathbf{Z}}$	0	0	0	0	0
	0	0	0	0	0
	0	0	0	0	0
	0	0	0	0	0
	0	0	0	0	0

Table B.21: Modelled PU2 20% Leak

$\tilde{\boldsymbol{\sigma}}$	0	0	0	0	0
$\tilde{\mathbf{Z}}$	0	0	0	0	0
	0	0	0	0	0
	0	0	0	0	0
	0	0	0	0	0
	0	0	0	0	0

Table B.22: Practical PU2 20% Leak

$\tilde{\boldsymbol{\sigma}}$	0	0	0	0	0
$\tilde{\mathbf{Z}}$	0	0	0	0	0
	0	0	0	0	0
	0	0	0	0	0
	0	0	0	0	0
	0	0	0	0	0

Table B.23: Modelled PU2 30% Leak

$\tilde{\boldsymbol{\sigma}}$	0	0	0	0	0
$\tilde{\mathbf{Z}}$	0	0	0	0	0
	0	0	0	0	0
	0	0	0	0	0
	0	0	0	0	0
	0	0	0	0	0

Table B.24: Practical PU2 30% Leak

$\tilde{\boldsymbol{\sigma}}$	0	0	0	0	0
$\tilde{\mathbf{Z}}$	0	0	0	0	0
	0	0	0	0	0
	0	0	0	0	0
	0	0	0	0	0
	0	0	0	0	0

B.3.5 Process Unit 1 stuck valve

Table B.25: Modelled PU1 stuck valve

$\tilde{\boldsymbol{\sigma}}$	−	−	−	−	−
$\tilde{\mathbf{Z}}$	−	0	0	−	+
	0	0	0	+	0
	0	0	0	0	+
	−	+	0	−	−
	+	0	0	0	+

Table B.26: Practical PU1 stuck valve

$\tilde{\boldsymbol{\sigma}}$	−	−	−	−	−
$\tilde{\mathbf{Z}}$	0	0	0	−	+
	0	0	0	+	0
	0	0	0	0	+
	−	+	0	0	−
	0	0	−	0	+

B.3.6 Process Unit 2 stuck valve

Table B.27: Modelled PU2 stuck valve

$\tilde{\boldsymbol{\sigma}}$	0	−	−	−	0
$\tilde{\mathbf{Z}}$	0	0	−	+	−
	0	+	0	−	0
	0	0	0	0	+
	0	0	−	+	+
	+	−	+	0	0

Table B.28: Practical PU2 stuck valve

$\tilde{\boldsymbol{\sigma}}$	0	0	−	0	0
$\tilde{\mathbf{Z}}$	0	0	−	+	0
	0	0	0	0	0
	0	0	0	0	0
	0	0	−	+	0
	0	0	+	0	0

B.3.7 Process Unit 1 Sensor drifts

Table B.29: Modelled PU1 2% sensor drift

$\tilde{\boldsymbol{\sigma}}$	0	−	−	−	−
$\tilde{\mathbf{Z}}$	0	0	0	0	+
	0	+	−	0	0
	0	0	+	−	+
	0	0	0	+	−
	0	−	0	+	+

Table B.30: Practical PU1 2% sensor drift

$\tilde{\boldsymbol{\sigma}}$	0	−	0	0	−
$\tilde{\mathbf{Z}}$	0	0	0	0	+
	0	0	0	0	0
	0	0	+	−	0
	0	0	0	0	−
	0	0	−	+	+

Table B.31: Modelled PU1 5% sensor drift

$\tilde{\boldsymbol{\sigma}}$	+	−	−	−	−
$\tilde{\mathbf{Z}}$	0	−	0	+	+
	−	+	−	0	0
	−	0	+	−	0
	0	0	0	+	−
	0	−	−	+	+

Table B.32: Practical PU1 5% sensor drift

$\tilde{\boldsymbol{\sigma}}$	+	−	−	−	−
$\tilde{\mathbf{Z}}$	0	−	0	+	+
	−	+	−	0	0
	−	+	+	−	0
	0	−	0	+	−
	0	0	−	+	+

B.3.8 Process Unit 2 Sensor drifts

Table B.33: Modelled PU2 2% sensor drift

$\tilde{\boldsymbol{\sigma}}$	0	−	−	−	−
$\tilde{\mathbf{Z}}$	0	0	−	0	−
	−	+	−	0	+
	−	−	+	−	0
	0	0	−	0	+
	+	−	−	+	−

Table B.34: Practical PU2 2% sensor drift

$\tilde{\boldsymbol{\sigma}}$	0	−	−	0	−
$\tilde{\mathbf{Z}}$	0	0	0	0	−
	−	+	−	0	0
	−	−	+	−	0
	0	0	0	0	+
	+	−	−	+	−

Table B.35: Modelled PU2 5% sensor drift

$\tilde{\boldsymbol{\sigma}}$	0	−	−	−	−
$\tilde{\mathbf{Z}}$	0	0	−	+	−
	−	+	−	0	+
	−	−	+	−	0
	+	0	−	+	+
	+	−	−	+	−

Table B.36: Practical PU2 5% sensor drift

$\tilde{\boldsymbol{\sigma}}$	0	−	−	−	−
$\tilde{\mathbf{Z}}$	0	0	0	0	−
	−	+	−	0	+
	−	−	+	−	+
	+	0	0	0	+
	+	−	−	+	−

B.3.9 Process Unit 1 fouling

Table B.37: Modelled PU1 20% fouling

$\tilde{\boldsymbol{\sigma}}$	+	0	0	0	0
$\tilde{\mathbf{Z}}$	0	0	0	0	0
	0	0	0	0	0
	0	0	0	0	0
	0	0	0	0	0
	−	0	0	0	0

Table B.38: Practical PU1 20% fouling

$\tilde{\boldsymbol{\sigma}}$	0	0	0	0	0
$\tilde{\mathbf{Z}}$	0	0	0	0	0
	0	0	0	0	0
	0	0	0	0	0
	0	0	0	0	0
	0	0	0	0	0

B.3.10 Process Unit 2 fouling

Table B.39: Modelled PU2 20% fouling

$\tilde{\boldsymbol{\sigma}}$	0	0	0	0	0
$\tilde{\mathbf{Z}}$	0	0	0	0	0
	0	0	0	0	0
	0	0	0	0	0
	0	0	0	0	0
	0	0	0	0	0

Table B.40: Practical PU2 20% fouling

$\tilde{\boldsymbol{\sigma}}$	0	0	0	0	0
$\tilde{\mathbf{Z}}$	0	0	0	0	+
	0	0	0	0	−
	0	0	0	0	+
	0	0	0	0	−
	0	0	0	0	+

APPENDIX

C

PRINCIPAL COMPONENT ANALYSIS ISOLATION RESULTS

C.1 Introduction

Appendix C is dedicated to the fault isolation results of PCA. As explained in Chapter 5, the fault signatures are simply the tabulated contribution values of each process variable (PV) during the process fault. These results are used when analysing the *degree* of isolation between fault types. The outlying contributions are highlighted in red for ease of inspection.

The appendix is structured similar to Chapter 5, where the results for each fault type and for each PU are allocated within a different subsection. The different sizes of the same fault type that occurs in the same PU are captured in a single table, to highlight the effect of different fault sizes for a given fault. Additionally, the highest contributors are only highlighted if the fault was detected in Chapter 5.

C.2 Fault signature results

C.2.1 Process Unit 1 clogs

Table C.1: Fault signature for model PU1 clogs

Fault size	L_1	L_2	T_1	T_2	F_1	F_2	F_3	F_4
10%	0.52	0.60	0.07	0.08	0.53	1.20	0.72	0.08
20%	0.54	0.78	0.17	0.13	0.58	3.17	1.50	0.09
30%	0.56	1.09	0.16	0.02	0.65	6.50	1.68	0.02

Table C.2: Fault signature for practical PU1 clogs

Fault size	L_1	L_2	T_1	T_2	F_1	F_2	F_3	F_4
10%	0.59	0.55	0.11	0.19	0.64	1.23	0.44	0.15
20%	0.63	0.60	0.13	0.22	0.77	1.51	0.59	0.17
30%	0.78	0.90	0.16	0.16	1.13	3.57	0.83	0.14

C.2.2 Process Unit 2 clogs

Table C.3: Fault signature for model PU2 clogs

Fault size	L_1	L_2	T_1	T_2	F_1	F_2	F_3	F_4
10%	0.59	2.16	0.41	0.73	0.61	19.60	1.12	1.83
20%	0.77	26.28	1.25	1.62	0.80	81.30	1.78	5.77
30%	1.26	382.93	2.19	2.21	1.35	182.06	2.13	8.24

Table C.4: Fault signature for practical PU2 clogs

Fault size	L_1	L_2	T_1	T_2	F_1	F_2	F_3	F_4
10%	0.92	1.30	0.20	0.22	0.95	6.91	0.56	1.07
20%	1.50	4.23	0.31	0.45	1.50	26.77	0.69	2.70
30%	5.42	341.01	1.23	0.56	5.36	99.83	1.10	6.30

C.2.3 Process Unit 1 leaks

Table C.5: Fault signature for model PU1 leaks

Fault size	L_1	L_2	T_1	T_2	F_1	F_2	F_3	F_4
10%	0.52	0.54	0.09	0.12	0.64	0.54	0.213	0.36
20%	0.53	0.53	0.17	0.13	1.01	0.54	0.22	0.27
30%	0.57	0.53	0.07	0.08	1.62	0.54	0.10	0.14

Table C.6: Fault signature for practical PU1 leaks

Fault size	L_1	L_2	T_1	T_2	F_1	F_2	F_3	F_4
10%	0.51	0.43	0.21	0.21	0.56	0.47	0.23	0.16
20%	0.62	0.53	0.21	0.23	1.57	0.53	0.25	0.18
30%	0.87	0.66	0.23	0.23	4.01	0.75	0.25	0.16

C.2.4 Process Unit 2 leaks

Table C.7: Fault signature for model PU2 leaks

Fault size	L_1	L_2	T_1	T_2	F_1	F_2	F_3	F_4
10%	0.52	0.55	0.14	0.15	0.52	0.62	0.18	0.19
20%	0.52	0.58	0.26	0.31	0.52	0.90	0.32	0.28
30%	0.52	0.63	0.18	0.19	0.52	1.53	0.24	0.20

Table C.8: Fault signature for practical PU2 leaks

Fault size	L_1	L_2	T_1	T_2	F_1	F_2	F_3	F_4
10%	0.56	0.56	0.18	0.24	0.59	0.61	0.25	0.21
20%	0.56	0.48	0.18	0.23	0.61	0.65	0.27	0.17
30%	0.60	0.62	0.18	0.22	0.65	0.87	0.27	0.19

C.2.5 Process Unit 1 stuck valve

Table C.9: Fault signature for model PU1 stuck valve

Fault size	L_1	L_2	T_1	T_2	F_1	F_2	F_3	F_4
N/A	39.86	0.64	0.60	0.21	0.07	1.68	1.42	0.28

Table C.10: Fault signature for practical PU1 stuck valve

Fault size	L_1	L_2	T_1	T_2	F_1	F_2	F_3	F_4
N/A	256.23	3.34	0.68	0.33	0.03	5.56	2.07	0.43

C.2.6 Process Unit 2 stuck valve

Table C.11: Fault signature for model PU2 stuck valve

Fault size	L_1	L_2	T_1	T_2	F_1	F_2	F_3	F_4
N/A	0.62	54.73	0.50	0.94	0.64	2.57	0.60	1.84

Table C.12: Fault signature for practical PU2 stuck valve

Fault size	L_1	L_2	T_1	T_2	F_1	F_2	F_3	F_4
N/A	2.49	146.93	0.69	0.43	2.61	0.26	0.59	0.32

C.2.7 Process Unit 1 sensor drifts

Table C.13: Fault signature for model PU1 sensor drifts

Fault size	L_1	L_2	T_1	T_2	F_1	F_2	F_3	F_4
2%	0.52	0.57	2.56	0.44	0.52	0.59	3.35	0.49
5%	0.54	0.80	34.29	0.64	0.54	0.83	13.05	0.91

Table C.14: Fault signature for practical PU1 sensor drifts

Fault size	L_1	L_2	T_1	T_2	F_1	F_2	F_3	F_4
2%	0.55	0.52	1.47	0.32	0.57	0.55	2.33	0.27
5%	0.67	0.67	18.32	0.98	0.68	0.66	8.56	0.75

C.2.8 Process Unit 2 sensor drifts

Table C.15: Fault signature for model PU2 sensor drifts

Fault size	L_1	L_2	T_1	T_2	F_1	F_2	F_3	F_4
2%	0.52	0.57	0.48	2.36	0.52	0.58	0.59	2.97
5%	0.54	0.75	1.10	31.76	0.53	0.77	1.96	11.89

Table C.16: Fault signature for practical PU2 sensor drifts

Fault size	L_1	L_2	T_1	T_2	F_1	F_2	F_3	F_4
2%	0.55	0.512	0.40	1.13	0.58	0.43	0.44	1.80
5%	0.58	0.47	0.52	17.37	0.59	0.43	0.73	6.80

C.2.9 Process Unit 1 fouling

Table C.17: Fault signature for model PU1 fouling

Fault size	L_1	L_2	T_1	T_2	F_1	F_2	F_3	F_4
N/A	0.51	0.54	0.15	0.35	0.51	0.54	1.98	1.13

Table C.18: Fault signature for practical PU1 fouling

Fault size	L_1	L_2	T_1	T_2	F_1	F_2	F_3	F_4
N/A	0.49	1.03	0.62	0.59	0.52	1.05	0.56	0.36

C.2.10 Process Unit 2 fouling

Table C.19: Fault signature for model PU2 fouling

Fault size	L_1	L_2	T_1	T_2	F_1	F_2	F_3	F_4
N/A	0.51	0.50	0.06	0.04	0.51	0.50	0.17	0.22

Table C.20: Fault signature for practical PU2 fouling

Fault size	L_1	L_2	T_1	T_2	F_1	F_2	F_3	F_4
N/A	0.56	0.69	0.02	0.01	0.57	0.68	0.05	0.01

APPENDIX

D

INSTRUMENTATION DESIGN & IMPLEMENTATION

D.1 Introduction

As part of this work, the author was tasked with the design of the process instrumentation of the practical process. This appendix aims to provide an overview of this design input, which includes the formal design documentation generated before the practical system's construction. The author deems it important that the design of the process be captured formally and thoroughly, as it will enable easier and safer process expansion for future studies.

The process design document is described first, which is followed by the instrumentation design documents. Finally, photos of the practical system are provided for a visual illustration of the implementation.

D.2 Piping & instrumentation diagram

Figure D.1 illustrates the piping & instrumentation diagram (P&ID) of the practical heated two-tank process, which was designed, developed and built by P. Oberholzer [116]. The purpose of this diagram is to provide an overview of the process by showing all major

process equipment involved and how they are connected. It also shows what process variables are measured and controlled. In this work, the P&ID served as the principal process design document. All engineering disciplines involved in the project were required to design according to the P&ID, thus ensuring inter-discipline compatibility. It is therefore appropriate to discuss this document first. It should be noted that this diagram is not current and only reflects the plant design as an 'approved for construction' revision.

D.2.1 Major process components

The large blocks in the diagram represent the major process components and have unique equipment tags. Table D.1 lists the service description of these components. A formal tagging philosophy was followed for the process equipment. The 'C-' prefix indicates external heat exchange components, while the 'F-' prefix represents storage components both internal and external to the process. Because the heat exchange system in F-N301 and F-N302 are not discrete components, they are identified under the former and latter tags. The label 'N3' indicates the location of the components. In this case, all components are located in engineering lab N3. The double-digit suffix is the final tag modifier for uniqueness.

Table D.1: Major process component service descriptions [116]

Equipment name	Service description
C-N301	External cold water heat exchanger (Chiller)
C-N302	External hot water reservoir (Geyser)
C-N303	External hot water heat exchanger (Gas heater)
F-N301	PU1 water tank
F-N302	PU2 water tank
F-N303	External cold water reservoir

D.2.2 Process piping

The solid lines in the diagram represent the process piping that connects the major components. These lines are also uniquely identifiable by their line number. The line number and their service description are given in Table D.2. The only process lines not indicated by solid lines are the copper tubes for heat exchange in F-N301 and F-N302, which are indicated as short-striped lines. As with the major process equipment, the process piping is formally labelled according to the tagging philosophy of the process design team. Note that the pipeline responsible for leakage emulation on PU2 is not shown on this diagram, since it was added as part of the construction phase.

Table D.2: Process line service description [116]

Line number	Service description
25–H2O–1701:01	Hot water feed to PU1
25–H2O–1702:02	Hot water return from PU1
25–H2O–1701:03	Hot water feed to PU2
25–H2O–1703:04	Hot water return from PU2
25–H2O–1701:13	Hot water circulation loop
25–H2O–1704:05	Cold water feed to PU1
25–H2O–1704:06	Cold water feed to PU2
25–H2O–1704:09	Cold water leak emulation for PU1
25–H2O–1702:10	Cold water drain from PU1 to reservoir
25–H2O–1703:11	Cold water drain from PU2 to reservoir
25–H2O–1703:08	Cold water return from PU2 to reservoir
25–H2O–1703:07	Cold water feed from PU1 to PU2
25–H2O–1704:12	Cold water circulation loop

D.2.3 Rotating machinery

Two types of rotating electrical machinery are included to maintain process operation, namely pumps and agitators (mixers). The pumps are required for line pressurization such that the process liquid can be transported to its destination. A total of six pumps were used as shown in the P&ID and are listed in Table D.3. Two agitators are included to ensure homogeneous temperature distribution throughout PU1 and PU2 and are also listed in Table D.3. The prefixes 'J-' and 'JM-' were used to uniquely describe the pumps and agitators, respectively. The suffixes follow the same philosophy as described in Section D.2.1.

Table D.3: Rotating machinery service description [116]

Tag number	Service description
J-N301	PU1 cold water feed pump
J-N302	PU2 cold water feed pump
J-N303	Cold water circulation pump
J-N304	PU1 hot water feed pump
J-N305	PU2 hot water feed pump
J-N306	Hot water circulation pump
JM-N301	PU1 agitator
JM-N302	PU2 agitator

D.2.4 Instrumentation

The instrumentation required for measurement and control is shown on the P&ID by the circle and blocked circle shapes. The plain circular devices are physical sensors, while the blocked circle shapes indicate their software configuration and more specifically their purpose, which may be either monitoring service or process control service. Control service loops have a continuous connection from the sensor through the software configuration block to a valve. The electrical connections between these components are distinguished from process piping by their short-striped lines. The list of process instrumentation is given in Table D.4 and serves as an index of the measurement hardware and the involved software, thus capturing its scope. It is compiled from the P&ID diagram.

Note that Table D.4 shows the instrumentation linked to the main process, which comprises PU1 and PU2. Temperature measurements $T_{1,in}$, $T_{2,in}$, T_3 and T_4 referred to in Chapter 3 are linked to the hot and cold water supply utilities C-N301, C-N302, C-N303 and F-N303 and are regarded to be external to the main process.

The first column shows the loop numbers. A loop is defined as the group of instruments and their software that perform a process function or service [117]. The latter function description is given in the second column. The third column shows the tag numbers, which follow a tagging philosophy similar to that of the major process components. All tags have the 'N3' designation to denote the laboratory they are located in. The first letter of the second segment describes the property of the process that is measured, and the second letter specifies the component of the loop. Finally, a sequence number is added as a suffix for uniqueness. For example, the tag 'N3-TV-001' describes a *valve* responsible for *temperature control* in *laboratory N3*.

The columns that follow provide extra information for every individual loop component. The flow, level and temperature transmitters all use 'IO-Link' for communication to the PLC, which is an industrial network communication protocol set out in standard IEC 61131-9:2022 [118]. All valve actuators are operated using analogue outputs (AO) from the PLC, which alternate between 4 to 20 mA to output a 0 to 100% valve open command.

Table D.5 shows the list of valves and their components that were installed for fault emulation, specifically clogging and leakage faults. These have the prefix 'U', denoting miscellaneous service. The stuck valve faults were implemented using normal control valves N3-LV-001 and N3-LV-002 and are shown in Table D.4. The sensor drift faults were implemented in software and are not shown here. The fouling faults also did not have dedicated instrumentation. As noted in Section D.2.2, the PU2 leak fault emulation line is not shown on the P&ID and therefore N3-UV-004 is also not shown. It is shown that valve N3-UV-003 is a manually controlled valve. It replaced the original automated clog valve at the discretion of the process design team to achieve a higher $F_{2,out}$.

The connection between these instruments is described in the next section.

D.3 Connection diagram

The first connection diagram is given in Fig. D.2. The figure shows how the main components are connected, as well as the connection to the instruments. The short striped lines indicate networking and instrument connections, while the solid lines indicate either power connections or panel wiring. The type of device, its manufacturer and model are detailed for every device except for the computer. All components left of the solid middle line in the figure are external to the process, meaning it is either located remotely or in a sealed control panel. The devices on the right of the line are physically connected to the process and are grouped into their origin PU.

The process is controlled by a Siemens S7-1200 PLC (middle left) that is configured and monitored by a generic computer (bottom left) with Siemens Totally Integrated Automation (TIA) Portal software. These devices communicate via a network switch using Ethernet protocol. The process sensors (middle and bottom right) are connected to an IO link master hub (bottom), which transmits the process measurements to the PLC via PROFINET protocol. The two protocols are compatible and are connected through the same network switch. This compatibility is advantageous in that the computer may also be used for instrument fault-finding via the IO link master hub. Furthermore, the use of IO-link compatible devices with the master hub system allows for effortless sensor expansion, should it be required by future studies.

All process valves are controlled with a 4 - 20 mA signal from two Siemens Analogue Output (AO) expansion modules (top right). Each value has a single cable that carries its control signal, as well as its power feed since they are motorized. For this reason, the design includes a terminal strip (top) with bridge pieces for power supply distribution. For process monitoring, a Siemens human-machine interface (HMI) module was installed during construction and is not shown on this diagram.

Figure D.3 shows the connection diagram of the 24 VDC power distribution system, which is responsible for powering the PLC, the AO modules, IO link master hub and valves. A 230 VAC supply is fed to two 24 VDC power supply units through individual circuit breakers for protection. Terminal strip X1 is used to split the supply. The Siemens LOGO! power supply is dedicated to the PLC, while the second power supply feeds the rest of the components. Separate terminal strips (X3 and X4) are used to split 24 VDC and 0 VDC.

The final diagram in Fig. D.4 shows the pump control interface. The pumps are 230 VAC rated, therefore a 230 VAC supply is routed through a circuit breaker and individual relays to each pump. The pumps do not have a dedicated power switch, so the relays directly

fulfil this role. Terminals 'A1' and 'A2' are on the coil side of the relay, thus providing valve control to the PLC. Terminals 'C' and 'NO' represent the contact on the side of the relay and will switch 230 VAC through to the pump as dictated by the PLC.

D.4 Implementation & system description

With the design documents described, the illustration of the completed process is in order. Photos of the completed practical heated two-tank process are provided in Fig. D.5 to Fig. D.11 and illustrate the process equipment described throughout Sections D.2 to D.3. Figure D.5 shows the overall process, including its external process utilities. Close-ups of PU1 and PU2 with their installed process sensors are shown in Figure D.6 and D.7 respectively. The process pumps described in Table D.3 are shown in Fig. D.8 and D.9. Figure D.10 shows the flowmeters, control valves and leak emulation valves. To illustrate the heat exchanger design, the heating coils of PU2 are shown in Fig. D.11. Finally, the numbered items in these figures are combined and referenced in Table D.6.

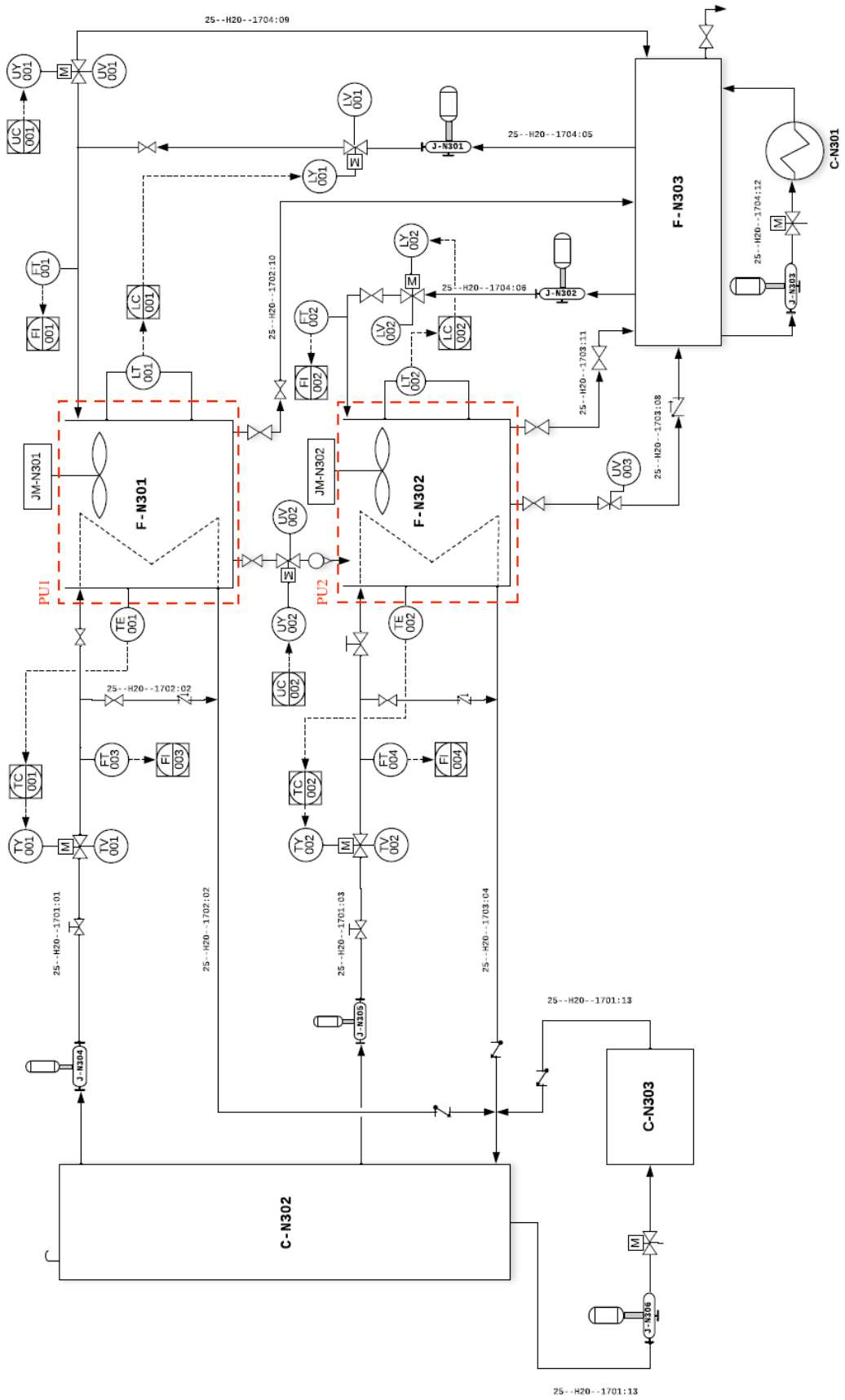


Figure D.1: Piping & instrumentation diagram of the heated two-tank process [116]

Table D.4: Measurement and control instrument list for fault emulation

Loop number	Service description	Tag number	IO type	Signal type	Range	Units	Instrument Type
N3-F-001	PU1 cold water feed	N3-FT-001	IO link	N/A	0.1-1.0	l/s	Flow meter
		N3-FI-001	N/A	N/A	N/A	N/A	Software indication
N3-F-002	PU2 cold water feed	N3-FT-002	IO link	N/A	0.1-1.0	l/s	Flow meter
		N3-FI-002	N/A	N/A	N/A	N/A	Software indication
N3-F-003	PU1 hot water feed	N3-FT-003	IO link	N/A	0.1-1.0	l/s	Flow meter
		N3-FI-003	N/A	N/A	N/A	N/A	Software indication
N3-F-004	PU2 hot water feed	N3-FT-004	IO link	N/A	0.1-1.0	l/s	Flow meter
		N3-FI-004	N/A	N/A	N/A	N/A	Software indication
N3-L-001	PU1 level control	N3-LV-001	N/A	N/A	N/A	N/A	Valve body
		N3-LY-001	AO	4-20 mA	0-100	%	Motorized actuator
		N3-LC-001	N/A	N/A	N/A	N/A	PID software
		N3-LT-001	IO link	N/A	0-0.7	m	Guided wave radar
N3-L-002	PU2 level control	N3-LV-002	N/A	N/A	N/A	N/A	Valve body
		N3-LY-002	AO	4-20 mA	0-100	%	Motorized actuator
		N3-LC-002	N/A	N/A	N/A	N/A	PID software
		N3-LT-002	IO link	N/A	0-0.7	m	Guided wave radar
N3-T-001	PU1 temperature control	N3-TV-001	N/A	N/A	N/A	N/A	Valve body
		N3-TY-001	AO	4-20 mA	0-100	%	Motorized actuator
		N3-TC-001	N/A	N/A	N/A	N/A	PID software
		N3-TE-001	IO link	N/A	0-149	°C	Pt1000 RTD
N3-T-002	PU2 temperature control	N3-TV-002	N/A	N/A	N/A	N/A	Valve body
		N3-TY-002	AO	4-20 mA	0-100	%	Motorized actuator
		N3-TC-002	N/A	N/A	N/A	N/A	PID software
		N3-TE-002	IO link	N/A	0-149	°C	Pt1000 RTD

Table D.5: Measurement and control instrument list for fault emulation

Loop number	Service description	Tag number	IO type	Signal type	Range	Units	Instrument Type
N3-U-001	PU1 leak fault emulation	N3-UC-001	N/A	N/A	N/A	N/A	Software Function
		N3-UV-001	N/A	N/A	N/A	N/A	Valve body
		N3-UY-001	AO	4-20 mA	0-100	%	Motorized actuator
N3-U-002	PU1 clog fault emulation	N3-UC-002	N/A	N/A	N/A	N/A	Software Function
		N3-UV-002	N/A	N/A	N/A	N/A	Valve body
		N3-UY-002	AO	4-20 mA	0-100	%	Motorized actuator
N3-U-003	PU2 clog fault emulation	N3-UV-003	N/A	N/A	N/A	N/A	Manual Valve
N3-U-004	PU2 leak fault emulation	N3-UC-004	N/A	N/A	N/A	N/A	Software Function
		N3-UV-004	N/A	N/A	N/A	N/A	Valve body
		N3-UY-004	AO	4-20 mA	0-100	%	Motorized actuator

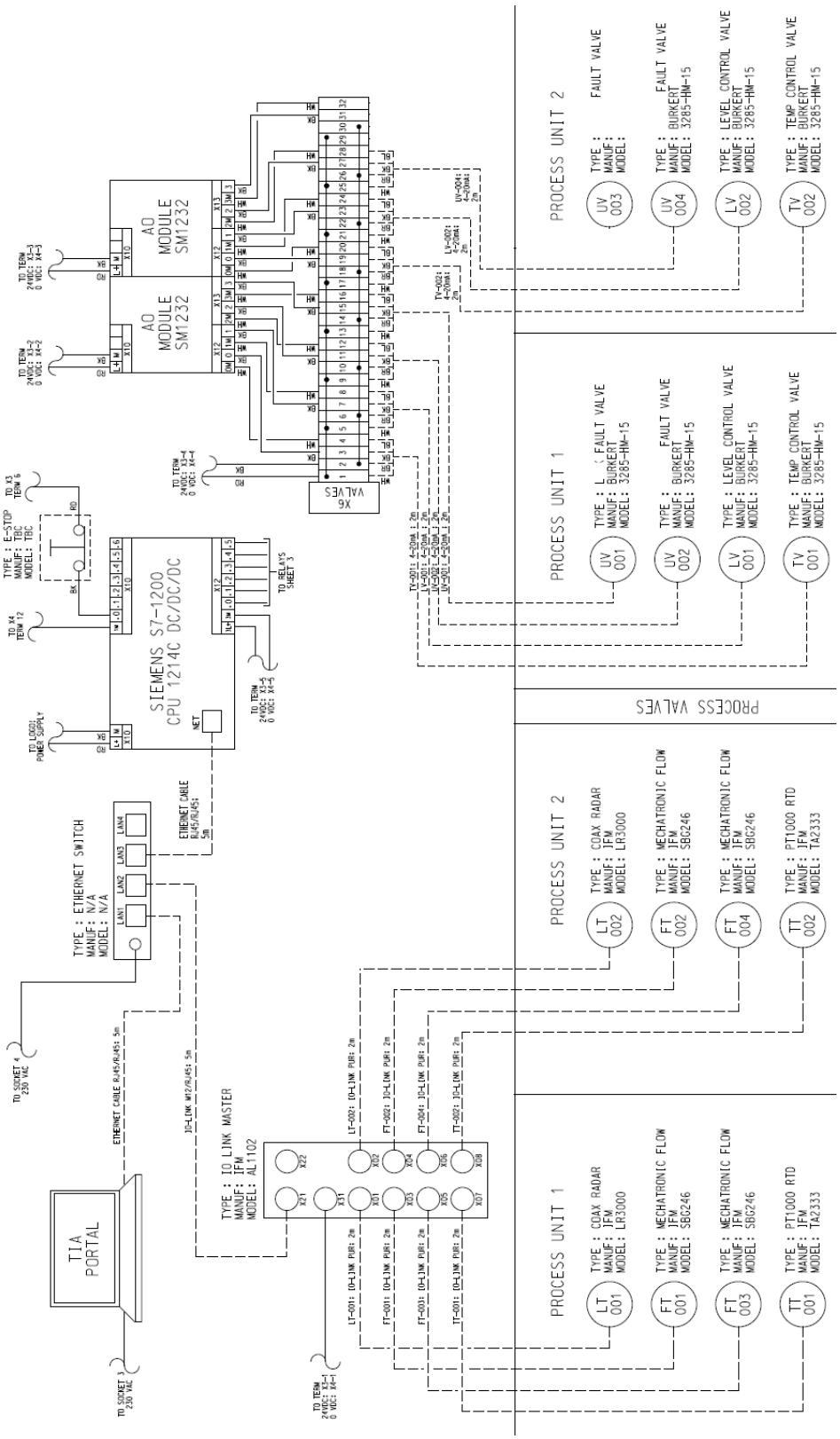


Figure D.2: General instrumentation connection diagram

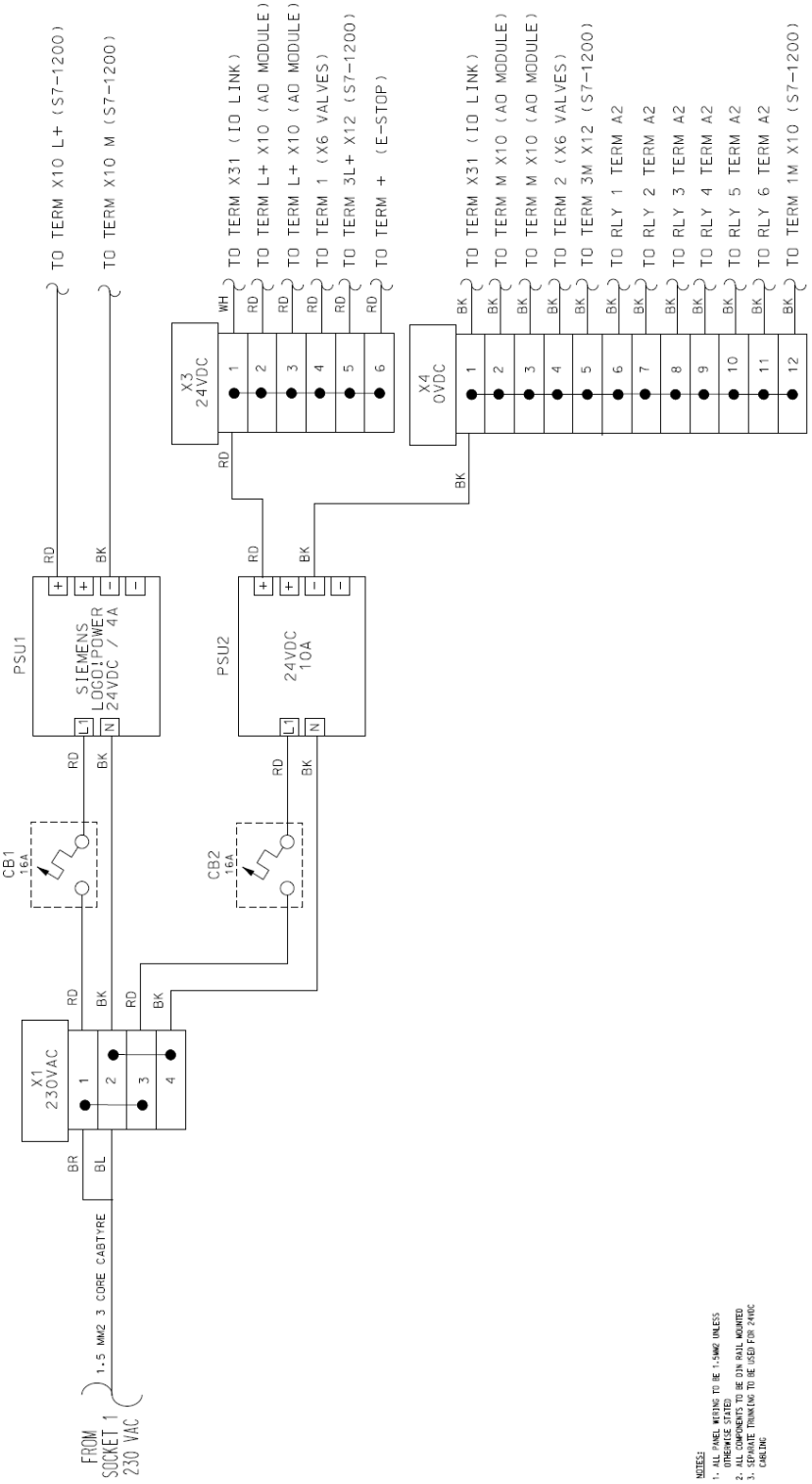


Figure D.3: Instrumentation 24 VDC power distribution

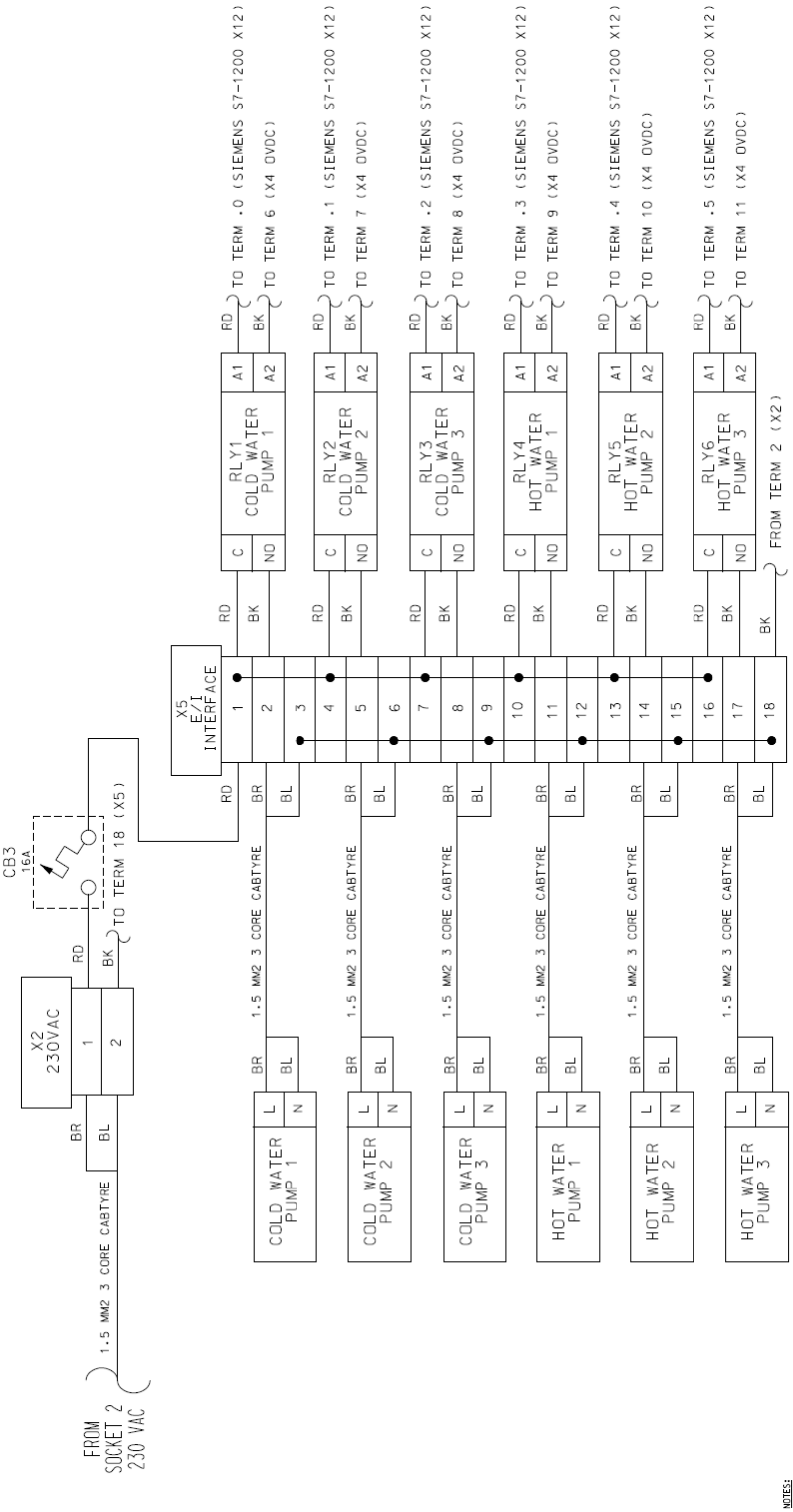


Figure D.4: Pump power and switching diagram

Table D.6: Practical heated two-tank component list for Fig. D.5 to D.11

Item number	Tag number	Item description
1	N/A	Control panel, PLC and HMI
2	F-N302	PU2 water tank
3	F-N303	External cold water reservoir
4	F-N301	PU1 water tank
5	C-N303	External hot water heat exchanger (Gas heater)
6	C-N302	External hot water reservoir (Geyser)
7	C-N301	External cold water heat exchanger (Chiller)
8	JM-N301	PU1 agitator
9	N3-UV-002	PU1 clog valve
10	N3-LT-001	PU1 level sensor
11	N3-TE-001	PU1 temperature sensor
12	JM-N302	PU2 agitator
13	N3-UV-003	PU2 clog valve
14	N3-LT-002	PU2 level sensor
15	N3-TE-001	PU1 temperature sensor
16	J-N302	PU2 cold water feed pump
17	J-N301	PU1 cold water feed pump
18	J-N303	Cold water circulation pump
19	J-N304	PU1 hot water feed pump
20	J-N305	PU2 hot water feed pump
21	J-N306	Hot water circulation pump
22	N3-TV-001	PU1 temperature control valve
23	N3-TV-002	PU2 temperature control valve
24	N3-FT-003	PU1 hot water flow meter
25	N3-FT-004	PU2 hot water flow meter
26	N3-UV-001	PU1 leak emulation valve
27	N3-LV-001	PU1 level control valve
28	N3-LV-002	PU2 level control valve
29	N3-UV-004	PU2 leak emulation valve
30	N3-FT-002	PU2 cold water flow meter
31	N3-FT-001	PU1 cold water flow meter
32	N/A	Heating coil for PU2
33	N/A	Agitator blades



Figure D.5: Photograph of practical heated two-tank process plant



Figure D.6: Photograph of PU1 and its sensors

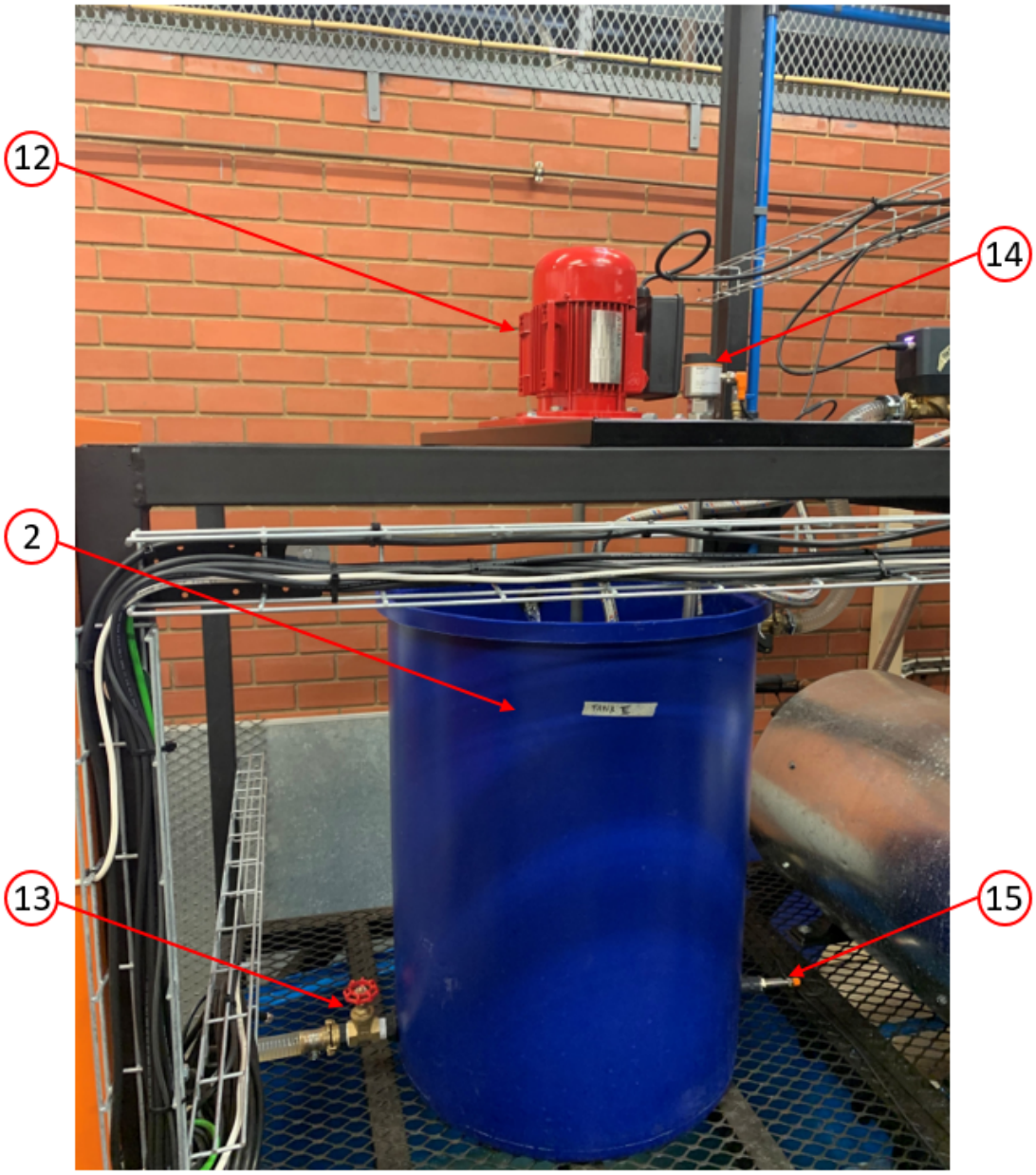


Figure D.7: Photograph of PU2 and its sensors



Figure D.8: Photograph of cold water pumps



Figure D.9: Photograph of hot water pumps



Figure D.10: Photograph of flowmeters, control valves and leak emulation valves

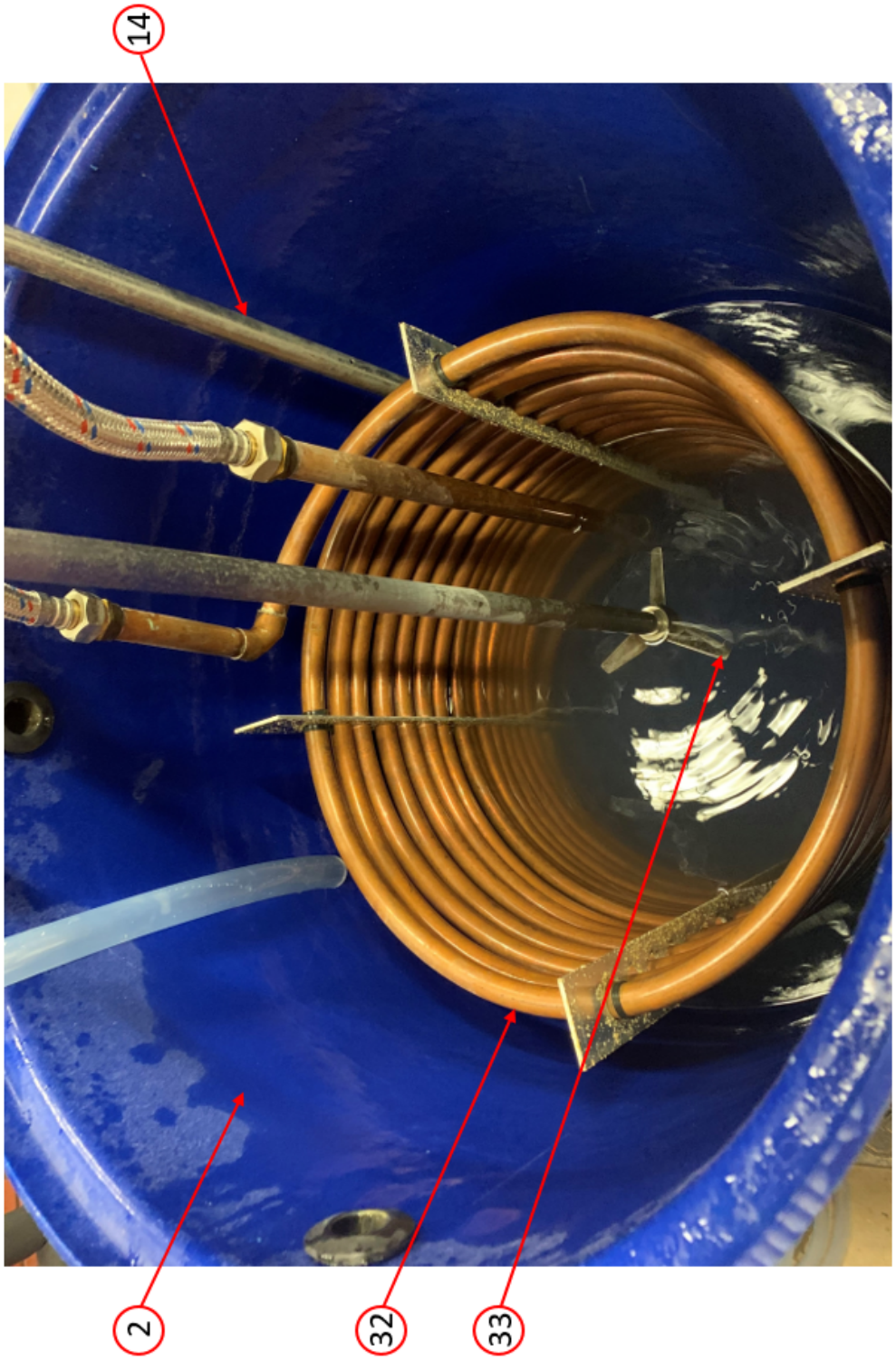


Figure D.11: Photograph of heat exchanger coil inside PU2